Focused ultrasound: a non-invasive brain stimulation modality

Joseph Blackmore

Wadham College

Department of Engineering Science



A thesis submitted for the degree of Doctor of Philosophy

Michaelmas Term 2018

Focused ultrasound: a non-invasive brain stimulation modality

by Joseph Blackmore, Wadham College,
supervised by Professor Robin Cleveland.

Abstract

Non-invasive brain stimulation techniques allow for excitation or inhibition of neural activity via externally applied stimuli. Recently, ultrasound (US) has been shown to stimulate neurons with better spatial localisation than existing electrical stimulation modalities. We present a review of the literature in both the central and peripheral nervous systems demonstrating a range of effects from de novo action potential generation in isolated cell preparations to cognitive responses in humans. However, several questions remain before the technique can become widespread. These include: methods to accurately model, and deliver, transcranial US to specific brain targets; the safety of the approach from both a mechanical and thermal standpoint; elucidation of the fundamental mechanisms through which acoustic perturbations result in nervous system modulation; and the development of monitoring techniques to confirm US focusing in vivo as well as to detect the induced effects. In this thesis, we focus on the delivery and safety aspects. We present numerical simulations using k-Wave and experimental measurements demonstrating focusing to areas of the visual cortex using ex-vivo human skulls with single-element transducers. We show that targeting of many areas can be achieved without the use of lenses or arrays. Furthermore, we conduct an in-depth safety review detailing the parameter spaces over which studies have been conducted and highlighting any damage areas. In current human studies the technique appears to be safe with minimal, if any, side effects. Finally, we report findings from a human pilot study with the aim of modulating sites within the visual cortex. We present direct evidence of strong non-specific auditory activation following bursts of US confirming previous animal studies. These effects can confound US neuromodulation trials and demands further attention before US can realise its potential as both a scientific instrument to probe brain function and as a therapeutic modality to modulate brain activity.

Acknowledgements

I extend my deepest gratitude to my supervisor, Prof. Robin Cleveland, for his expert teaching, guidance and advice throughout my DPhil. I consider myself incredibly lucky to have been given the opportunity to be involved in all aspects of the scientific process as well as to work with such a diverse set of techniques, methods and people. This is merely a testament to Robin's propensity as a mentor and willingness to allow me to engage in, and help shape, the development of the FUN project. Thank you for everything.

I would also like to recognise all of the collaborators with whom I have had the pleasure of working: Dr. Chris Butler, Dr. Verena Braun and Dr. Michele Veldsman for endless FUN and all things neurological; Dr. Jerome Sallet for his contributions in the pursuit of FUN as well as countless pig-related puns; Dr. Zahid Padamsey for introducing me to the art of electrophysiology; and Dr. Shamit Shrivastava for always challenging conventional wisdom. Thank you all for expanding my horizons and constantly teaching me new things.

To the BUBBL group and all its members who contribute to making it such an exceptional research environment, thank you for all your help, advice and contributions. There are too many people to thank individually but a special mention to Kya for sharing my passion for coffee and Catherine for mocking said obsession. Furthermore, I'm indebted to Daphne Cunningham for all of her help and Jim Fisk and David Salisbury in the workshop for the construction of flawless creations always in good humour.

To my family, thank you for always being there, supporting me and letting me choose my own path. Thanks to all of my friends who have made Oxford such an enjoyable place to both work and live for so many years and in particular, to Rachel, for being a constant source of happiness.

Finally, I would like to thank Wadham College for supporting me during both degrees over the past 8 years, the Doctoral Training Centre for laying the foundations of the DPhil and the Engineering and Physical Sciences Research Council and the National Institute of Health for paying the bills.

Contents

Abstract i

Acknowledgements i

List of Abbreviations and Symbols x

1 Introduction 1

1.1 Motivation . . . 2
1.2 Neuromodulation . . . 3
1.2.1 Applications . . . 6
1.2.2 Invasive approaches . . . 7
1.2.3 Non-invasive methods . . . 13
1.3 Ultrasonic neuromodulation . . . 16
1.3.1 Central nervous system . . . 18
1.3.2 Peripheral nervous system . . . 28
1.3.3 Mechanisms . . . 31
1.3.4 Summary . . . 33
1.4 Transcranial ultrasound targeting . . . 35
1.4.1 Head anatomy . . . 35
1.4.2 Skull bone properties . . . 35
1.4.3 Time reversal . . . 37
1.4.4 Direct measurement . . . 39
1.4.5 MR-ARFI techniques . . . 40
1.4.6 Ultrasonic stars . . . 41
1.4.7 Computational techniques . . . 42
1.5 Monitoring . . . 45

2 Acoustic & thermal solvers 47

2.1 Linear acoustic theory . . . 48
2.2 Elastic wave propagation . . . 50
2.2.1 Linear elasticity . . . 50
2.2.2 Elastodynamics . . . 51
2.2.3 Viscoelastic media . . . 52
2.3 Numerical implementation . . . 53
2.3.1 k-Wave fluid solver . . . 54

2.3.2 k-Wave elastic solver . . . 58
2.3.3 Angular spectrum methods . . . 59
2.4 Test cases & transducer calibration . . . 62
2.4.1 Geometric source implementation . . . 62
2.4.2 Acoustic holography . . . 63
2.4.3 Experimental calibration . . . 65
2.5 Thermal modelling . . . 67
2.5.1 Bioheat equation . . . 67
2.5.2 Numerical solver . . . 68
2.5.3 Test case . . . 68

3 Transcranial ultrasound focusing 71
3.1 Introduction . . . 72
3.2 Methods . . . 75
3.2.1 Medical images & dataset . . . 75
3.2.2 Ultrasound source . . . 77
3.2.3 Computational modelling . . . 78
3.2.4 Mesh resolution study . . . 79
3.2.5 Experimental setup . . . 85
3.3 Simulation results . . . 85
3.3.1 Point source simulations . . . 85
3.3.2 Transducer optimisation . . . 87
3.3.3 Forward simulations . . . 90
3.3.4 Sensitivity to acoustic properties . . . 95
3.3.5 Transducer location sensitivity . . . 98
3.3.6 Effect of transducer angle . . . 101
3.3.7 Elastic simulations . . . 104
3.4 Experimental validation . . . 105
3.5 Depth study . . . 112
3.6 Segmentation comparisons . . . 115
3.6.1 Homogeneous vs. inhomogeneous skull maps . . . 115
3.6.2 MRI vs. CT segmentation . . . 118
3.7 FFA correction . . . 122
3.7.1 Aperture size . . . 122
3.7.2 Phase and amplitude correction . . . 125
3.8 Discussion . . . 128

4 Safety review 134

4.1 Introduction . . . 135
4.2 Ultrasound physics . . . 136
4.2.1 Parameters . . . 136
4.2.2 Bioeffects . . . 137
4.3 Safety metrics . . . 139
4.4 Safety guidelines . . . 140
4.5 Literature review . . . 141
4.5.1 Central nervous system . . . 141
4.5.2 Peripheral nervous system . . . 143
4.5.3 Review of acoustic parameters . . . 143
4.5.4 Thermal effects . . . 147
4.6 Discussion . . . 148

5 Human pilot study **151**
5.1 Introduction . . . 152
5.2 Methods . . . 154
5.2.1 Subjects . . . 154
5.2.2 Magnetic resonance imaging (MRI) . . . 154
5.2.3 Ultrasound parameters & delivery . . . 155
5.2.4 Subject-specific modelling . . . 158
5.2.5 Electroencephalography (EEG) . . . 161
5.2.6 Stereotactic neuronavigation . . . 161
5.2.7 Combined setup . . . 162
5.2.8 Behavioural tasks . . . 164
5.3 Results . . . 168
5.3.1 Predicted acoustic and thermal fields . . . 168
5.3.2 Phosphene perception . . . 172
5.3.3 Auditory effects . . . 172
5.3.4 Behaviour . . . 177
5.3.5 EEG . . . 179
5.3.6 Safety . . . 179
5.4 Discussion . . . 180

6 Conclusions & future work **184**
6.1 Summary . . . 185
6.2 Future work . . . 190
6.3 Conclusions . . . 192

A Mechanisms **194**
A.1 Introduction . . . 194
A.2 Methods . . . 195
A.2.1 Organotypic slices . . . 195
A.2.2 Microscope setup . . . 195
A.2.3 Electrophysiological recordings . . . 196
A.2.4 Sonication parameters . . . 197
A.3 Results . . . 197
A.4 Discussion . . . 199

B US neuromodulation literature synopsis **200**
B.1 CNS studies . . . 200
B.2 PNS studies . . . 207

C US neuromodulation parameters **211**

Bibliography **215**

List of Abbreviations and Symbols

Acronyms

ADV	Acoustic droplet vapourisation
AP	Action potential
ARF	Acoustic radiation force
ARFI	Acoustic radiation force imaging
ASM	Angular spectrum method
BBB	Blood brain barrier
BD	Burst duration
BDC	Burst duty cycle
BDNF	Brain derived neurotrophic factor
BI	Burst interval
BOLD	Blood oxygenation level dependent
CAP	Compound action potential
CFL	Courant-Friedrichs-Lewy number
CNS	Central nervous system
CSF	Cerebrospinal fluid
CT	Computed tomography
CW	Continuous wave
DBS	Deep brain stimulation
DC	Duty cycle
ECoG	Electrocorticography
EEG	Electroencephalography
EMG	Electromyography
ERP	Event-related potential
FDA	Food and drug administration
FD	Finite difference
FFA	Face fusiform area
FFT	Fast Fourier transform
FM	Fluorescent molecule
fMRI	Functional magnetic resonance imaging
FT	Fourier transform
GECI	Genetically-encoded calcium indicator
H&E	Haemotoxylin and Eosin (staining)

HU	Hounsfield unit
HW	Hamming window
ICF	Intracortical facilitation
ISI	Inter-stimulus interval
LFP	Local field potential
M1	Primary motor cortex
MEA	Microelectrode array
MEP	Motor evoked potential
MI	Mechanical index
MRI	Magnetic resonance imaging
MT	Middle temporal area
NIBS	Non-invasive brain stimulation
ODE	Ordinary differential equation
PL	Pulse length
PML	Perfectly matched layer
PNP	Peak negative pressure
PNS	Peripheral nervous system
PPP	Points per period
PPW	Points per wavelength
PS	Pseudospectral
SEP	Somatosensory evoked potential
SICI	Short interval intracortical inhibition
SPBA	Spatial-peak, burst-averaged
SPPA	Spatial-peak, pulse-averaged
SPTA	Spatial-peak, temporal-averaged
SWI	Susceptibility-weighted imaging
tACS	Transcranial alternating current stimulation
tES	Transcranial electric stimulation
tDCS	Transcranial direct current stimulation
TI	Thermal index
TMS	Transcranial magnetic stimulation
TPJ	Temporoparietal junction
tRNS	Transcranial random noise stimulation
TRP	Transient receptor potential
UCA	Ultrasound contrast agent
US	Ultrasound
V1	Primary visual cortex

Symbols

C	Fourth order stiffness tensor	[Pa]
I	Intensity	[W/m^2]
K	Bulk modulus	[Pa]
$\mathbf{S}_F$	Force source (k-Wave)	[m/s^2]
S_M	Mass source (k-Wave)	[kg/(m^3 s)]
T	Temperature	[°C]
V	Volume	[m^3]
W	Power	[W]
a	Source radius	[m]
c	Speed of sound	[m/s]
c_p	Specific heat capacity (at constant pressure)	[J/(kg K)]
f	Frequency	[Hz]
$\mathbf{g}$	Body forces per unit volume	[kg/(m^2 s^2)]
k	Wavenumber	[1/m]
n	Attenuation exponent	
p	Pressure	[Pa]
q	Heat deposition rate	[W/cm^3]
s	Entropy	[J/K]
t	Time	[s]
$\mathbf{u}$	Particle displacement	[m]
$\tilde{u}, \tilde{v}$	Spatial wavenumbers	[1/m]
$\mathbf{v}$	Particle velocity	[m/s]
w	Blood perfusion rate	[1/s]
$\mathbf{x}$	Location vector	[m]
z_{rayl}	Rayleigh distance	[m]
α	Attenuation, $\alpha = \alpha_0 f^n$	[dB/cm]
α_0	Attenuation coefficient	[dB/(cm MHz^n)]
β_T	Isothermal compressibility	[1/Pa]
γ	Deformation angle	[rad]
δ_{ij}	Kronecker delta	
$\boldsymbol{\epsilon}$	Strain tensor	
η	Shear viscosity coefficient	[Pa s]
κ	Thermal conductivity	[W/(m K)]
λ	Lamé's first parameter	[Pa]
μ	Lamé's second parameter: shear modulus	[Pa]
ψ	Scalar potential	

ρ	Density	[kg/m^3]
$\boldsymbol{\sigma}$	Stress tensor	[Pa]
θ	ASM filtering angle	[rad]
χ	Compressional viscosity coefficient	[Pa s]
$\boldsymbol{\psi}$	Vector potential	

1

Introduction

This chapter provides motivation and background for the research reported in this thesis. The concept of neuromodulation is introduced along with possible applications in both clinical and research settings followed by a general introduction to invasive and non-invasive brain stimulation (NIBS) methods. The use of ultrasound (US) as a neuromodulatory technique is then described, reviewing findings in both the central and peripheral nervous systems along with plausible mechanistic underpinnings. Finally, methods to transcranially focus US along with modelling techniques to predict in-situ pressure fields are presented as well as monitoring strategies to confirm focusing and evaluate the induced responses.

1.1 Motivation

Brain stimulation techniques are vital tools in order to probe neurological processes from a cellular scale all the way up to a systems level. Approaches such as the local injection of pharmacological agents (Amiez et al., 2006), micro-stimulation (Histed et al., 2009), and optogenetics (Boyden, 2011) allow for precise neural manipulation of individual cells or brain areas with high spatial precision in animal models. However in humans, optogenetics-based methods are not viable as they require genetic manipulation, injections are inherently invasive and, whilst deep brain stimulation (Perlmutter and Mink, 2006) has been effective in a clinical setting for the treatment of diseases such as Parkinson's disease, it is not viable for probing neural function in healthy volunteers.

The development of non-invasive brain stimulation (NIBS) methods (Polanía et al., 2018) has provided neuroscientists with a tool for modulating neural activity in healthy humans in order to further investigate brain function. The two main established modalities are transcranial electric stimulation (tES) (Nitsche et al., 2008) and transcranial magnetic stimulation (TMS) (Walsh and Cowey, 2000) but both suffer from diffuse fields that are limited in scope to the cortical surface (Deng et al., 2013; Faria et al., 2012).

Ultrasound (US) has recently emerged as a potential alternative NIBS method whereby mechanical stimulation can be delivered with increased focality and penetration depths over its existing electrically-based counterparts, which promises to make US a powerful tool for neuro-scientific research as well as in a clinical setting for the treatment of a plethora of neurological disorders.

Numerous findings both in vitro and in vivo have demonstrated the ability to manipulate neural activity through the application of US, and these are reviewed in Sec. 1.3. However, despite these promising discoveries in animal models, several

challenges remain before US can be considered a viable neuromodulatory modality in humans. Certainly, preliminary studies have already demonstrated that ultrasonic stimulation can modulate the human brain but a number of outstanding questions require further investigation before this approach can become widespread. These include: accurate modelling of transcranial US wave propagation and the resultant in situ pressure distributions; the safety of the approach from both a mechanical and thermal perspective; a more complete mechanistic understanding; and monitoring both in terms of confirming US focusing as well as for the detection of neural modulation.

The aim of this thesis is to address some of these unresolved topics in order to further develop US as a feasible NIBS method. In particular, a numerical modelling pipeline for the placement of a single-element transducer to transcranially focus to a given brain target is developed (Chapter 3) and a safety review of published neuromodulatory US parameters is outlined to aid US parameter selection (Chapter 4). Building on this preliminary work, the findings of the first European human pilot study utilising US to modulate areas of the visual cortex are reported (Chapter 5).

1.2 Neuromodulation

Neuromodulation can be defined in multiple ways. In a neurobiology context, neuromodulation refers to the set of chemicals (neuromodulators) that are released by neurons to regulate a population of surrounding neurons as opposed to neurotransmitters that are typically released by a pre-synaptic neuron to modulate the activity of a directly adjacent neuron across a synapse. However, in this thesis, by neuromodulation we are pertaining to the alteration of nervous system activity through the delivery of an external stimulus. As such, this description is very generalised and the specifics of how nerve activity is modified includes numerous effects over a range of spatial and temporal scales. For example, it could refer to the direct triggering

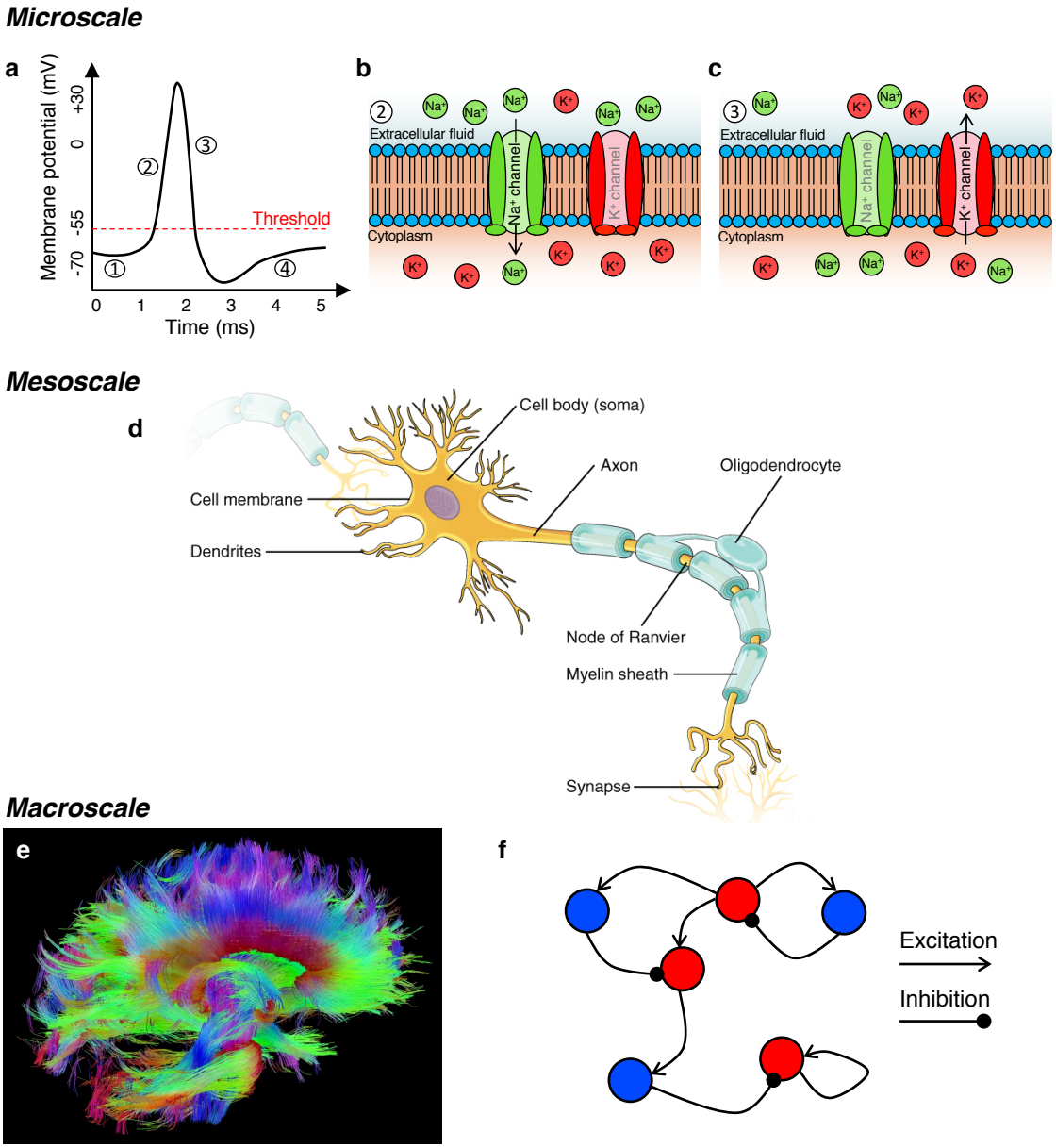


Fig. 1.1: Multi-scale view of brain function. Microscale, a Action potential (AP) profile. Stimuli, either external or from synaptic inputs, depolarise the resting membrane potential (1) and, if of sufficient amplitude to reach the threshold potential ($-55\,\text{mV}$), an impulse is generated through the opening and closing of different ion channels. **b** Voltage-gated sodium channels are opened (2) as a result of the changes in membrane potential allowing the flow of sodium ions into the cell. **c** This is followed by repolarisation (3) through the opening of potassium voltage-gated channels and potassium ions leave the cell. Finally, a sodium-potassium pump (not shown) exchanges sodium and potassium ions to restore the cell to its resting state during the refractory period (4) before the cell can fire again. **Mesoscale, d** Individual neurons or groups of neurons. The neuron is comprised of dendrites where synaptic inputs are received from other neurons, a cell body and an axon. The axon is wrapped in a myelin sheath formed by oligodendrocytes. Small gaps are present in the myelin sheath termed the Nodes of Ranvier in order to speed up the propagation of APs. These APs propagate down the axon to the terminals where they trigger neurotransmitter release across synapses to modulate the activity of downstream neurons. Image reproduced from Lumen-Learning (2017). **Macroscale** At the macroscale, millions are neurons are interconnected through a network. **e** Visualisation of white matter tracts from the Human Connectome Project (Van Essen et al., 2012) depicting the connectivity of the brain. The fibres are colour-coded by direction. **f** Neuronal networks can be considered as brain circuits between connected excitatory and inhibitory nodes in systems level approaches.

of action potentials (APs) through ion channel opening (Fig. 1.1a–c), the resultant secretion of a multitude of different chemical messengers and proteins that regulate neural activity, the inhibition or excitation of populations of neurons through coupled brain circuits (Fig. 1.1f) or the synchronisation or desynchronisation of connected nodes of a larger neuronal network, to name but a few.

It is important to note that rarely are these effects isolated and often direct activation of specific neurons or local brain areas leads to indirect activation of the wider network. Moreover, the exact form of the stimulus, whether electrical, magnetic, photic or mechanical, along with its duration and intensity can also lead to widely differing neuronal responses.

This section describes a number of different types of neuromodulatory interventions, their associated impacts on neurological tissue and corresponding monitoring modalities to detect the resultant neural modulation. Just as the brain can be studied over a range of spatial scales from a reductionist approach of subcellular components through to a systems levels as shown in Fig. 1.1, so too can neuromodulatory approaches be applied over a broad spectrum of length scales. Fig. 1.2 depicts the associated spatial and temporal resolution for a range of techniques, each of which will be discussed in more detail in the following subsections. Broadly, the methodologies can be split into two categories: invasive and non-invasive techniques. In general, the invasive techniques are applied to in vitro and in vivo setups and non-invasive approaches are reserved for modulation of the human brain. The exception to this is microstimulation that is utilised clinically to modulate deep targets for the treatment of diseases such as Parkinson's disease (Perlmutter and Mink, 2006) as well as intra-cortically for applications such as sensory neuroprostheses (Flesher et al., 2016) and as a neurosurgical aid (Yang et al., 2014).

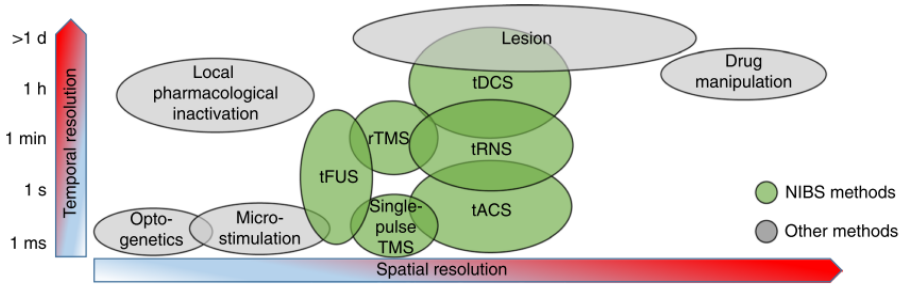


Fig. 1.2: Overview of brain intervention modalities with their corresponding spatial and temporal scales. Reproduced from Polanía et al. (2018).

1.2.1 Applications

Neuromodulation and the manipulation of neuronal activity has a two-fold importance. The first is from a basic scientific research perspective to understand brain function and cast light on how networks of neurons can give rise to some of the biggest mysteries in neuroscience, for instance, memory, consciousness and behaviour. Undeniably, much of our current knowledge concerning the brain has arisen from individuals with lesions resulting in particular deficits enabling associative structure-function relations to be derived. Consequently, methods to reversibility modulate specific brain targets are powerful neuroscientific tools for advancing our understanding of not only local sites but also their interactions as part of a more extensive network.

The second is a clinical need whereby disease states may be interrupted by extrinsic stimuli to treat a range of neurological disorders such as movement tremors (Perlmutter and Mink, 2006), depression (Nitsche et al., 2008; Rossi et al., 2009) and epilepsy (Rossi et al., 2009). As evidenced by deep brain stimulation (DBS), exogenous signals can have favourable outcomes (Perlmutter and Mink, 2006) but it is typically a late stage measure due the requirement of surgical implantation which is associated with infection risks and other complications that can give rise to morbidity and mortality. Non-invasive counterpart techniques are therefore exciting prospects removing the requirement to open the skull and potentially increasing the

scope of these treatments to wider patient groups.

1.2.2 Invasive approaches

Neuromodulation through inserted electrodes in various configurations has been instrumental in furthering our understanding of electrophysiology. Perhaps most famously, Hodgkin and Huxley performed intracellular electrode recordings of squid giant axons to reveal AP generation through the opening of voltage-sensitive sodium and potassium ion channels and form the basis of a set of differential equations to model AP initiation and propagation (Hodgkin and Huxley, 1952).

Intracellular recordings involve piercing the cell membrane with a sharp microelectrode that couples ionic currents in the cytoplasm into electron currents in the wire (Brette and Destexhe, 2012; Lampl et al., 1999). The potential, relative to an extracellular reference electrode, thus allows direct recordings from a single cell. In voltage clamp mode, the cell potential is maintained via a differential amplifier and the current simultaneously measured (Hodgkin et al., 1952). By applying step changes to the voltage, ion channel responses can be studied and different states revealed. Conversely, by injecting current, the cell potential is allowed to vary naturally and hence the cell's response to changes in current can be probed.

Building on this work, the patch clamp technique further increases the resolution of such recordings down to the level of single ion channels (Neher and Sakmann, 1976; Sakmann and Neher, 1984). Various configurations of this approach can be employed allowing access to either whole cells or patches of the membrane from both the cytoplasmic and extracellular sides. The basic approach is the same, however, whereby a small glass micropipette is moved close to the membrane of a cell and when gentle suction is applied, a tight resistive seal is formed over a patch of the membrane resulting in attachment of the cell. Subsequent removal of the pipette, additional suction or antibiotics then allow the different arrangements to be obtained.

Manipulation of the bath solution to contain only certain ions, replacing ions with impermeable ones or chemically blocking ion channels, allows specific ion channels to be isolated. Consequently, through voltage clamp experiments, the kinetics and sensitivity of different ion channels to different stimuli can be elucidated. It is then possible to classify ion channels not only as to which ions they permit passage to but also their responsiveness to modulation via different stimuli such as voltage, chemical-binding or mechanical deformation.

The development of optical imaging and spectroscopy techniques over recent years has also provided unparalleled spatial and temporal resolution for studying different aspects of neuronal function. A plethora of dyes now exist that are sensitive to a range of different molecules. One such important class of fluorescent molecule (FM) probes are calcium-sensitive dyes (Bootman et al., 2013; Paredes et al., 2009) which can be utilised to indirectly record AP activity via the back-propagating calcium wave into the dendritic arbor as well as functionally map synaptic inputs through dendritic calcium transients. Additionally, the loading of these dyes can allow for both single-cell and cell population recordings. The former can be achieved through combination with traditional electrophysiological approaches such as sharp microelectrodes and patch pipettes allowing a particular dye to be directly injected into the cell to probe neuronal calcium-signalling mechanisms. Conversely, local populations of neurons can be simultaneously loaded through bathing in acetoxymethyl (AM) ester dye variants that are membrane permeable (Paredes et al., 2009). The remaining extracellular dye can then be washed away leaving multiple loaded cells to monitor the activity of cell networks.

Another use of FM dyes is the study of the plasma membrane, embedded ion channels and their conformational states (i.e. open, closed or inactivated) in response to different stimuli. The FMs can either intercalate with the membrane or bind to specific sites depending on the subject of interest. For instance, to study the state

of the lipid bilayer, FMs can intercalate with the membrane and shift their emission spectra dependent on the membrane fluidity (Harris et al., 2002). Alternatively, to explore ion channel proteins, Förster resonance energy transfer (FRET) (Gordon et al., 1998), a technique that is sensitive to small changes in distance between two fluorophores through the transfer of energy from a donor to an acceptor molecule can be employed (Kusch and Zifarelli, 2014). Consequently, if the fluorophores are tagged to different parts of a membrane channel protein, different conformational states in these proteins can be detected. Moreover, combining such spectroscopic approaches with patch clamping, known as patch-clamp fluorometry (Kusch and Zifarelli, 2014), results in a powerful technique for characterising ion channels simultaneously detecting ionic currents and conformational changes.

Electrodes inserted into the extracellular space between neurons can also be used to measure electrical potentials and deliver currents with the advantage of not needing to disrupt the cell membrane. Such extracellular recordings can detect both extracellular action potentials (EAPs) if sufficiently close to the origin of the AP ($<$100 µm) and local field potentials (LFPs) as shown in Fig. 1.3. The LFP comprises the low-pass filtered signal below 300 Hz and is thought to represent the synchronised input to the area via longer-lasting synaptic inputs rather than the fast AP fluctuations or spikes (at $\sim$1 kHz) (Buzsáki et al., 2012; Obien et al., 2015). An important distinction between extracellular recordings and intracellular ones is that extracellular measurements detect changes in the field caused by ionic currents from not only the closest neuron but also all other surrounding cells, including non-neuronal cells such as glial cells. The sensitivity of the electrodes are therefore highly tip-size and placement dependent: smaller tips located close to a cell allow individual cells to be isolated whereas larger tips can grant detection from multiple cells simultaneously, termed single-unit and multi-unit recordings, respectively (Tehovnik, 2006). Conversely, intracellular recordings are restricted to only the ionic activity of the targeted cell.

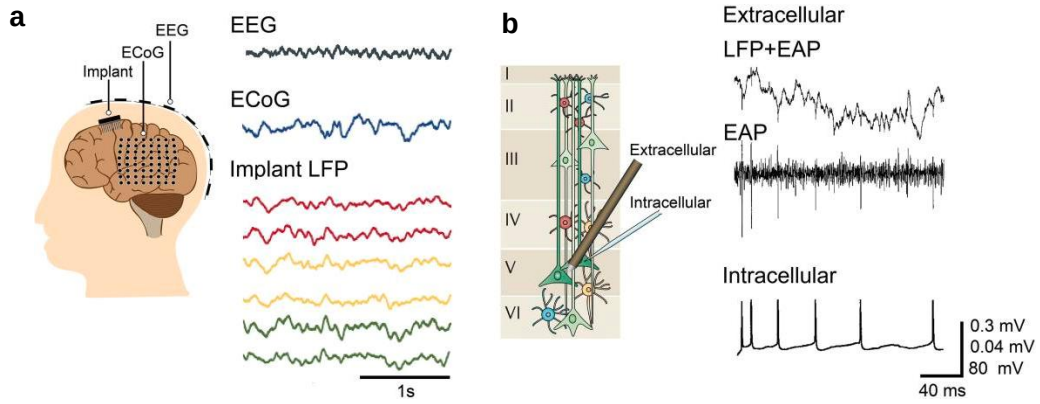


Fig. 1.3: Recordings from electrodes placed at different locations. **a** Typical traces from human recordings showing local field potentials (LFPs) through electrocorticography (ECoG) or implanted electrodes on the brain surface or from electroencephalography (EEG) where electrodes are placed on the scalp. Signal amplitudes are much larger for ECoG/implanted electrodes than for EEG. **b** Representative waveforms from intracellular and extracellular recordings of a pyramidal neuron. The extracellular trace is noisier but filtering allows extraction of both LFPs and extracellular action potentials (EAPs) which correlate with the more precise intracellular recordings of action potentials from a single cell. Figure reproduced from Obien et al. (2015).

Patch-clamp techniques require expert training to perform as well as being extremely time consuming and although more automated systems have been developed that can be applied to in vivo setups and record from multiple neurons simultaneously (Kodandaramaiah et al., 2012), they are still limited to measurements from a handful of cells. In comparison, extracellular electrodes are much easier to extend to monitor hundreds of different sites at the same time through the advent of on-chip microelectrode arrays (MEAs) (Obien et al., 2015). The development of these systems has advanced significantly in recent years and the reader is referred to the following review for a more comprehensive history of the technology (Obien et al., 2015). However, undoubtedly these tools used in conjunction with neuronal cultures, brain slices and increasingly in vivo, are shedding new light on brain network architecture, function and the importance of specific signals such as bursting and synchronous oscillations.

From a stimulation perspective, current can also be injected through electrodes to modulate neuronal activity. In awake animals and humans, the exact placement of the implanted electrodes has led to a host of different terminologies, for exam-

ple electrocorticography (ECoG) (Yang et al., 2014), intracortical stimulation (ICS) (Flesher et al., 2016) and DBS (Perlmutter and Mink, 2006), which can all be loosely categorised under the umbrella term microstimulation (Histed et al., 2013). The effects of microstimulation can also be split into two types: direct and indirect. Direct activation refers to the immediate stimulation of a neuron through depolarisation of its cell membrane and the subsequent triggering of an AP or activation of its synaptic terminals. AP propagation is typically initiated at the initial segment or the nodes of Ranvier which have the highest density of sodium channels thus making them the most excitable parts of a neuron (Histed et al., 2013). The current level required to generate an AP is proportional to the square of the distance between the neuron and the electrode. Different length pulses also change the current threshold to stimulate a response and this strength-duration relation (Tehovnik, 2006) is characterised by a hyperbolic curve with the minimum current amplitude of infinite duration that reaches the depolarisation threshold of the cell known as the rheobase current. In practise, inserted electrodes can generate direct activation up to a few millimetres from the electrode tip (Histed et al., 2013; Tehovnik, 2006).

Indirect effects are generated from the subsequent triggering of postsynaptic neurons and downstream pathways through synaptic release from the directly activated neuron (Histed et al., 2013). Consequently, relatively small direct effects can be amplified into much larger bouts of spiking activity via the network architecture. This often means that the behavioural manifestations of microstimulation are a result of the induced indirect effects that are distributed both spatially and temporally much further afield than the original site of activation.

As a consequence of these distributed effects, it can be difficult to unpick the underlying mechanism of action following stimulation of a particular brain site. A good example of this is DBS for the treatment of Parkinson's disease and associated pathological firing patterns in the basal ganglia such as atypical beta oscillations (Ashkan

et al., 2017; Perlmutter and Mink, 2006). The original hypothesis for favourable outcomes following DBS of deep, thalamic nuclei was that the stimulation resulted in the inhibition of overactive sites that occur due to the neurodegenerative dopamine depletion (Ashkan et al., 2017). The slightly counter-intuitive inhibition through stimulation can result from the stimulation of neurons that release inhibitory neurotransmitters dampening the activity of the local network. However, this theory was disproved and activity was actually shown to increase before quickly diminishing following the end of stimulation (Ashkan et al., 2017). Since this discovery, numerous theories have been proposed including excitation of both efferent and afferent axonal pathways to other connected structures (Hashimoto et al., 2003; Perlmutter and Mink, 2006), disruption of the pathological oscillations rather than a reduction in neural firing (Little et al., 2013) and normalisation of irregular bursting activity (Rubin and Terman, 2004). Added to this, DBS has been shown to activate not only neurons but also glial cells which modulate neuronal activity through secretion of neurotransmitters (Ashkan et al., 2017; Hamilton and Attwell, 2010), as well offer neuroprotective effects through increased levels of neurotrophic factors (Ho et al., 2014) and electrotaxis of progenitor cells towards the DBS current (Ashkan et al., 2017). This merely serves to underline that seemingly simple stimuli can rapidly give rise to very complex outcomes through the coupling and interaction of both biological and electrical networks.

The field of optogenetics (Boyden, 2011) holds great promise for untangling these complex, highly connected networks through targeted excitation or inhibition of specific sets of neurons or neuronal projections. This is made possible via the discovery of genes that encode opsins which are activated in response to light (Sineshchekov et al., 2002; Zemelman et al., 2002). Consequently, specific ion channels that either depolarise or hyperpolarise neurons can be triggered over very fast timescales, and in combination with electrophysiological tools, can be used for casual exploration of neuronal communication. An excellent review of the technique in combination

with a plethora of complementary approaches for use in systems neuroscience can be found here (Kim et al., 2017a) but perhaps the most exciting application of this technique is specific genetic manipulation in animal lines through the implementation of viral vectors that can be targeted to a range of different cell types. This, in combination with genetically-encoded calcium indicator (GECI) fluorescence imaging (Paredes et al., 2009; Pérez Koldenkova and Nagai, 2013), enables the simultaneous neuromodulation and recording of hundreds of neurons in awake, behaving and free-moving animals (Rajasethupathy et al., 2015).

Ultimately, electrophysiological, spectroscopic and optogenetic techniques are potent tools for probing brain functions such as neuronal signalling, communication and computation (Kim et al., 2017a; Obien et al., 2015; Tehovnik, 2006), synaptic plasticity (Padamsey and Emptage, 2011) and brain development in in vitro cell cultures and organotypics as well as increasingly in awake, behaving animals (Rajasethupathy et al., 2015). They are also vital approaches for providing key insights into the fundamental transduction of different stimuli into neural activity and thus may help to provide a mechanistic underpinning for the non-invasive stimulation modalities described in the following section.

1.2.3 Non-invasive methods

Non-invasive neuromodulatory modalities have to overcome the additional barrier imposed by the skull. Therefore, it is more difficult to focus stimuli to a particular brain target. The established methods are all electrically-based: tES consists of placing electrodes on the scalp to deliver weak currents through the brain and TMS uses an extracorporeal magnetic coil to produce electric currents inside the brain via electromagnetic induction.

Several variations of tES exist using either direct currents (tDCS) (Nitsche et al., 2008), alternating currents (tACS) (Herrmann et al., 2013) or random noise (tRNS)

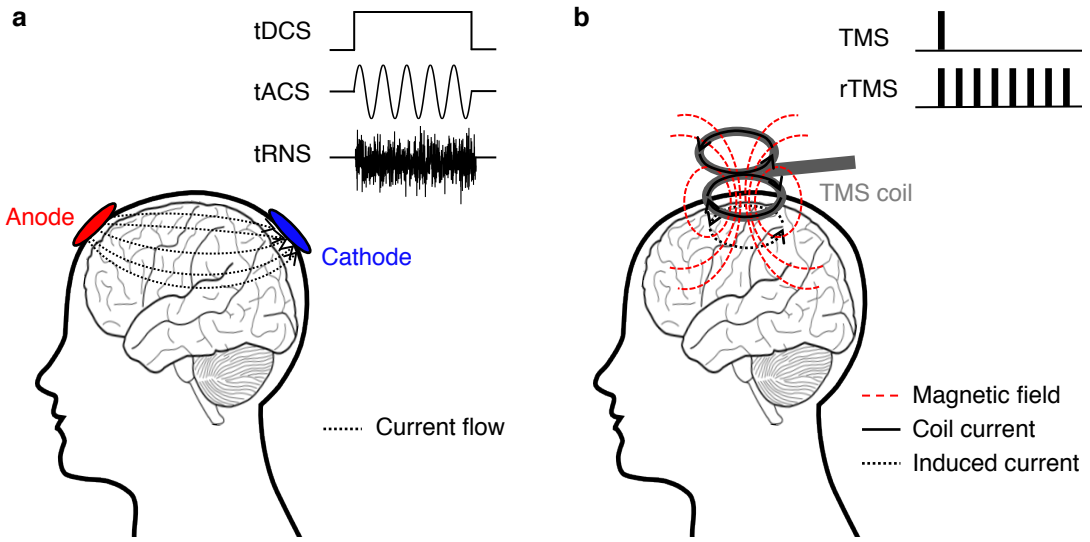


Fig. 1.4: Electrically-based non-invasive brain stimulation (NIBS) modalities. **a** Transcranial electric stimulation (tES) is the delivery of a weak current to the brain through the placement of electrodes on the scalp. The form of the applied current intensity distinguishes the different types of electrical stimulation: direct current (tDCS), alternating current (tACS) or random noise (tRNS). **b** Transcranial magnetic stimulation (TMS) utilises a magnetic field generator or coil (typically ring or, in this case, figure-8 in topology) to induce electric currents in the brain though electromagnetic induction. Repetitive TMS whereby repeated pulses are given at a specified frequency is referred to as rTMS.

(Terney et al., 2008) as the stimulatory input. However, all these approaches result in a highly diffuse electric field that cannot be localised to a specific brain target; reducing the size of one of the electrodes can increase the focality but still results in $\sim$10 cm^2 of the brain surface area within 50 % of the maximum power (Faria et al., 2012).

TMS can also be applied in different forms, either as short, single pulses or repeatedly at a specific frequency known as repetitive TMS (rTMS). Whilst TMS is more focal than tES, traditional ring and figure-8 coil designs still suffer from diffuse fields (volumes on the order of many cm^3) that decay exponentially in amplitude from the brain surface with depth, limiting their scope to the cortical surface. At a depth of 1.5 cm, the lateral spread of the magnetic field is over 10 cm^2 (Deng et al., 2013). Despite these spatial limitations, the functional resolution of TMS is thought to be somewhat higher as demonstrated by specific motor movements following stimulation of different parts of the motor cortex. More recent coil configurations,

for example the H-coil (Zangen et al., 2005), also provide potential for stimulating deeper brain targets (at a depth of 4–6 cm) although it is noted that the advantage of the H-coil over conventional figure-8 coils is disputed as the improved half-value depth (distance from the cortical surface to the deepest point where the electric field strength is half the maximum value on the cortical surface) of 22–72 % is offset by increases in the tangential spread of 406–811 % compared to the Magstim 70 mm figure-8 coil (Deng et al., 2013).

Mechanistically, as with DBS, there is much debate about the exact route by which neural activity is influenced by NIBS methods and how it leads to the disruption of pathological activity as well as inducing cognitive and behavioural changes (Cirillo et al., 2016; Gellner et al., 2016; Giordano et al., 2017; Klomjai et al., 2015). In TMS, the fast changing magnetic field is strong enough to directly depolarise the cell membrane and stimulate de novo APs (Klomjai et al., 2015). However, in tES the weak currents are not strong enough to reach the threshold for AP elicitation and so the smaller subthreshold changes in membrane potential are thought to adjust the excitability of neurons rather than directly initiate APs (Giordano et al., 2017). In the context of tACS and rTMS, brain oscillations are considered more important with neural entrainment and associated plasticity postulated as potential mechanisms (Herrmann et al., 2013).

The most promising electrical modality for stimulating neurons at depth without activating tissue at the brain surface is temporal interference (TI) which uses multiple high frequency electric fields that do not cause neural activation except where they overlap, the subsequent interference thereby delivering a lower frequency stimulus in the required firing rate range to stimulate neurons (Grossman et al., 2017). To date, this technique has only been demonstrated in mice but should be scalable for use in humans.

A promising electrical modality for stimulating neurons at depth without activating

tissue at the brain surface is temporal interference (TI) which uses multiple high frequency electric fields that do not cause neural activation except where they overlap, the subsequent interference thereby delivering a lower frequency stimulus in the required firing rate range to stimulate neurons (Grossman et al., 2017). To date, this technique has only been demonstrated in mice but efforts are underway to transition the approach into humans although it remains to be seen whether sufficient electric field strengths can be generated at depth given the larger skull and brain.

Whilst NIBS modalities are undoubtedly exciting tools for probing neurological function and cognition allowing casual structure-function relations to be uncovered through direct stimulation rather than relying on sparse data from the analysis of brain lesions, caution should be taken when analysing the results from these experiments. Extremely high variability is inherent in the data produced from NIBS studies owing to numerous factors: anatomical variability between participants, differences in cognitive state and subtle stimulatory effects coupled with incomplete mechanistic underpinnings to name but a few. Although some of these complications can be mitigated, for example, by using integrated neuro-navigation systems that utilise fMRI brain scans to ensure targeting of the correct area, the field and in particular, tES, has been plagued by a number of dubious results. On replication of the same experiments, the effects were not reproducible pointing to insufficient controls and sample sizes (Jalali et al., 2017). A key consideration in the design of new NIBS modalities is therefore robust experimental design to warrant more confidence in the reported outcomes (Jalali et al., 2017; Minarik et al., 2016).

1.3 Ultrasonic neuromodulation

The methods described thus far have focused on inducing neural activation through the use of applied electric fields in keeping with the Hodgkin-Huxley model of AP triggering through electrochemical coupling (Hodgkin and Huxley, 1952). However,

mechanical forces within the body and specifically the brain also play a major role in cell functions including proliferation, signalling and differentiation (Heimburg and Jackson, 2005; Mueller and Tyler, 2014; Tyler, 2012; Wang and Thampatty, 2006).

Focused US is a way of non-invasively delivering mechanical forces to cells deep within the body in the form of an acoustic pressure wave which can result in numerous bioeffects, both thermal and mechanical, depending on the specific pulsing regime (ter Haar, 2010). The acoustic waves can be focused to a particular location with a spatial resolution on the order of the wavelength of the driving frequency ($\sim$3 mm at 0.5 MHz). As the focusing is achieved through constructive interference of the incident waves, a focal spot can be formed at depth without affecting tissue elsewhere along the propagation path.

Therapeutic delivery of US to the brain was first conducted in the 1950s in order to thermally ablate a distinct volume of tissue resulting in the formation of a lesion (Fry et al., 1955). This therapy, known as high-intensity focused ultrasound or HIFU, permanently destroys a region of tissue and has applications for treating brain cancers (Martin et al., 2014) and other neurological disorders such as tremors whereby ablation of a specific brain area can lead to significant symptom improvements (Lipsman et al., 2014; Wang et al., 2015). Additionally, shorter FUS pulses in combination with intravenously-injected US contrast agents can be used to open the blood brain barrier via mechanical mechanisms (Hynynen et al., 2005; McDannold et al., 2012; Sheikov et al., 2008) and locally deliver therapeutic agents ranging from small molecule drugs (Treat et al., 2007) to viral vectors (Alonso et al., 2013). HIFU could therefore be utilised for delivering drugs in order to achieve pharmacological neuromodulation of specific brain targets (Airan et al., 2017).

However, US alone, at lower intensities can result in direct neuromodulation of neurons (Khraiche et al., 2008; Tufail et al., 2010; Tyler et al., 2008) without the addition of any other therapeutic agents. The purpose of this section is therefore to

summarise the work over the past several decades demonstrating the effects of US on neural tissue in both the central and peripheral nervous systems.

1.3.1 Central nervous system

US is capable of eliciting both excitatory and suppressive effects on central nervous system (CNS) tissue depending on the nature of the pulsing regime incident on the tissue. US-induced suppression of neural activity was first observed in the 1950s (Fry et al., 1958) where evoked potentials where first reversibly, and then permanently, suppressed as the intensity was increased when sonicating for over 20 s. Shorter pulses have also demonstrated supressive effects including the temporary dilation of the cat's pupils (Ballantine et al., 1960) and spreading depolarisation waves in rats (Koroleva et al., 1986).

Electrophysiological tools in combination with hippocampal slices provided the first evidence that US could directly stimulate neurons over a range of temporal scales. LFP recordings measured both enhancement and suppression of electrically-evoked field potentials following exposure times of 2–15 min (Bachtold et al., 1998; Rinaldi et al., 1991); MEA recordings revealed increased firing rates of primary hippocampal neurons following 1 ms (Khraiche et al., 2008) and repeated 2–20 µs (Choi et al., 2013; Kim et al., 2017b) US pulses; and whole-cell patch clamp recordings of individual CA1 pyramidal neurons confirmed AP firing in response to five short US pulses of length 22.7 µs (Tyler et al., 2008). Comparison of LFPs between US and optogenetic stimulation showed strong similarities for pyramidal neuron stimulation although the amplitude of the US-induced response was 10–20 fold lower (Moore et al., 2015).

Subcellular responses to US have also been reported: sodium and calcium transients were generated following US stimulation which were subsequently abolished following application of pharmacological agents indicating US-triggering of voltage-gated ion channels. These transients were also evident in glial cells producing a larger

mean fluorescence change of 1.4 compared to 1.14 for the pyramidal neurons suggesting glia may have increased sensitivity to US stimulation. Moreover, US induced vesicle exocytosis and synaptic transmission which further contributed to network activity (Tyler et al., 2008).

Additionally, these excitatory responses have been reported in vivo: US targeted to the motor cortex and hippocampus in anaesthetised mice resulted in increased cortical spiking on LFP recordings, as well as a period of after-discharge activity lasting for up to 3 s containing gamma (40–100 Hz) and sharp-wave ripple (160–200 Hz) band components (Tufail et al., 2010). The application of TTX, a voltage-gated sodium channel blocker, strongly attenuated US-evoked activity consistent with the results from hippocampal slice experiments (Tyler et al., 2008). The activity was accompanied by tail twitches and electromyography (EMG) spikes with lower temporal-averaged intensities (range: 20.6–162.7 mW/cm^2) and lower frequencies (range: 0.25–0.5 MHz) resulting in more robust EMG responses but without affecting latency times. Finally, the levels of a number of neurotrophic factors in the hippocampus were also significantly enhanced following pulsed US exposure (Lin et al., 2015; Tufail et al., 2010; Yang et al., 2015). Two of these factors, brain-derived neurotrophic factor (BDNF) and glial cell-line derived neurotrophic factor (GDNF) raise intriguing questions of whether US can be used to stimulate hippocampal plasticity with implications for probing learning and memory, as well as offering neuroprotective effects for neurodegenerative conditions such as Alzheimer's and Parkinson's disease (Liu et al., 2017; Zhao et al., 2017).

As well as modulating the expression of BDNF, the level of extracellular neurotransmitters has been shown to be US-dependent with increased serotonin, dopamine and GABA levels with respect to controls in anaesthetised rats for up to 2 h following a 20 min US exposure at 175 mW/cm^2 I_{SPTA} (Min et al., 2011b; Yang et al., 2012). It should be noted that the sampling site for the neurotransmitter levels (frontal

lobe) was located away from the sonication site (thalamus). Therefore, these findings highlight the ability to use US, not only to transiently alter neuronal activity through increased spiking as has previously been shown (Tufail et al., 2010; Tyler et al., 2008), but also to produce longer-lasting effects that affect the global connectivity of the brain possibly through modulation of the inhibitory GABAergic pathway (Min et al., 2011b).

Numerous studies have focused on stimulating the motor cortex in rodents (Gulick et al., 2017; Han et al., 201; Kamimura et al., 2016; Kim et al., 2014a; King et al., 2013, 2014; Li et al., 2016; Mehić et al., 2014; Ye et al., 2015; Yoo et al., 2011b; Younan et al., 2013) with EMG recordings and motor movements, primarily paw and whisker motion, providing quantification of the robustness of a response. This has enabled parametrisation studies to be carried out to determine more effective stimulus parameters. One key finding is that the threshold intensity required to produce a response increases with the carrier frequency of the US at frequencies in the low-megahertz range as demonstrated by a reduced EMG amplitude as frequency was raised from 0.25 to 0.5 MHz (Tufail et al., 2010); increased success rates (the ratio of contractions to the total number of sonication trials) at lower frequencies for a fixed intensity between 0.25 and 0.6 MHz (King et al., 2013); reduced threshold intensities at 0.35 MHz compared to 0.65 MHz (Kim et al., 2014a); and increasing intensities to provide a given success rate over a much wider frequency band of 0.3 to 2.9 MHz albeit with a flatter profile in the sub-megahertz range (Ye et al., 2015). This frequency dependence can be accounted for by two different explanations: a cavitation-based mechanism as the cavitation threshold increases with frequency (Church et al., 2015) or as the result of reduced focal spot sizes with increased frequency. Therefore, if the response is non-linear such that the local response reaches a maximum, the volume of activated tissue may drive the response. A model incorporating these two factors showed good agreement with in vivo mouse data consistent with an ARF mechanism whereby higher frequencies are actually

more effective at inducing a local response but activate smaller volumes of tissue thus requiring higher intensites to modulate behaviour (Menz et al., 2017). However, this theory was unsupported by results comparing planar and focused transducers at low frequencies (0.3–0.6 MHz) (Ye et al., 2015).

In addition, other US parameters have been studied. Increasing the PRF in the range of 100–3000 Hz resulted in greater responses (King et al., 2013). A BDC of 50 % and burst duration of 300 ms over a range of pulse lengths, 1–5 ms, resulted in the lowest intensity threshold for eliciting a motor response (Kim et al., 2014a).

However, the studies do provide conflicting evidence over a number of points, for example, one group claim pulsed US (Kim et al., 2014a) is more effective at producing motor responses whereas another suggests continuous wave US is better (King et al., 2013). The relationship between temporal-averaged US intensity and response amplitudes or success rates also varies with the correlation found to be negative (Tufail et al., 2010), flat with all-or-nothing responses (King et al., 2013), or positive (Kamimura et al., 2016; Mehić et al., 2014).

The precise targeting of specific parts of the motor cortex has also been shown to have significant effects on the responses. The average latency times significantly reduced for both neck and tail EMGs when moving the US focus from rostral to caudal brain locations, whilst the amplitudes of the EMG decreased for the neck but increased for the tail (King et al., 2014) pointing to more complex interactions between the acoustic field and induced brain network activity. Higher frequencies may also be beneficial in this regard as they can pinpoint smaller brain targets offering increased anatomical specificity. 5 MHz US was shown to be effective at inducing EMG responses despite the observed trend that higher frequencies require higher intensities to induce activity, and resulted in much shorter latency times versus 1 MHz (45 ms and 208 ms, respectively) (Li et al., 2016).

Much higher frequency US, 43 MHz, has been demonstrated to induce US-mediated modulatory effects in isolated salamander retinas. US evoked strong responses in ganglion cells that were independent of the pulse length and PRF above 15 Hz (Menz et al., 2013). Activity was only correlated with temporal-averaged intensity and saturated above 10–30 W/cm^2. Following blockade of synaptic transmission, the US response was abolished indicating US did not directly activate ganglion cells, and thus requires synaptic transmission. At 43 MHz, cavitation activity is unlikely and so an ARF-based mechanism provides a better description of the data, particularly as on and off responses were recorded from US pulses. Conversely, at 0.2 MHz, motor movements due to US exposure were associated with a 3 s refractory period providing evidence that a recovery time of an US-specific mechanism was required, consistent with a cavitation mechanism (Gulick et al., 2017). Consequently, it might be that at different frequencies, different mechanisms exist for coupling acoustic energy into neural activity.

Similarly to TMS, the functional specificity of FUS-induced neuromodulation may be somewhat smaller than the intensity or pressure full-width half-maximum focal volumes. Glucose uptake as measured by PET-imaging was used to assess induced neural activity and the activated region was reported to correspond to the full-width 90 %-maximum of the intensity field (Kim et al., 2014b).

In general, whilst these studies have uncovered certain trends, the results are highly variable. The explanation is likely to be multi-faceted with differences in experimental setup, anatomical variations and complex interactions between the stimulation of competing inhibitory and stimulatory networks all contributing to the high variance of responses. Another crucial parameter that has been shown to significantly alter experimental outcomes is the depth of anaesthesia the animals are under during the stimulation. In particular, US-induced responses are only evident under a light state of anaesthesia (King et al., 2013; Younan et al., 2013). A more in depth study look-

ing at ketamine revealed that US-induced motor responses were abolished for more than 20 min following ketamine injection. This was attributed to ketamine blocking US-triggered calcium transients as shown by fluorescence imaging of cortical cell cultures (Han et al., 201). It has also been reported that US reduced anaesthesia times following administration of a single anaesthetic dose by 20 min as measured by pinch response and voluntary movement (Yoo et al., 2011b) and even, remarkably, could awaken an individual from a coma (Monti et al., 2016).

Although the motor cortex has been the subject of the majority of studies in small animal models, the visual system has been studied in small animals but also in larger animals and humans allowing electrophysiological measurements (electroencephalography, EEG) and imaging techniques (functional magnetic resonance imaging, fMRI) to be combined with behavioural and cognitive assessments. Visual-evoked potentials (VEPs) were suppressed in a rabbit model following pulsed sonication at 0.69 MHz. The effect lasted for 10 min and the suppressive outcome was confirmed by blood-oxygenation-level-dependent (BOLD) fMRI (Yoo et al., 2011a). Similar responses were revealed in rats along with VEP enhancement through adjustment of the TDC or intensity of the US sequence (Kim et al., 2015). Below 1 % TDC the VEP was not modulated indicating a threshold for observing a response which is consistent with findings from the motor cortex (King et al., 2013). At 5 %, the magnitude of the P1 component minus the N1 component was reduced by approximately 13 %. Increasing the duty cycle to 8.3 % or the I_{SPPA} from 1 to 5 W/cm^2 led to an increase of P1-N1 close to 10 %.

Similar EEG and EMG responses were observed in both pigs and sheep. In sheep, repeated stimulation of both primary visual and sensorimotor areas was explored leading to EMG and EEG responses, respectively, (Lee et al., 2016c) and in pigs, thalamic targeting also lead to reversible suppression of somatosensory-evoked potentials (SEPs) (Dallapiazza et al., 2018).

In awake monkeys, US was targeted to the frontal eye field (FEF) during an antisaccade task (Deffieux et al., 2013). Ipsilateral mean latencies were significantly slowed following FUS exposure although the same results were not observed in prosaccade tasks. These results demonstrated for the first time the ability to use FUS as a neurostimulation tool to modulate high-level cognitive behaviour (Deffieux et al., 2013). A second paper by the same group measured multiple single neuron recordings in a connected brain region paving the way for future studies investigating network connectivity changes (Wattiez et al., 2017). They recorded significant modulation of approximately 40 % of neurons in this connected region closely matching the reported value in hippocampal slices that 30 % of neurons were stimulated albeit in this instance, the stimulation and recording sites were coincident (Tyler et al., 2008). Behavourial modulation following right-side FEF sonication during a visual task was also observed shifting animal's choices to the leftward target and vice versa, left-side FEF stimulation shifted choices to the rightward target (Kubanek et al., 2017a).

Futhermore, longer term connectivity changes have been identified in non-human primates following an offline US stimulation protocol. 40 s of 250 kHz US in 30 ms pulses at 10 Hz was delivered 30 min prior to fMRI acquisition; the impact of the sonication was to reduce the coupling between the stimulated area and regions with which it is interconnected (Folloni et al., 2018) or, to enhance strongly connected regions, typically close to the targeted site, whilst reducing the activity coupling to weakly connected regions (Verhagen et al., 2018).

Based on the evidence from animal models (Tyler et al., 2008; Yoo et al., 2011a), it has been suggested that FUS would be a safe method to be used in humans. The first US stimulation for neuromodulation of the human brain was conducted with a diagnostic imaging probe operating at 8 MHz placed over the posterior frontal cortex for 15 s (Hameroff et al., 2013) and consequently led to significant improvements in mood, but not pain, scores in chronic pain volunteers. At this frequency, very little

of incident acoustic energy is likely to penetrate the skull and so subsequent studies have all focused on sub-megahertz frequencies utilising US sequences very similar to those found to be most effective in small animal parametrisation studies.

Following successful median nerve stimulation via US which activated somatosensory pathways within the brain (Legon et al., 2012) (see Sec. 1.3.2), the next step was to try and modulate the induced SEPs with US targeted to the primary somatosensory cortex (S1) in healthy volunteers (Legon et al., 2014). Attenuation of the SEP was reported along with specific modulation of alpha (7–12 Hz), beta (13–20 Hz) and gamma (30–55 Hz) frequency bands at an US frequency of 0.5 MHz, 500 ms pulse length at a 36 % BDC and an I_{SPPA} of 5.9 W/cm^2. Moreover, improvements in two-point touch and frequency discrimination tasks also followed FUS sonication. Further analysis of the EEG data revealed modulation of both intrinsic and evoked EEG dynamics (Mueller et al., 2014). Overall, these findings demonstrated the use of FUS to non-invasively modulate cortical processes in humans.

Specifically targeting the hand primary somatosensory cortex (S1), secondary somatosensory cortex (S2) or both areas simultaneously with FUS was able to induce peripheral sensations in volunteers (Lee et al., 2016a, 2015). The reported sensations varied from tingling and numbness to itching and coolness as well as ranging in their location from fingertips all the way up to the axilla. The distribution in location of the induced peripheral sensations points to the misalignment of the US focus and the target location and highlights a key problem in scaling up from smaller animals to humans. This difficulty in ensuring correct targeting is further discussed in the Sec. 1.4. A similar issue was evident in a study delivering US to the primary visual cortex (V1) where retrospective simulations revealed misalignment problems. However, in the volunteers where the US was correctly focused, 300 ms US bursts at a 50 % BDC, driving frequency of 270 kHz and I_{SPPA} ranging between 1.2 and 6.6 W/cm^2, induced phosphene perception and was associated with EEG modulation

(Lee et al., 2016b). Concurrent fMRI maps confirmed activation of the target site as well as showing activity in connected visual and higher-order cognitive pathways. A similar pattern of activation has been observed following phosphene perception from TMS (Lee et al., 2016b).

Combined magnetic and US stimulation has been used to examine US modulatory effects in the human motor cortex (M1) (Legon et al., 2018b). US was paired with a number of established TMS protocols and a burst of 500 ms at 500 kHz was delivered 100 ms prior to the TMS pulse. It attenuated single-pulse motor evoked potentials (MEPs). In paired pulse protocols, two TMS pulses are delivered at a specified time interval which determines if the MEP is inhibited or promoted. For short intervals, the MEP is inhibited (short interval intracortical inhibition or SICI) whereas for longer intervals it is facilitated (intracortical facilitation or ICF) (Ziemann et al., 1996). US attenuated ICF but had no effect on SICI. The cortical silent period, an interruption of voluntary muscle contraction following M1 stimulation (Wilson et al., 1993), was not affected by US stimulation but US did reduce reaction times in a stimulus response task (Legon et al., 2018b).

The simultaneous acquisition of fMRI data from both 3T and 7T MRI scanners in conjunction with FUS stimulation to cortical and sub-cortical regions has been explored (Ai et al., 2016). Whilst image artefacts from the FUS source cannot be completely eliminated, they can be reduced to an acceptable level in order to detect cortical activity close to the transducer. Moreover, targeting of deeper, thalamic regions also suppressed SEP components along with time-locked gamma band ($\sim$80 Hz) inhibition and reduction in performance for a two-point discrimination task (Legon et al., 2018a).

As a cautionary note, some reports in animal models have suggested that the neuromodulatory outcomes may be the result of indirect widespread auditory activation (Guo et al., 2018; Sato et al., 2018). In guinea pigs, strong responses in the pri-

mary auditory cortex (A1) were observed independent of the sonicated brain target as evidenced by spike counts on electrode arrays following 220 kHz US exposures. Consistent responses were reported for single pulses of length 0.1–10 ms, repeated pulses in the PRF range of 10 Hz to 16 kHz and pressure amplitudes between 25 kPa and 2 MPa, specifically chosen to mimic sequences in the literature shown to induce CNS modulation (Guo et al., 2018). Transection of the auditory nerve or removal of the cochlear fluid also abolished the activity (Guo et al., 2018). In transgenic mice, GECI flourescence imaging revealed a strong resemblance between the activity produced by audible sound and 80 ms, 500 kHz US bursts with 0.2 ms pulses at PRF of 1.5 kHz (Sato et al., 2018). Whilst these effects are unlikely to explain the the induction of AP propagation in cell preparations (Tyler et al., 2008) or the modulation of saccadic behaviours (Deffieux et al., 2013), they warrant further investigation as they may confound US neuromodulation human trials.

Neuromodulatory effects have also been observed following the intravenous injection of US contrast agents (UCAs) and US sonication for BBB opening (Chu et al., 2015; Downs et al., 2015). In rats, 400 kHz US at a mechanical index (MI) of 0.55 (0.35 MPa) with injected microbubbles produced transient SEP amplitude modulation (less than 1 h) without affecting latency times or inducing damage (Chu et al., 2015). Increasing the MI to 0.8 (0.51 MPa) resulted in red blood cell extravasation and was associated with prolonged SEP amplitude and latency suppression. However, without microbubble injection, 0.8-MI US did not induce BBB opening (Chu et al., 2015). Furthermore, in monkeys, BBB opening was associated with a significant error reduction during a visuomotor task (Downs et al., 2015). Although this protocol, where agents are injected, is not viable for healthy volunteers, these results raise intriguing questions about a combined beneficial effect of BBB opening not only to deliver a pharmacological agent but also producing a direct behavioural change.

Alternative exogenous agents have also been developed to sensitise neurons to the applied US field: piezoelectric nanoparticles couple acoustic energy into an electric field generating calcium transients (Marino et al., 2015) and network activity (Rojas et al., 2018) at pressures as low as 1–2 kPa.

Finally, analogous to optogenetics (Fenno et al., 2011), the term sonogenetics has also been coined and investigated through genetic manipulation of C. Elegans with (Ibsen et al., 2015) and without microbubbles (Kubanek et al., 2017b). Expression or misexpression of specific ion channel sub-units found in touch sensitive neurons led to US-induced behaviour and therefore offer the potential to selectively and noninvasively stimulate only genetically altered neurons without requiring surgical intervention to deliver light as in optogenetic approaches.

1.3.2 Peripheral nervous system

Ultrasonic neuromodulation applied to the peripheral nervous system (PNS) has been conducted in parallel to the work in the CNS. At a similar time to the first studies noticing reversible effects in the brain, it was discovered that US sonication of the peripheral nerves could first increase spiking activity and then depress spontaneous activity in an initially reversible, and then permanent manner (Fry et al., 1950; Lele, 1963; Young and Henneman, 1961). At the same time, conduction velocities increased with the applied ultrasonic dose. Both of these results were replicated by heat application (Lele, 1963). Differential blocking of mammalian nerves has also been observed with the smallest, C fibres, being the most responsive and the largest, A-α, being the least sensitive (Legon et al., 2012; Lele, 1963; Young and Henneman, 1961). As the C-fibres carry pain signals from receptors, this opens the obvious question as to whether US can be used to suppress pain.

A number of more recent studies confirmed these findings showing that evoked potential amplitudes could be initially increased by up to 9 % before decreasing at higher

intensities (Colucci et al., 2009; Foley et al., 2008; Tsui et al., 2005). These long pulse (5 s – 5 min) sonications are primarily attributed to thermal effects. Short pulses (0.5 ms) of US have also been shown to modulate electrically-induced compound action potentials (CAPs) with either early enhancement or suppression depending on the latency time between the applied US pulse and electrically-induced CAP (Mihran et al., 1990). These pulses have an estimated temperature rise of 0.025 °C and so thermal effects are unlikely to be driving the observed responses, suggesting a mechanical mechanism may play a role. Reductions in conduction velocities (Juan et al., 2014; Wahab et al., 2012) also point to a non-thermal mechanism as the conduction velocity is expected to increase with temperature (Lele, 1963).

Both ARF and cavitation-based mechanisms have been proposed to account for US-mediated PNS modulation: the cumulative radiation force was shown to negatively correlate with reductions in both conduction velocities and AP amplitudes following electrical stimulation via an electrode (Wahab et al., 2012) whereas in ex vivo crab axons, de novo APs could be excited only when inertial cavitation signatures were simultaneously acquired on passive cavitation detectors (Wright et al., 2017, 2015). It should be noted that the minimum pressure required to induce direct AP generation was 1.8 MPa, on the order of a magnitude higher than the lowest pressures required to modulate electrically-induced APs (0.1 MPa) (Wahab et al., 2012).

In injured animals models, neuropathic tissue has been shown to be more sensitive to US than healthy tissue (Tych et al., 2013) as well as improving regeneration and recovery following crush injury linked with increased BDNF levels (Ni et al., 2016). US has also shown benefits in the treatment of other diseases. For example, in bladder dysfunction, US inhibited rhythmic bladder contractions with longer latencies and refractory periods compared to electrical stimulation (Casella et al., 2017).

A recent in vivo study in mice also required higher pressures (a minimum of 3.2 MPa)

to induce EMG activity and visible muscle responses following sonication of the sciatic nerve. A break period of 20–30 s improved the success rate of subsequent stimulation to 92 % (Downs et al., 2018). This regeneration phase is similar to that reported in the CNS targeting US to motor cortex where a 3 s refractory period was described (Gulick et al., 2017). Moreover, shock waves of 50 MPa in amplitude are capable of directly generating CAPs with a similar shape to electrically-induced CAPs but lower amplitudes (Schelling et al., 1994). Movement of the shock wave focus away from the nerve abolished CAP generation until air bubbles were injected. Overall, these results lend support to a cavitation-based mechanism for generating de novo APs in peripheral nerves.

However, at 350 kHz, pressures of only 0.53 MPa induced eyeball movements in rats following sonication of the abducens nerve (Kim et al., 2012). The extent of the movement grew after each 200 ms burst for 10 repeated bursts at a burst interval of 1 s. Although at a higher frequency of 650 kHz, movements could not be induced.

Gavrilov *et al.*, made a series of pioneering contributions to the field. Initial experiments in the Pacician corpuscle, a mammalian mechanoreceptor, reported the induction of APs following US exposure at 0.48 MHz between 0.4 and 2.5 W/cm^2, with increasing potential amplitudes as the intensity was increased (Gavrilov et al., 1977b). Translating these results into humans, a range of tactile sensations were elicited following short US pulses (1–100 ms) targeted to the hand or forearm (Gavrilov et al., 1977a). As the pulse length was further increased, sensations were present at the start and end of the waveform as well as estimated displacements matching mechanical displacements required to stimulate receptors, indicating the acoustic radiation force might be the mechanistic driving force behind the sensations (Gavrilov, 1984). With increasing intensity, the sensations also changed in nature from tactile to temperature and finally pain perception. Before US intensities reached the level to cause the onset of pain, cavitation signals were also detected. In auditory nerves, it was

shown that sonication lead to evoked potentials in the brain at intensities as low as $0.01\,\mathrm{W/cm^2}$ and with a similar form to those induced by sound stimuli (Gavrilov et al., 1977b). Consequently, it was postulated that US may have applications to both diagnosing neurological diseases based on US tacile sensation response as well as the encoding of auditory information for the deaf.

A hypothesis that variability in the intensity required to elicit tactile sensations in different tissues and individuals was related to the density of mechanoreceptors, made initially by Gavrilov (Gavrilov, 1984), was supported by a subsequent study in humans (Dickey et al., 2012). The sensitivity of individuals showed a sigmoidal relationship with respect to intensity with an average intensity of $106.4\,\mathrm{W/cm^2}$ to reach a 90 % threshold response rate at 1.1 MHz.

Modifying the sequence parameters could also change the induced sensations (Lee et al., 2014; Legon et al., 2012) and their associated brain activity as quantified by EEG and BOLD fMRI maps showing activation of different cortical and sub-cortical regions depending on the pulse incident on the fingertip (Legon et al., 2012). Although thermal sensations were maximal over a band of intensities (I_{SPTA} = 10–$30\,\mathrm{W/cm^2}$), vibrotactile and nociception responses continued to increase for the range of intensities tested, up to $100\,\mathrm{W/cm^2}$ (Lee et al., 2014).

1.3.3 Mechanisms

Despite the numerous reports of US-induced effects on nervous system activity, the underlying mechanisms of how the acoustic wave is transduced into neural modulation remains unclear. An understanding of the fundamental processes involved will undoubtedly guide US parameter selection and experimental design culminating in more robust, highly specific modulatory outcomes.

To date, several mechanisms have been proposed many of which originate from a

paradigm shift in the comprehension of nerve pulse propagation. Historically, nerve impulses have been considered as electrical phenomena where depolarisation of the cell membrane beyond a certain threshold leads to an all-or-nothing excitatory response that propagates down the nerve. However, it is now clear that the electrical fluctuations are accompanied by mechanical, chemical and thermal changes (Bulychev et al., 2004; Tasaki, 1995) as well as conformational changes in the state of the cell membrane and embedded membrane proteins (Luzzati et al., 1999). As a result, modulation of nervous system activity can be achieved through the application of a range of stimuli including electrical (Hodgkin and Huxley, 1952), chemical (Newman and Zahs, 1998; Tasaki et al., 1962), mechanical (Falleroni et al., 2018; Newman and Zahs, 1998) and thermal (Chapman, 1967; Shapiro et al., 2012), with mechanical regulation providing a basis for ultrasonic neuromodulation.

The plausible mechanisms through which mechanical perturbations introduced through US sonication can lead to AP generation and the adjustment of neural activity include: (i) the generation of capacitive currents due to membrane displacements (Heimburg, 2012; Plaksin et al., 2014), (ii) the activation of mechanosensitive channels (Brohawn, 2015; Kubanek et al., 2016; Morris, 2012), (iii) the opening of pores in the lipid bilayer, so-called sonoporation (Tatat and Dunn, 1992; Wunderlich et al., 2009), and (iv) coupling to membrane waves along the axon (El Hady and Machta, 2015; Kim et al., 2007; Shrivastava and Schneider, 2014). These mechanistic routes are not independent and so combinations of these pathways, and potentially others, may result in the observed US neurostimulation responses. A detailed discussion of each of these mechanisms, and others, is beyond the scope of this introduction and so the reader is referred to Blackmore et al. (2019) for a more in-depth review.

Alongside the mechanically induced effects, absorption of the US wave leads to temperature rises which may also result in thermal neuromodulation dependent on the incident waveform. A similar thermal absorption mechanism is used to achieve

infra-red neural stimulation (Chernov and Roe, 2014). Temperature changes on the order of a few degrees can affect neural activity, altering the amplitude and duration of APs, spiking rates and afterhyperpolarisation kinetics (Lee et al., 2005; Thompson et al., 1985). Certain ion channels are also known to exhibit thermosensitivity (Cesare et al., 1999).

In addition, the role of cell types, in particular glial cells, demands attention. Glial cells fill the space between neuronal elements in brain and traditionally were believed to provide a soft connective tissue that provides structural support (Pogoda and Janmey, 2018). However, recent research suggests a more critical role of these cells in the brain for neuronal function (Fields, 2015; Min and Nevian, 2012) as well as functioning as a source and mediator for calcium waves (Chesler, 2003; Newman and Zahs, 1998). Mechanical stimulus is known to be efficient at exciting calcium waves in glial cells making them a potential target for US stimulation of the brain (Newman and Zahs, 1998).

It is also noted that in the presence of a microbubble, neurostimulation by US seems to be enhanced, potentially by pore formation. For example, intracellular Ca^{2+} waves have been observed following microbubble collapse (Li et al., 2018) with a fast wave occurring when pores in the membrane were created by the microbubble collapse but a slower wave when it was not. The Piezo-1 Ca^{2+} channel has also been observed to be activated by 2 MHz US but only in the presence of microbubbles (Pan et al., 2018). However, the focus of most neurostimulation studies has been to avoid the use of microbubbles as they increase the risk for injury.

1.3.4 Summary

The table below serves as a short summary of the key findings in ultrasonic neuromodulation providing a top-line overview with some of the most important results.

Finding	Top-line overview	References
Cellular and chemical responses	Patch clamp recordings and microscopy confirmed direct AP firing following US exposure along with both neuronal and glial cell activation. Specific ion channels have also been shown to be triggered by US as well as the modulation of neurotransmitter and neurotrophic factors.	Liu et al. (2017); Min et al. (2011b); Tufail et al. (2010); Tyler et al. (2008); Yang et al. (2012); Zhao et al. (2017)
EMG and motor responses in rodents	A large amount of data has been collected on US-induced motor movements in rodents including parametrisation studies of different US sequences. It was found that the intensity to induce a response increases with US frequency but this can be explained by both cavitational and ARF-based hypotheses.	Gulick et al. (2017); Han et al. (201); Kamimura et al. (2016); Kim et al. (2014a); King et al. (2013, 2014); Mehić et al. (2014); Ye et al. (2015); Yoo et al. (2011b); Younan et al. (2013)
Non-specific auditory activation	Widespread auditory activation has been detected in mouse and guinea pig models independent of the sonicated brain region and demands further attention due its potential to confound ultrasonic neuromodulatory outcomes.	Guo et al. (2018); Sato et al. (2018)
Network and connectivity effects	In monkeys and non-human primates, the effects of US stimulation on connected brain regions away from the stimulation site have been identified. The connections between highly interconnected regions appear to be strengthened whilst being reduced for those that are weakly coupled with effects lasting for up to 2 h. In humans, fMRI confirmed visual and higher-order network activation following V1 stimulation.	Folloni et al. (2018); Lee et al. (2016b); Verhagen et al. (2018); Wattiez et al. (2017)
Modulation of human EEG dynamics	The majority of human work to date has focused on modulating evoked potentials with effects seen in visual, motor and somatosensory areas. The modulation of participants' performance in discrimination tasks as well as phosphene and peripheral sensation perception provide glimpses of US's ability to induce stronger and more complex responses. However, whilst TMS-induced MEP amplitudes were inhibited by US, the absence of a report of MEPs being directly initiated by US suggests that the stimulatory effect of FUS may be more subtle than for TMS where MEPs and motor movements can be induced.	Lee et al. (2016a, 2015, 2016b); Legon et al. (2018a,b, 2014)

Table 1.1: Summary of key ultrasonic neuromodulation results.

1.4 Transcranial ultrasound targeting

1.4.1 Head anatomy

The human brain is enclosed by the meninges, skull and scalp as depicted in Fig. 1.5. The skull is composed of hard inner and outer layers of cortical bone (called tables) and a core of cancellous bone (the diploë). Beneath the skull, are the meninges as shown in Fig. 1.5a, a set of three fibrous, connective tissues. The outermost is the dura mater, a dense, collagenous tissue that is separated from the skull by the epidural space. The second is a delicate membrane of fine collagenous fibres that form a web-like structure and is known as the arachnoid mater. The innermost layer is the pia mater, a thin, translucent, elastic membrane directly on top of the brain. The space between the arachnoid and pia layers is called the subarachnoid space and is filled with cerebrospinal fluid (CSF) produced in the choroid plexus. The CSF cushions and protects the central nervous system.

The brain itself is divided into two cerebral hemispheres, left and right. The composition of the brain also varies: the outer layer, known as the cerebral cortex, is composed of neurons and their supporting cells with its grey colour giving rise to the name grey matter. Underneath the grey matter are myelinated nerve fibres and pathways known as the white matter and embedded deep within the white matter are aggregates of neurons (grey matter) termed subcortical nuclei.

1.4.2 Skull bone properties

The skull is the primary challenge for delivery of US into the brain for neuromodulation and other therapeutic applications. Skull bone is a highly heterogeneous structure that has both a higher density and sound speed than soft tissue resulting in a large impedance mismatch (3–4 fold). Moreover, it is a multi-layered structure with a hard cortical shell and an inner cancellous layer comprised of calcified bone

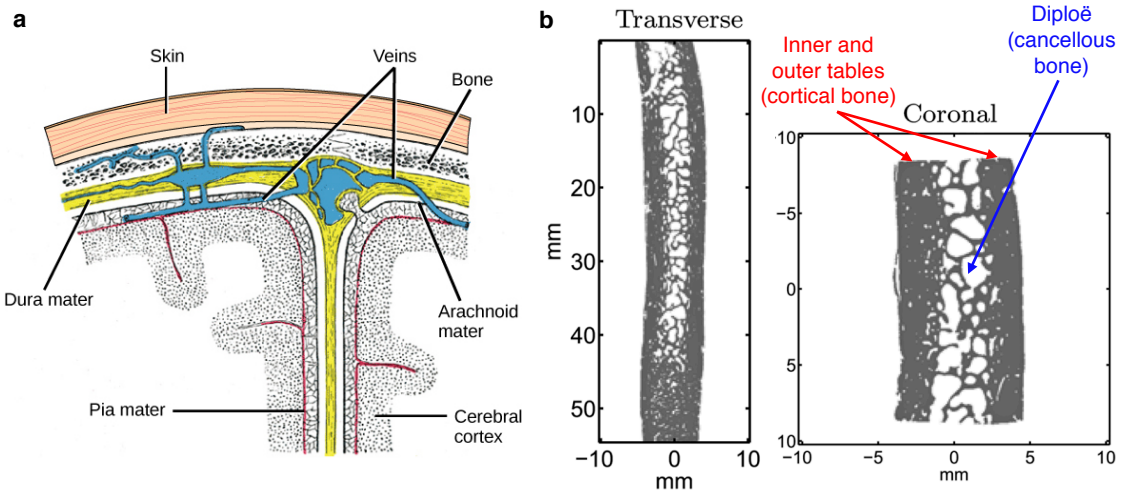


Fig. 1.5: Human head and skull bone anatomy and structure. **a** Anatomy of meninges. Reproduced from Tsairas (2014). **b** Micro-CT images of a human skull bone sample. Sections in two planes with a resolution of 10 µm. Inner and outer tables and diploe layers are indicated. Adapted from Pinton et al. (2012a).

arranged in a trabecular structure filled with blood and fat as depicted in Fig. 1.5b. The average size of each trabeculae is between 50 µm and 150 µm with separations of 0.5–2 mm which is on the order of the wavelength of US at 1 MHz (1.5 mm) (Chaffaï et al., 2000). As such, this internal layer results in strong scattering of the acoustic wave at frequencies above 1 MHz (Pinton et al., 2010) effectively making the skull a low pass frequency filter thereby limiting the viable frequency range for effective transmission.

The presence of hair may also increase losses; a study in an ex vivo cadaver model reported a temperature elevation drop of 17 % at 710 kHz but negligible losses at 220 kHz due the additional of human hair (Eames et al., 2013).

In rodents, the thin skull bone allows US to easily penetrate into the brain but standing waves can be formed from reflections off the opposite side of the skull leading to complex fields and pressure hotspots away from the target location (Constans et al., 2017; Younan et al., 2013). Therefore, in scaling up from small animals to large animals and humans, the thicker skull presents different challenges: primarily increased attenuation and aberration of the acoustic wave (Fry and Barger, 1978; White et al.,

1978) thereby shifting the intended focus inside the brain. Consequently, methods to determine the induced beam distortion as well as correction strategies to overcome it are required to effectively focus US transcranially to a specified target.

Capturing all of the underlying physics of US propagation through skull bone is highly complex. As an elastic medium, the skull supports both longitudinal and shear waves and the subsequent mode conversion between the two. In addition, the two phase composition of the cancellous bone resembles a poroelastic media and as such can give rise to two different compressional waves coined the slow and fast waves. These originate from the relative motion between the solid and fluid components with the fast wave corresponding to in phase movement and the slow wave, out of phase movement as predicted by Biot theory (Williams, 1992). However, the amplitudes and sound speeds of the two compressional waves are highly sensitive to model parameters including porosity, sample thickness and tortuosity (Fellah et al., 2004) and angle with respect to the trabecular alignment (Hosokawa and Otani, 1998).

Conventional medical imaging modalities do not have the resolution to resolve this inner bone structure and hence analysis of such models for transcranial wave propagation is unfeasible given the strong dependence of the solution on model parameters. In any case, at perpendicular incidence slow and fast waves have previously been shown to be almost unidentifiable in the time domain with only very small differences in wave speeds (Hoffman et al., 2012; Hosokawa and Otani, 1998). Accordingly, the skull bone is commonly treated as either an effective fluid or an elastic medium without consideration of its true biphasic nature.

1.4.3 Time reversal

Early studies using US as a therapeutic tool in the brain performed craniotomies to remove a portion of the skull circumventing propagation through the cranium and

providing direct acoustic access to the brain (Fry et al., 1960; Ram et al., 2006). Simple, geometrically-focused transducers could then be employed to generate thermal lesions in the tissue as prescribed sites. When delivering US non-invasively, transmission through the skull can distort the beam thus requiring more complex targeting strategies. The extent of the induced aberrations is linked to the driving frequency. Around 250 kHz, where the thickness of the skull is typically on the order of one US wavelength in bone, distortions are minimised and for a hemispherical array has been shown to result in focal shifts of less than 2 mm (Yin and Hynynen, 2005). However, for smaller apertures or increased frequencies, the errors increase and can necessitate correction methods to reform the focus at the intended site. To implement these corrections physically, multi-element arrays comprised of hundreds of individually adjustable elements are typically utilised. The development of acoustic lenses for transcranial therapies can also correct for focal distortions in a subject-specific manner effectively turned a transducer in a high resolution array at a much reduced cost (Maimbourg et al., 2018).

The time reversal approach is commonly used to focus waves through aberrating media and relies on an acoustic source at the target location (either an actual source or a reflector) from which divergent waves are detected and recorded on an array of receivers. The waveforms are then played backwards in time through the array and the resultant waves refocus on to the target-source location Fink (1992). Time reversal methods are made possible due to the reciprocal properties of the lossless wave equation due to the second-order time derivative operator. This consequence means that if a solution to the pressure field propagating in the forwards direction is a solution, then the temporally-reversed field is also a solution, so-called back-propagation. It is noted that the addition of losses to the wave equation in the form of frequency-dependent attenuation, as is the case for biological media, results in an odd-order time derivative operator and hence in degradation of the time reversal properties.

One biomedical application of time-reversal has been lithotripsy for the treatment of kidney stones (Thomas et al., 1996), which are a naturally reflective target. The approach has subsequently been applied to transcranial therapies but this requires an implanted, artifical source, for example, a hydrophone or monoelement transducer (Thomas and Fink, 1996). Moreover, as the skull is a strongly attenuating and aberrating layer, this breaks the invariant nature of time reversal. However, through the use of techniques such as amplitude compensation, the approach can still be applied to yield successful results (Tanter et al., 1998; Thomas and Fink, 1996). The ability to steer the focal spot has also been demonstrated by combining conventional beamsteering approaches with backpropagation (Tanter et al., 1998). A full review of time reversal is given by Fink et al. (2003).

1.4.4 Direct measurement

The placement of an implanted hydrophone at the focus can be used to correct for skull-induced phase distortions through the measurement of the pressure waveforms and phase shifts for each individual element. This approach was first employed with a 64-element 2D-array to focus through the skull (Hynynen and Jolesz, 1998). Each element was powered separately so as to precisely measure the relevant phase shift through that portion of the skull. Applying the corresponding time delays thus eliminated the skull-induced aberrations allowing the beam to be correctly focused albeit at a peak pressure of 40 % of that in water at 0.6 MHz and just 5 % at 1.58 MHz (Hynynen and Jolesz, 1998).

A more minimally invasive approach using a catheter-inserted hydrophone through the vascular network was also proposed (Clement and Hynynen, 2002c). The hydrophone is set at a single location and through the use of beam steering methods that account for the presence of the skull and a priori pressure measurements at locations remote to the focus in the absence of the skull, lesions were produced

10 mm away from the receiver in ex vivo bovine tissue. The theory had previously been applied to soft tissue (Seip et al., 1994) but this was the first time it had been applied transcranially with an ex vivo skull. It was also demonstrated in vivo in a rabbit through an ex vivo human skull with focal steering of ∼5 mm although this was associated with a reduction in temperature elevation (Hynynen et al., 2004).

1.4.5 MR-ARFI techniques

Rather than direct measurement of the US field which requires implantation of a hydrophone, measurements of tissue displacement due to the ARF which can be measured non-invasively with MRI have been proposed to correct for phase aberrations (Urban et al., 2007). The basic principle for phased arrays is that maximising the tissue displacement induced at the focus optimises focusing at this point due to the fact that acoustic intensity is proportional to the displacement. Consequently, by changing the phase of each element individually until the maximum displacement is achieved, optimal focusing can be obtained. However, for large arrays this process requires many iterations as well as the contribution of any given element being so small that it becomes undetectable.

Adapative focusing techniques combined with magnetic resonance acoustic radiation force imaging (MR-ARFI) (McDannold et al., 2008) to measure the displacements resulted in an increased focal intensity by a factor of 5 in a gel phantom (Larrat et al., 2010). The method is based on generating virtual transducers from linear combinations of elements with spatially encoded signals in order to optimise the phases of all elements simultaneously (Herbert et al., 2009). Although the acquisition time was not optimized in the study and took 2.5 h for 64 channels, the authors estimated a total time of 4 min for 512 channels was achievable.

A subsequent study (Marsac et al., 2012) using the same method with a 512-element array and cadaver heads reported a 2.2-fold increase in the acoustic intensity com-

pared to the non-corrected beam and a 1.5-fold increase over aberration correction via an acoustic simulation based on CT scans. Whilst the total acquisition time took 2 h, an alternative element encoding scheme using a reduced the number of acquisitions required less than 20 % of the time to achieve 90 % of the non-aberrated intensity (Kaye et al., 2012). Splitting the transducer elements into 4 segments can also help reduce the total acquisition time requiring only ∼100 displacement measurements to be taken which could be completed within 2 min. A maximal displacement of 27 % compared to 12 % for a CT-based correction and 40 % for gold-standard, hydrophone method was achieved (Hertzberg et al., 2010).

1.4.6 Ultrasonic stars

To solve the problem of the absence of acoustic sources within the brain, a non-invasive method was proposed based on generating a cavitation bubble at the target location; the subsequent shock wave produced by the collapse of the bubble acts as an acoustic source, which the authors termed an ultrasonic star (Pernot et al., 2006). One array at 0.9 MHz was used to initiate the cavitation bubble and a second imaging array at 3.5 MHz detected the emitted shock wave on which time reversal could then be performed to refocus at the target. This was initially validated in a gelatin phantom with agar scatterers behind a rubber aberrator.

The concept was subsequently improved to allow for accurate initial transcranial positioning of the bubble (Gâteau et al., 2010). This was achieved using a two-step adaptive focusing technique. The first step targets the desired location through the skull using a 3D finite-difference simulation based on CT images of the skull and then a high-intensity pulse is emitted to induce a cavitation bubble. The second step is then the time reversal of the acoustic emission to maximise the pressure at the focal spot. Although the initial simulation is computationally expensive, it need only be performed once as beam steering can be employed following the acoustic

emission of the bubble.

To introduce more stable bubbles and reduce the pressures required to generate cavitation, a technique called transcranial acoustic droplet vaporisation (ADV) was developed (Haworth et al., 2008). Although only a proof-of-concept study, the ultimate aim was to inject liquid droplets which could be vaporised by low-frequency, spherically focused US, shown to suffer less focal distortion (Yin and Hynynen, 2005). The resulting ADV bubbles could then be used as point-scatterers for time reversal aberration correction.

1.4.7 Computational techniques

Advances in computational power have enabled the time reversal method to be applied in silico with virtual sources propagated numerically through medical-imaging derived tissue maps to determine the required corrections. Sun & Hynynen (Hynynen and Sun, 1999; Sun and Hynynen, 1998) were the first to take advantage of MRI data to obtain a digitised human skull profile. The skull was treated as a homogeneous layer with properties obtained through weighted averages of the inner table, diploe and outer table. Via the use of a numerical model, that is essentially an extension of the Rayleigh-Sommerfeld integral to account for multiple layers, phase corrections could be applied to achieve sharp focusing through the skull.

Whilst MRI can give the external structure of the skull bone, CT data can also provide internal information from which three bone layers could be segmented corresponding to the inner and outer tables and the trabecular structure (Clement and Hynynen, 2002b). Within each of these layers, an effective sound speed was defined, derived from the CT density data, from which the expected phase shifts across the skull could be estimated. Using this approach, 79 % of the pressure amplitude of the ideal, phase-corrected case in the absence of the skull was achieved.

The use of CT density information to inform local acoustic property assignment was further extended through the definition of a porosity parameter calculated from the Hounsfield units at each voxel and an assumed linear mixture rule treating the skull as a composition of skull and water (Aubry et al., 2003; Carter and Hayes, 1977; Rho et al., 1995). Experimental validation was achieved using ex vivo human skulls. A three dimensional finite difference time domain solver for the linear wave equation was used to propagate a virtual point source at the focus out through the skull on to the array receiver where the waveforms were recorded. Upon time reversal and re-emission of the waveforms on a physical, 300-element, 1 MHz array, 90 % of the peak pressure obtained using an implanted hydrophone was reached (Marquet et al., 2009). Furthermore, in a cadaver model, the accuracy of time reversal focusing was shown to be within a few millimetres as verified by MR thermometry (Chauvet et al., 2013).

Solving the full wave equation is computationally expensive. So, in an attempt to reduce computational times, several other numerical schemes have been developed: a hybrid approach starting with a Rayleigh integral method to propagate the waves from the transducer up to the skull surface followed by a fluid-solid finite-element method through the skull and finally an angular spectrum method inside the skull up to the focus (Pulkkinen et al., 2011); a simplified one parameter (phase) spherical projection model for propagating the wavefront outside the skull after finite difference transcranial simulation (Pinton et al., 2012b); a wavevector-frequency domain algorithm, analogous to the angular spectrum method (Clement and Hynynen, 2002a); and k-space time reversal methods (Jing et al., 2012; Treeby and Cox, 2010a) allowing for precise focusing at much coarser grid spacings, down to only 2.56 grid points per wavelength (Jing et al., 2012) compared to 10–20 for finite difference methods.

Additionally, more simplistic methods such as ray-tracing have been previously im-

plemented. However, a study comparing four aberration-correction methods ranging from semi-analytical methods to fully simulation based found that the simulation-based techniques produced much tighter focal spots (by a factor of 5.2 on average) than distance-based or ray-tracing phase correction methods (Kyriakou et al., 2015).

Computational methods have also been applied to reducing hot spots and secondary foci induced by the skull through the additional of extra point sources in the time reversal protocol (Leduc et al., 2012), investigating standing wave effects for different transducer apertures and locations (Song et al., 2012) and modelling non-linearity for high intensity brain applications (Pinton et al., 2011). Furthermore, shear wave effects can impact upon the transcranial US field. Purely elastic mode propagation actually exhibits less focal distortion than compressional propagation (owing to the similarity between the bone shear wave speed and speed of sound in water) albeit at only 35–55 % of the peak amplitude of longitudinal mode propagation (Clement et al., 2004).

Specifically for neuromodulation applications, numerical error sources arising from time reversal simulations have been studied indicating that the largest errors are likely to be from staircasing (Robertson et al., 2017a) and uncertainties in the acoustic properties (Robertson et al., 2017b). Additionally, simulations have been conducted to analyse the in situ fields produced by single-element transducers in murine, primate (Constans et al., 2017) and human (Mueller et al., 2017; Robertson et al., 2017a) skulls suggesting these simpler sources are viable for brain stimulation targeting.

In sum, computational modelling is the only currently feasible method for determining appropriate source conditions to focus within the brain for neuromodulation given the invasivity of direct measurement approaches and higher intensities required to induce measurable responses either through the ARFI or ultrasonic stars. Moreover, these methods require additional equipment such as MRI and transducer

arrays which may also preclude their use at this stage. In terms of the sources themselves, initial studies suggest single-element transducers in the 250–500 kHz range are feasible for focusing to some brain areas but it is likely lens and array-based designs may be required to target deeper structures, achieve increased specificity and stimulate more complex brain architectures and pathways.

1.5 Monitoring

Whilst numerical modelling is an invaluable tool in determining the required source conditions for transcranial targeting, the ability to monitor where US is being delivered would enable confirmation that the intended brain target is being stimulated. For thermal ablation applications, low-powered sonications raising the tissue by a few degrees can be utilised in combination with MR thermometry (Rieke and Pauly, 2008) to determine the US focus. However, for neuromodulation applications where thermal rises are estimated to be negligible in the majority of cases, this technique is not viable for monitoring purposes. Indeed, MR thermometry did not detect any temperature changes for frequencies between 220 kHz and 1.145 MHz up to pressures of 1 MPa (Dallapiazza et al., 2018).

As discussed in the previous section, MR-ARFI offers a non-thermal monitoring mechanism with tissue displacements encoded as phase shifts (Kaye and Pauly, 2014). However, this technique is still under development and typically requires higher pressures than those needed to induce neuromodulation, albeit at shorter pulse lengths, in order to image the subsequent tissue displacements (Hersh et al., 2018; Liu et al., 2015). Therefore the safety of this approach for brain applications must also be established. Consequently, there is still a need to develop monitoring techniques for non-thermal US pulse sequences.

In terms of monitoring brain activity, EEG and fMRI are the cornerstones of non-

invasive techniques. EEG uses multiple electrodes placed on the scalp to measure evoked potentials but is relatively superficial making it difficult to monitor the activity of deep-seated targets. One group have explored tagging deep brain volumes using a unique, high frequency electrical signal generated by US above the normal frequency range for neural firing rates thus extending the use of EEG to deep brain targets (Darvas et al., 2016). fMRI approaches are more applicable to measuring brain activity at deeper targets with 3D spatial mapping as well as for investigating connectivity between different brain areas. This makes for a powerful tool for monitoring real-time US-induced brain activity as well as longer term connectivity effects but does require an MR-compatible source to run a trial inside the scanner and there are also concerns that acoustic pressure-mediated mechano-vascular coupling may also give rise to BOLD signals (Lee et al., 2016b) and therefore needs further investigation.

As as alternative to fMRI, functional US imaging (Macé et al., 2011) may prove to be a useful modality or imaging microvascular dynamics in the brains of small animals at a superior temporal resolution but for now the technique is not scalable to large animals and humans due to the increased skull thickness.

2

Acoustic & thermal solvers

The purpose of this chapter is to introduce the theoretical underpinning behind the numerical techniques used in subsequent chapters. The fundamental governing equations for 3D acoustic wave propagation in both fluids and elastic media are given along with numerical methods to solve them – primarily, k-Wave and the angular spectrum method. Validation of the numerical models is achieved through analytical test cases for focused and unfocused transducers. Source characterisation through acoustic holography and calibration of the Sonic Concepts H-107 transducer is also presented. Finally, the Pennes bioheat equation and its numerical implementation are also given in order to determine the thermal fields generated from pressure distributions obtained using the acoustic solvers.

2.1 Linear acoustic theory

Fluid systems can be described by four fundamental equations: the conservation of mass, momentum and energy combined with an equation of state to relate between thermodynamic variables. The following analysis serves to introduce the equations along with their key assumptions and so the reader is referred to seminal texts for a more comprehensive understanding (Blackstock, 2000; Landau and Lifshitz, 1987; Morse and Ingard, 1968; Pierce, 1990).

It is assumed that as the sound wave passes through the medium it introduces a small perturbation to each of the variables (pressure p, density ρ, and particle velocity $\mathbf{v}$). For a homogeneous medium at rest, each of the variables can therefore be written as the sum of an ambient, uniform quantity denoted by a subscript 0 and a perturbed acoustic quantity, denoted by a $'$ as given by:

$$p(\mathbf{x}, t) = p_0 + p'(\mathbf{x}, t), \tag{2.1}$$

$$\rho(\mathbf{x}, t) = \rho_0 + \rho'(\mathbf{x}, t), \tag{2.2}$$

$$\mathbf{v}(\mathbf{x}, t) = \mathbf{v}'(\mathbf{x}, t). \tag{2.3}$$

The continuity equation is,

$$\frac{\partial \rho}{\partial t} = -\nabla \cdot (\rho \mathbf{v}). \tag{2.4}$$

Substituting equations (2.2) and (2.3) into (2.5), and neglecting second order terms of acoustic variables yields the linearised continuity equation:

$$\frac{\partial \rho'}{\partial t} = -\rho_0 \nabla \cdot \mathbf{v}'. \tag{2.5}$$

The equation for conservation of momentum for an inviscid fluid, also known as Euler's equation, is

$$\frac{\partial \mathbf{u}}{\partial t} + (\mathbf{v}.\nabla)\mathbf{v} = -\frac{\nabla p}{\rho}. \tag{2.6}$$

Using the same approximations as described above, Eq. (2.6) reduces to

$$\frac{\partial \mathbf{v}'}{\partial t} = -\frac{1}{\rho_0}\nabla p'. \tag{2.7}$$

Equations (2.5) and (2.7) contain three unknowns $\mathbf{v}'$, p', and ρ'. The equation of state allows any state variable to be expressed as a function of any other two, for example $p = p(\rho, s)$ where s is the entropy of the fluid, and thus we can eliminate one of the unknowns. To first order, a small change in pressure can be related to small changes in density and entropy,

$$\delta p = \Big(\frac{\partial p}{\partial \rho}\Big)\delta\rho + \Big(\frac{\partial p}{\partial s}\Big)\delta s. \tag{2.8}$$

If the motion induced by a sound wave is assumed lossless and adiabatic, then $\delta s = 0$, and the linear equation of state becomes

$$p' = \frac{\partial p}{\partial \rho}\Big|_0 \rho' = c_0^2 \rho', \tag{2.9}$$

where the speed sound in the fluid is defined as $c_0 = \sqrt{\frac{\partial p}{\partial \rho}\Big|_0}$. From Eq. (2.9) and

due to the requirement of $|\rho'| \ll \rho_0$ in deriving the linearised continuity equation (2.5), the stipulation on the size of the pressure perturbation can be determined as $|p'| \ll \rho_0 c_0^2$.

Combining the time derivation of Eq. (2.5) with the divergence of Eq. (2.7) and using Eq. (2.8) to eliminate ρ results in the second-order lossless wave equation,

$$\nabla^2 p - \frac{1}{c_0^2}\frac{\partial^2 p}{\partial t^2} = 0, \tag{2.10}$$

where the acoustic pressure p' has been redefined as p. Losses can be incorporated into the wave equation for thermoviscous fluids but for tissue where the mechanisms are not fully understood, losses are generally added in ad hoc and this will be detailed in Sec. 2.3.1.

2.2 Elastic wave propagation

2.2.1 Linear elasticity

Solid materials support shear stresses and hence the medium also supports transverse waves in addition to longitudinal waves. Once more, in this section, the key equations for the derivation of wave propagation in elastic and viscoelastic media are introduced but for a fuller description, the reader is referred to the following seminal text (Kolsky, 1963).

In linear elasticity, small deformations (strains) are assumed to be linearly related to the applied stresses. This statement is known as Hooke's law and holds experimentally for many materials. It can be expressed as

$$\boldsymbol{\sigma} = \mathsf{C} : \boldsymbol{\epsilon}, \tag{2.11}$$

where $\boldsymbol{\sigma}$ is the stress tensor, $\boldsymbol{\epsilon}$ is the strain tensor and C is the fourth-order stiffness tensor. For an isotropic medium, this expression collapses to just six unknown stresses and strains which are related by two constants, the Lamé parameters, μ and λ, as given by the following relation in Einstein summation notation:

$$\sigma_{ij} = \lambda \epsilon_{kk} \delta_{ij} + 2\mu \epsilon_{ij}, \tag{2.12}$$

where δ_{ij} is the Kronecker delta function. The equation of state for linear elastic materials is taken into account through Hooke's law from the definition of isothermal compressibility, $\beta_T = -\frac{1}{V}\left(\frac{\partial V}{\partial p}\right)_T$, where the bulk modulus K is defined as the inverse of compressibility and related to the Lamé parameters by $\lambda = K - \frac{2}{3}\mu$.

The strain-displacement relationship is given by,

$$\boldsymbol{\epsilon} = \frac{1}{2}\Big(\nabla \mathbf{u} + (\nabla \mathbf{u})^T\Big), \tag{2.13}$$

where $\mathbf{u}$ is the displacement vector (not velocity) and holds for small displacements where for the shear strains, $\gamma \approx \tan\gamma$, where γ is the angle of rotation for a small element of material that has been deformed.

2.2.2 Elastodynamics

The elastodynamic equations describe waves in an elastic material and are formed by the combination of the conservation of momentum with Hooke's law. Conservation of momentum, an expression of Newton's second law, can be derived independently of any constitutive law by considering a force balance over a small solid element,

$$\rho_0 \frac{\partial^2 \mathbf{u}}{\partial t^2} = \rho_0 \mathbf{g} + \nabla \cdot \boldsymbol{\sigma}, \tag{2.14}$$

where $\mathbf{g}$ are the body forces per unit volume. Substitution of (2.12) and (2.13) into (2.14) and neglecting any body forces results in the Navier equation,

$$\rho_0 \frac{\partial^2 \mathbf{u}}{\partial t^2} = (\lambda + \mu)\nabla(\nabla \cdot \mathbf{u}) + \mu \nabla^2 \mathbf{u}. \tag{2.15}$$

Following Helmholtz decomposition, the displacement vector, $\mathbf{u}$, can be represented as the sum of a scalar and vector potentials, $\mathbf{u} = \nabla\phi + \nabla \times \boldsymbol{\psi}$. Consequently, substitution into (2.15), and noting that $\nabla \times \nabla\phi = 0$ and $\nabla \cdot (\nabla \times \boldsymbol{\psi}) = 0$, results in two separate wave equations,

$$0 = \nabla\left(\rho_0 \frac{\partial^2 \phi}{\partial t^2} - (\lambda + 2\mu)\nabla^2 \phi\right) + \nabla \times \left(\rho_0 \frac{\partial^2 \boldsymbol{\psi}}{\partial t^2} - \mu \nabla^2 \boldsymbol{\psi}\right). \tag{2.16}$$

Re-writing Eq. (2.16) in the standard wave equation form reveals the wave speed for each of the separate propagating components,

$$\frac{\partial^2 \mathbf{u_l}}{\partial t^2} - c_l \nabla^2 \mathbf{u_l} = 0, c_l = \sqrt{\frac{\lambda + 2\mu}{\rho_0}}, \tag{2.17}$$

$$\frac{\partial^2 \mathbf{u_t}}{\partial t^2} - c_t \nabla^2 \mathbf{u_t} = 0, c_t = \sqrt{\frac{\mu}{\rho_0}}. \tag{2.18}$$

The displacement $\mathbf{u_l} = \nabla\phi$ represents the longitudinal or compressional wave and $\mathbf{u_t} = \nabla \times \boldsymbol{\psi}$, the transverse or shear wave which is not present in liquids or gases due to the absence of shear stress.

2.2.3 Viscoelastic media

Unlike elastic materials which immediately return to their original state once the applied stresses are removed, viscoelastic media exhibit time-dependent strain. The

classical model for such materials is the Kelvin-Voigt spring-dashpot system. Applying this model to both the shear and and normal stresses of an elastic medium results in the following modified constitutive law (Treeby and Cox, 2014),

$$\sigma_{ij} = \lambda\epsilon_{kk}\delta_{ij} + \chi\frac{\partial}{\partial t}(\epsilon_{kk})\delta_{ij} + 2\mu\epsilon_{ij} + 2\eta\frac{\partial}{\partial t}(\epsilon_{ij}), \tag{2.19}$$

where χ and η are the compressional and shear viscosity coefficients, respectively. Substitution of (2.19) and (2.13) into the equation of motion (2.14) yields a modified form of the Navier equation applicable for describing waves in viscoelastic media,

$$\rho_0\frac{\partial^2\mathbf{u}}{\partial t^2} = (\lambda+\mu)\nabla(\nabla\cdot\mathbf{u}) + (\chi+\eta)\Big(\nabla\cdot\frac{\partial\mathbf{u}}{\partial t}\Big) + \mu\nabla^2\mathbf{u} + \eta\nabla^2\frac{\partial\mathbf{u}}{\partial t}. \tag{2.20}$$

2.3 Numerical implementation

Whilst some analytical solutions exist for wave propagation in homogeneous media, for more complex, heterogeneous topologies with spatially-varying acoustic properties, the sounds fields must be solved numerically. A range of numerical methods for the solution of acoustic wave propagation exist including: finite difference (FD), finite element, finite volume, boundary element and particle-based. The choice of solver for a given problem invariably depends on a number of factors and the comparison between the different options could be the subject of a lengthy treatise in itself. To summarise in short, the open source k-Wave toolbox (Treeby and Cox, 2010a) based on a k-space pseudospectral (PS) time domain solver was selected owing to its superior accuracy at fewer points per wavelength over its FD counterparts thus reducing the computational burden. For source characterisation the angular spectrum method (ASM) was also utilised in order to match physical and numerical source conditions.

In this section, the numerical implementation of the equations described in Sections 2.1 & 2.2 are briefly described along with some key points pertaining to the realisation of spectral methods in practise. Again, this is not meant to be an exhaustive summary of spectral domain methods and their use in solving acoustic problems but rather a short introduction to the solver employed in this thesis highlighting some of the principal concepts. For a more thorough analysis, the k-Wave manual and associated papers (Treeby and Cox, 2010a,b) prove excellent resources that can be supplemented by additional texts on spectral method implementation (Trefethen, 2000).

2.3.1 k-Wave fluid solver

k-Wave is an open source, MATLAB toolbox for simulating acoustic wave propagation in 1-3 dimensions (Treeby and Cox, 2010a). The solver is based on a modified set of the fundamental set of acoustic equations given in Sec. 2.1 to include source terms, absorption and, if required, non-linearity.

Acoustic absorption in biological tissues has been shown to be well described by a power law as given by $\alpha = \alpha_0 f^n$ where α is the absorption in dB/cm, α_0 is a constant, f is the frequency and n is the exponent, typically close to 1 (Duck, 1990). k-Wave implements this power law dependence through the use of a fractional Laplacian with two terms, one for absorption and one for dispersion. This is entered into the equation of state as the operator, L, but is only valid for $0 < n < 3$, $n \neq 1$ due to the specific formulation employed (Treeby and Cox, 2010b).

For a heterogeneous medium with absorption, the set of equations therefore becomes:

$$\frac{\partial \rho}{\partial t} = -\rho_0 \nabla \cdot \mathbf{v} - \mathbf{v} \cdot \nabla \rho_0 + S_M, \tag{2.21}$$

$$\frac{\partial \mathbf{v}}{\partial t} = -\frac{1}{\rho_0} \nabla p + \mathbf{S}_F, \tag{2.22}$$

$$p = c_0^2 \Big(\rho + \mathbf{u} \cdot \nabla \rho_0 - L\rho \Big). \tag{2.23}$$

where $\mathbf{u}$ is the particle displacement and $S_M, \mathbf{S}_F$ are source terms as described in the following section. Non-linear terms can also be included (Treeby et al., 2012) but in this thesis only linear simulations are considered.

Source implementation

Source terms can be inserted into k-Wave as either a force source (a body force per unit mass) to the momentum conservation equation (2.22) or a mass source (input of mass per unit volume) to the mass conservation equation (2.21). The k-Wave convention is that a free-space "pressure source" corresponds to a mass source (S_M) that acts as a monopole and a free-space "velocity source" corresponds to a force source ($\mathbf{S}_F$) that acts as a dipole. It is noted that this may cause confusion as in many acoustics texts, a velocity source, such as a moving transducer surface, is referred to as a mass source as it is equivalent to an injection of mass, and pressure source can refer to a force source as the gradient of pressure leads to a force in the momentum equation.

k-Wave simulations for each source type with the corresponding analytical solution are presented in Fig. 2.1. A free-space pressure source matches closely with the Rayleigh solution for uniform velocity source distribution in an infinite baffle acting as a monopole,

$$p_r = \rho_0 c_0 v_0 [e^{-ikz} - e^{-ik\sqrt{z^2+a^2}}], \tag{2.24}$$

where a is the source radius, k is the wavenumber and z is the axial distance (Blackstock, 2000); and a free-space velocity source agrees with the Mellow solution, a dipole source for a resilient disk in free space (Mellow, 2008).

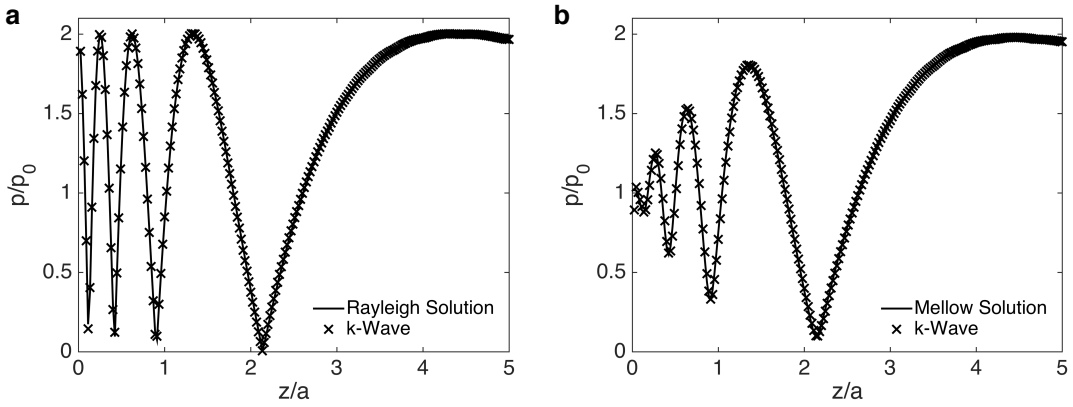


Fig. 2.1: k-Wave source conditions. 6 mm diameter, circular, unfocused piston transducer. k-Wave simulations compared to the Rayleigh and Mellow analytical solutions. Pressures are normalised by the source pressure, $p_0 = \rho_0 c_0 u_0$. **a** Free-space pressure source. **b** Free-space velocity source.

Pseudospectral k-space method

The discretisation and numerical solution of Eqs. (2.21), (2.22) & (2.23) is achieved by utilising a k-space corrected PS technique referring to the calculation of spatial gradients in the spectral domain coupled with a finite difference (FD) scheme in the time domain. For conventional FD methods, gradients are estimated by fitting a polynomial to a number of surrounding nodes from which the derivative is calculated, referred to as a local approximation. Increasing either the order of the polynomial or the number of points fitted will serve to increase the accuracy of the approach. The PS method is essentially the FD scheme taken to its limit: that is, rather than using a limited order polynomial to fit a number of local grid points, a Fourier series is fitted to all of the data in a given dimension and is thus known as a global method. As the basis functions are now sinusoidal, theoretically, only two points

per wavelength are required compared to 10 or more for FD schemes.

FD approximations introduce numerical errors into the solution; these errors are controlled by constraining the size of the timestep to ensure stability. This requirement can be determined through von Neumann stability analysis to determine the relationship between timestep and grid size for which the errors remain bounded. k-space techniques attempt to relax this requirement in order that larger timesteps can be utilised by correcting for the dispersion error. Whilst the modifications are strictly only exact for homogeneous media, they also provide increased stability for heterogeneous simulations (Cox et al., 2007; Treeby and Cox, 2010a).

The end result of k-space corrected PS solvers is a higher degree of accuracy achieved with fewer grid points per wavelength compared to other numerical schemes. This is particularly useful for large-scale, three-dimensional computations in order to reduce the memory requirements and computational times.

Stability

The stability of a numerical scheme relates to the growth of errors over time. Typically, to ensure convergence and stability, the Courant-Friedrichs-Lewy (CFL) number, defined as the distance a wave can travel in one timestep:

$$CFL \equiv c_o \frac{\Delta t}{\Delta x}, \tag{2.25}$$

is quoted. For k-Wave, a default CFL number of 0.3 is employed to balance accuracy and computational speed. Initial simulations (data not shown) confirmed this as an appropriate choice and so this value was used for all subsequent fluid simulations.

Perfectly matched layer

The use of spectral methods introduces additional challenges at the boundaries of the simulation domain. For the Fourier collocation method, the use of the fast Fourier Transform (FFT) by definition requires the field to be periodic and hence effectively results in mirror sources. In order to reduce the effect of these adjacent wavefronts propagating into the simulation domain and distorting the field without substantially increasing the computational grid, a perfectly matched layer can be implemented. This layer of a small number of grid points at the computational boundary acts as an absorber to significantly attenuate as well as prevent reflections of the outgoing waves through this boundary.

In the majority of simulations implemented in this thesis, a PML of 10 grid points was used which results in attenuation of the transmitted wave (the wave that wraps around the domain due to the periodicity of the FFT) by 84 dB and the reflected wave by 65 dB.

2.3.2 k-Wave elastic solver

Much of the preceding analysis for the fluid-based solver is also valid for the elastic solver although there are some important differences. In this instance, the modified Navier equation (2.20) is solved as two first-order coupled partial differential equations: (2.19) and (2.14) both written in terms of particle velocity. The classical Kelvin-Voigt model results in frequency squared attenuation and hence attenuation values were adjusted to match the required power law formulations at the driving frequency of 500 kHz.

The CFL was also reduced to 0.1 as the numerical implementation of the elastodynamic equations does not use a k-space corrected scheme and hence smaller time steps are required to ensure accuracy and stability for the leapfrog FD method

(Firouzi et al., 2012; Treeby et al., 2014). Finally, source terms are required in terms of stresses and so a pressure source is entered as $\sigma_{ij} = -p\delta_{ij}$ where p is the hydrostatic pressure.

2.3.3 Angular spectrum methods

The ASM allows for propagation of a complex acoustic field from one plane to a second parallel plane accounting for diffraction effects. Mathematically, this can be derived from the Helmhlotz equation (2.26) which assumes a time harmonic solution to the linear, lossless wave equation (2.10) where ϕ is the velocity potential and $k = 2\pi f/c_0$ is the wavenumber.

$$\nabla^2\phi + k^2\phi = 0. \tag{2.26}$$

Taking 2D spatial Fourier Transforms (FTs) in the x-y plane and assuming propagation in the $+z$ direction, Eq. (2.26) is transformed into a series of uncoupled ordinary differential equations (ODEs). Each ODE describes the propagation of a plane wave at a specific angle relative to the z-axis and the solution at a distance z is just the superposition of all the ODEs. Consequently, the solution of the field at any arbitrary z-plane can be obtained in the spatial frequency domain, where $\Phi(\tilde{u}, \tilde{v}, z) = G(\tilde{u}, \tilde{v})e^{ik_z z}$ is the Fourier transformed velocity potential as a function of spatial frequencies $\tilde{u}$ and $\tilde{v}$ and propagation depth, z. The expression $G(\tilde{u}, \tilde{v})e^{ik_z z}$ is known as the Angular Spectrum and is comprised of two parts: the FT of the source condition, $G(\tilde{u}, \tilde{v})$, multiplied by a propagation factor, $e^{ik_z z}$, which independently propagates each plane wave through a distance, z, based on the perpendicular wavenumber, k_z. The final solution at a given plane can then obtained by applying the inverse FT of $\Phi(\tilde{u}, \tilde{v}, z)$.

Source conditions can be implemented as either a normal velocity distribution $v_{z0}(x, y)$

or a pressure distribution $p_0(x, y)$ specified over a 2D x-y plane. Converting this to a velocity potential distribution is then achieved through the definition of the velocity potential $v = \nabla\phi$ and the linear momentum equation (2.7) as follows: $p = -\rho_0 \frac{\partial \phi}{\partial t}, v_z = \frac{\partial \phi}{\partial z}$. In the frequency domain, these derivatives are replaced by multiplications: $p = -i2\pi f \rho_0 \phi$, $v_z = ik_z\phi$.

Acoustic Holography

One particular application of the ASM is for acoustic holography to characterise US sources and quantify source vibrations (Sapozhnikov et al., 2015). The approach requires an input plane obtained from experimental measurements which can then be propagated to any arbitrary depth in either the forwards or backwards direction. This is illustrated in Fig. 2.2 using simulated k-Wave data for the H-107 transducer in freefield to obtain a nearfield plane, 26 mm from the back surface of the vibrating source. Both the amplitude and phase information are shown in Fig. 2.2b, e, respectively. This plane is then back-propagated to an equivalent source plane (Fig. 2.2a, d) and forward propagated to the focal plane (Fig. 2.2c, f). The ASM simulations were conducted using the same grid spacing as the k-Wave grid, 0.468 mm, but zero-padded to increase the domain size from 300^2 to 1024^2 in order to reduce the interference from mirror sources. This technique is applied to experimental measurements for the H-107 transducer in Sec. 2.4.2 to allow direct comparison between simulations and experiments.

Filtering

Whilst the ASM method can be used to easily propagate pressure distributions through adjacent parallel planes, mirror sources, introduced by the inherent periodicity assumed through the use of the FFT, can leak into the resultant field and act as a substantial source of error. To reduce the impact of these mirror sources, homogeneous wave components propagating at high angles of incidence need to be

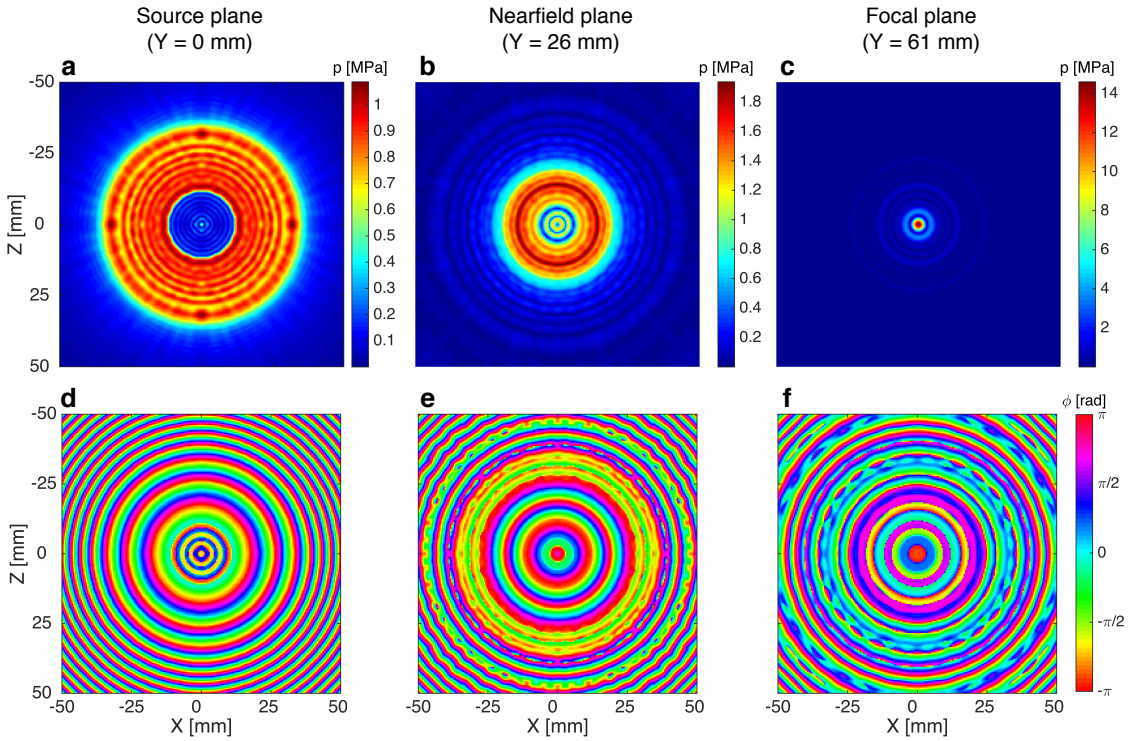


Fig. 2.2: Angular spectrum method (ASM) plane propagation. Sonic Concepts H-107 500 kHz transducer. **b, e** Amplitude and phase of a nearfield plane (26 mm from the source) obtained from a k-Wave freefield fluid-based simulation. **a, d** ASM Back-propagation to the source. **c, f** ASM forward propagation to the focal plane.

removed to prevent their interaction with the field. Two solutions therefore exist to improve the accuracy of the ASM approach: 1) careful selection of the domain size and grid spacing in order to limit the angular range and therefore truncate the homogeneous plane wave components at a certain angle; and 2) application of a low-pass filter to attenuate or remove these components based on their angle as given by:

$$\theta = \arccos\left(\frac{k_z}{k}\right). \tag{2.27}$$

To demonstrate this, Fig. 2.3 displays the axial and radial (at a depth of $0.334 z_{rayl}$ and at z_{rayl}) pressure profiles for a 1 MHz, 15 mm radius circular piston source. The unfiltered ASM simulation is compared to a Hamming window (HW) low-pass filtered case relative to either the Rayleigh solution (2.24) on-axis or the Hutchins

numerical solution (Hutchins et al., 1986) for the radial profiles. Ripples creep into the unfiltered solution at ∼1/3 of the Rayleigh distance axially and approximately one source radius from the centreline in the lateral direction but these can be recovered by utilising the smoothed low pass filter which can be implemented at a much reduced computational cost compared to zero-padding the domain (Blackmore et al., 2018).

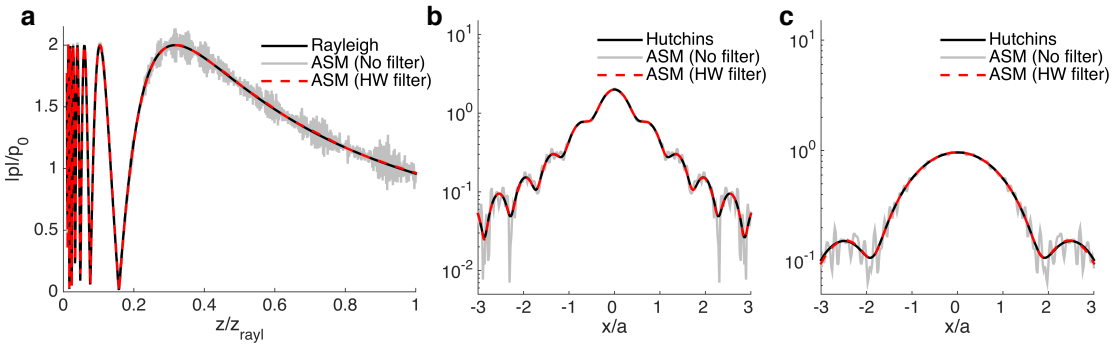


Fig. 2.3: Comparison of filtered and unfiltered angular spectrum method (ASM) pressure fields with analytical expressions. Pressure fields are for a 1 MHz, a = 15 mm radius unfocused piston source. Pressures are relative to the source pressure, $p_0 = \rho_0 c_0 u_0$. **a** Axial distribution against the on-axis Rayleigh solution. **b** Radial distribution at $z_1 = 0.334 z_{rayl}$ against the Hutchins solution (log-scale). **c** Radial distribution at $z_2 = z_{rayl}$ against the Hutchins solution (log-scale).

2.4 Test cases & transducer calibration

This section serves to benchmark the k-Wave solver relative to known freefield analytical solutions and experimental scans to test the accuracy of the solver. The spatial mesh resolution was set as (0.468 mm) which corresponds to 6.4 points per wavelength (PPW) in water. A CFL number of 0.3 therefore gives 21.2 points per period (PPP). Characterisation of the H-107 transducer is achieved through a back-propagated source plane condition to directly match between simulations and experiments as well as calibration of the source over a range of input voltages.

2.4.1 Geometric source implementation

A geometric bowl implementation of the H-107 transducer in freefield was the first test case considered. The simulated field in the axial direction is compared to the

analytical O'Neil solution (O'Neil, 1949) (Fig. 2.4a) and in the focal radial plane to the numerical Chen solution (Chen et al., 1993) (Fig. 2.4b). The pressures were normalised by the source pressure in both cases. Whilst the field shape is consistent between the two plots, k-Wave underpredicts the focal gain by 10.5 % relative to the O'Neil solution and 3.5 % relative to the Chen solution. The exact reason for this is unclear but stair-casing effects may have contributed. In order to avoid this scaling issue, a back-propagated source plane from a hydrophone scan was implemented rather than using geometric source condition as outlined in Sec. 2.4.2.

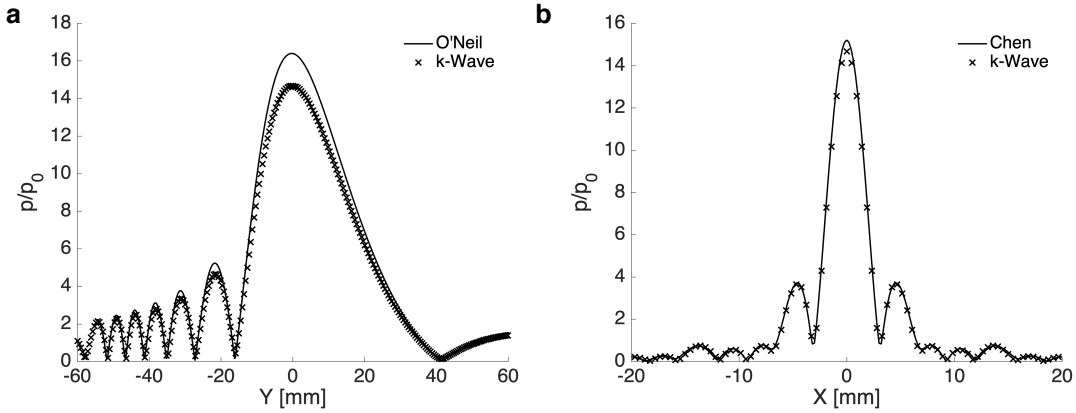


Fig. 2.4: Comparison between k-Wave and analytical/numerical solutions for a geometrically focused transducer. Geometric source implementation of a focused Sonic Concepts H-107 transducer. Pressures scaled relative to the source pressure, p_0. **a** Axial distribution versus O'Neil solution. **b** Focal radial distribution versus Chen solution.

2.4.2 Acoustic holography

As described in Sec. 2.3.3, acoustic holography is a technique for characterising ultrasonic transducers. A lateral raster scan was performed in the nearfield of the H-107 transducer, 26 mm from the radiating surface, with a spacing of 0.5 mm and width of 70 mm as shown in Fig. 2.5b, e where steady state phase and amplitudes have been extracted. This plane was then propagated to the source (0 mm) and to the focus (61 mm) using the ASM. In comparison to the simulated data in Fig. 2.2, the planes are less symmetric with local differences evident. This may in part be explained by inhomogeneities in the radiating surface and small inherent measurement

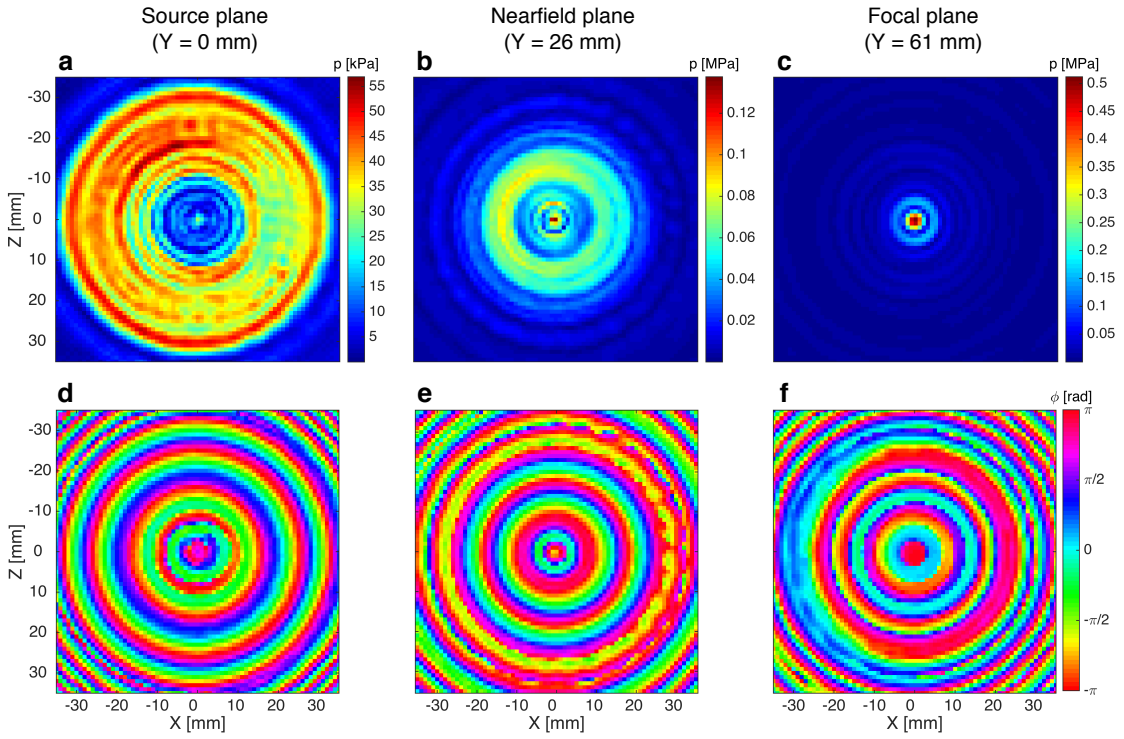


Fig. 2.5: Angular spectrum method (ASM) plane propagation. Sonic Concepts H-107 500 kHz transducer. **b, e** Amplitude and phase of a nearfield plane (26 mm from the source) obtained from experimental hydrophone measurements. **a, d** ASM back-propagation to the source. **c, f** ASM forward propagation to the focal plane.

errors. However, the left-right asymmetry is probably a result of a slight rotational misalignment of the hydrophone which, whilst also manifesting in the source plane, is not an issue at the focus where the beam is concentrated. It is also possible that the asymmetry is an inherent property of the source.

The back-propagated source plane in Fig. 2.5a, d was then interpolated on to a grid of spacing 0.468 mm to match the lateral CT resolution and inputted as the source for a freefield k-Wave simulation and re-compared to hydrophone measurements over radial and axial line scans. Fig. 2.6a displays the axial profile with the idealised O'Neil solution, scaled to the maximum simulated pressure, shown for comparison purposes. It is clear that the back-propagated source plane provides a better description of the real source than the O'Neil solution, the profile of which differs strongly either side of the focal spot leading to incorrect predictions of all the null locations by several mm. In contrast, the holographic k-Wave simulation shows

very good agreement particularly over the main lobe from −20 to 25 mm with an error of less than 2 % at the focal spot. There is some divergence in the nearfield: despite close alignment of the first two nulls between measurements and simulation, the preceding peaks are underpredicted by 13.9 and 24.1 % corresponding with 1.5 and 2 mm positional errors, with the errors increasing towards the transducer.

The radial distribution at the focus shows a closer match between the k-Wave holographic simulation, hydrophone measurements and the numerical Chen solution (Chen et al., 1993) although the back-propagated source plane is still superior. The locations of the peaks and nulls are well captured across the whole plotted domain out to 20 mm.

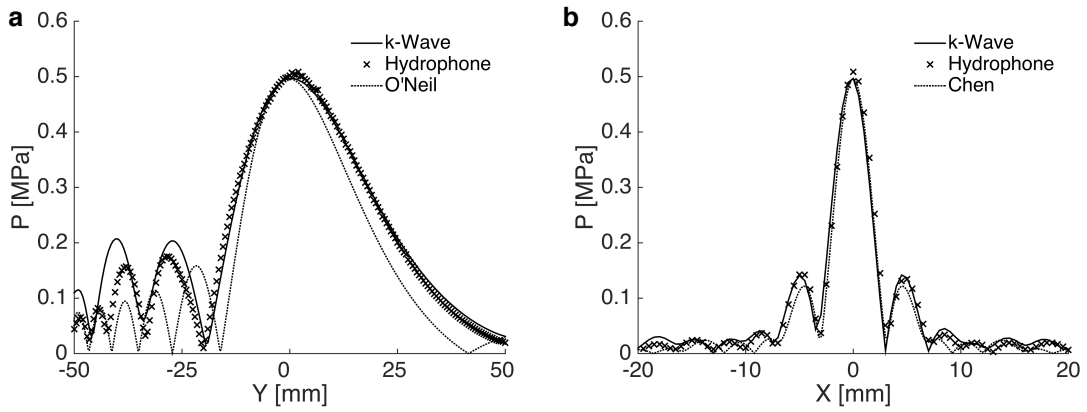


Fig. 2.6: Comparison of freefield H-107 modelling and experimental results. Back-propagated nearfield plane source (from hydrophone measurements) implementation in k-Wave against analytical solutions and hydrophone measurements. **a** Axial distribution with O'Neil solution. **b** Focal radial distribution with Chen solution.

2.4.3 Experimental calibration

Focal pressure calibration of the H-107 device was completed up to a peak output amplifier voltage of 60 V which corresponds to a maximum peak positive pressure of ∼2 MPa. Fig. 2.7a depicts either the maximum pressure anywhere in the waveform, the maximum pressure of a steady state window after ringdown, the FFT-extracted fundamental pressure or the peak negative pressure. The difference between the two maximum pressure terms is illustrated in Fig. 2.7b which arises as the result of an

initial higher pressure cycle that subsequently rings down to steady state; this is an innate property of the source. Ten repeat pressure measurements were taken at each voltage step; the values were highly repeatable with error bars smaller than the symbol size and hence are not shown.

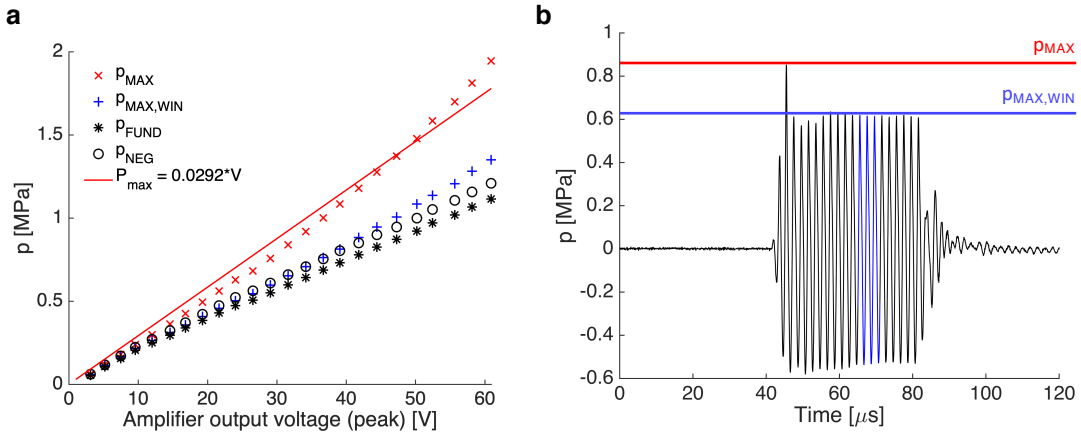


Fig. 2.7: H-107 focal pressure calibration, a The maximum pressure anywhere in the waveform (p_{MAX}), the maximum steady state, windowed pressure ($p_{MAX,WIN}$), the maximum peak negative pressure (p_{NEG}), and the FFT-extracted steady state fundamental pressure (p_{FUND}) as a function of amplifier output voltage. **b** Illustration of typical focal waveform with definitions of the two different maximum pressures occurring at different time points.

For the human pilot study (Chapter 5), the maximum overall pressure was used as a safety limit based on the data presented in Chapter 4. The relationship between amplifier output voltage was approximately linear and so a linear regression was performed as shown by the red line in Fig. 2.7a. The upper value of 60 V corresponds to the maximum amplifier voltage utilised in the human trial. The overall maximum pressure is approximately 25–30 % higher than the windowed maximum pressure. It is also noted that the peak negative pressure could have been used for the safety limit as this is what drives cavitation and hence mechanical safety concerns (see Sec. 4.3) and the negative portion of the waveform does not exhibit the same ring down phenomenon.

The growing disparity between the maximum windowed pressure and fundamental pressure represents increased non-linearities in the pressure waveform. Energy is

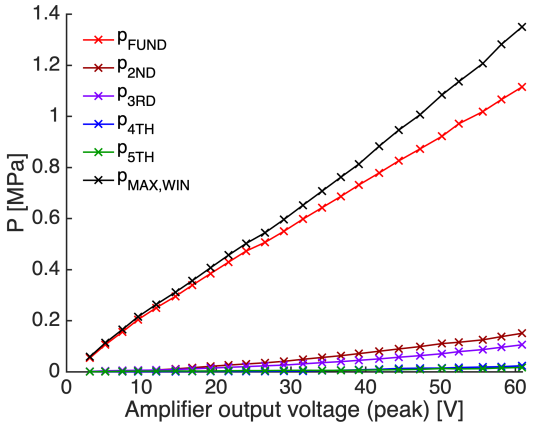


Fig. 2.8: H-107 non-linear harmonic growth. The power content in the fundamental and 2nd through 5th harmonics along with the maximum peak positive pressure over the windowed steady state waveform are plotted as a function of amplifier output voltage.

converted into higher harmonics as shown in Fig. 2.8. At the highest amplifier output employed (60 V), the fundamental accounts for 84 % of the total power in the waveform. Since this is in freefield and for transcranial propagation, much of the incident energy will have been reflected, attenuated or refracted (particularly in the skull situated closer to the transducer), the non-linear effects were deemed not to be important and hence only linear simulations were considered.

2.5 Thermal modelling

Ultrasonic absorption in biological tissues leads to heat deposition and consequently thermal modelling is required to assess the associated temperature rises. Thermal modelling was carried out in Chapter 5 to assess temperature elevations in the skull bone and brain tissue on a subject-specific basis following acoustic simulations to determine in situ pressure fields.

2.5.1 Bioheat equation

The Pennes bio-heat transfer equation (2.28) is used to model the temperature changes, a modified form of the heat diffusion equation incorporating blood perfusion

losses and heat deposition (Pennes, 1948).

$$\rho c_{p,t} \frac{\partial T}{\partial t} = \kappa \nabla^2 T + w \rho_b c_{p,b} (T - T_a) + q, \tag{2.28}$$

where T is the local temperature, T_a is the arterial temperature, κ is the tissue thermal conductivity, ρ is the tissue density, $c_{p,t}$ is the tissue specific heat capacity, w is the blood perfusion rate, ρ_b is the blood density, $c_{p,b}$ is the blood specific heat capacity, and $q =$ is the rate of heat production. For US, $q = 2\alpha I$ where α is the absorption and the acoustic intensity, I, can be calculated using the plane wave assumption such that $I = p^2/2\rho_0 c_0$ (Nyborg, 1981).

2.5.2 Numerical solver

The k-Wave toolbox includes a k-space PS scheme for solving the Pennes bio-heat equation. For homogeneous media, the k-space correction leads to an exact formulation that is unconditionally stable for any arbitrarily large timestep. In a heterogeneous medium, this does not hold and so some initial test cases were performed to assess stability over a range of timesteps.

2.5.3 Test case

A simplified skull geometry was created as shown in Fig. 2.9a comprised of a 5 mm strip of skull bone surrounded by tissue. A spherical Gaussian heat distribution of radius 2 mm was defined in the centre the bone layer with an elongated, ellipsoidal volume 7.5 mm into the tissue to mimic the expected pressure fields produced by an incident focused US transducer. Heat deposition amplitudes were estimated assuming a pressure of 0.6 MPa at the centre of the ellipsoidal distribution and 1.0 MPa in the skull bone, and generic tissue (scalp) thermal parameters (see Sec. 5.2.4). Heating was applied for 0.3 s mimicking a typical US neuromodulation burst. The

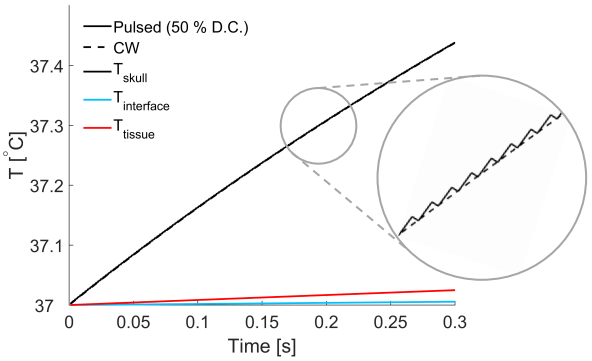


Fig. 2.10: k-Wave thermal solver: bursted versus continuous wave (CW) comparison. A CW heating pulse at half the intensity of the 50 % duty cycle, bursted waveform was compared to determine whether the individual pulses must be captured to accurately estimate the overall temperature rise.

temporal profile of the temperature at three points: in the skull, the tissue and at the interface were recorded as indicated by the crosses in Fig. 2.9a.

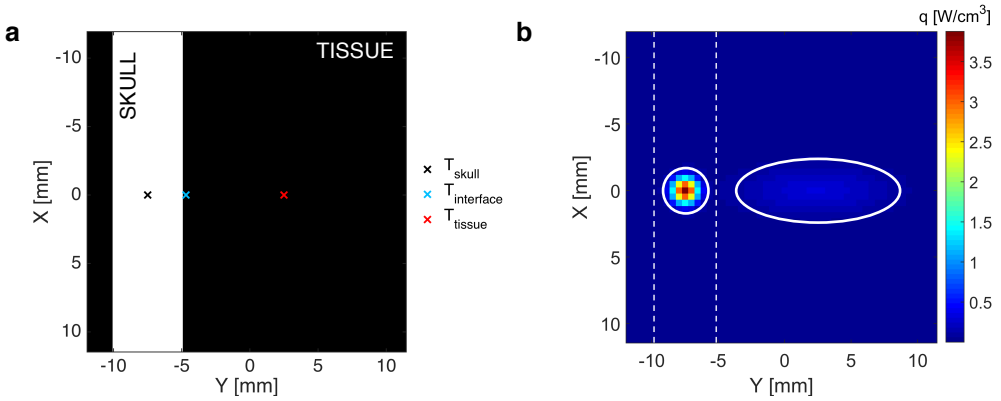


Fig. 2.9: k-Wave thermal solver: test case setup. a Cross-sectional view of simulation domain in XY-plane. The crosses show locations in the centre of the skull, at the interface and 7.5 mm into the tissue at which the temperature was measured. **b** Input heating distribution comprising two Gaussian distributions: one spherical in the skull bone and one ellipsoidal in the tissue to mimic focused US sonication.

As typical human neuromodulation bursts consist of a sequence of repeated pulses rather than a continuous wave (CW) sonication, the initial set of simulations compared a 300 ms, 50 % duty cycle burst with a 300 ms CW pulse at half the intensity in order for larger timesteps to be utilised. In this case, timesteps of 0.1 ms were used for both simulations. The results show that the difference between bursted and CW was less than 0.01 °C (see zoomed inset in Fig. 2.10). Therefore, an aver-

aged heating intensity over the total burst duration is sufficient to capture the total temperature rise without modelling each individual pulse.

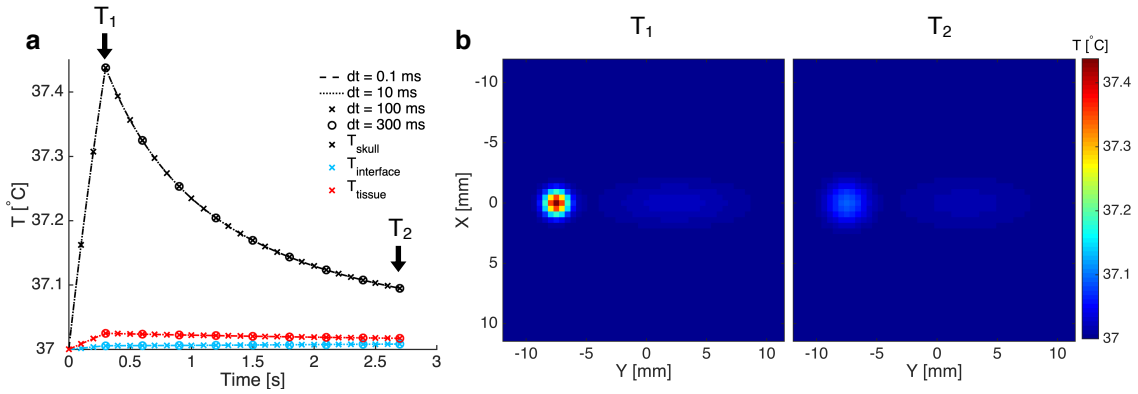


Fig. 2.11: k-Wave thermal solver: effect of timestep. **a** Temperature curves for three points in the simulated domain: in the skull bone, at the interface and in the tissue as indicated by the crosses in Fig. 2.9a. Four different timesteps: 0.1, 10, 100 and 300 ms were considered. **b** Spatial temperature maps at the end of the heating phase (T_1) and cooling period (T_2).

Further simulations where then performed for averaged intensities over the burst duration with a range of different timesteps (1–300 ms). In these simulations, the temperature was modelled for one heating burst and the subsequent cooling period. The estimated thermal rises as a function of time and the spatial temperature distributions at the end of the heating (T_1) and cooling (T_2) periods are shown in Fig. 2.11a, b, respectively. The maximum temperature rise occurred in the skull bone reaching 0.44 °C which reduced to 0.09 °C at the end of the cooling period; in the tissue, the maximal temperature elevation was 0.02 °C. It can be seen that the predicted temperature profiles are identical over this range of timesteps and so all simulations reported later were calculated with a timestep of 300 ms corresponding to the length of the applied US burst in Sec. 5.2.3.

3

Transcranial ultrasound focusing

This chapter details the modelling of a single-element, focused transducer for transcranial targeting of regions within the visual cortex. A modelling pipeline is described for optimising the placement of a single-element transducer to focus to a given brain site based on the concept of time reversal. The sensitivity of transcranial US fields to changes in acoustic properties, incident source angle, perturbations in transducer location and orientation, and the inclusion of shear wave modelling are presented. Validation of the modelling is then achieved through experimentally-obtained hydrophone measurements in an ex vivo human skull. The impact of segmentation techniques from both CT and MR imaging modalities are also considered. Finally, correction methods are explored for focusing through regions of the skull that are intractable to targeting with a single-element transducer regardless of its placement.

3.1 Introduction

A unifying theme of ultrasonic brain therapies is the need to focus US waves transcranially to a specific target site, compensating for skull-induced aberrations and determining accurate in situ intensities as discussed in Sec. 1.4. In the case of ablative modalities, such as for the treatment of essential tremor (Elias et al., 2013; Magara et al., 2014), and blood-brain barrier opening (Lipsman et al., 2018; McDannold et al., 2012), large multi-element arrays are utilised to achieve precise spatial control of the focal US fields confining effects to a very limited volume of tissue. However, the complexity and cost associated with such approaches is extensive and consequently, at this early stage of research into US-induced neural modulation, can be prohibitory as well as potentially unnecessary. In addition, to compete with tES and TMS NIBS methods which are relatively inexpensive, the setup needs to be cost effective.

Single-element transducers are much simpler in design and although they lack the focal specificity that can be achieved through array-based targeting, there are several advantages to be had. The first is that these transducers are much easier to implement practically for use in conjunction with human behavioural trials both in terms of alignment and coupling; a surface area of a few cm^2 may be coupled to the scalp via careful manipulation of a participant's hair and application of US coupling gel whereas an array covering much of the accessible head, will clearly require more sophisticated coupling strategies as well as potentially requiring the hair to be shaved. Moreover, many of the current targets for studying ultrasonic neuromodulation are located close to the cortical surface and are on the order of $1\,cm^3$ in size. This focal size is well within the reach of a focused, single-element US transducer and in fact, for focusing US close to the skull, array designs suffer due to the high oblique incidence of some elements and long travel paths from elements on the far side of the head.

As the US neuromodulation field progresses, it is possible to envision array-based designs coming to the fore to achieve more precise, deep targeting as well as potentially patterned stimulation for activation of more complex brain architectures and pathways. However, the single-element device may also play a role in the clinic for treatment of neurological disorders; its simplicity and ease of implementation allowing it to be quickly introduced into both the healthcare system and neuro-research field. Evidently, widespread implementation of US for neurostimulation is still a way off, but an early consideration of the possible end goals motivates the research of transcranial US devices across a range of complexities and cost scales.

The complications involved in focusing US waves across the skull have been previously discussed in Sec. 1.4 along with trans-skull focusing strategies. Typically, these correction methods rely on computational models built from participant-specific medical imaging datasets and utilise time reversal methods to determine appropriate source conditions for targeting to a specific brain site. Forward propagation simulations of these optimised source conditions can also be calculated to estimate internal pressure fields.

In this chapter, the efficacy of utilising single-element, geometrically-focused transducers to focus to different regions in the visual cortex is assessed. To determine the optimal placement of the transducer, a slightly modified time reversal simulation protocol is employed, whereby rather than implement the method to inform the source conditions of a multi-element array, the signals from the target location are used to optimise single-element transducer placement. Subsequent forward simulations are then computed to determine the variation in transcranial pressure distributions for different transducer locations and assess the specificity.

Accurate modelling of transcranial US propagation is essential for neuromodulation applications to predict in situ focal regions and amplitudes both from a safety perspective and to causally link sonication of a particular brain site to behavioural

and electro-physiological outcomes. Retrospective modelling has indicated that in previous human studies, a misalignment between the US focus and intended target may have contributed to unresponsive trials (Lee et al., 2015, 2016b). Moreover, recent papers citing brain activation via auditory pathways in response to US exposure (Guo et al., 2018; Sato et al., 2018) also motivates the use of modelling to ensure coincidence between focus and target as well for the planning of sham sites where confirmation is required that the US focus and a particular brain region do not overlap.

Many factors can impact upon the estimated pressure fields. To understand the main error sources the following parameters were considered: errors in acoustic properties, the effect of transducer angle, the influence of shear waves, and the sensitivity of small perturbations in source location (Sec. 3.3.4–3.3.7). To validate the simulations, experimental measurements using ex vivo human skulls in a water tank were conducted and are presented in Sec. 3.4.

For deriving skull property maps, CT is the gold standard for transcranial acoustic simulations with high contrast achieved in bone easily distinguishing it from the surrounding soft tissues. Differences in the x-ray attenuation across the skull also provide additional information for the assignment of local acoustic properties rather than simply treating the skull as a homogeneous medium. However, CT x-rays result in exposure to ionising radiation which for healthy subjects is an unnecessary risk. Consequently, in the context of neuromodulation studies, segmentation from structural MRI scans poses a more attractive option which can be combined with the fMRI session already required for the determination of an individual's anatomical brain sites. The downside of extracting skull bone information from MRI is that segmentation is more complicated owing to the very low contrast between bone and adjacent CSF and dural matter. The minimal contrast also prevents local property assignment with binary segmentation the best that can be currently achieved.

Therefore, transcranial pressure field differences were quantified for simulations using homogeneous and inhomogeneous property maps obtained through segmentation of the same raw CT data in addition to a comparison between binary segmentation of MR and CT co-registered scans.

Finally, certain anatomical skull features such as the petrous ridge (see Fig. 3.1) introduce substantial heterogeneities in the skull transmission paths for targets that underlie those regions. Consequently, strong fragmentation of the in situ field results. For such sites, phase and amplitude based correction methods are examined to determine whether manipulation of the source conditions can refocus the US waves to the intended targets.

3.2 Methods

3.2.1 Medical images & dataset

Direct comparison between simulated and experimental results was achieved through the use of an ex vivo human, male skull. A CT scan of the skull with a lateral resolution of 0.468 mm and a slice thickness of 0.5 mm formed the basis of the simulations. The dataset was linearly interpolated on to a uniform grid with a spacing of 0.468 mm in all dimensions. The skull was modelled as being immersed in water to mimic the experimental conditions.

Brain targets were created using Neurosynth (Yarkoni et al., 2011), a platform for automatically combining the activation maps of multiple neuroimaging studies. Masks were downloaded for V1, FFA and MT in MNI space (a standardised coordinate system named after the Montreal Neurological Institute where it originated). The masks were split by hemisphere to create bilateral regions of interest and the peak voxels were extracted. The MNI coordinates were then transformed into subject space for the ex vivo skull to give the target sites. These targets correspond to

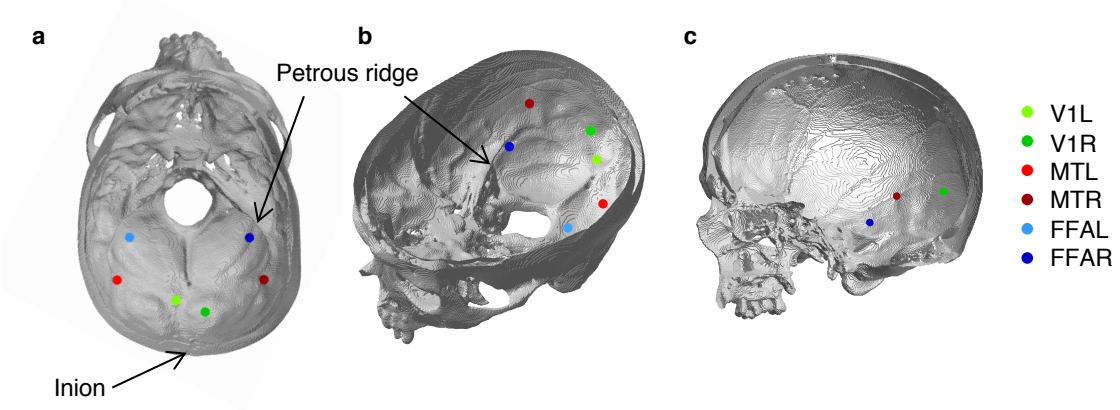


Fig. 3.1: Visual targets superimposed on to an ex vivo human skull. V1: primary visual cortex. MT: middle temporal area. FFA: face fusiform area. L, R indicate left or right hemisphere. Notable topological skull features are also labelled. **a, b** Skull sectioned in transverse plane and **c** Right hemisphere targets in sagittal plane.

the primary visual input (V1), the middle temporal visual area which is involved in motion perception processing (MT/V5) and the fusiform face area (FFA) which is a specialised region for facial recognition. Both V1 and MT are located close to the cortical surface whereas FFA is both deeper and closer to the skull base. Each of the bilateral targets are denoted L or R to denote the hemisphere in which it is located as shown in Fig. 3.1. Two notable topological skull features, the inion and petrous ridge, are also marked.

Segmentation

The majority of simulations were computed using a material property map obtained via threshold segmentation of the CT data on a binary basis to assign either skull bone or water values to a particular grid point and thus assumes the properties of skull bone are homogeneous. Inhomogeneous property assignment using the Hounsfield unit information is considered in Sec. 3.6.1 and MR-based segmentation in Sec. 3.6.2.

Depth study

To investigate focusing efficacy dependence on target depth, a series of targets were defined along a line segment orientated approximately through the visual cortex in a half skull CT image dataset spaced at 9 mm intervals (Fig. 3.2). The dataset was converted into simulation space by applying threshold segmentation and then interpolated on to a uniform 0.468 mm grid.

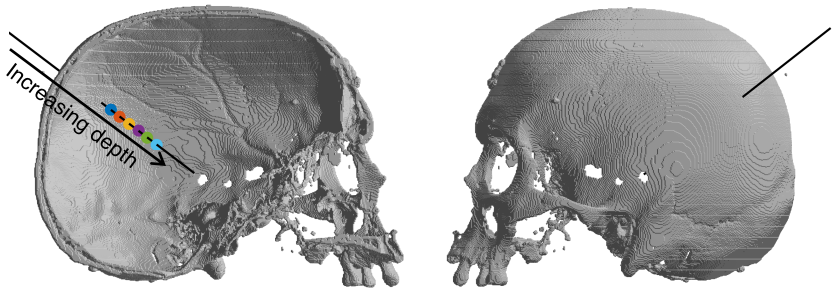


Fig. 3.2: Target depth study in ex vivo human half skull. Targets indicated by coloured markers along line segment approximately through the visual cortex.

3.2.2 Ultrasound source

The US transducer employed was a single-element, geometrically-focused transducer with centre frequency of 500 kHz, an outer radius of 32 mm, a central cut-out of radius 11.3 mm and a geometric focal length of 63.2 mm (H-107, Sonic Concepts Inc, Bothell, WA, USA). The frequency was chosen as it is widely used in ultrasonic neuromodulation (Sec. 1.3) where is provides a trade-off between focal spot size and aberration reduction. Lower frequencies exhibit reduced focal distortion but result in larger focal volumes, lower radiation force, and increase the risk of standing waves. 500 kHz has also previously been shown to effectively modulate neural function in both animals (King et al., 2013; Tufail et al., 2010) and humans (Legon et al., 2018a,b, 2014).

3.2.3 Computational modelling

Fluid solver

Numerical modelling of acoustic wave propagation through the skull was carried out using k-Wave, an open source, k-space, pseudospectral, time-domain solver (Treeby and Cox, 2010a,b). Previous numerical analysis of the use of k-Wave for modelling transcranial US fields has been conducted (Robertson et al., 2017a,b) and applied to modelling transcranial US propagation in nonhuman primates (Constans et al., 2017; Top et al., 2016) and humans (Mueller et al., 2017). The model and its underlying equations are discussed in more detail in Sec. 2.3.1. The majority of simulations assumed the skull to be an effective fluid and hence neglected the impact of shear waves. Modelling the skull as an elastic medium and including shear wave effects was considered in Sec. 3.3.6 and Sec. 3.3.7. Acoustic properties were assigned as given in Table 3.1.

The source condition for the single-element transducer was implemented as a back-propagated experimentally-measured nearfield plane, obtained using a needle hydrophone (HNA needle hydrophone, 400 µm, ONDA, Sunnyvale, CA, USA). This captured any source inhomogeneities as well as eliminating any staircasing errors that arise from defining a curved surface on a Cartesian grid. Further details can be found in Sec. 2.4.2.

Only linear simulations were considered as neuromodulation applications typically utilise intensities below which non-linear effects become significant. Previous work has also found the difference between linear and non-linear simulations to be less than 1 % (Mueller et al., 2017).

Simulations were carried out at a grid spacing of 0.468 mm (matching that of the lateral resolution of the CT dataset), which yields 6.36 PPW at 500 kHz in water; and a Courant-Friedrichs-Lewy (CFL) number equal to 0.3 based on the maximum

		Compressional		Shear	
Material	Density, ρ_0 [kg/m^3]	Sound speed, c_0 [m/s]	Attenuation, α [dB/cm]	Sound speed, c_s [m/s]	Attenuation, α_s [dB/cm]
Water	1000	1488	0	0	0
Skull	1732	2820	$8.83\text{f}^{1.43}$	1500	28.9f^2

Table 3.1: Acoustic properties. Compressional and shear properties for skull bone and water (Treeby and Cox, 2014). Attenuation data given in power law form, $\alpha = \alpha_0 f^n$.

sound speed. These parameters were selected based on the mesh resolution study in Sec. 3.2.4, showing good convergence without necessitating an overly extensive computational cost. Simulations were run for a total time of 100 cycles which allowed the steady state pressure distribution to be established accounting for any interactions and reflections from the skull as determined by preliminary simulations. Fields were then extracted over the last 2 periods. Simulation spaces had a spatial grid of 300 points per dimension plus an additional 10 point absorbing perfectly matched layer. Consequently, the domain width was 140.4 mm in each direction with the target location placed at the centre point and hence simulations did not capture reflections off of the back wall of the skull. Larger simulations including the whole skull and experiments with the back skull wall intact did not show any significant differences and thus the effect of standing waves was deemed negligible and the domain size reduced to improve computational times.

Fluid-based simulations were carried out on a local machine with an NVIDIA Titan Xp GPU with 12 GB of onboard RAM and each simulation took approximately 4 min to run.

3.2.4 Mesh resolution study

Reduction in the spatial mesh at a fixed CFL of 0.3 from 3.2 PPW to 12.7 PPW (in water), corresponding to double and half the lateral grid spacing of the CT scan, was conducted for freefield and skull simulations at location V1R (defined in Sec. 3.2.1). In both cases, the back-propagated source plane condition was imple-

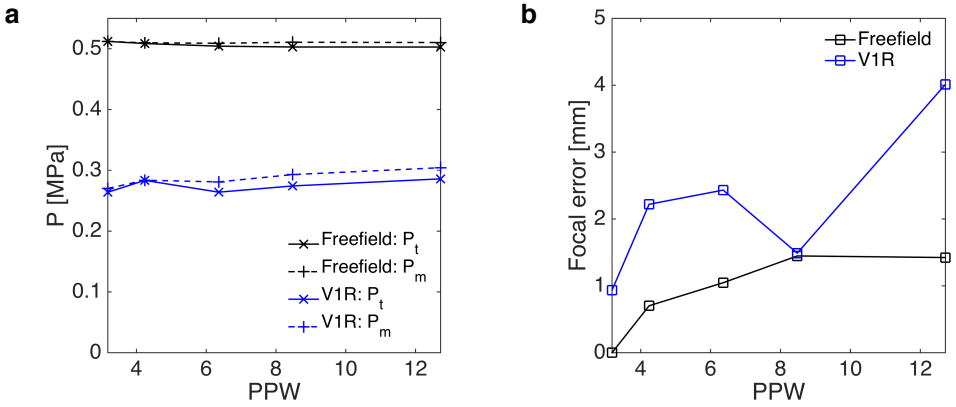


Fig. 3.3: k-Wave mesh resolution study. Freefield (black) and transcranial propagation (blue) simulations. **a** Target (P_t) and maximum (P_m) pressure as a function of PPW. **b** Focal error (difference between the location of P_t and P_m) as a function of PPW.

mented. The variations in target (P_t) and maximum (P_m) pressure as a function of PPW are shown in Fig. 3.3a and the variation in focal error (the distance between the maximum and target pressures) is shown in Fig. 3.3b.

For the freefield case, the pressure values have completely converged above 6.4 PPW and for the skull case, the magnitudes increase but only by up to 8 % at 12.7 PPW compared to the nominal 6.4 PPW. In terms of the focal error, for freefield there is again only slight differences beyond 6.4 PPW (<0.5 mm increase). Conversely, for the skull simulations, the error is not monotonic with the location of maximum pressure shifting along the axial direction by an additional ±1.5 mm. Given that the brain targets of interest in this thesis are on the order of 0.5–1 cm^3, small, millimetric, axial positional errors are acceptable. This, coupled with only minimal increases in predicted pressures motivated the selection of 6.4 PPW (the nominal CT resolution without additional interpolation) for all subsequent simulations in keeping with the resolution used in previous k-Wave studies (Mueller et al., 2017; Top et al., 2016).

It is noted that a more extensive mesh resolution study can be found in Robertson et al. (2017a) for a point source simulation. It was shown that to achieve mean intensity or positional errors over the received transducer surface of less than 10 %, PPW of over 20 may be required. However, this was done using a simplified geometrically

defined spherical shell bone layer. For CT data, the values are simply interpolated to achieve finer resolution – no further information is available and so these errors may be inherent to simulations based on medical imaging datasets. In terms of predicting focal pressures and locations, the mesh reduction study conducted here suggests that simulations at 6.4 PPW are justifiable.

Elastic solver

To model the impact of shear waves, the k-Wave elastic solver described in Sec. 2.3.2 was employed. This model assumes Kelvin-Voigt material behaviour and hence frequency squared attenuation. Consequently, the compressional attenuation value in Table 3.1 was also modified to match the required absolute attenuation at the transducer's centre frequency of 500 kHz. The CFL number was reduced to 0.1 to ensure stability as the scheme was not k-space corrected. The reduced timestep and additional memory requirements for the computation of the elastic code meant that simulations had to carried out on a GPU cluster with simulation times on the order of 8 h.

Proposed modelling pipeline

The proposed pipeline developed in this section is intended to optimise the placement of a single-element transducer so as to maximise the pressure at the target location and confine the focal volume as best possible to the intended target without sonicating off-target regions. Motivated by time reversal (Fink, 1992; Fink et al., 2003), the procedure is as follows which matches the steps in Fig. 3.4:

a Participant-specific structural (skull bone) information is obtained via segmentation of CT or MRI scans. Target brain sites are also acquired by extraction of the peak activation sites from an fMRI task. In this chapter, the data are obtained from an ex vivo human skull and brain targets are inserted as per

Sec. 3.2.1.

b A numerical point source is placed at the target location within the brain. Acoustic waves are then propagated out through the skull to a spherical surface which corresponds to a sphere of radius equal to the focal length of the transducer. This spherical surface therefore represents the set of all possible transducer locations to refocus to the target location.

c The phase and amplitude of the steady state waveform at every grid point located within one grid point of the sphere are extracted via a discrete Fourier Transform and interpolated on to the exact spherical surface to mitigate staircasing errors due to the finite grid spacing. These distributions are used to determine the optimal transducer location to focus through the skull to the target site. This was either done manually via visual inspection of the phase distribution or as the output of an optimisation algorithm (see Fig. 3.5) neglecting any locations that resulted in a collision between the transducer and the skull.

d Once a transducer location was selected, the forwards simulation was then performed to calculate the in situ pressure fields and assess the resultant focal spot and pressure amplitudes. The following metrics were used to quantify the focusing efficacy of different transducer sites: target pressure, the pressure at the exact target centre; maximum pressure, the highest pressure anywhere inside the skull cavity; focus error, the Euclidean distance between the target and maximum pressure coordinates; and the $-6\,\mathrm{dB}$ volume relative to the maximum internal pressure.

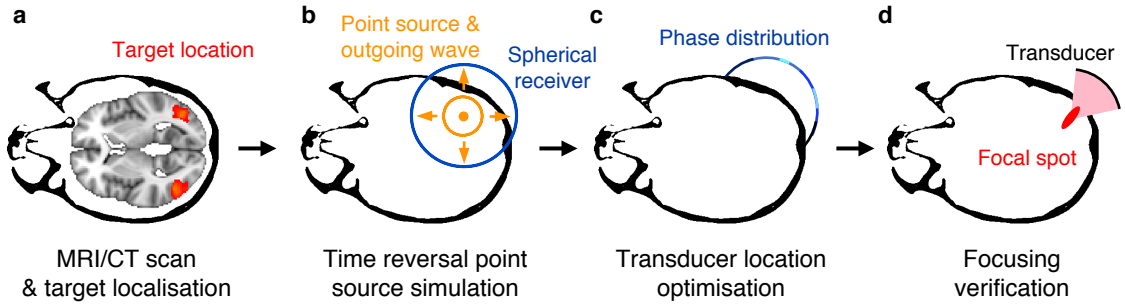


Fig. 3.4: Proposed modelling pipeline for determining single-element transducer position. **a** Structural information obtained from CT/MRI scans and target location acquired from peak activation site during fMRI task. **b** Acoustic point source placed at target location and wave propagated outwards through the skull to a spherical receiver of radius equal to the focal length of the transducer, corresponding to the set of all possible transducer positions. **c** The steady state phase distribution is extracted on this surface informing the optimal placement of the transducer either through manual selection or the output of an optimisation algorithm. **d** Confirmation of required focusing and estimation of in situ intensities is achieved by simulating waves emitted from the transducer incident to the target from the optimised location.

Optimisation algorithms

A number of different optimisation algorithms were tested to identify the optimal transducer location using either just the phase (ϕ) information or the phase and amplitude (A) information. The error functions that were considered were: the maximum phase error equivalent to the L-infinity norm over the surface, Eq. (3.1); the least squares of the phase residuals, Eq. (3.2); the least squares of the phase residuals multiplied by the amplitude squared, Eq. (3.3); and the least squares of the phase residuals normalised by the amplitude squared, Eq. (3.4).

$$e_1 = \min_{x \in X}\left(\max_{x \in T} |\phi_x - \bar{\phi}|\right), \tag{3.1}$$

$$e_2 = \min_{x \in X}\left(\sum_{x \in T} (\phi_x - \bar{\phi})^2\right), \tag{3.2}$$

$$e_3 = \min_{x \in X}\left(\sum_{x \in T} A_x^2 (\phi_x - \bar{\phi})^2\right), \tag{3.3}$$

$$e_4 = \min_{x \in X}\left(\sum_{x \in T} \frac{1}{A_x^2} (\phi_x - \bar{\phi})^2\right). \tag{3.4}$$

Equation (3.3) serves to penalise locations at high phase errors where more of the US

energy is transmitted through the skull whereas Eq. (3.4) acts to bias the function to favour higher amplitude areas. Fig. 3.5 gives a representative example of the process. For each point x on the sphere X, a subset of points, $T \subset X$, are evaluated that correspond to all the points that would lie on the transducer's radiating surface if it was placed with its centre point at x (Fig. 3.5a). T is defined more explicitly as $T \subset X, T = \{x \in X | r_{min} \leq \delta \geq r_{max}\}$ or the subset of points in X for a given x that lie within the distance bounds r_{min} and r_{max} corresponding to the outer and inner edges of the transducer, respectively. The errors are calculated relative to the mean phase ($\bar{\phi}$) over the transducer surface for each location. The minimum of the resultant distribution, neglecting any centre points where the transducer clashes with, or lies within, the skull is then selected as the optimal location. As an example, Fig. 3.5b shows phase distribution for a particular x location over the subset T with points outside the transducer surface shaded black.

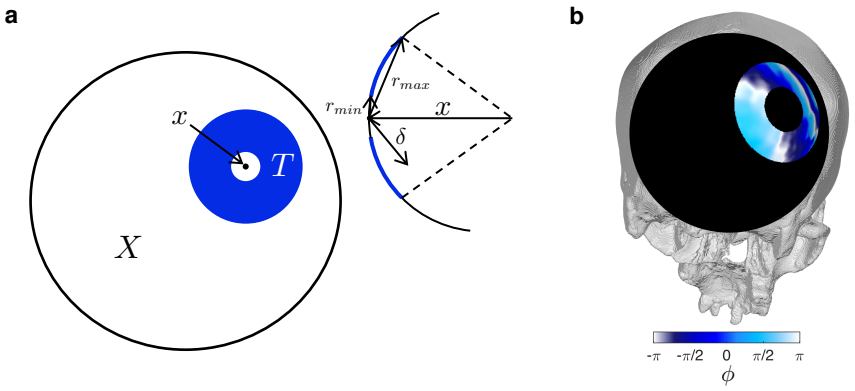


Fig. 3.5: Optimisation algorithm implementation, a Schematic depicting point selection for optimisation routine to determine optimal transducer location. X is the set of all radial positions x that lie on the spherical surface. For each x, the set of points, $T \subset X, T = \{x \in X | r_{min} \leq \delta \geq r_{max}\}$, that lie on the transducer surface are evaluated using Eqs. (3.1) - (3.4). The transducer location is then chosen to minimise these functions. **b** Phase distribution over transducer surface for a given x. Points outside the transducer surface are shaded black.

L1-norm variants of Eq. (3.2) – (3.4) were also tested but did not significantly affect the outcomes and hence are not shown here. Additionally, phase unwrapping techniques were considered but did not prove viable over the spherical surface as large smoothing filters were required to remove discontinuities.

3.2.5 Experimental setup

Experiments were carried out in a degassed water tank with the skull also degassed for 36 h prior to the experiment commencing. The frontal portion of the skull bone was removed in order to allow access with a fibre-optic hydrophone with a tip size of 100 µm (Precision Acoustics, Dorset, UK) as shown in Fig. 3.6.

The transducer was connected through a 55 dB broadband amplifier (1140LA, E&I, Rochester, NY, USA) and a matching network and driven a signal generator (33250A, Agilent, Santa Clara, USA).

In order to correctly align all the experimental appartus (the skull, transducer and hydrophone) the following procedure was used. The freefield focus was first located with the hydrophone and defined as the axis centre point. The hydrophone was then withdrawn on a 3D-positioning system in order to allow room for the skull to be inserted. A 3D-printed holder (Maimbourg et al., 2018) was created for each target location in order to orientate the skull with respect to the transducer. This was then fixed to a mount which slid over the transducer. The hydrophone could then be returned to the focus corresponding to the target location inside the skull cavity with confidence that all the elements were correctly aligned. 2D raster scans in the focal plane (normal to the propagation path, Y) of size 33^2 with a 0.5 mm spacing were then performed at the focal plane, 10 mm deeper into the skull cavity and 10 mm closer to the skull surface.

3.3 Simulation results

3.3.1 Point source simulations

The phase distributions for point source simulations located at each of the six visual targets are shown in Fig. 3.7 with the colour map selected to prevent phase wrapping

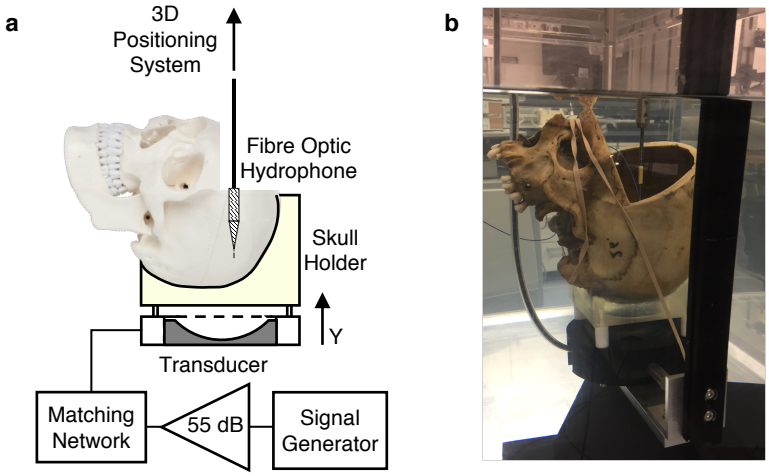


Fig. 3.6: Experimental validation setup, a Schematic of equipment: 3D-printed skull holder clips around skull and fixes it to a specific orientation and depth with respect to the transducer when slid over it. A fibre-optic hydrophone on a 3D-positioning system is then inserted into the skull cavity to record the resultant transcranial acoustic waveforms. **b** Image of experimental setup.

artefacts. Simulations were conducted in native CT space. Regions of coherent phase are evident for all of the peripheral targets (V1 and MT) and appear over an area roughly normally incident to the skull bone overlying the target site. The V1R distribution (Fig. 3.7a) is the most symmetric whereas both the MT phases are slightly skewed towards the front of the skull. In the case of V1L (Fig. 3.7d), whilst there is still a region where the phase changes are smoother, the field is more broken up. This appears to emerge due to the V1 target on the left being closer to the centreline and thus more shielded by the inion, the lump of the bone at the back of the skull (Fig. 3.1). This structure is less uniform than the surrounding skull bone and hence seems to disrupt the more coherent phase pattern observed for V1R.

FFA, located both deeper and lower within the skull results in a highly fragmented phase distribution across the whole spherical surface (Fig. 3.7c, f). As with V1L, the underlying explanation as to why this occurs appears to be the non-uniform shape of the skull between the source and receiver: in this case, the petrous ridge as identified in Fig. 3.1.

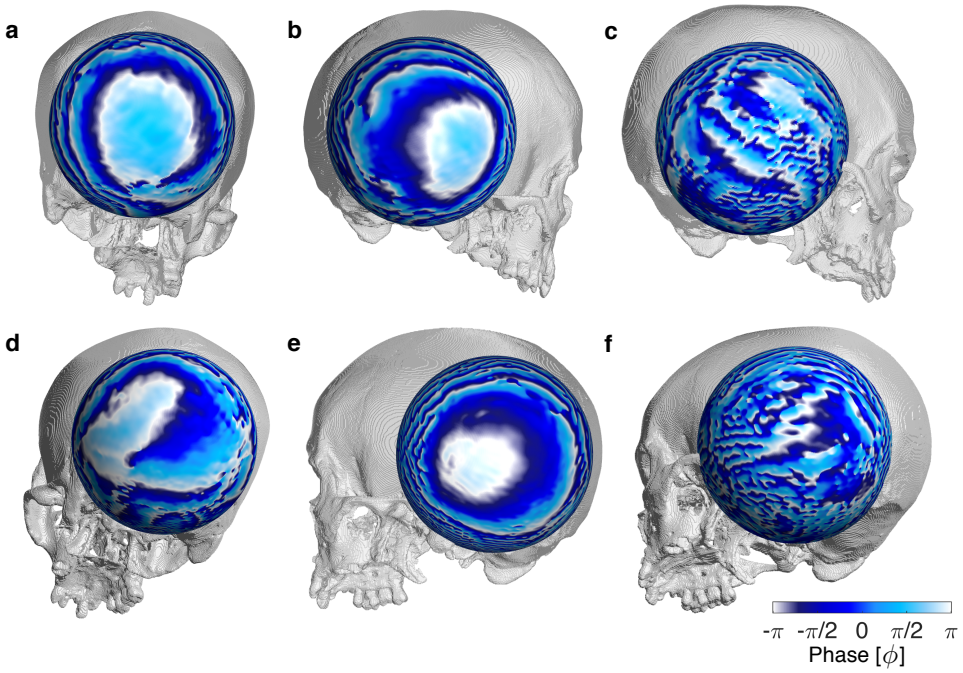


Fig. 3.7: Point source simulation phase distributions. Steady state phase extracted over a sphere whose radius is equal to the focal length of the H-107, focused single-element transducer. **a** V1R, **b** MTR, **c** FFAR, **d** V1L, **e** MTL, **f** FFAL.

3.3.2 Transducer optimisation

The outputs of the point source simulations were fed into the optimisation algorithms given in Eqs. (3.1) – (3.4). The resultant error distributions for the right hemisphere targets are shown in Fig. 3.8 alongside the extracted phase and amplitude data. The highest amplitude regions coincide with the location of more uniform phase areas. The minima of each distribution and hence optimised transducer centre point are

shown in Fig. 3.9 overlaid on to the phase field for each target.

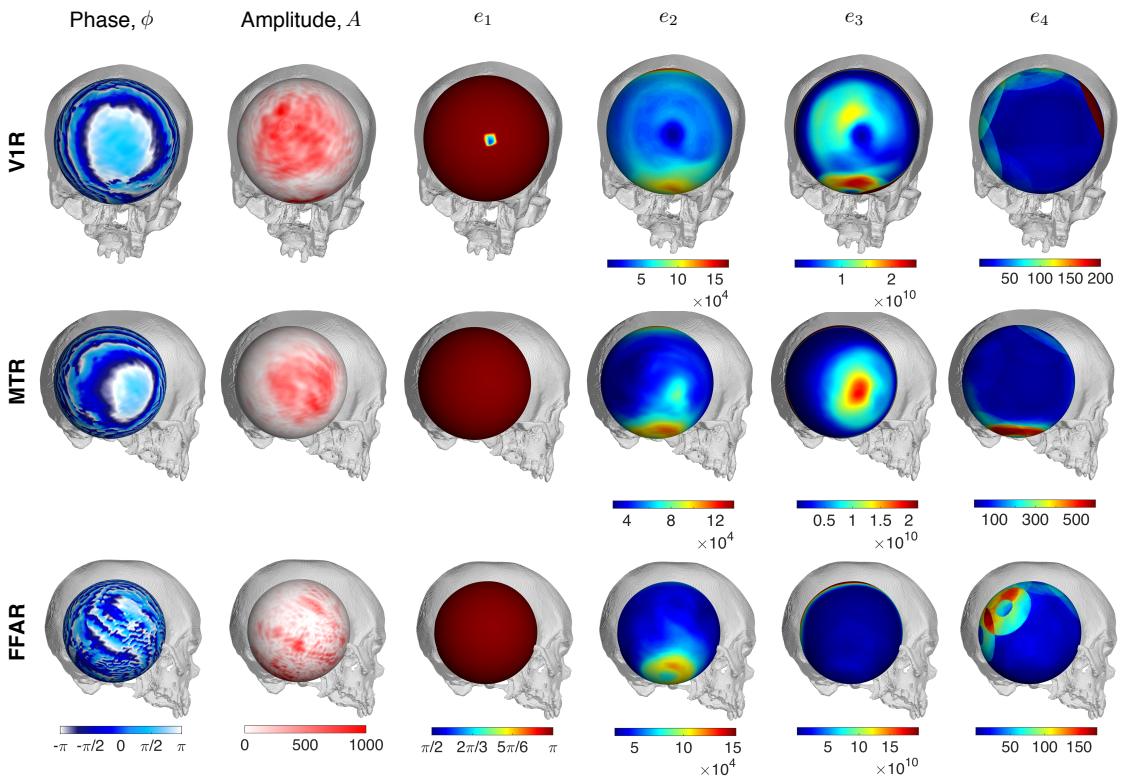


Fig. 3.8: Optimisation algorithm results. Phase (first column), amplitude (second column) and error distributions (columns three to six): maximum phase difference (e_1), least squared phase error (e_2), least squared phase error multiplied by amplitude squared (e_3), and least squared phase error normalised by the amplitude squared (e_4), are shown for the visual targets in the right hemisphere.

Focusing on the fields for e_1, it is clear that only for V1R is there a spherical segment into which the transducer fits where the maximum absolute phase error is less than π, the maximum possible error for a phase distribution bounded between $-\pi$ and π. For the other targets, the maximum phase error is always π, independent of the transducer location as indicated by the red, monochromatic colour distribution in column three. Consequently, the locations selected through this algorithm (Fig. 3.9) for all targets except V1R are merely the result of numerical noise leading to tiny perturbations around π and do not really correspond to anything physical.

For V1R all the metrics produce a similar result except e_3. Even though visual insepection of e_3 (Fig. 3.8) appears to match the centre location, the optimal position

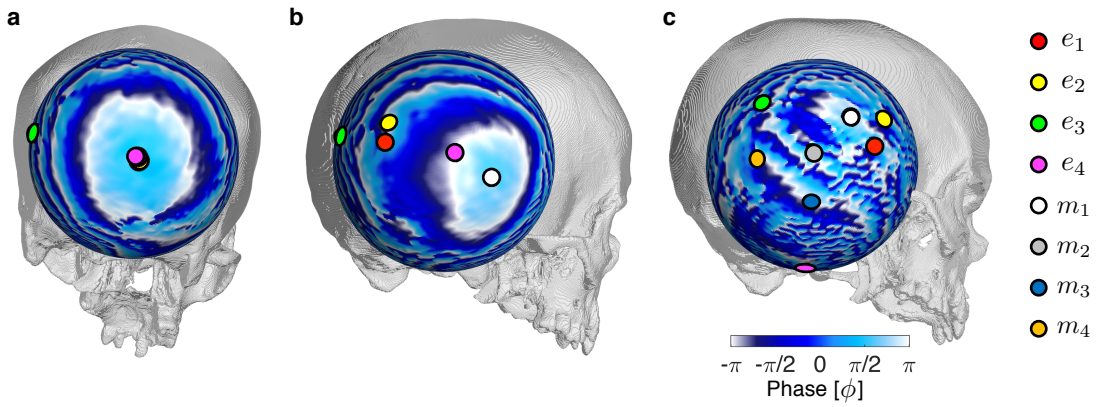


Fig. 3.9: Optimisation algorithm optimal transducer locations. Centre points of single-element transducer overlaid on to phase distributions. **a** V1R. **b** MTR. **c** FFAR.

predicted by e_3 is actually on the left hand side of the sphere as depicted in Fig. 3.9a. The transducer 'imprints' observed around the edges of the e_4 colour maps are the consequence of anomalous, high value points in the amplitude distribution, the division of which leads to the observed distortions wherever an anomalous point lies within T. Nevertheless, despite this, the minima coincides closely with e_1 and e_2.

For MTR, the error distributions do not exhibit a confined, obvious minima as seen for V1R. The optimal locations are thus spread along a horizontal line over the surface with different points for each error function (Fig. 3.9b). Visual inspection of the phase field suggests the best location is in the centre of the uniform phase region; this point was manually selected and denoted m_1 in Fig. 3.9b to compare against the locations determined by optimisation. The asymmetry of the phase distribution appears to preclude selection of this point via the evaluated error functions as oscillations between $-\pi$ and π occur much more rapidly to the right of this region than to the left and as such will incur higher penalties pushing the optimal location to the left.

The optimisation of FFAR produced a diverse range of locations Fig. 3.9c. In a similar fashion to MTR, manual locations were selected although the choice was less obvious in this scenario due to the highly fragmented phase field. Four locations

were chosen spanning different surface areas. m_1 coincides with a small region of more coherent phase towards the top, m_2 roughly central on the surface and m_3 and m_4 lower down.

3.3.3 Forward simulations

To assess the performance of each selected transducer location, forward simulations were performed, that is the transducer was placed at the optimal location and the acoustic field in the skull calculated. For these simulations, the segmented skull map was rotated to align the source with the Y-axis in order to define the ASM back-propagated source plane as outlined in Sec. 2.4.2. It is noted that this will inevitably introduce some staircasing of the skull surface but ensures a repeatable source condition.

Fig. 3.10 displays the forward pressure fields for a selection of optimal transducer placements. The -6 dB pressure contours are shown with the transducer visible through the translucent skull in order to capture any off axis hotspots. Further detail is then given in the 2D plots taken through the transducer axes with the full field shown in grey, and -3, -6 and -12 dB contours overlaid along with the skull outline. The target location is depicted by a cross and maximum pressure site by a circle. Typically, the maximum pressure does not exactly coincide with the 2D slices and so is only shown on the 3D plots.

The full results for each of the considered transducer locations are presented in Table 3.2 with the simulated freefield metrics shown for reference purposes. The locations/rows highlighted in bold correspond to the most effective locations for focusing to each target as shown in Fig. 3.10. The focal error is the Euclidean distance between the maximum internal pressure (o) and target (+) locations with -6 dB volumes calculated with respect to the maximum pressure.

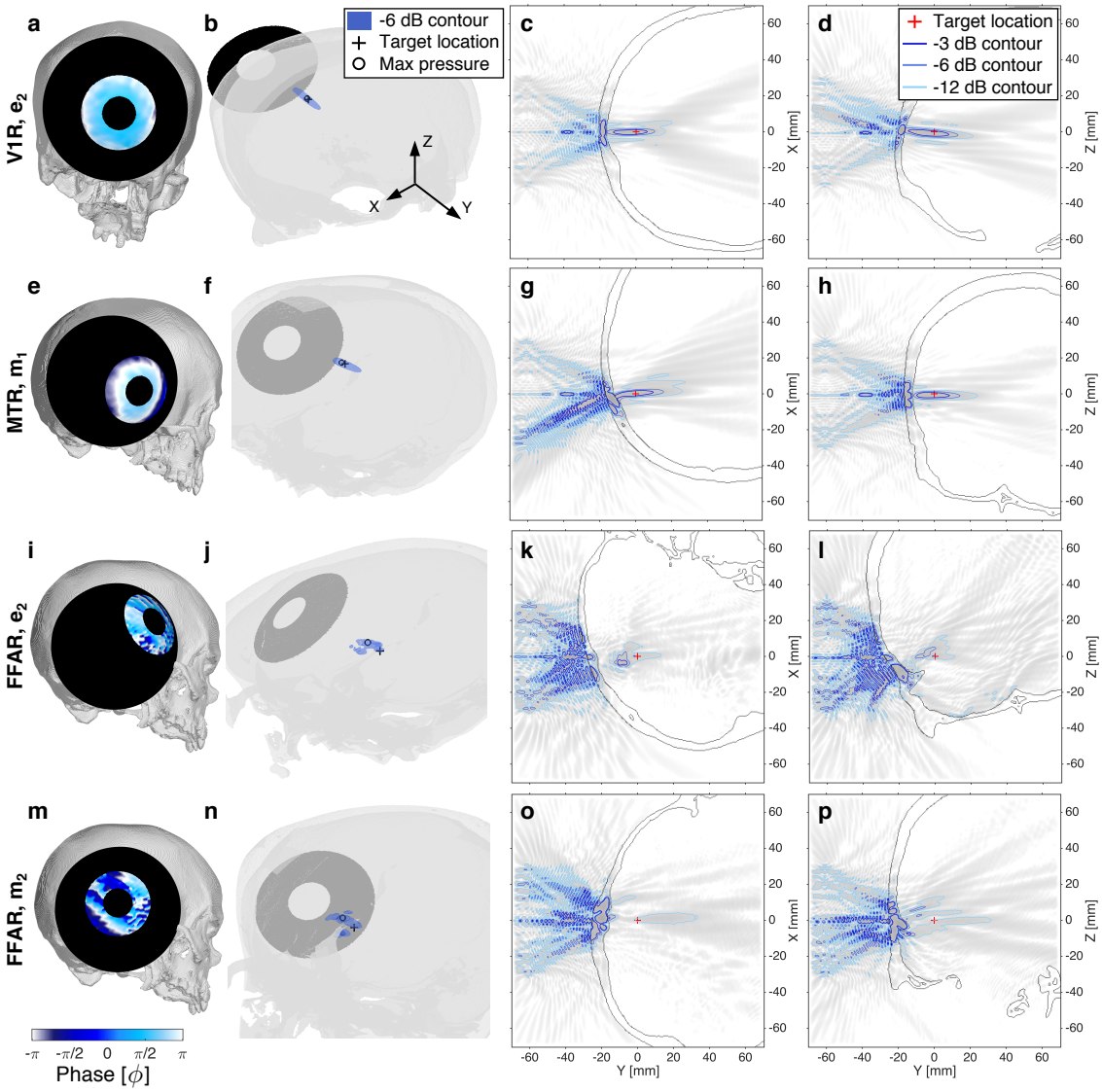


Fig. 3.10: Contour plots and associated phase distributions for the optimal transducer placements for each visual target: V1R e_2 (top row), MTR m_1 (second row), FFAR e_2 (third row) and FFAR m_2 (bottom row). **a, e, i, m** Phase distributions obtained from point source simulations with regions outside the transducer surface at the selected position shaded black. **b, f, j, n** 3D visualisation of -6 dB pressure contours resulting from refocusing at the given transducer location along with maximum and target pressure locations. **c, d, g, h, k, l, o, p** 2D pressure fields in XY and YZ-planes with overlaid -3, -6 and -12 dB contours.

The point source phase distributions prove to be a good predictor of the ability to refocus to the target. The most coherent phase region was observed for V1R and this corresponds to the highest target pressure and lowest focal error. Whereas, the incoherent phase pattern for FFAR is indicative of low pressures delivered to the intended target with maximum pressures over 10 mm away. Analysis of the tabulated data would actually lead to the conclusion that e_4 is the best location to target FFA from with a reduced focal error. However, this orientation transmits US partially through the hole left by the cervical vertebrae in the ex vivo skull and is thus not a feasible solution in practice.

The target pressures reduced from 52 % of the freefield value for V1R, to 42 % at MTR and just 10 % at FFAR. In terms of focal alignment, 94.0 % of the maximum pressure was achieved at the target for V1R and 95.5 % for MTR correlating with focus errors of just 2.43 mm and 3.28 mm respectively. For FFAR, the cigar-shaped focus is broken up with the maximum pressure located 12.42 mm and 11.41 mm away from the target site (e_2 and m_2, respectively).

The −6 dB focal volume trend is less obvious. Where similar focal topologies to the freefield case are observed (V1R: e_1, e_2 and e_3, MTR: m_1), the volumes are consistent with the freefield value albeit slightly reduced. This decrease may be attributed to the skull overlying part of the ellipsoidal −6 dB contours, the voxels of which are not included in the volume estimation. The other transducer placements that were considered for these two targets exhibited increased focal volumes coupled with low target and maximum pressures suggesting much of the energy was reflected due to the higher incident angles of the transducer with respect to the skull.

The shape of the 3D −6 dB contours for FFAR diverge from the ellipsoidal freefield profile with the maximum pressures located closer to the skull. For the m_2 location, the contour splits around the petrous ridge. However, the focal volumes for FFAR are all below 1 cm^3 despite the more distorted pressure fields with the maximum

Target	Transducer placement	Target Pressure [MPa]	Max Pressure [MPa]	Focus error [mm]	−6 dB volume [cm^3]
Freefield	-	0.505	0.507	0.94	0.33
V1R	e_1	0.268	0.284	2.43	0.27
	e_2	**0.264**	**0.281**	**2.43**	**0.28**
	e_3	0.007	0.022	27.08	3.50
	e_4	0.273	0.291	2.39	0.27
MTR	e_1	0.047	0.072	9.95	1.30
	e_2	0.038	0.058	10.97	1.31
	e_3	0.001	0.019	31.94	4.64
	e_4	0.095	0.233	3.31	0.36
	m_1	**0.212**	**0.222**	**3.28**	**0.28**
FFAR	e_1	0.031	0.127	16.55	0.52
	e_2	**0.049**	**0.116**	**12.42**	**0.33**
	e_3	0.006	0.094	19.48	0.01
	e_4	0.111	0.221	4.91	0.54
	m_1	0.020	0.147	12.19	0.32
	m_2	**0.049**	**0.160**	**11.41**	**0.49**
	m_3	0.020	0.126	12.16	0.43
	m_4	0.018	0.091	19.57	0.42

Table 3.2: Simulated focusing efficacy for different visual targets. Results corresponding to the transducer locations depicted in Fig. 3.9 are displayed.

pressure locations situated much closer to the inner skull surface.

The overlying skull structure of the petrous ridge, through which FFA must be accessed for the fixed focal length transducer employed in this study, appears to be the main cause as to why this brain area is so difficult to focus US to. To confirm this, a further simulation was performed whereby the internal skull contour was modified to mimic the external geometry which a fixed thickness of ∼5 mm. Fig. 3.11 compares simulations through the skull with and without the petrous ridge. With the ridge artificially removed, the field no longer fragments and is focused accurately over the intended FFA site. The ellipsoidal focal volume is restored and the field resembles those of the optimised locations for V1R and MTR. Furthermore, a target pressure of 0.225 MPa is consistent with the values for the peripheral targets, 97.3 % of the maximum pressure located just 0.81 mm away.

Whilst forwards results of the left hemisphere targets are not shown, they followed

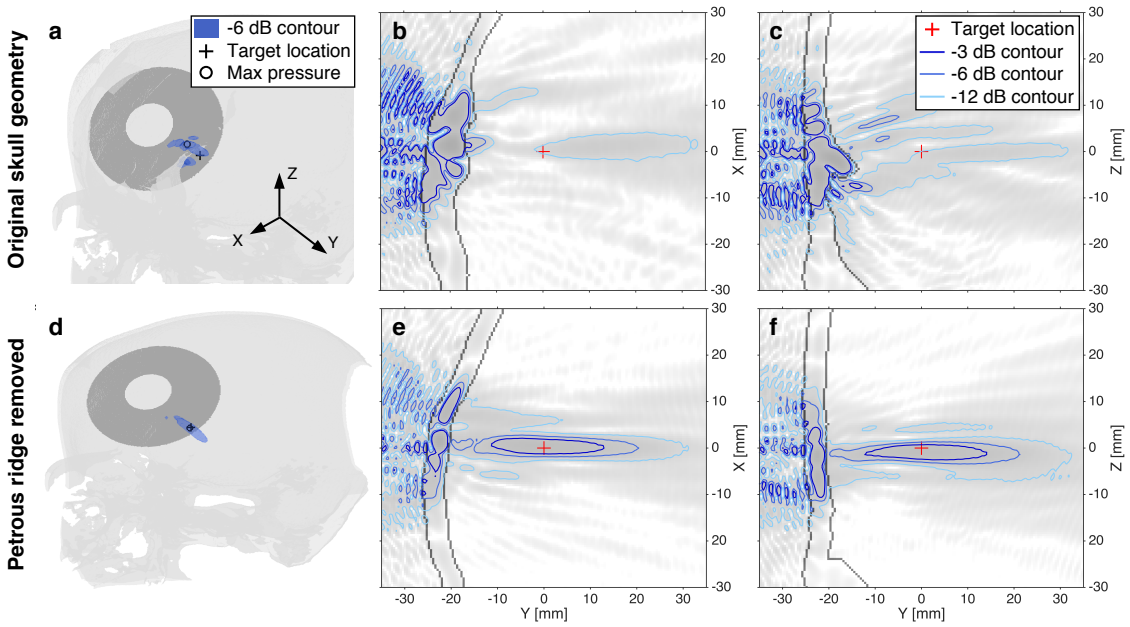


Fig. 3.11: The effect of the petrous ridge on transcranial pressure fields for targeting FFA. Simulations at site m_2 with the original skull topology (top row) and with the petrous ridge artificially removed by matching the inner skull surface to the outer surface with a constant thickness of 4.68 mm. **a, d** 3D −6 dB pressure contours. **b, c, e, f** 2D pressure fields in XY and YZ-planes with overlaid −3, −6 and −12 dB contours.

a very similar qualitative pattern. The slight exception being V1L where the split phase field resulted in the focus remaining ellipsoidal but steered off-target implying that the increased thickness of the inion resulted in an asymmetry of the path lengths within the bone and hence US waves on the side closer to the skull centreline reached the intended focus faster than those from the other side, pushing the observed focus off to the side.

3.3.4 Sensitivity to acoustic properties

Wide variation in the acoustic property values for skull bone have been reported in the literature (Fry and Barger, 1978; Hasgall et al., 2018; Robertson et al., 2017b). A database that collates tissue properties from multiple studies lists speed of sound measurements ranging from approximately 1850–2450 m/s for trabecular bone, 2200–4200 m/s for cortical bone and density differences between 1080–1350 kg/m^3 for cancellous bone and 1800–2100 kg/m^3 for cortical bone (Hasgall et al., 2018). Attenuation values also vary substantially and are strongly frequency dependent (Fry and Barger, 1978; White et al., 2006). Therefore, this section concerns the effect of variation in the assigned acoustic properties of skull bone on the in situ pressure fields.

The effect of variation in the assigned acoustic properties of skull bone are displayed in Fig. 3.12 for the transducer located at V1R e_2 and at FFAR m_2. Each property, sound speed, density or attenuation, was varied independently in increments of 10 % in the range of −50 to 50 %. Typically, increases in any of the acoustic properties result in a decrease in the pressure amplitudes and vice versa, reductions in any of the parameters increase the focal pressures. For attenuation, the result is simply attributed to increased absorption removing more energy from the US wave whereas for density and sound speed, the increased acoustic impedance changes the coupling between the skull and surrounding media – in this case, water. However, the effect of sound speed errors are clearly much more pronounced than for density as well as exhibiting a more oscillatory response as a function of property changes compared to attenuation and density which have a smoother, more monotonic relation. This increased sensitivity to sound speed differences over density is likely due to refraction effects changing the angle by which US waves exit the skull bone and hence modifying the focal interference pattern.

In the FFAR example, the effect of refraction results in dramatically increased target

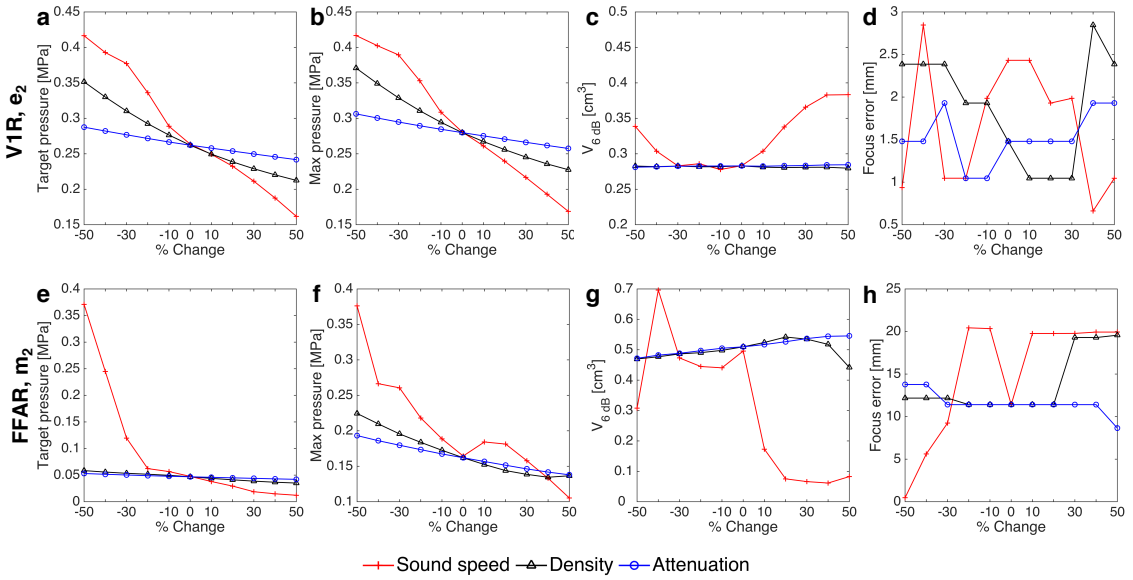


Fig. 3.12: Acoustic property sensitivity. The effect of 10% incremental changes from −50 to 50 % of sound speed (red), density (black) and attenuation (blue) are show for two targets: V1R e_2 (top row) and FFAR m_2 (bottom row). The following metrics for each target are reported: **a, e** target pressure, **b, f** max pressure, **c, g** −6 dB contour volume and **d, h** focus error (the Euclidean distance between the target and maximum pressure coordinates).

pressures once the sound speed was reduced past 20 %. The 3D and 2D on-axis pressure fields are depicted in Fig. 3.13 and show how the focus reforms as the sound speed is dropped to 50 % of the default skull bone value. This equates to a value of 1410 m/s which closely matches that of water (1488 m/s) and hence refraction effects are minimised. As the sound speed is increased, the angle of refraction also increases thus resulting in distortion of the wavefronts. For more uniform skull thicknesses and profiles (for example, V1R and MTR), the refraction effects are more symmetric and so the field is more resilient – some small axial changes in the peak pressure occur but the cigar-shaped focal topology is preserved. However, when more heterogeneous skull structures, such as the petrous ridge, are introduced into the aberrating layer, the refraction effects are more pronounced due to the non-symmetric, non-uniform bone profile and this is magnified at higher sound speeds. Another way of interpreting this is that the sound speed of the medium places a limit on the heterogeneity of the skull bone through which the focus can be maintained.

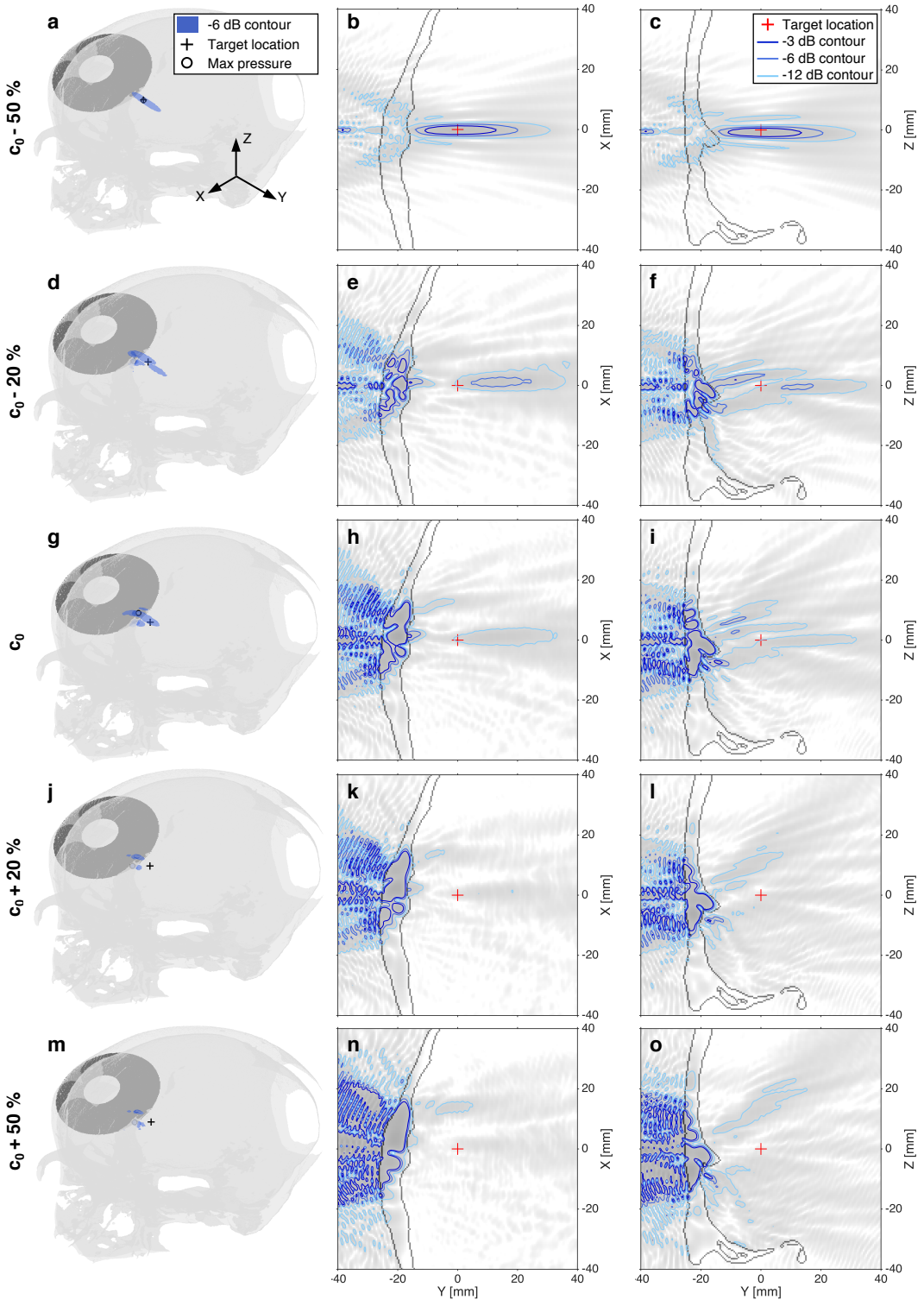


Fig. 3.13: FFAR $\mathbf{m_2}$ sound speed effects. The focal volumes for targeting FFAR are shown for default sound speed properties (middle row) along with ±20 % and ±50 % changes (top and bottom rows). **a, d, g, j, m** 3D −6 dB pressure contour volumes, **b, c, e, f, h, i, k, l, n, o** 2D pressure fields in XY and YZ-planes with overlaid −3, −6 and −12 dB contours.

Taking the lower limit of the reported sound speed values for trabecular bone, the upper limit for cortical bone and comparing these to the values utilised in this study, gives a possible sound speed error of between −34 and 49 %. This translates to an approximate target pressure error of between 43 and −39 % for V1R e_2 and between 151 and −74 % for FFAR m_2 as shown in Figs. 3.12a, e. As the maximum and target pressures are close to coinciding for V1R, similar magnitude errors are observed for the maximum pressure sensitivity (39 to −40 %) but the disparate nature of the target and maximum pressure amplitudes and locations for FFAR serves to reduce the sensitivity of the maximum pressure but still spans a reasonably wide range (58 to −36 %).

Differences in the −6 dB contour volumes (Fig. 3.12c, g) are almost completely insensitive to changes in density and attenuation parameters but do respond to sound speed alterations generally increasing in either direction. For V1R this results in a maximum increase in volume of 36 % at a 50 % higher sound speed with smaller increases at lower sound speeds. For FFAR, the effects are more stochastic with the volume changing up to −85 %.

Finally, focal position errors are captured in Figs. 3.12d, h. For V1R these are capped at 3 mm for all parameter adjustments tested. In the FFAR scenario, positioning errors generally increase with increasing parameter values but tend to zero for decreasing sound speeds down to −50 % where the focus coincides directly with the target location as shown in Fig. 3.13a.

3.3.5 Transducer location sensitivity

In this section, the sensitivity of the simulated fields to small rotational and translational perturbations that might plausibly be introduced when aligning the transducer in practise is considered. Optical tracking neuro-navigation systems such as the Rogue Resolutions BrainSight device are capable of delivering positioning accu-

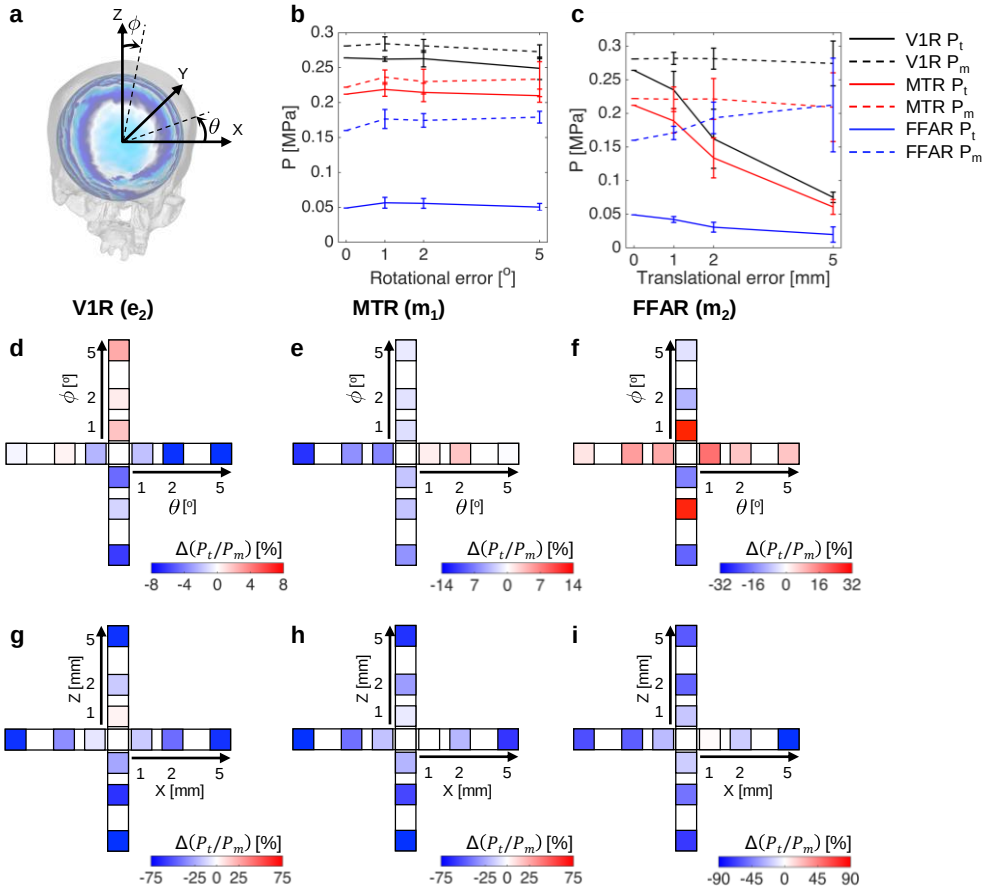


Fig. 3.14: Transducer positioning sensitivity. **a** Coordinate system relative to the transducer surface through which translations and rotations were defined. **b** Averaged target (P_t) and maximum (P_m) pressures for 1, 2 and 5° of rotation in both the positive and negative θ and ϕ directions for each visual target. Bars represent the standard deviation. **d, e, f** Colour maps of errors in P_t/P_m relative to the original transducer location show the spatial sensitivity to each rotation. **c** Averaged P_t and P_m for 1, 2 and 5 mm of translation in both the positive and negative X and Z directions for each visual target. Bars represent the standard deviation. **g, h, i** Colour maps of errors in P_t/P_m relative to the original transducer location show the spatial sensitivity to each translation.

racies of within 3 mm. Therefore, the optimal transducer locations as described in Sec. 3.3.3 were rotated about the target location by up to 5° and also offset in both the X and Z directions by up to 5 mm, which represents the worst case scenario.

The coordinate system to which the rotations and translations are relative to is shown in Fig. 3.14a: θ is in the XY-plane and ϕ is in the YZ-plane. The origin is located at the target site and the skull is rotated with respect to the transducer to keep the source plane coplanar with the simulation grid. The averaged target and maximum pressures as a function of rotational or translational error over all

directions are presented in Figs. 3.14b, c. The error bars represent the standard deviation and the corresponding spatial maps in terms of percent changes of target (P_t) to maximum (P_m) pressure ratio relative to the optimal centre location are shown in Figs. 3.14d–i. This parameter is important practically as the objective is to maximise the pressure delivered to the target subject to a maximum pressure safety threshold constraint that applies anywhere in the brain. A ratio of 1 indicates the maximum pressure is at the target which would be the optimum.

The optimised locations for V1R and MTR are both robust to rotational errors with maximum changes in P_t/P_m of $-8\,\%$ and $-14\,\%$ respectively. The spatial maps indicate that the ratio tends to decrease away from the centre point except in one direction ($+\phi$ for V1R and $+\theta$ for MTR) where some marginal increases can be seen – 2.6 % and 3.5 %, respectively. The map for FFAR does not follow any particular trend and is much more sensitive to small rotational perturbations resulting in errors of between -20 and 32 %. In terms of an overall upper bound increase in maximum pressures for all rotations considered, V1R is the most unaffected increasing by only up to 4.6 % whereas MTR and FFAR display larger differences of up to 21.6 % and 22.7 %, respectively.

The susceptibility to translational errors is more severe but also makes intuitive sense with the focal spot shifted laterally away from the intended target. In all cases, the target pressure is therefore the dominant term substantially reducing as the transducer is translated laterally resulting in drops in the P_t to P_m ratio of up 75 % for V1R and MTR and up to 90 % for FFAR at 5 mm offsets. The exception to this is the maximum pressure for FFAR which increases by up to 73 % at a 5 mm translation in the negative Z direction. It should be noted that in reality, the target brain regions are on the order of 1 cm^3 and so small translations may not be a problem; in this study the effects are highlighted as the target is defined by a single voxel.

3.3.6 Effect of transducer angle

Another factor that will alter the transcranial pressure fields is the incident angle between the source and skull surface. Here, larger variations in source angle are considered rather than small perturbations as in the previous section. To decouple angle effects from those associated with transmitting through different skull topologies as would inevitably occur rotating the skull with respect to the transducer, a simplified spherical shell skull model was created with an average radius of 8 cm and a constant thickness of 5.6 mm. A target location 15 mm inside the skull was defined and the spherical shell rotated about this point in the XY-plane only, in steps of 5° from 0–45°. The same simulation set was performed with the elastic solver, and with the sound speed reduced by 30 % corresponding to the minimum expected skull value (see Sec. 3.3.4). The XY-planes for angles of 0, 30 and 45° are displayed in Fig. 3.15.

At normal incidence, the transcranial US fields for the three different cases (fluid solver, elastic solver and fluid solver at c_0 −30 %) are very similar in profile, the only difference a small split in the −3 dB contour close to the skull in Fig. 3.15a. Conversely, at 30° the fields start to diverge. Whilst ellipsoidal focal regions are preserved for the lower sound speed even up to an angle of 45°, at the nominal sound speed, for both fluid and elastic simulations, the fields begin to show asymmetries at 30° and have spread out substantially at 45° incidence. The inclusion of shear wave modelling does lead to small changes in the pressure distribution with offsets in the target pressure shifting the contours. At 45° this manifests in the −3 and −6 dB contours extending further into the skull, although the larger −12 dB is largely unaffected.

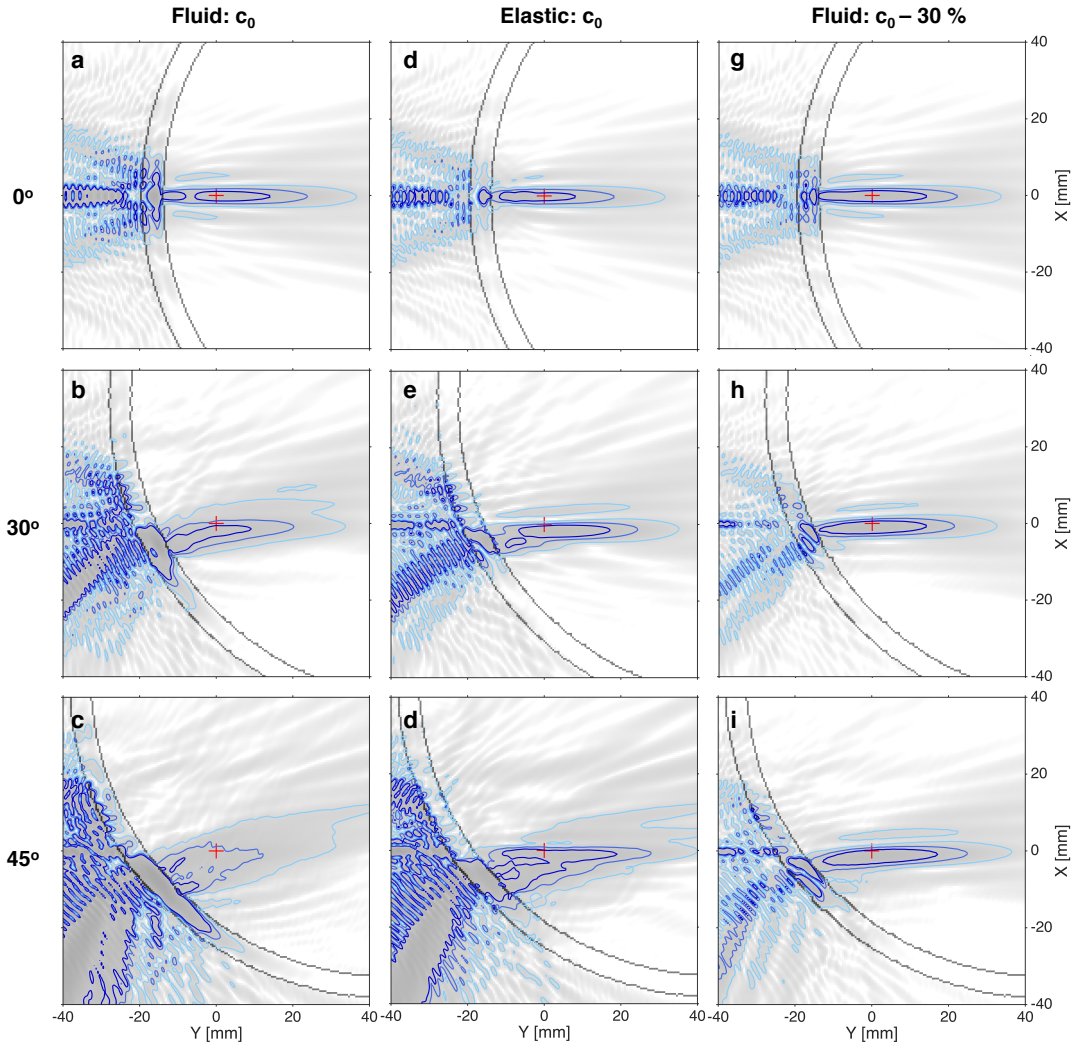


Fig. 3.15: Sensitivity of pressure distributions to incident angle at different sound speeds in a simplified spherical skull topology. Target location (red cross) located 15 mm from spherical skull geometry. Spherical layer rotated in the XY-plane relative to the transducer. 2D pressure fields in the XY-plane with overlaid −3, −6 and −12 dB contours at 0, 30 and 45° incident angles at **a, b, c** fluid-based solver at the nominal sound speed, c_0, **d, e, f** elastic solver at c_0, and **g, h, i** fluid-based solver at a 30 % reduced sound speed.

A more quantitative analysis of the angle effects through the target and maximum pressures as well as the −12 dB contours is depicted in Fig. 3.16. All simulation sets follow a similar pressure trend: the normal incidence values are conserved until about 15° after which a steady decline occurs. The −12 dB plot, however, shows a marked difference originating at angles greater than 25° with the volume increasing over 4-fold up to 45° as the field spreads considerably for both the fluid-based and elastic simulations at the nominal sound speed value. Simulations at the lower sound

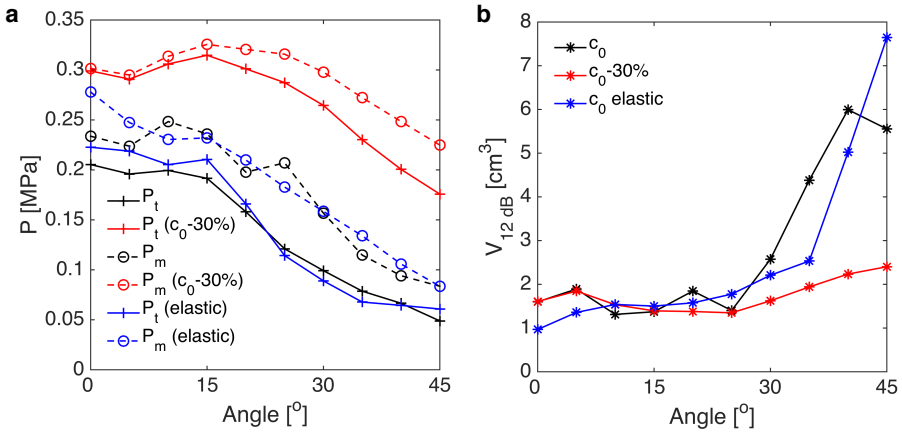


Fig. 3.16: Quantitative pressure distribution results for varying source incident angles. Simulations for the fluid and elastic solvers at the nominal sound speed (c_0), and the fluid solver at c_0 −30 % were analysed. **a** Changes in target (P_t) and maximum (P_m) pressures as a function of incident angle. **b** Changes in −12 dB contour volume as a function of incident angle.

speed also show a rise in volume but its gradient is more gradual increasing only by ∼75 % from 25 to 45°, confirming the increased robustness to higher incident angles for aberrating layers at lower sound speeds. In essence, this can again be interpreted that speed of sound in the skull places a constraint on the maximum incident angle at which the brain can be targeted through the skull before the ellipsoidal focal specificity is lost. Comparing the elastic and fluid simulations at the same sound speed, only small differences can be observed.

Although the focused source has an inherent angle distribution of -30 to 30°, the results presented in this section agree well with a simple critical angle prediction based on Snell's law. For the nominal sound speed, a value of 31.8° is calculated which matches closely to the angle at which the −12 dB contours diverge. For the reduced sound speed, this increases to 48.9° which may explain why the fields are more resistant. Conversely, the shear wave speed (1500 m/s) has the highest critical angle of 82.7° and so elastic waves should be the most robust. As the pressures only marginally differ between the elastic and fluid case, this suggests that little of the incident beam is being converted into a shear wave.

3.3.7 Elastic simulations

The previous section considered shear wave modelling for a simplified spherical shell skull model. Here, the influence of shear waves on the pressure distributions for the following real skull geometries is presented: V1R e_2, FFAR m_2 and FFAR e_2, as depicted in Fig. 3.17. For the shallower V1R target where the focus is preserved, the biggest difference between the elastic and fluid simulations lies within the skull where the hotspot is substantially reduced by 0.26 MPa for the elastic case. Although the field morphology is consistent, an amplitude drop of 0.07 MPa (27.5 %) is noted at the focus with a similar magnitude reduction in the maximum pressure (28.9 %) which is also shifted by 2.39 mm. Similarly, for FFAR m_2 which is close to normally incident with respect to the skull surface, the inclusion of shear wave modelling serves to reduce the intracranial pressures: a small loss in maximum pressure (6.9 %) with a shift in location by 2.73 mm. The target amplitude variation is more significant at −56 % although due to the focal fragmentation the values are much lower; in absolute terms, a difference of −0.027 MPa.

FFAR e_2 is at a higher incident angle relative to the skull and so greater elastic effects might be anticipated. Again, the largest offset is at the outer skull surface, a difference of 0.22 MPa. However, focally, the elastic simulation results in an increased pressure estimation of 67 % although the maximum pressure increase is less pronounced at 9.5 %. Whilst similar features can be noted between the two simulations, the elastic field shape is slightly more spread than the fluid-based distribution.

To conclude, whilst the impact of shear wave modelling does lead to some modification of the local pressure fields and amplitudes, particularly at higher incident angles, the predictions are not substantially different. Therefore, this supports the use of the fluid-based solver which can be computed in under a hundredth of the time required to run the elastic code.

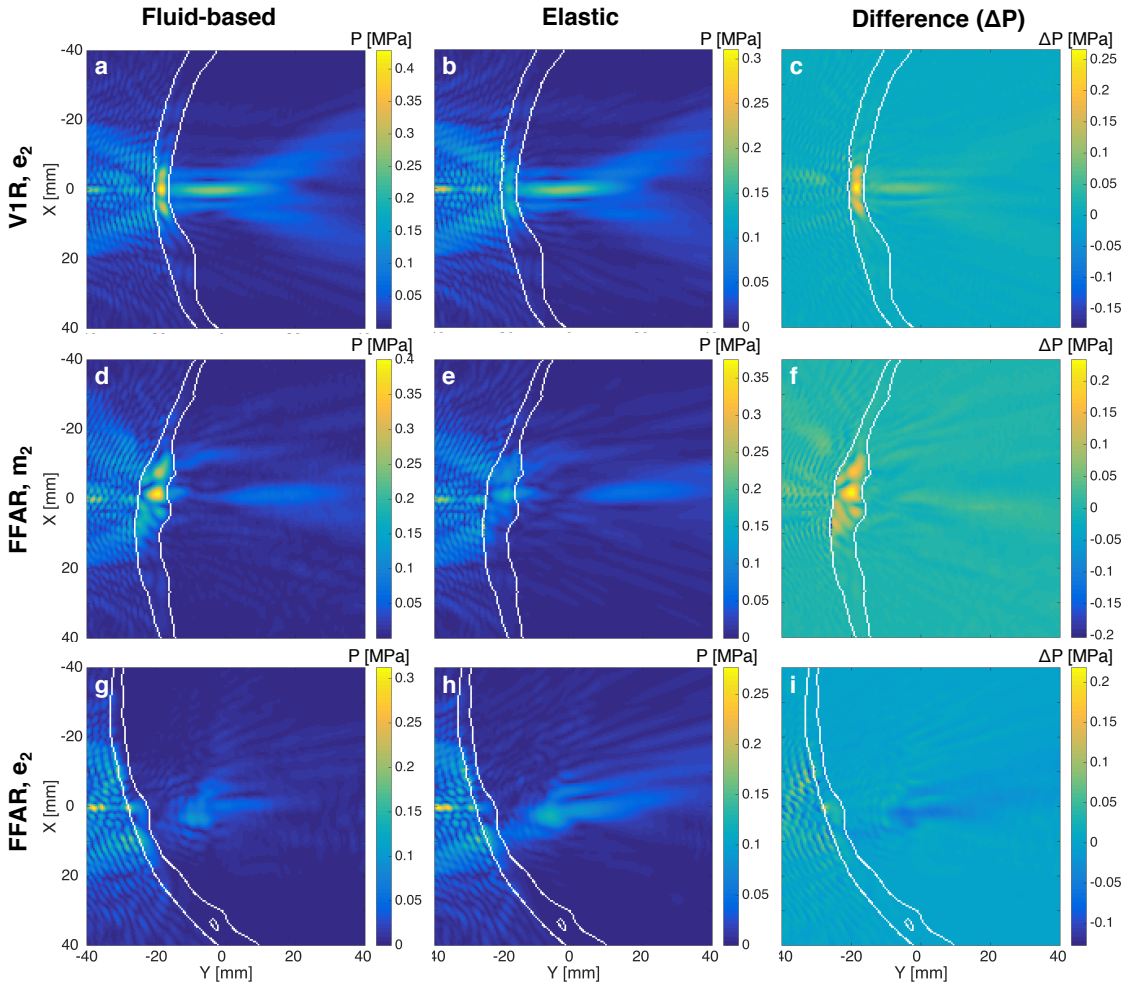


Fig. 3.17: Comparison of elastic and fluid-based simulations. All axial XY-planes through transducer centre for targeting V1R e_2 (top row), FFAR m_2 (middle row) and FFAR e_2 (bottom row). **a, d, g** Fluid-based simulations. **b, e, h** Elastic simulations. **c, f, i** Difference between simulations (elastic subtracted from fluid).

3.4 Experimental validation

Experimental comparisons with fluid-based simulations based on threshold-segmented CT scans are presented in this section for four optimised transducer locations: V1R e_2, MTR m_1, FFAR m_2 and FFAR e_2. Fig. 3.18 shows the simulated fields (top row) and experimental hydrophone measurements (bottom row) for three lateral planes: at the focus and both 10 mm shallower and deeper into the skull for V1R e_2. The upper limit of the colour map is defined independently for the simulation and experimental data and is set as the maximum pressure observed in any of the

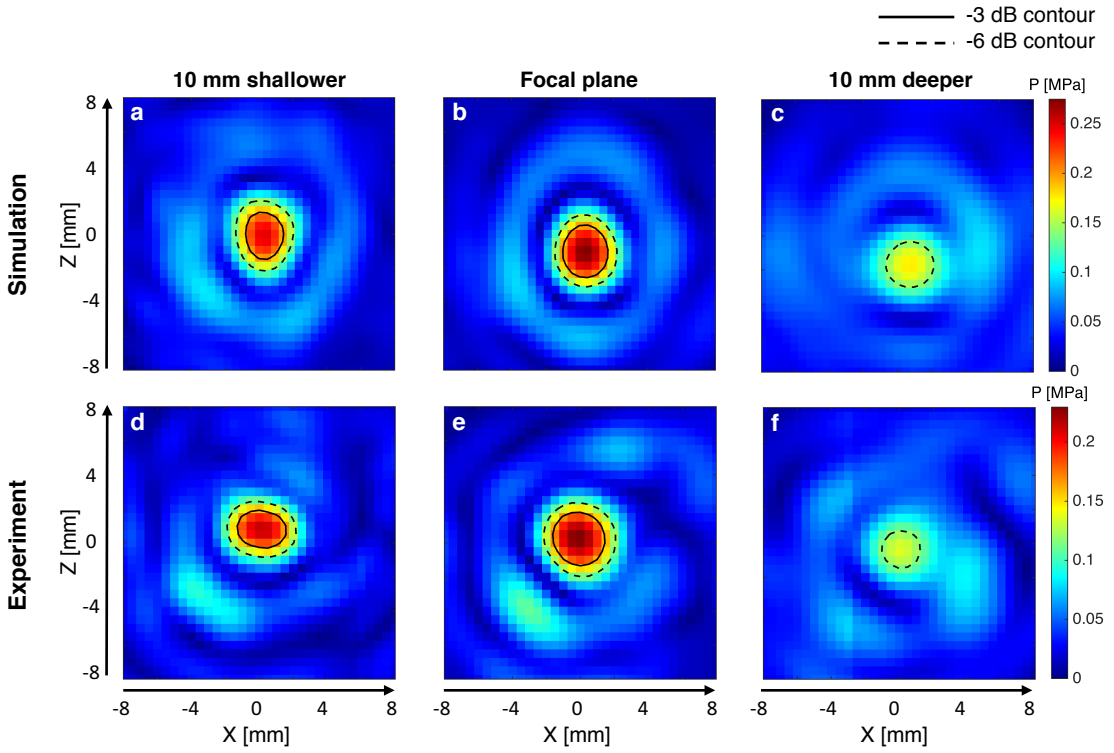


Fig. 3.18: V1R e_2 experimental comparison. Simulated pressures (top row) and experimental hydrophone measurements (bottom row) for three transverse planes: **a, d** 10 mm closer to the skull, **b, e** at the focal length/target location and **c, f** 10 mm deeper into the skull. −3 dB (solid line) and −6 dB (dashed line) contours are overlaid. Colour maps and contours are relative to the maximum pressure at any location in any of the three planes for both the simulated and experimentally-obtained values. Target location at (0, 0).

three planes. The −3 and −6 dB contours are also relative to this value.

Very close agreement between the hydrophone measurements and simulated pressures is achieved for targeting of V1R as shown in Fig. 3.18. The target location is taken to be the pressure value of the voxel at (0,0): experimentally measured as 0.228 MPa versus the simulated value of 0.264 MPa, a 15.8 % overestimate. If the maximum pressure anywhere in the focal plane is instead taken, the difference increases a little to 19.6 %: 0.230 MPa (measured) versus 0.275 MPa (simulated). The location of this maximum pressure and hence centre of the contours is one grid point down from the target for the simulated field and one grid point up for the experimentally-obtained measurements giving an error of approximately 1 mm. The size of the −3 dB contours at this plane is consistent (∼3 mm circles) although small

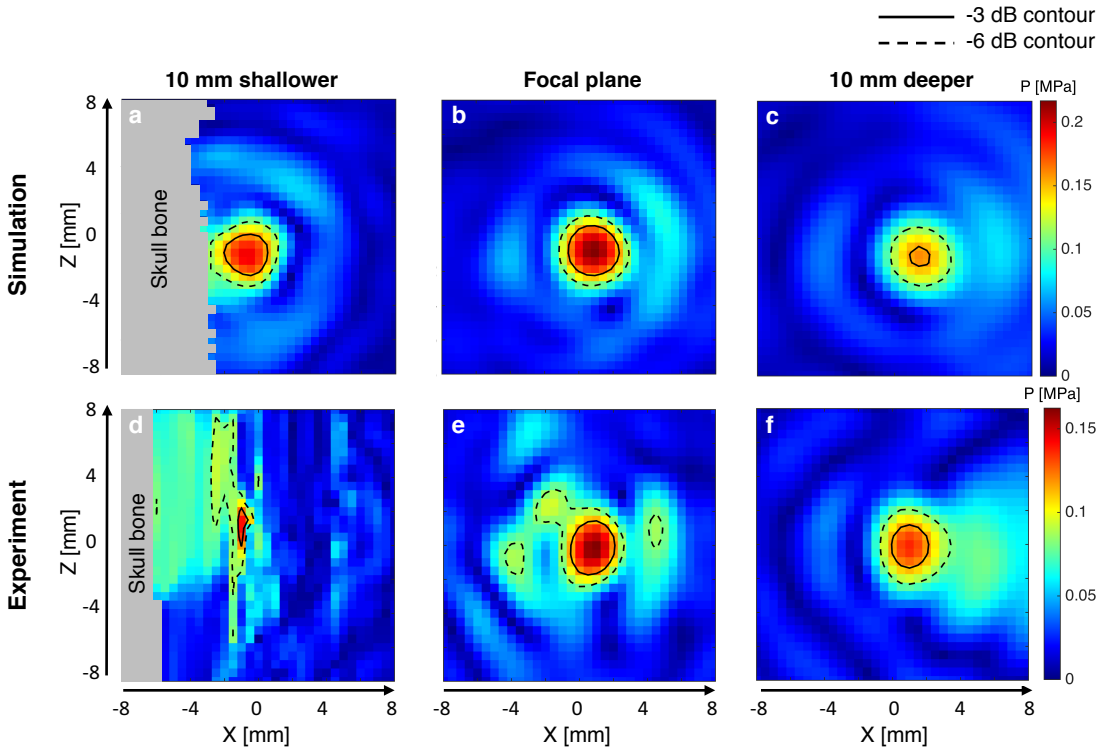


Fig. 3.19: MTR $\mathbf{m_1}$ experimental comparison. Simulated pressures (top row) and experimental hydrophone measurements (bottom row) for three transverse planes: **a, d** 10 mm closer to the skull, **b, e** at the focal length/target location and **c, f** 10 mm deeper into the skull. −3 dB (solid line) and −6 dB (dashed line) contours are overlaid. Colour maps and contours are relative to the maximum pressure at any location in any of the three planes for both the simulated and experimentally-obtained values. Target location at (0, 0). Skull bone locations are shaded in grey corresponding to the material map in simulation space (**a**) or where the hydrophone broke due to the collision with the skull (**d**).

deviations in the contour shapes are observed in the planes either side of the focus.

Whilst for MTR it is apparent that local differences are more evident than for V1R as depicted in Fig. 3.19, a coherent focal spot, as simulated, is again confirmed. The amplitude of the experimentally-measured side lobes is raised relative to the simulated case and this is emphasised by small regions of the side lobes included in the −6 dB contour. In both cases the max pressure location is shifted to the right and the locations lie within 1 grid point of each other, the simulated value of 0.217 MPa overpredicting the experimental figure of 0.162 MPa, a 34 % overestimate. The asymmetry of the field with higher side lobe amplitudes in the positive x-direction is also conserved although in the post focal plane, the size of this region

as observed experimentally was larger than that predicted by simulations.

Pre-focally, a mistake was made in conducting the fibre-optic hydrophone measurements in that the plane 10 mm closer to the skull resulted in a collision of the hydrophone with the skull. Although the pressure readings are not useful here, it does serve as a useful comparison of the alignment of the setup. The simulated voxels assigned skull bone properties and those estimated to be skull in the experiment, taken to be any points after which the hydrophone broke (scanning in columns from right to left), are shaded in grey – Fig. 3.19a & d. Comparing the two would suggest that the experimental plane is possibly a little deeper into the skull than the simulated plane (as the skull bone curves and so a greater proportion of the plane is comprised of skull as you move towards the transducer) but at most it is a 2 mm offset. The true experimental skull contour may also be underpredicted here as it is possible the hydrophone came into contact with the skull before breaking. There is also evidence of standing wave effects between the hydrophone and the skull before the fibre broke (Fig. 3.19d). Either way, the accidental finding proves the 3D-printed skull holder alignment is within a few mm.

Targeting FFA directly through the petrous ridge from location m_2 results in a shift of the focal spot away from the target location. It is evident that the simulations and hydrophone measurements do not match as closely here with much greater fragmentation observed experimentally as shown in Fig. 3.20. That said, the locations of the main hot spots are reasonably well conserved in the focal plane (1.4 mm error) and deeper into the skull cavity (1.1 mm error). The biggest discrepancy in amplitudes is also observed in this plane, 10 mm closer to the skull: the simulated field features a main higher intensity spot surrounding by two other elevated pressure regions whereas the hydrophone measurements reveal significantly more fractured profile. The maximum pressure in these planes is predicted to be 0.159 MPa located at (2.8, 3.3) but measured as 0.085 MPa located at (1, 0), an offset of 3.8 mm and

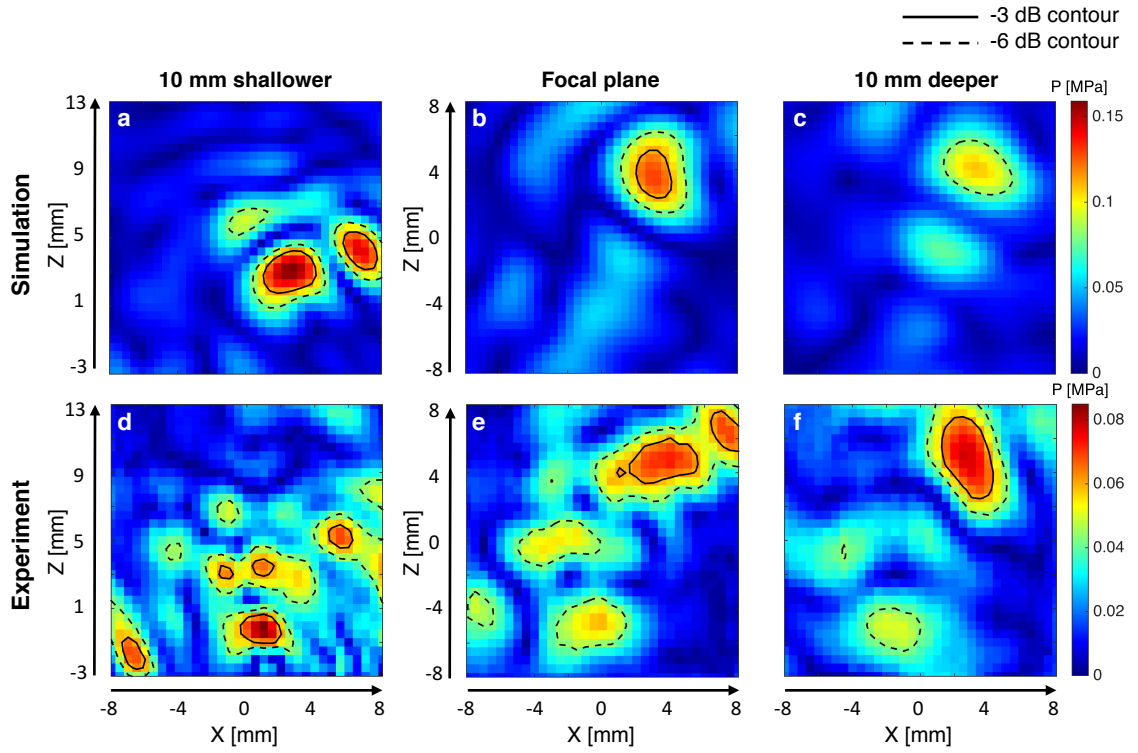


Fig. 3.20: FFAR $\mathbf{m_2}$ lower transducer location experimental comparison. Simulated pressures (top row) and experimental hydrophone measurements (bottom row) for three transverse planes: **a, d** 10 mm closer to the skull (N.B. planes shifted 5 mm vertically in Z to avoid collision with the skull), **b, e** at the focal length/target location and **c, f** 10 mm deeper into the skull. −3 dB (solid line) and −6 dB (dashed line) contours are overlaid. Colour maps and contours are relative to the maximum pressure at any location in any of the three planes for both the simulated and experimentally-obtained values. Target location at (0, 0).

overprediction by 87 %.

A similar trend is apparent in the other planes: the energy is concentrated in one spot in the simulations but is more spread for the experimental measurements. The predicted and observed maximum pressure locations are closer together (1.9 mm) in the focal plane and 1.1 mm post focally. The amplitudes are again higher for the simulations but the error reduces with depth: 79 and 38 %, respectively, for the two planes. The target pressure shows closer agreement: predicted as 0.049 MPa and observed to be 0.042 MPa or a 17 % difference.

The largest disparity between the simulated and measured fields is for FFAR e_2, at an increased incident angle. It is evident that whilst the simulations predict a

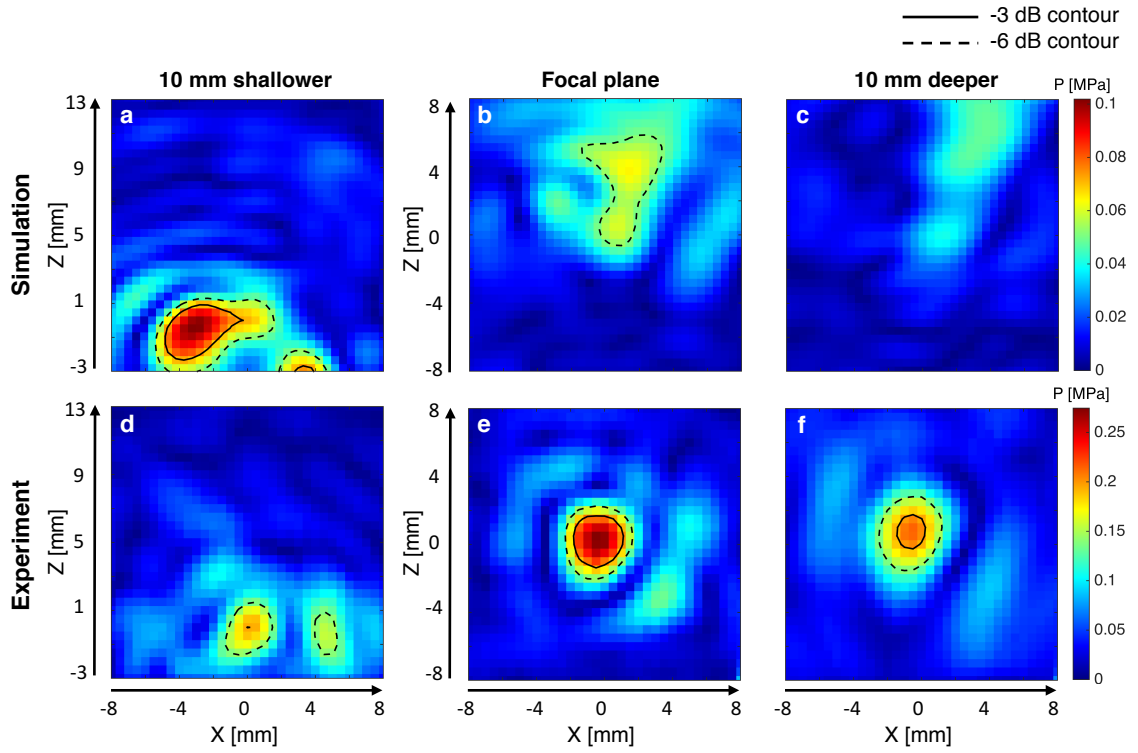


Fig. 3.21: FFAR e_2 upper transducer location experimental comparison. Simulated pressures (top row) and experimental hydrophone measurements (bottom row) for three transverse planes: **a, d** 10 mm closer to the skull (N.B. planes shifted 5 mm vertically in Z to avoid collision with the skull), **b, e** at the focal length/target location and **c, f** 10 mm deeper into the skull. −3 dB (solid line) and −6 dB (dashed line) contours are overlaid. Colour maps and contours are relative to the maximum pressure at any location in any of the three planes for both the simulated and experimentally-obtained values. Target location at (0, 0).

field that is shifted and distorted, experimentally, an almost perfect focus is formed over the target. Consequently, the experimental target pressure is over 5-fold higher with the value of 0.275 MPa consistent with the magnitudes for targeting V1R and MTR. The maximum simulated pressure in the focal plane is also shifted by 4.0 mm in the positive Z direction; in magnitude it is just higher than the target amplitude and less than the pre-focal high intensity region at 0.102 MPa. This value is closer to matching the experimental value of 0.195 MPa but still 48 % lower. This suggests that employing higher incident angles increases the risk of overexposing tissue, that is, the actual pressures are greater than those simulated.

An explanation for this disagreement lies with the assigned sound speed values for

the skull. Whilst for targeting from location m_2, a 50 % reduction in sound speed was required to reform the focus as shown in Fig. 3.12e – such a value is very similar to that of water and therefore unphysical, thus all but eliminating refraction effects. However, targeting from e_2 positions the transducer higher resulting in an increased angle of incidence relative to the skull but prevents having to deliver US through the petrous ridge. This scenario is analogous to that considered in Sec. 3.3.6 with a more uniform overlying skull bone where it was shown that the sound speed imposes a limit of the maximum angle through which the focus can be maintained. Consequently, a smaller sound reduction at e_2 is enough to reform the focus at the target site and produce close agreement with the experimental results.

This is illustrated in Fig. 3.22 with the target and maximum pressures for FFAR e_2 and m_2 plotted as a function of sound speed. The blue bar indicates an estimated sound speed error in the range 25–35 % that is consistent with the experimentally-measured pressures for both FFAR transducer locations. At a sound speed of 1974 m/s, 30 % of the nominal value, the simulated target pressure matches very closely with the experimental measurement: 0.254 MPa, an underestimate by just 7.6 %. This sound speed does fit within the range of measured skull bone properties albeit at the lower end for trabecular bone (Hasgall et al., 2018).

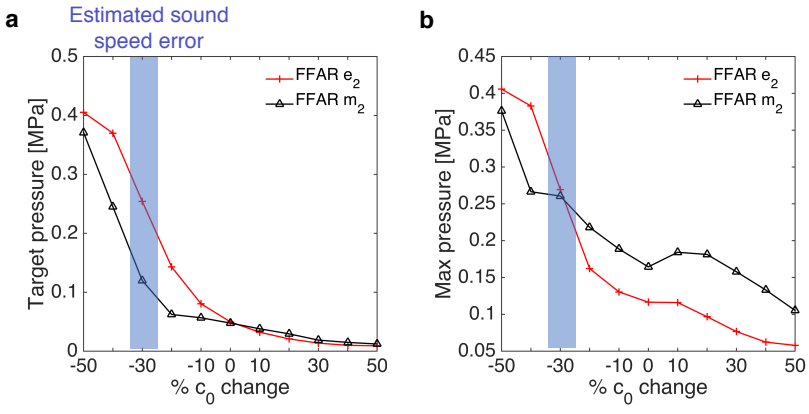


Fig. 3.22: FFAR sound speed effects. Comparison of **a** target and **b** maximum pressures as a function of sound speed, c_0, for transducer locations e_2 and m_2 focused to FFA. The blue bar indicates a sound speed error of approximately 30 % that matches experimentally-obtained pressure measurements.

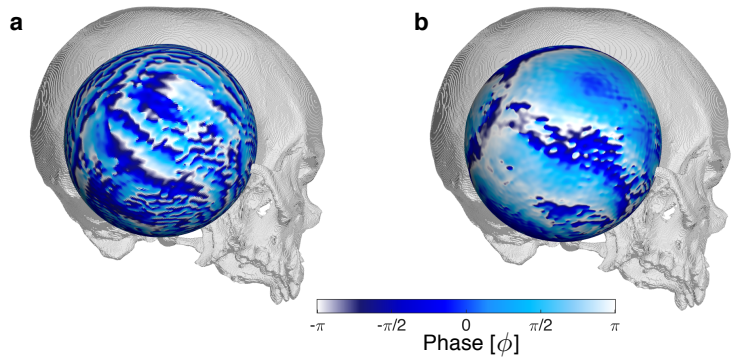


Fig. 3.23: FFAR point source simulations phase distributions for varying sound speeds. **a** Phase profile for nominal sound speed. **b** Phase field for 30 % reduced sound speed.

Further to this, reducing the sound speed by the same amount for the point source simulation at FFA and again extracting the phase over a spherical surface, reveals regions of coherent phase lying either side of a more fragmented stripe which follows the topology of the petrous ridge (Fig. 3.23). FFAR e_2 lies in the centre of the top region of reduced rate of change of phase. This therefore demonstrates that US can be focused to FFA by targeting from above the petrous ridge in spite of the increasing angle of incidence but, at higher sound speeds, this path is not viable due to the increased refraction as a consequence of targeting the curved surface at an angle. This finding highlights the sensitivity of the simulations to errors in sound speed assignment within the skull bone therefore motivating the need for more accurate sound speed property characterisation, potentially in a subject-specific manner. For scenarios where heterogeneous skull structures exist or strong refraction occurs due to an angled transducer trajectory coupled with high sound speeds in the skull, an array-based design might be able to correct for the induced aberrations. This will be investigated in Sec. 3.7.

3.5 Depth study

The same modelling pipeline as given in Fig. 3.4 combined with least squares phase error optimisation (Eq. (3.2)) was used for determining the transducer locations for

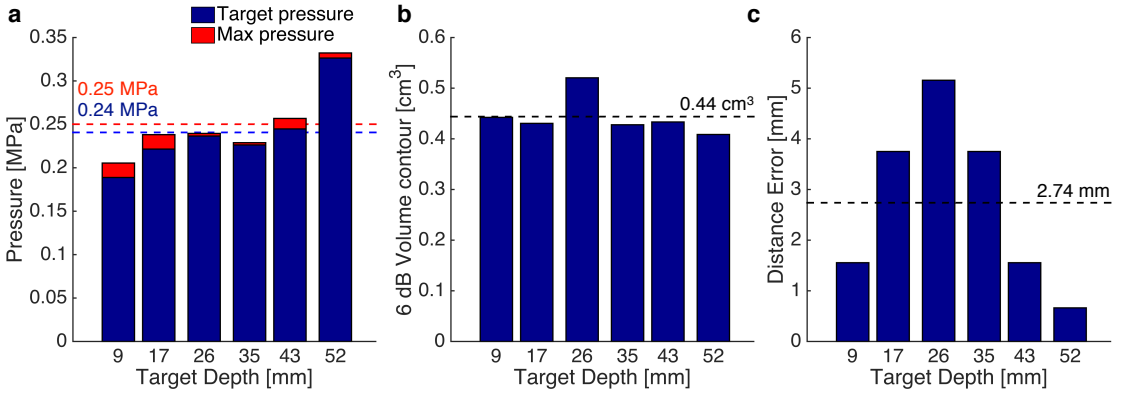


Fig. 3.24: Target depth study: focusing efficacy results. **a** Target and maximum pressures, **b** −6 dB contour volumes and **c** Focus error (Euclidean distance between target and max pressure locations). Mean values over the whole depth range are indicated on dashed lines.

focusing along the line segment to targets of increasing depth. It should be noted that the overlying skull structure for this region is very uniform and does not exhibit any skull features (for example, the inion or petrous ridge) that disrupt the smooth surfaces. The quantitative results for the six targets up to a maximum of 52 mm, corresponding to the the maximum depth that could be achieved without collision of the transducer with the skull, are presented in Fig. 3.24. The target and maximum pressures are shown to be very consistent over middle depth targets (17–43 mm) with only up to a 6.6 % change relative to the mean for these four targets. Close to the skull, the target pressure amplitude is 21.6 % lower than the mean value over the entire range whereas as the greatest depth, the target pressure is boosted by 36.6 %. In terms of focal volumes, the values are very consistent over the full range averaging 0.44 cm^3. The distance error between target and maximum shows more deviation as a function of depth increasing from 1.6 mm close to the skull to a maximum of 5.2 mm at a depth of 26 mm before reducing down to 0.6 mm for the deepest target.

The pressure distributions for three of the targets – shallow (9 mm), intermediate (26 mm) and deep (52 mm) – for the 2D on-axis XY and YZ planes are displayed in Fig. 3.25 alongside the phase fields for the point source simulations. Areas of coherent phase are observed in each case and again correspond with the ability

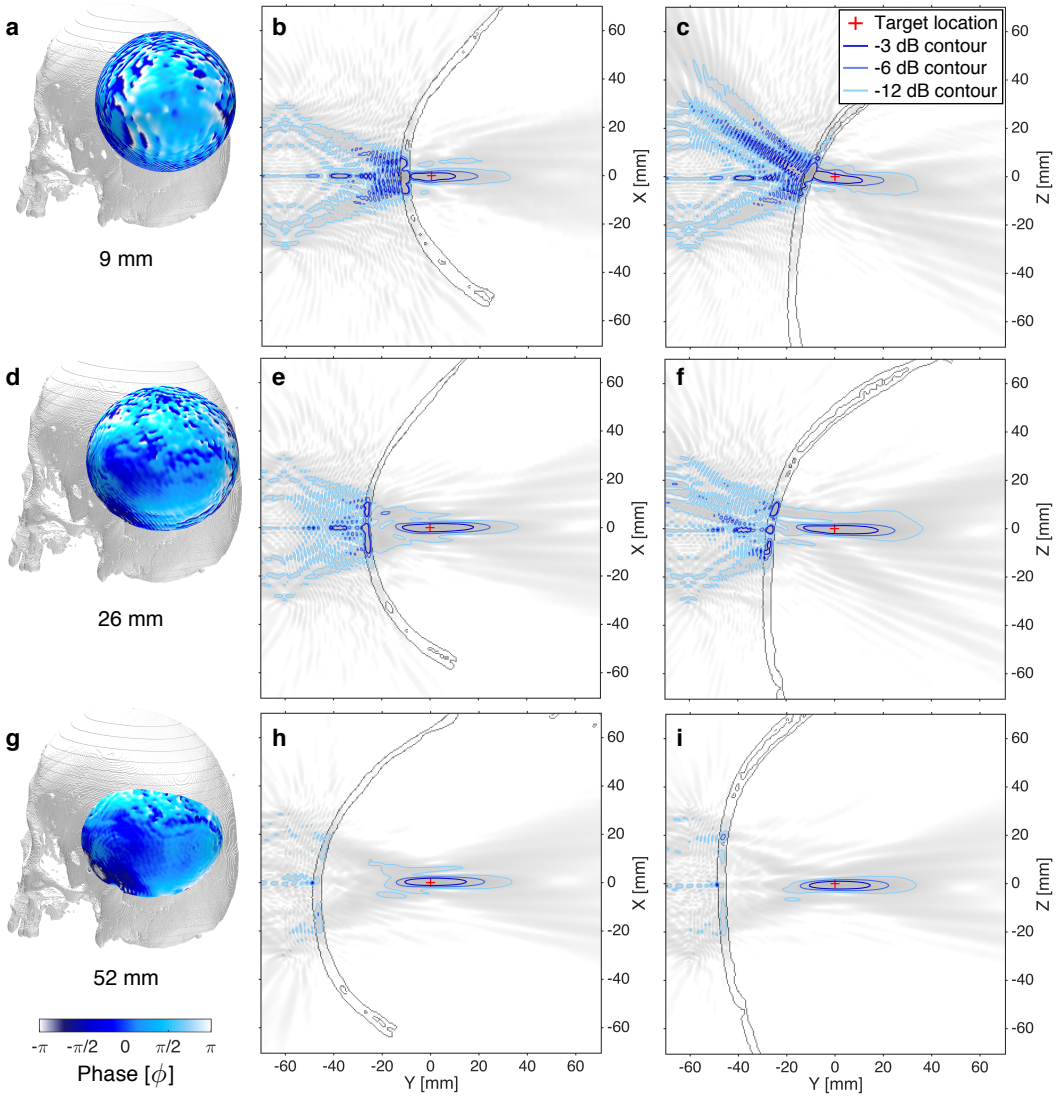


Fig. 3.25: Target depth study: contour plots. 2D pressure distribution plots with overlaid −3, −6 and −12 dB contour levels for XY-planes (**b, e, h**) and YZ-planes (**c, f, i**) along with the corresponding point source phase distributions (**a, d, g**) for a shallow target (top row), intermediate depth target (middle row) and deep target (bottom row). Target location at (0, 0) depicted by red cross.

to form a tight focal spot. Ellipsoidal −3 dB and −6 dB contours are achieved at all target depths. The −12 dB contour shows more deviation dependent on the target depth but is still relatively confined to encapsulating the focal region without excessive fragmentation. This therefore demonstrates the ability to focus at depth using a single-element transducer provided the overlying skull topology is uniform.

3.6 Segmentation comparisons

3.6.1 Homogeneous vs. inhomogeneous skull maps

CT threshold segmentation resulting in a homogeneous skull map and conversion of the HUs into a local inhomogeneous property map are compared in this section.

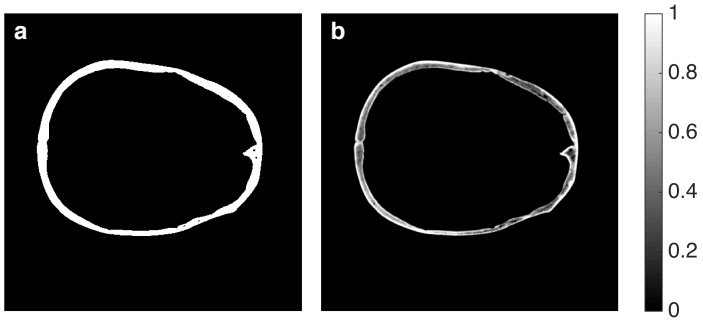


Fig. 3.26: CT segmentation comparison. **a** Binary threshold segmentation (skull bone = 1, water = 0). **b** Inhomogeneous material property assignment based on the CT attenuation data and application of mixture rules (Eq. (3.6)–(3.8)). Plotted map is $1 - \Gamma$ where Γ is the porosity defined by Eq. (3.5).

The differences in the two segmentation approaches (threshold or local) are shown in Fig. 3.26 for a transverse plane of the ex vivo human skull. In Fig. 3.26a, all voxels with a HU value above 0 were labelled as skull bone and those below 0 to water in a binary array. The inhomogeneous map was calculated based on the porosity parameter, Γ, as given in Eq. (3.5),

$$\Gamma = 1 - \frac{HU}{\tau}, \tag{3.5}$$

which normalises the data between water (0 HU) and skull bone. The cortical bone threshold, τ, was chosen to be either 1000, 1250 or 1500 HU. Fig. 3.26b shows $1-\Gamma$ for a cortical bone threshold of 1250 with 1 therefore corresponding to pure cortical bone, 0 to pure water and intermediate values to a mixture of the two. Acoustic properties were then assigned based on the following mixture rules:

$$c = c_{min} + (c_{max} - c_{min})(1 - \Gamma), \tag{3.6}$$

$$\rho = \rho_{min} + (\rho_{max} - \rho_{min})(1 - \Gamma), \tag{3.7}$$

$$\alpha_0 = \alpha_{0,min} + (\alpha_{0,max} - \alpha_{0,min})(1 - \Gamma). \tag{3.8}$$

These equations require maximum and minimum acoustic properties rather than averaged skull values as listed in Table 3.1. Therefore, the maximum properties correspond to that of cortical bone: $c_{max} = 3100\,\mathrm{m/s}$, $\rho_{max} = 1900\,\mathrm{kg/m^3}$ (Maimbourg et al., 2018). The minimum values are that of water: $c_{min} = 1488\,\mathrm{m/s}$, $\rho_{min} = 1000\,\mathrm{kg/m^3}$. Finally, the attenuation coefficient values were obtained from power law fits of skull bone attenuation data obtained from White et al. (2006) as described by Treeby and Cox (2014) using the lower and upper limits to give values of $\alpha_{0,min} = 0.72\,\mathrm{dB/(cm\,MHz^n)}$ and of $\alpha_{0,max}$ =12.16 $\mathrm{dB/(cm\,MHz^n)}$ where $n = 1.16$.

Fig. 3.27 displays XY-plane colour maps for V1R e_2 and FFAR m_2 as well as the target and maximum pressures obtained experimentally (E), for simulated homogeneous map (SH) and simulated inhomogeneous maps at three different cortical bone thresholds (SI1: 1000, SI2: 1250, SI3: 1500).

Analysis of the colour maps reveals that the field distributions do not differ substantially in shape between the two segmentation approaches inside the skull but within the skull contours there are more noticeable differences. This region also shows the greatest discrepancy between the predicted pressure amplitudes with lower pressures, on the order of a 0.05–0.1 MPa reduction, for the inhomogeneous model.

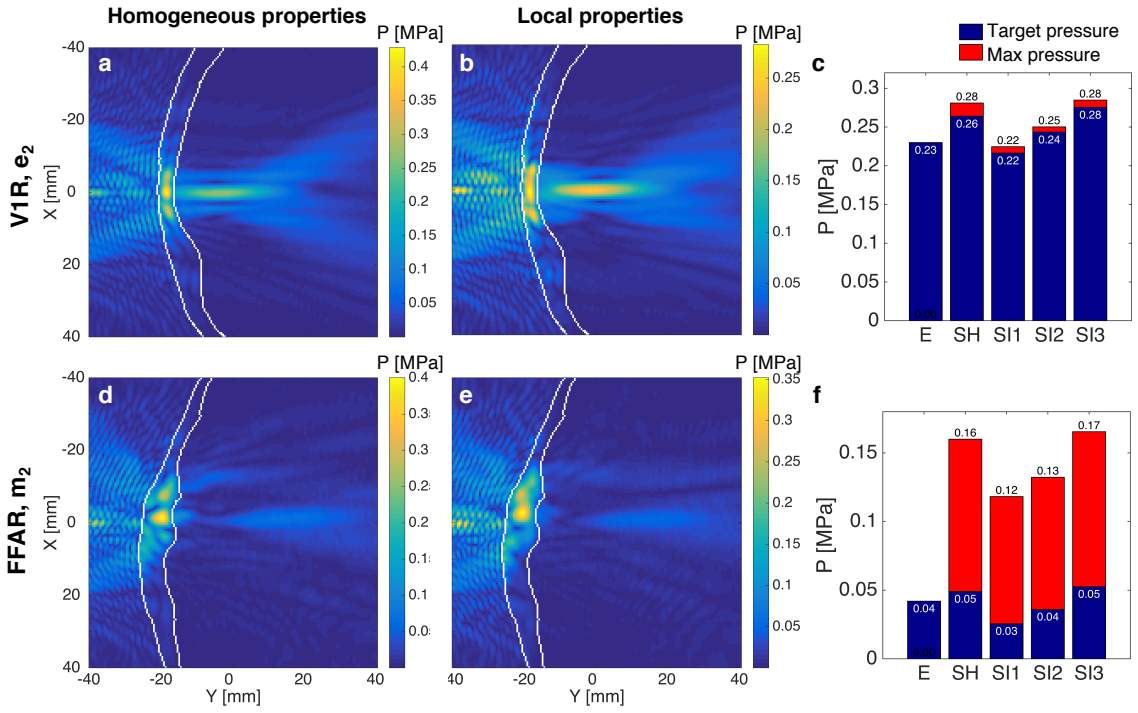


Fig. 3.27: Simulation comparison between homogeneous and inhomogeneous material properties. Axial XY-plane pressure distributions of inhomogeneous simulations with a cortical bone threshold of 1250 HU for **a, c** V1R e_2 and **b, d** FFAR m_2. Skull bone edges are illustrated in white. **c, f** Comparison of target and maximum pressures for each target between experimental (E), homogeneous skull map simulations (SH) and inhomogeneous map simulations for three different cortical bone thresholds: 1000 (SI1), 1250 (SI2) and 1500 (SI3).

Considering the bar plots, the effect of increasing the cortical bone HU threshold serves to increase the predicted pressures consistent with a higher bone threshold reducing the number of voxels assigned to higher sound speeds, densities and attenuation values and hence reducing the impedance mismatch and refraction effects.

The target pressures can be directly compared to the experimental hydrophone measurements. For V1R, the homogeneous simulation overpredicted the pressure by 14.8 % whilst the inhomogeneous simulations underpredicted the pressure by 5.9 % and then overpredicted the pressure by 5.9 and 19.8 % as the HU threshold was raised from 1000 to 1500. A similar pattern emerged for FFAR with the homogeneous simulations 16.7 % above the experimental value with inhomogeneous simulations at −39.3, −14.4 and 25.0 % respectively.

3.6.2 MRI vs. CT segmentation

For segmentation via MRI scans, the MARS (Morphologically and Anatomically accuRate Segmentation) toolbox was employed which is a probabilistic, automated MRI segmentation tool that can be applied to a range of MRI maps including T1 and T2-weighted images (Huang and Parra, 2015).

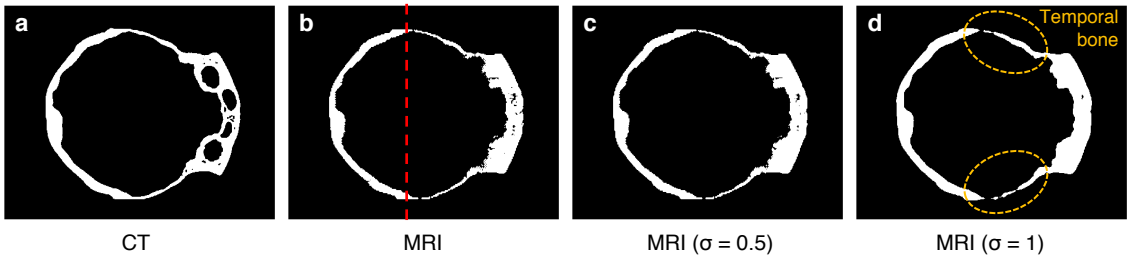


Fig. 3.28: Skull segmentation comparison between CT and MRI. a Threshold segmentation of CT data. **b** MRI-derived skull map based on the MARS algorithm. Deviations most noticeable to the right of the red dashed line. **c, d** Gaussian smoothing applied to the MR-segmented skull with different standard deviations, σ. Smoothing tends to increase small gaps in the temporal bone as indicated by the region enclosed in orange.

To compare between segmentation from either MRI or CT, data were obtained from an anonymised human subject who had undergone imaging through both modalities. The scans were co-registered using the FieldTrip MATLAB toolbox (Oostenveld et al., 2011) to bring them into the same space and visual targets were again created from transformation of the MNI coordinates into subject space. Fig. 3.28 depicts the segmented binary skull bone map acquired either through threshold segmentation of the CT data (Fig. 3.28a) or via application of the MARS framework to the MRI data (Fig. 3.28b). Both medical imaging datasets had a lateral resolution of 0.5 mm and so this resolution was used for the k-Wave simulations corresponding to 5.95 PPW in water. The MR-derived map is noisier and exhibits a thinned temporal bone with some small gaps noticeable. However, reasonable agreement is achieved to the left of the red dashed line roughly corresponding to the skull bone through which the visual cortex can be targeted. A series of Gaussian smoothing filters were applied to remove some of the noise; the standard deviation, σ, defines the

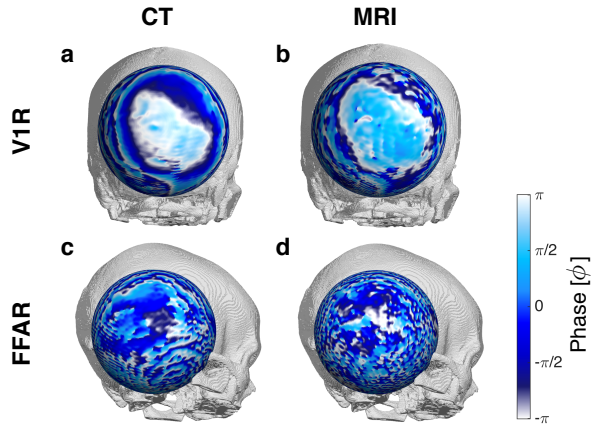


Fig. 3.29: Comparison of point source simulations between MRI and CT-derived skull maps. Phase distributions from point source simulations located at V1R and FFAR based on **a, c** CT and **b, d** MRI scans.

spread of the Gaussian distribution and hence the amount of smoothing as defined by the MATLAB function imgaussfilt. Two examples are shown in Fig. 3.28c, d. The drawback of the filtering is that the holes in the temporal bone are enlarged, particularly at higher σ values, as indicated by the orange contours, although for visual cortex targeting this is not a concern.

Point source simulations were conducted using maps obtained from unsmoothed MR and CT-based segmentation. The phase fields for the V1R and FFAR simulations for each segmentation method are depicted in Fig. 3.29. Although variations are evident between the distributions, the main regions of coherent phase are consistent. The differences in the finer details and the absolute values were not unexpected given that a phase error of 26.7° results from the assignment of one extra voxel as skull bone rather than water and vice versa. However, as the phase distributions are used to inform transducer positioning rather than directly fed in as source conditions, these differences were not a major concern.

Transducer locations were selected manually from the phase distributions of point source simulations computed using the CT dataset with the same positions then set for the CT, MR and smoothed MR simulations in order to compare the forward

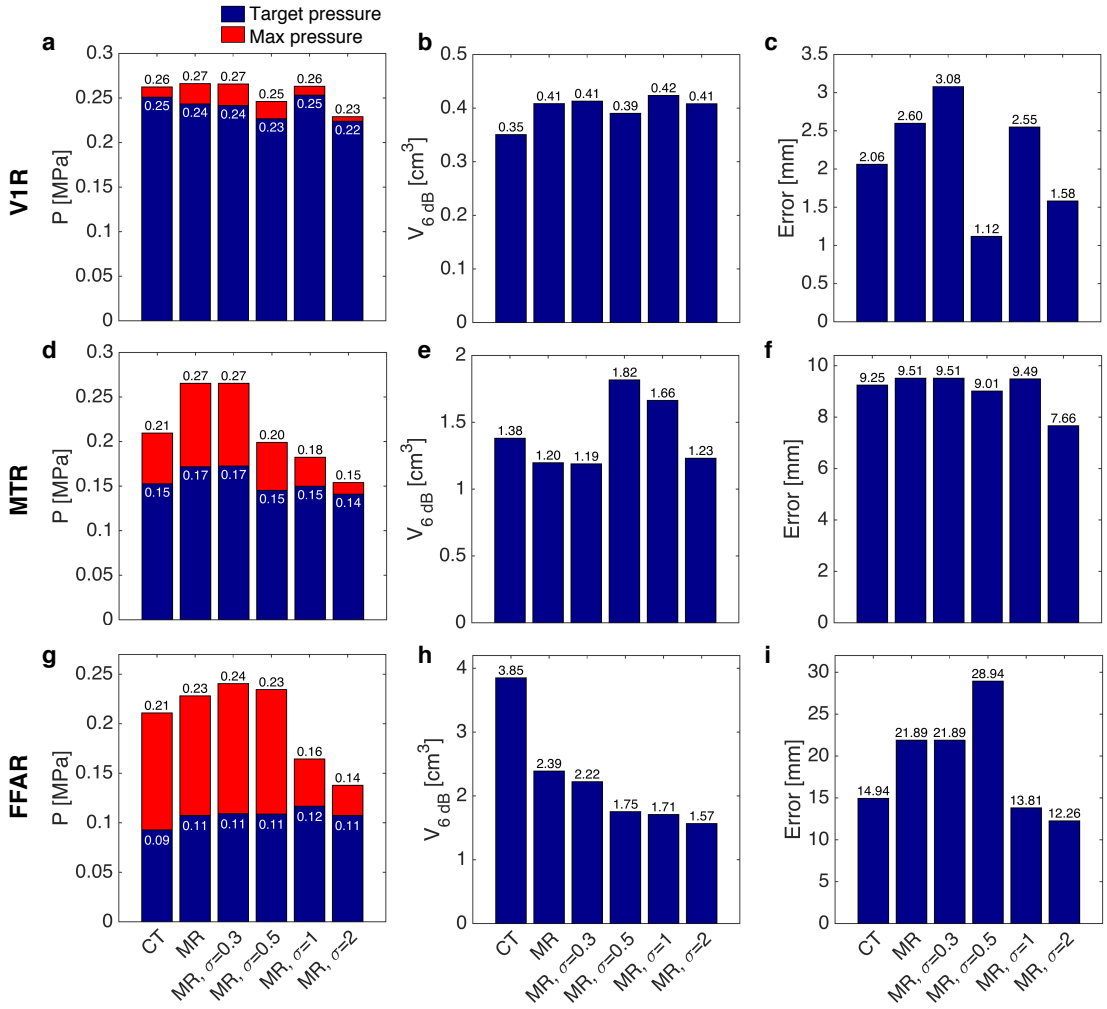


Fig. 3.30: Simulation transcranial ultrasound field differences between MR and CT-derived skull maps. Six different cases were tested derived from a co-registered CT and MRI dataset: CT, MRI, and four smoothed MRI maps (σ = 0.3, 0.5, 1 and 2) for the three visual targets in the right hemisphere. **a, d, g** Target and maximum pressures. **b, e, h** −6 dB volumes. **c, f, i** Focus error (Euclidean distance between target and max pressure locations).

simulations. The Gaussian smoothing parameter, σ, was varied in the range $0.3 \leq \sigma \leq 2$. The results of the forwards simulations for both CT and MR-segmented binary maps are shown in Fig. 3.30. With an experimental comparison not possible for this dataset, the CT simulations were considered the gold standard to which the MR-based simulations are compared.

Comparison between the CT and unsmoothed MR map simulations, shows reasonably close agreement in terms of target and maximum pressures. The MR-based simulations showed differences of −3.0, 12.5 and 15.8 % for the target pressures and

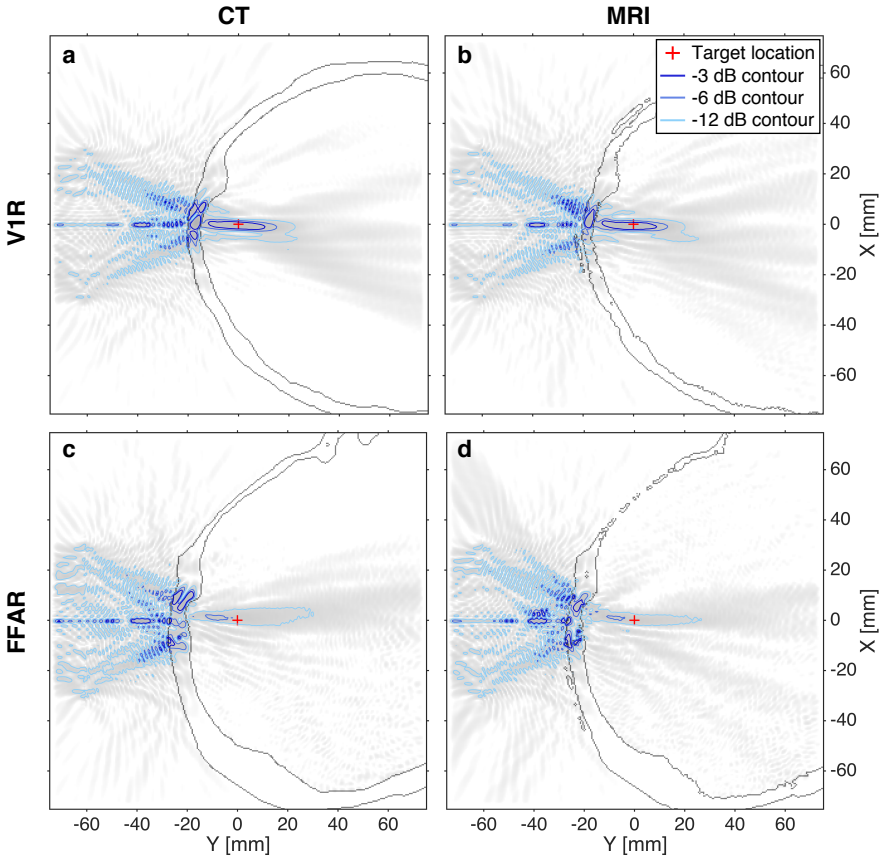


Fig. 3.31: Comparison of forward simulations between MRI and CT-derived skull maps. 2D pressure fields in the XY-plane with overlaid −3, −6 and −12 dB contours for **a, c** CT-based and **b, d** MR-based single-element transducer simulations. Segmented skull profiles for the corresponding scan are also shown.

1.4, 26.7 and 8.2 % for the maximum pressures relative to the CT-based simulations for V1R, MTR and FFAR respectively. V1R and MTR also show consistent focal volumes and errors: less than a 20 % volume estimation difference with focus error differences less than 0.5 mm. Larger discrepancies are observed for FFAR with a 7 mm shift in focal error and a 40 % reduction in focal volume.

Overall, Gaussian smoothing does not appear to reduce the inconsistencies between the simulations computed with maps from the two imaging modalities; in fact, in general, they are exacerbated. Filtering with σ between 0.5 and 1 can produce better agreement in some specific instances, for example the target and maximum pressures fall more in line with the CT-obtained values for MTR but diverge for V1R and FFAR. Consequently, the application of smoothing filters was not employed further

to increase the accuracy of the simulations.

The forward XY-fields for V1R and FFAR can be directly compared between the CT (Fig. 3.31a, c) and unfiltered MR-based (Fig. 3.31b, d) simulations. A strong qualitative agreement is achieved for both target sites although some local differences are noticeable, namely at lower amplitudes away from the focus with small deviations in the −12 dB contours. In terms of the skull maps, holes in the temporal window are evident (even in this unfiltered MR-segmented image) as well as some small areas outside of the main skull profile. Whilst the small anomalous regions external to the primary surface do not appear to excessively modify the simulated fields, the gaps in the temporal bone are likely to be problematic when conducting US simulations to target brain sites underlying these areas.

3.7 FFA correction

Whilst experimental results (Fig. 3.21) demonstrated the ability to focus to FFA via placement of the single-element transducer at a higher location avoiding transmission directly through the petrous ridge but at a greater incident angle with respect to the skull, variation in the anatomical location of FFA along with consideration of the scalp and overlying soft tissues, can prohibit such paths from being viable. Consequently, the purpose of this section is to examine alterations and correction methods to the source, still of a fixed focal length, and assess whether these are credible strategies for improving targeting and focality through the petrous ridge.

3.7.1 Aperture size

A simple modification is to increase the aperture of the source which will increase the focal gain and reduce the axial focal width. Three source radii were considered: 32 mm, matching the H-107 transducer but without a central cut-out, 48 and 60 mm.

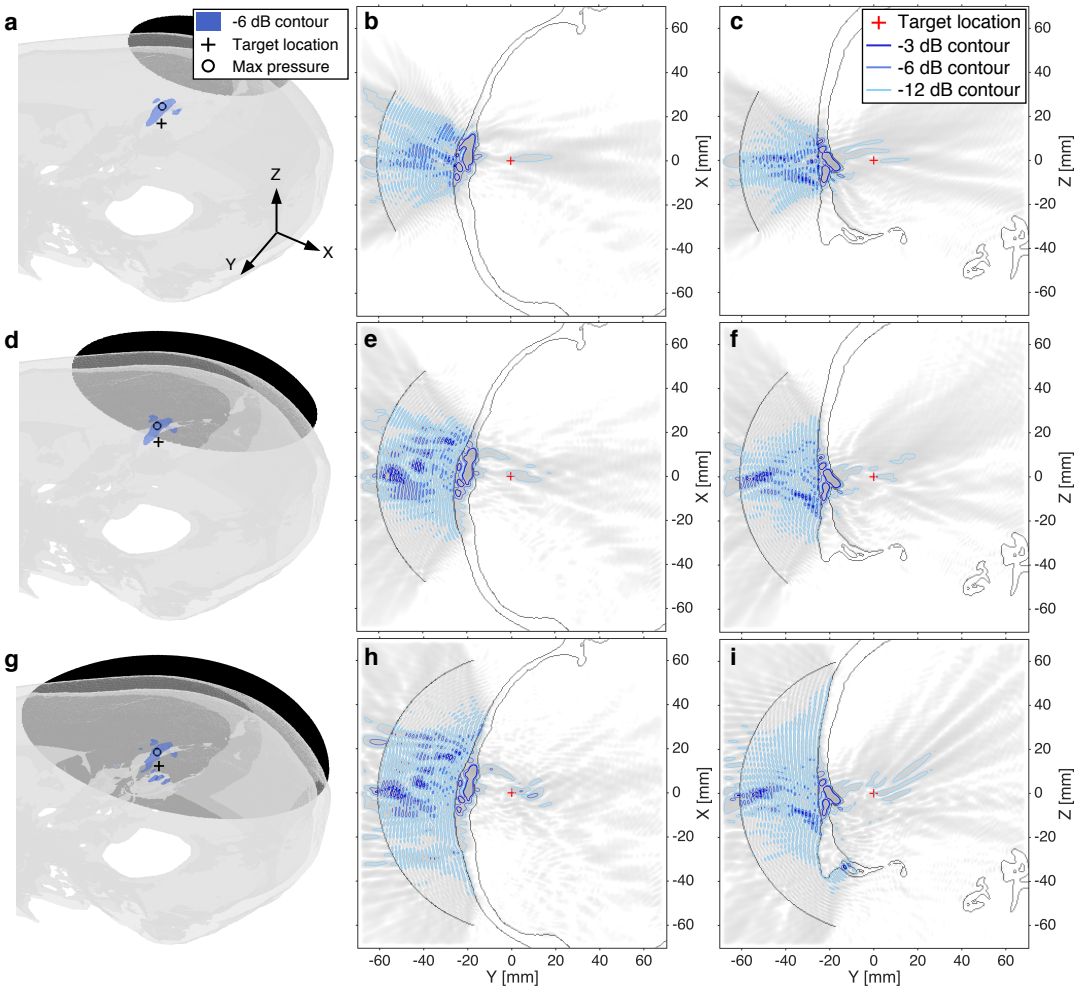


Fig. 3.32: Effect of increasing aperture on FFA m_2 simulated pressure fields. Forward simulation plots for a geometric transducer implementation with a fixed focal length of 63.2 mm and varying source radius of 32 mm (top row), 48 mm (middle row) and 60 mm (bottom row). **a, d, g** 3D −6 dB pressure contour volumes, **b, c, e, f, h, i** 2D pressure fields in XY and YZ-planes with overlaid −3, −6 and −12 dB contours.

The results for the nominal sound speed of 2820 m/s are displayed in Fig. 3.32. It is evident that even the largest aperture is not able to overcome the induced aberrations of the strongly heterogeneous skull bone with the main hotspot refracted upwards in all cases. Whilst in the XY-plane the geometry of the transducer surface somewhat mirrors the curvature of the skull bone, in the YZ-plane, the skull bone is much flatter and hence the additional source surface area is angled very obliquely with the ray angles likely above the critical angle of 31.2° for this ratio of sound speeds.

If, however, the bone sound speed is dropped by 30 % to match the estimated sound

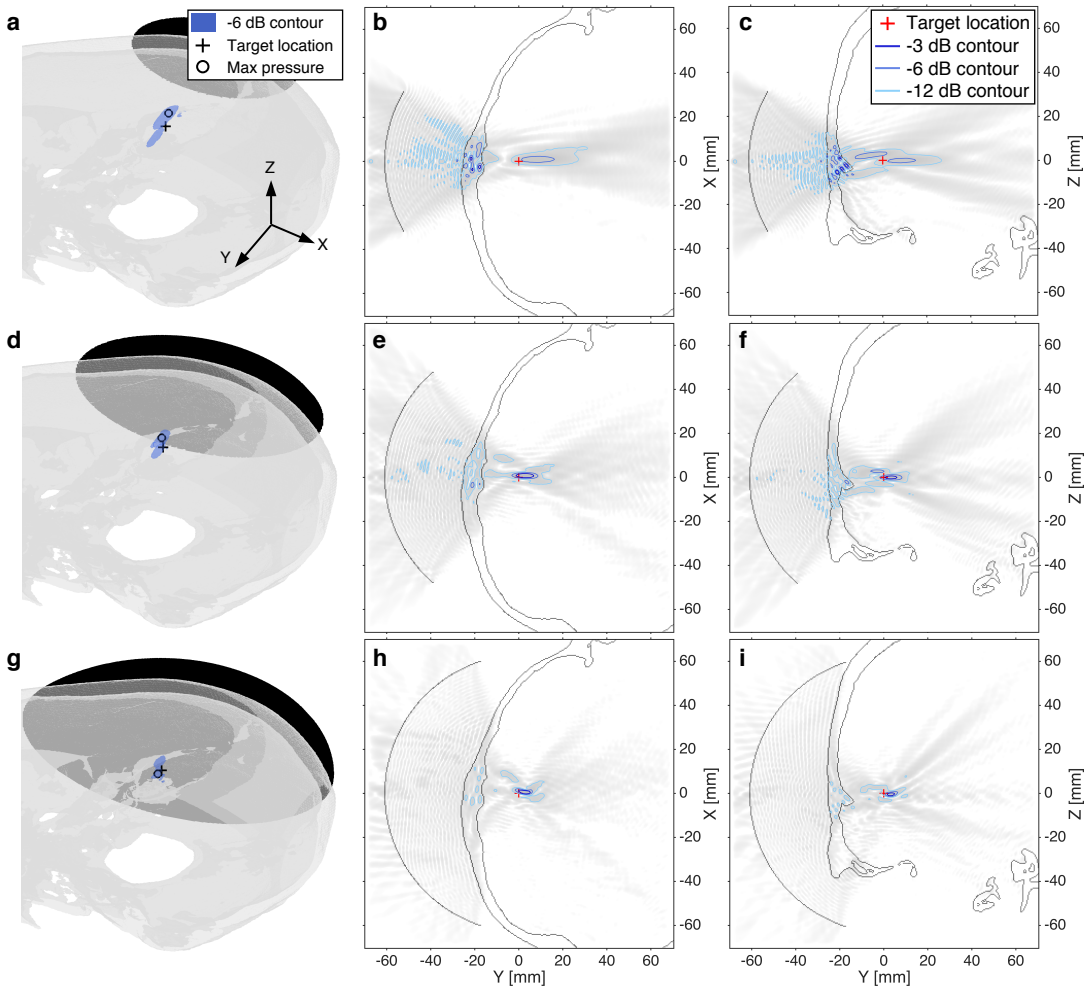


Fig. 3.33: Effect of aperture on FFA m_2 simulated pressure fields, c_0 −30 %. Forward simulation plots for a geometric transducer implementation with a fixed focal length of 63.2 mm and varying source radius of 32 mm (top row), 48 mm (middle row) and 60 mm (bottom row). **a, d, g** 3D −6 dB pressure contour volumes, **b, c, e, f, h, i** 2D pressure fields in XY and YZ planes with overlaid −3, −6 and −12 dB contours.

speed of the skull as discussed in Sec. 3.4, the effect of increasing the aperture is more promising as shown in Fig. 3.33 but still does not work perfectly. Although there is substantially more energy deposition at the target location, off-target regions of higher pressure still exist even at a source radius of 60 mm. The reduction in the focal size that is associated with an increased aperture naturally leads to more specific targeting. The downside of this is that whilst the higher aperture source reduces the volume of higher intensity regions away from the main focus, the focus itself is more easily misaligned from the intended target. This is illustrated in Fig. 3.33h, i where the target location lies outside the −6 dB contour despite being just a few

mm from the centre of the focal spot.

Ultimately, increasing the aperture of the single-element source alone is unlikely to be beneficial as it cannot correct for the induced aberrations from highly heterogeneous skull bone with high sound speeds. Although for lower sound speeds, the approach is more effective, coupling of the transducer to the scalp will be more difficult owing to the increased size and reduced focal sizes may actually be disadvantageous depending on the size of the intended brain target.

3.7.2 Phase and amplitude correction

Alternatively, manipulation of the phase and amplitude across the aperture of the source can also be employed to correct for skull-induced aberrations. Here, the time reversal method informed such choices with either the phase alone or both phase and amplitude directly adjusted. Consequently, the simulations take no account of how this would be implemented in practice, for example through an array or a lens, and thus are idealised models.

Amplitude compensation was applied in two forms: (1) higher amplitude areas from the point source simulation were promoted relative to the mean, that is where low amplitudes were received, low amplitudes were transmitted as stated in Eq. (3.9), and (2) the amplitudes were inverted relative to the mean and subject to a maximum ratio of 5 as given by Eq. (3.10). The subscript x denotes received variables from the point source simulations, $\bar{A}$ is the mean amplitude over the receiver and s refers to the retransmitted source waveforms

$$p_s = \frac{A_x}{\bar{A}} \exp(i(2\pi f t - \phi_x)). \tag{3.9}$$

$$p_s = \begin{cases} \frac{\bar{A}}{A_x} \exp(i(2\pi f t - \phi_x)), & \text{if} \frac{\bar{A}}{A_x} \leq 5, \\ 5 \exp(i(2\pi f t - \phi_x)), & \text{if} \frac{\bar{A}}{A_x} > 5. \end{cases} \tag{3.10}$$

Fig. 3.34 shows the in situ pressure distributions for uncorrected, phase only correction, and both types of amplitude and phase correction to refocus to FFA m_2. Looking at the 3D volumes in the first column it can be seen that none of the correction strategies is perfect, each suffering from off-target high amplitude regions with the maximum internal pressure still located close to the skull surface, substantially offset from the FFA site. The on-axis planes for phase only and phase and amplitude (2) correction are very similar with the target within the −3 dB contour whilst the alternative phase and amplitude (1) adjustment only promotes the target to within −6 dB of the maximum pressure. However, the higher target pressure amplitude achieved by phase only and phase and amplitude (2) correction is countered by the elevation in more off-target regions resulting in a highly fractured field (Fig. 3.34d, j). Therefore, in spite of the lower target to maximum pressure ratio obtained through the phase and amplitude (1) strategy, it exhibits greater focal specificity constrained mainly along the axis of the transducer.

The target to maximum pressure ratio and −6 dB volume metrics for each of the modified source conditions considered in this section are plotted in Fig. 3.35. The bars are colour-coded corresponding to simulations for aperture adjustment (blue), aperture adjustment at a lower sound speed (green), time reversal corrections (red) and a combined increased aperture time reversal (magenta). As discussed in Sec. 3.7.1, increasing the aperture is not successful at the nominal skull sound speed, but if this value is reduced to match the experimentally-inferred value, better results are obtained. However, the concurrent reduction in focal spot size means that even small focal errors can give rise to large differences between the target and maximum pressure with volumes on the order of 0.1 cm^3. This also explains why the ratio of

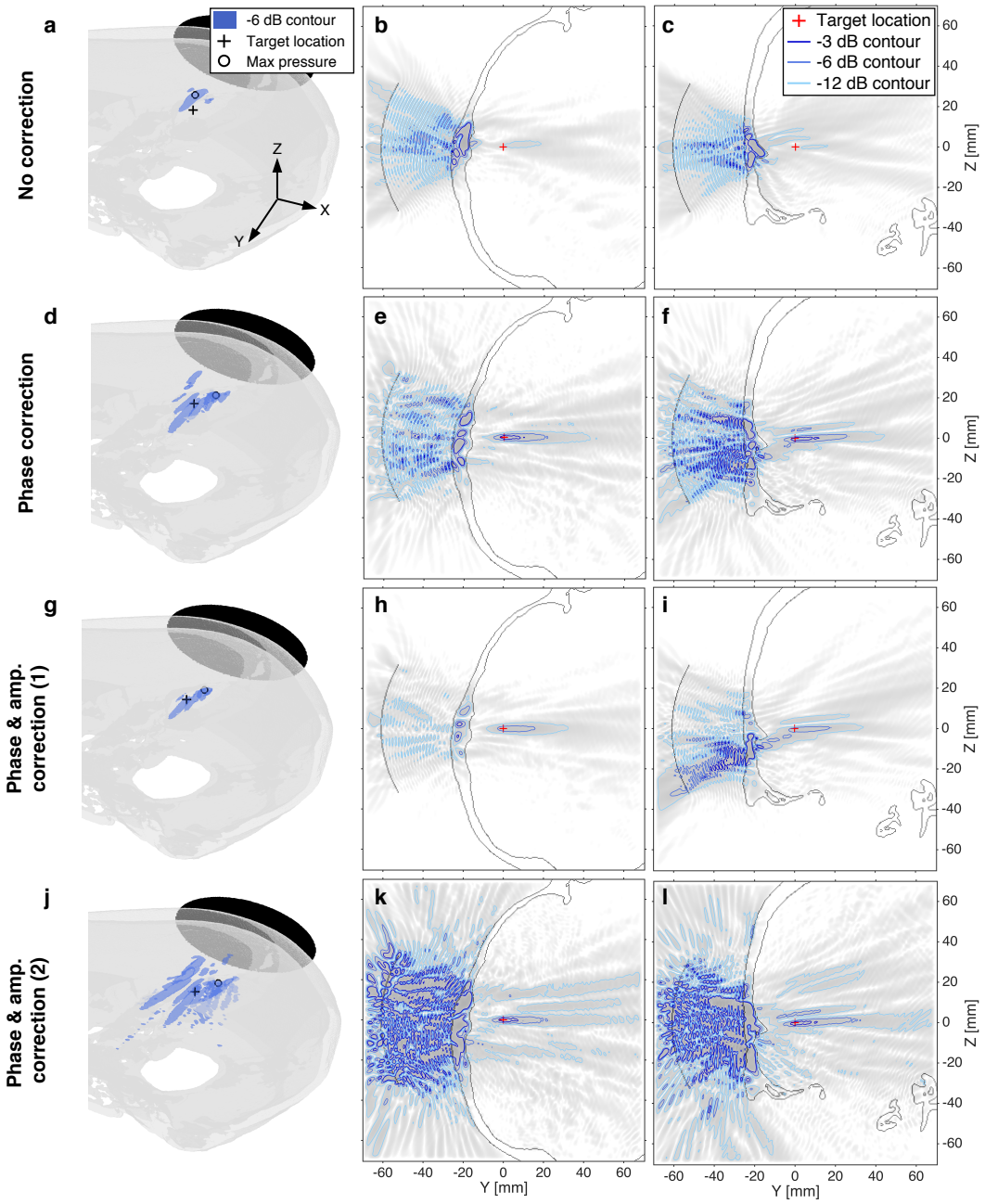


Fig. 3.34: Phase and amplitude correction for targeting FFAR $\mathrm{m_2}$. Geometric source implementation with focal length of 63.2 mm and radius 32 mm with uniform phase and amplitude (top row), phase correction (second row), phase and amplitude correction (bottom two rows) corresponding to Eq. (3.9) and Eq. (3.10). Phase and amplitudes were adjusted according to the output of point source simulations as per the time reversal methodology.

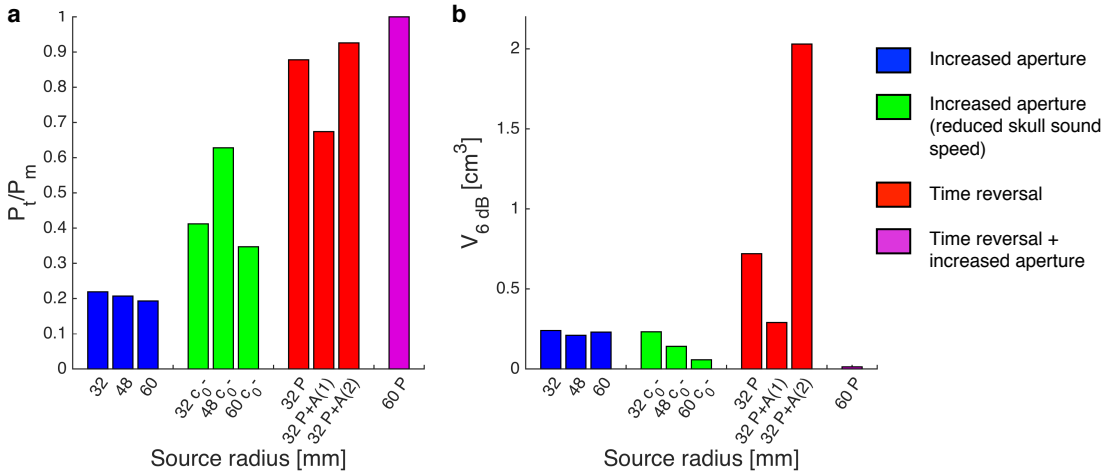


Fig. 3.35: FFA $\mathbf{m_2}$ correction or modification strategy results. Simulations are split into the following sections: increased aperture (blue), increased aperture at a reduced sound speed (green), time reversal techniques (red), and combined time reversal with an increased aperture (magenta). All source conditions were geometric with a focal length of 63.2 mm and a source radius ranging from 32 to 60 mm. c_o- denotes a reduction in the skull sound speed by 30 %, P, phase correction, $P + A(1)$, phase and amplitude correction and $P + A(2)$, phase and amplitude correction (2). **a** Ratio of target (P_t) to maximum (P_m) pressures. **b** -6 dB volume contours.

P_t to P_m drops as the aperture is expanded from a source radius of 48 mm to 60 mm.

Time reversal implementation of the nominal source radius of 32 mm, boosts the pressure ratio closer to 1 but is correlated with a larger -6 dB volumes due to higher amplitude off-target regions. One final simulation was conducted using phase correction of the 60 mm source: this was able to correct for the small offset in focal position resulting in perfect co-alignment of the focus and target.

3.8 Discussion

The efficacy of targeting different areas of the visual cortex with a single-element transducer has been thoroughly examined in this chapter. A pipeline based on the time reversal concept was developed in order to determine the optimal placement of the transducer to focus to a given location. A number of optimisation algorithms were tested to do this automatically with least squares phase optimisation performing effectively for symmetric phase distributions as observed for V1R. However, the

algorithm is not robust to skewed phase distributions such as MTR and hence visual inspection of the phase fields appears a more reliable method for transducer location selection.

Inspection of the point source phase distributions proves a good predictor of the ability to refocus to the target site with coherent phase regions linked with high focal alignment and specificity whereas fragmented phase patterns correlate with a high degree of distortion and aberration from the ellipsoidal freefield profile. Ultimately, the coherence of both the phase distributions and forward fields is a function of the heterogeneity of the skull between source and receiver or source and target. This indicates that much of the posterior brain can be effectively targeted with a single-element transducer owing to the relatively uniform skull profile as demonstrated by targeting of V1 and MT. Even at increased depths ($\sim$50 mm), focal spots can be maintained so long as the skull strucutre remains uniform as shown by the depth study in Sec. 3.5. However, particular anatomical features, namely the petrous ridge and to a lesser extent the inion, make focusing to some brain sites more challenging leading to focal misalignment and elevated off-target regions as shown for the targeting of FFAR as well as the V1L point source distribution.

In general, approximately normal incidence between the transducer centre and skull bone appears to give the best results as well as being the most robust to errors in sound speed properties. However, where anatomical features block the normal incidence path, increasing the angle of the transducer can be an effective targeting strategy as evidenced by FFAR e_2. That said, this is only viable for lower skull sound speeds as demonstrated in Sec. 3.3.6 and, if the scalp and overlying soft tissues are also considered, such oblique paths may also be intractable.

The effect of shear waves also appears to be angle dependent. While local variations exist for each of the targets between the elastic and fluid-based solvers in both directions, acting to either raise or lower the pressure amplitudes at different locations

within the field, a general trend is evident. At normal incidence, the elastic solver typically predicts lower pressure levels with drops in the maximum pressure of up to 30 % and redirects energy away from the geometric focus reducing target pressures by 27.5 % for V1R and 56 % for FFAR. At higher angles, the shear waves can raise amplitudes increasing the maximum and target pressure by 9.5 % and 67 %, respectively, for FFAR e_2. Ultimately, the overall field patterns do not appear to change substantially but the shear waves give rise to small re-arrangements in the pressure profile that can adjust the pressure amplitudes in an angle-dependent manner.

Nonetheless, fluid-based k-Wave simulations showed good agreement with experimental hydrophone measurements. For V1R and MTR, the pressure fields matched closely with the simulations overpredicting the amplitudes in the range 20–35 %. For FFAR, this discrepancy was magnified to between 38 and 87 % with better agreement at increased depth into the skull. The simulation correctly predicted the locations of the main focal spot but did not capture the additional fragmentation seen in the experimental scans.

Analysis of the FFAR e_2 reveals the increased sensitivity of sound speed errors at higher incident angles with a tight focal spot achieved experimentally despite poor predicted fields. As a wide range of skull sound speeds have been reported in the literature, selection of such transducer placements should be treated with caution due to the potential for large disparities between numerical models and experiments. An estimated sound speed error of 25 to 35 % was inferred from comparison of simulations conducted over a range of sound speeds with the experimental data. Consequently, for V1R and MTR, the effect of reducing the skull sound speed which serves to increase the focal pressures may have been cancelled out by neglection of shear wave effects which act to reduce the amplitudes at normally incident angles. Taking V1R as an example, both effects equate to a difference of ∼30 % thus almost perfectly counterbalancing each other. In the future, advances in US-based skull

mapping methodologies may allow subject-specific sound speeds to be elucidated further increasing the accuracy of simulations rather than assigning standardised or averaged skull bone properties.

Small perturbations in transducer location were also studied to mimic expected variations during the during a behavioural trial due to head motion. For V1R and MTR, the differences introduced by rotation of the source were modest, adjusting the target to maximum pressure ratio by less than 14 % even at 5° angles relative to the optimised location. The pressures also tended to decrease away from the nominal transducer location. For FFAR, more stochasticity was apparent with changes up to 32 % for just a 1° rotation. In terms of translational positioning adjustments, much larger changes in the target to maximum pressure ratio were observed although this is mainly due to the focus being shifted away from the target which was defined as a single voxel. Analysis of the maximum pressure change is perhaps a better metric here with increases limited to within 20 % for V1R and MTR but up to 73 % at a 5 mm offset for FFAR. This highlights the need for real-time subject tracking to align the transducer rather than relying on external anatomical features or EEG-electrode sites as well for real-time correction of head movements in order to minimise positioning errors.

A comparison of homogeneous and inhomogeneous acoustic property assignment from CT data did not show substantial differences between the models. The largest differences lie within the skull bone itself with some small differences in pressure amplitudes at the target and inside the skull but without much alteration in the field shape. For the inhomogeneous simulations, a cortical bone threshold of 1250 HU showed the closest match with experimental data with the predictions out by 5.9 and −14.4 % for V1R and FFAR, respectively, compared to 14.8 and 16.7 % for the homogeneous simulations. With good agreement between the homogeneous simulations and experimental data, simulations in a co-registered patient dataset

were conducted to assess the efficacy of segmenting skull bone using MRI scans. The resultant simulations from material maps created using each modality were closely matched with target pressures for MR-based models within 12 % of the CT-simulated values for V1R and MTR and 22 % overpredicted for FFAR. These results support the use of MRI as a viable alternative to CT for posterior brain targets thus allowing structural and functional scans to be combined in a single MR session without any risk of exposure to ionising radiation. It is noted that around the temporal window, some small gaps were evident following MR-based probabilistic segmentation and so greater disparities are likely for targeting through this area.

Finally, methods were explored to correct for the petrous ridge induced aberrations. Phase and amplitude compensation for the nominal transducer aperture was a partial success increasing the pressure at the target but still exhibiting substantial regions of elevated pressures off-target. Increasing the aperture at the nominal sound speed was not shown to offer any benefit but at a reduced sound speed, a tight focal spot was formed close to, but not coinciding with, the target. Combining phase correction with a large aperture produced the optimal result of coincidence between the maximum pressure and intended target. However, the focal volume ($<0.1\,\mathrm{cm}^3$) whilst offering the potential of increased specificity is likely more susceptible to misalignment through errors in transducer placement and limits in tracking resolution. Moreover, at the current state of US-induced neuromodulation, too much focality might actual be a disadvantage, if the response is driven through a critical volume of activated tissue as has been previously postulated. It is also noted that no practical considerations were given to implementing these correction methods physically but the data suggest that a lens-based or even small array-based strategy might not be sufficient to correct for the distortions induced through this highly non-uniform region of skull. Ultimately, a larger array design such as the ExAblate system may be required for accurate targeting of FFA although this will need further verification.

In sum, we have shown that single-element transducers are capable of focusing to many areas within the visual cortex via correct transducer placement alone and it is plausible that this extends to many other brain sites with uniform overlying skull structures. For locations under pronounced variations in skull thickness, focusing is more challenging and so more sophisticated targeting strategies are required. We designed a computational framework to form the basis of this analysis in order to place single-element transducers to focus to any given brain target and assess the in situ pressures. Simulations took ∼4 min to run and thus the fields from multiple locations can be rapidly computed to determine the optimal transducer placement. In general, normal incidence between the transducer and skull produces the best focusing results whilst minimising the sensitivity to acoustic property errors and increased pressures through shear wave coupling. The key parameter is the speed of sound in the skull which effectively places a constraint on both the maximum angle, and heterogeneity of the skull bone through which the focus can be maintained.

The simulations were validated experimentally using an ex vivo human skull and the predicted values were within 20 to 35 % of the experimental measurements for sites were the freefield focus profile was preserved with close agreement between the field morphologies. Through the petrous ridge, greater differences were observed and although the main location of highest amplitude was well predicted, more field fragmentation was seen experimentally leading to the simulated pressures being overpredicted by between 38 and 87 %. In all cases, simulations overestimated the pressure values and so this may provide a built-in safety margin although it is noted this will be dependent on the participant-specific skull sound speed. Ultimately, our findings highlight the need for subject-specific modelling to uniquely define source locations and amplitudes for each participant in order to ensure coincidence between target and focus as well as to limit pressure amplitudes to a prescribed safety threshold.

4

Safety review

Establishing the safety of US in the brain is paramount to enabling FUS as a viable NIBS method. A description of typically utilised US pulsing sequences is given along with parameter definitions over a range of time scales and a brief introduction to inducible bioeffects. Parameter spaces obtained from the literature used for ultrasonic neuromodulation and the outcomes of any completed histological or damage assessments are then presented before a discussion of existing US safety guidelines and their applicability to the pulses employed for brain stimulation applications. This work forms part of a larger review as presented in Blackmore et al. (2019).

4.1 Introduction

The majority of ultrasonic safety guidelines and metrics have been developed for diagnostic imaging purposes which utilise very short US pulses, usually 1-10 cycles. These limits are essentially designed to minimise the chance of inducing bioeffects that will affect tissue function. However, in the context of US therapies, these bioeffects are precisely the mechanisms through which US is thought to confer a therapeutic response. As such, there is a need to design new US safety regulations to account for this paradigm shift where the goal is no longer simply to diminish the chances of US-induced changes within the body but rather to maximise the therapeutic effect whilst minimising side effects. The exact trade-off between these two responses will clearly depend on the therapy, the patient and the desired outcome and thus it is likely guidelines will vary for different applications.

Although at this stage US neuromodulation is not being used in a clinical setting to treat disease, there is a similar objective for early human trials in healthy volunteers: to induce bioeffects that will result in modulation of neural function without eliciting any damage. To that end, this chapter serves to review all published data relating to US neuromodulation from in vitro cell cultures and animal models through to human level in order to inform future US parameter selection. The outcomes and any reported safety data for each study are summarised in short in the tables in Appendix B; a more detailed synopsis of the safety data is given in Sec. 4.5.1 and Sec. 4.5.2. The extracted parameter spaces are plotted in Sec. 4.5.3 indicating where any damage was reported.

As a highly interdisciplinary field, the language and parameter definitions for US neuromodulation are varied as a consequence of researchers from different backgrounds, and this can lead to confusion, particularly given the multiple time scales involved in US pulsing sequences. Consequently, we have explicitly defined a stan-

dardised parameter set in Sec. 4.2.1 so as to avoid these ambiguities. A short description of the underlying physics for the two main bioeffects (cavitation and the ARF) thought to influence nervous system activity is also included. The diagnostic safety metrics and guidelines are then given to provide a starting point for interpreting the parameter spaces obtained through the literature review although ultimately, an updated set of guidelines that better represent the pulses utilised in neuromodulation applications should be devised.

4.2 Ultrasound physics

4.2.1 Parameters

Careful description of the US parameters is key to defining the sequences utilised for inducing ultrasonic neuromodulation. Typically, the sequences are defined over multiple time scales with up to three layers as shown in Fig. 4.1. At the shortest time scales, or inner layer, are the individual pulses of US. The pulses have an associated pulse repetition frequency (PRF) and are repeated at this frequency for a length of time defined by the burst duration (BD) comprising the middle layer. The burst duty cycle (BDC), or duty cycle over a BD, is therefore the pulse length (PL) multiplied by the PRF. Each burst comprises one distinct trial and these are delivered at a burst repetition frequency (BRF). The time between each burst is defined as the inter-stimulus interval (ISI). The BRF is thus the inverse of the sum of the BD and and ISI. The final, outer later, refers to the total time (TT) of the experiment and has an associated total duty cycle (TDC) that refers to the duty cycle over the whole experiment accounting for the ISI between bursts.

The variety of time scales present in the sequences means that intensity values can also be reported over multiple time scales. Here, the spatial-peak, pulse-averaged intensity (I_{SPPA}) will be defined as the average intensity of an individual pulse (PL).

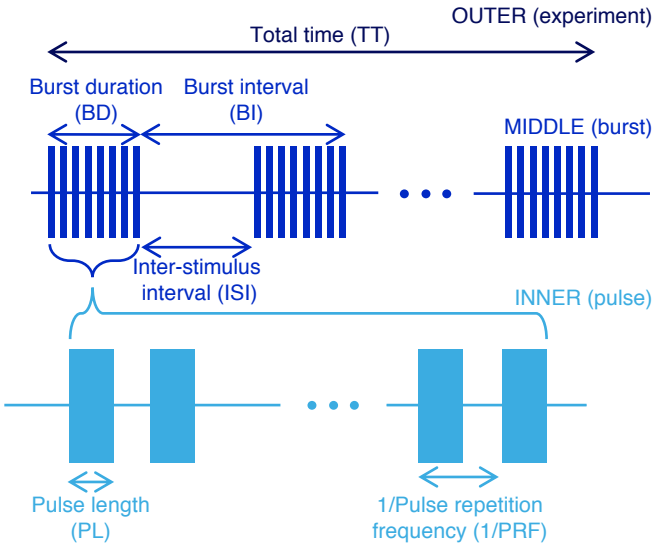


Fig. 4.1: Schematic of ultrasound sequences and associated parameters typically utilised for ultrasonic neuromodulation.

The spatial-peak, burst-averaged intensity (I_{SPBA}) refers to the intensity averaged over one BD and the spatial-peak, temporal-averaged intensity (I_{SPTA}) is the intensity averaged over the total experimental time, including the ISI. For sequences that do not employ bursts of short US pulses, but rather use longer, continuous wave US pulses, the burst parameters (BD and BI) are not relevant to defining the pulsing sequence and PL, ISI and TT are sufficient to characterise the sequences. All of the parameters with associated abbreviations and units are shown in Table 4.1.

4.2.2 Bioeffects

US can result in the deposition of both mechanical and thermal energy in the medium that it passes through. Of particular importance to neuromodulation applications, are the mechanical effects acoustic radiation force (ARF) and cavitation. These are both well studied topics (Dalecki, 2004). Here, we give a brief synopsis and highlight the key parameters. The ARF occurs due to attenuation in the tissue removing momentum from the wave, which results in a net force on the tissue (Palmeri and Nightingale, 2011). For a time-harmonic, progressive, plane wave the force per unit volume of tissue is given by (Nyborg, 1965):

Parameter	Abbreviation	Unit
Frequency	f	MHz
Pressure (peak instantaneous)	p	MPa
Intensity: spatial-peak, pulse-averaged	I_{SPPA}	W/cm^2
Intensity: spatial-peak, burst-averaged	I_{SPBA}	W/cm^2
Intensity: spatial-peak, temporal-averaged	I_{SPTA}	mW/cm^2
Pulse length	PL	ms
Pulse repetition frequency	PRF	Hz
Burst duration	BD	ms
Burst repetition frequency	BRF	Hz
Burst duty cycle	BDC	%
Burst interval	BI	s
Inter-stimulus interval	ISI	s
Total duty cycle	TDC	%
Number of pulses/bursts/trials	N	–
Total time	TT	s
Mechanical index	MI	–
Thermal index	TI	–

Table 4.1: Definitions of ultrasound parameters.

$$F_{ARF} = \frac{2\alpha I}{c_0} \simeq \frac{\alpha_0}{\rho_0 c_0^2} f p^2 \tag{4.1}$$

where α is the attenuation, I is the local intensity of the acoustic field, c_0 is the speed of sound, and ρ_0 is the density. Attenuation in biological tissues follows a power law dependence of the form $\alpha = \alpha_0.f^n$, where the exponent n ranges between 1 and 1.5. Here, we have assumed a linear relation ($n = 1$) in order to estimate the ARF and hence in the second form of Eq. (4.1), the ARF can be seen to vary linearly with frequency and with the square of the pressure amplitude, p.

Acoustic cavitation is the generation of voids or bubbles within the tissue due to the tensile phase of the acoustic wave exceeding a threshold (Plesset and Prosperetti, 1977). Once formed, the cavity oscillates in response to the acoustic wave which can result in acoustic emissions, jetting and streaming which can induce bioeffects (Coussios and Roy, 2008). The threshold for acoustic cavitation depends on the peak negative pressure, frequency, and duration of the US and is also sensitive to

the tissue properties. It will be described more in the Sec. 4.5.1.

4.3 Safety metrics

The safety of US pulses for diagnostic imaging has been extensively studied (Duck, 2008). Three metrics are typically quoted to ensure the safety of the incident US pulse: intensity, thermal index (TI) and mechanical index (MI). The TI is a measure of heating within the tissue. It is defined as the ratio of the acoustic power (W_p) to the power required to raise the tissue by one degree C (W_{deg}) as given in Eq. (4.2). Related to this, the estimated temperature rises can be calculated from Eq. (4.3) which is an approximation to the Pennes bioheat transfer equation (2.28).

$$TI = \frac{W_p}{W_{deg}} \tag{4.2}$$

$$\frac{dT}{dt} = \frac{2\alpha I}{\rho_0 c_p} \simeq \frac{\alpha_0}{\rho_0^2 c_0 c_p} f p^2 \tag{4.3}$$

The MI is a measure of cavitation related to the degree of induced bubble activity and hence to the probability of mechanical damage occurring within the tissue (Apfel and Holland, 1991). The MI is defined as the ratio of peak negative pressure (PNP) in MPa to the square root of the frequency in MHz,

$$MI = \frac{PNP}{\sqrt{f}}. \tag{4.4}$$

It should be noted that the MI was originally developed for short imaging pulses in water and blood to assess the likelihood of cavitation and so its applicability to longer pulses utilised for ultrasonic neuromodulation is unclear. However, subsequent studies have examined the use of MI for similar, longer US pulses utilised

in ARF imaging which suggest that a modification of the frequency exponent from 0.5 to 0.75 shows a better fit with theoretical data (Church et al., 2015). However, experimentally obtained cavitation thresholds in tissue are much higher than the theoretical predictions which suggests that the assumption of optimally sized cavitation nuclei existing in tissue is incorrect (Church et al., 2015). For injected gas-encapsulated UCAs, an alternative measure, the cavitation index, has also been developed to predict cavitation activity and modifies the frequency exponent in the MI to 1. The associated thresholds for UCA rupture and subharmonic cavitation emissions are consequently much lower (Bader and Holland, 2013). Therefore, whilst the exact form of the index to predict cavitation in tissue for long US pulses is under debate, we will use the MI as a reference for discussing the mechanical safety of neuromodulation US sequences given that this is the parameter quoted in most of the US safety guidelines. It may be that keeping pressure amplitudes below the MI limit is unnecessarily restrictive for neuromodulation, however, until validated safety studies have been carried out, particularly in brain tissue, it seems unwise to exceed the diagnostic MI limit at present.

4.4 Safety guidelines

The FDA guidelines for diagnostic US imaging devices complying with the output display standard, are as follows: the I_{SPTA} must not exceed 720 mW/cm^2, the I_{SPPA} must not exceed 190 W/cm^2, the TI must not exceed 6 and the MI must not exceed 1.9 (Duck, 2007). The British Medical Ultrasound Society also has a set of guidelines for diagnostic imaging: the TI must be less than or equal to 0.7 for unlimited time or less than 3 if the duration is less than 1 minute. The MI should also be less than 0.7 if UCAs are used, as there is a risk of cavitation above this threshold (BUM, 2010; Apfel and Holland, 1991).

Whilst these thresholds provide upper limits to the intensities that should be em-

ployed for neuromodulation applications, the ALARA (as low as reasonably achievable) principle may also apply if thresholds for modulatory effects are below these safety limits.

4.5 Literature review

Many of the studies on ultrasonic neuromodulation have also published safety data relating to any damage, or the absence of damage, that occurred as a result of the stimulation. The published data related to such safety concerns will be reviewed in this section. Fig. 4.2–4.5 display the parameter spaces utilised to date for neuromodulation in the CNS and PNS, respectively, indicating where any histological assessments have been conducted and if any damage was observed.

4.5.1 Central nervous system

The early work in hippocampal slices and mice conducted a series of assays to assess safety. In slices, repeated stimulation every 8 min for 36–48 h did not alter the structure of cell membranes (Tyler et al., 2008). There was no sign of BBB damage or changes in synaptic morphology, density or cortical neuropil structure (up to $I_{SPTA} = 142.20\,mW/cm^2$), no neurological abnormalities during rotorod or wire-hanging tasks and no increase in the density of apoptotic neurons or glial cells (up to $300\,mW/cm^2$) (Tufail et al., 2010).

Further histological assessments including H&E staining and TUNEL assays have been conducted following stimulation in a number of animal studies and revealed no damage as shown in Fig. 4.2 & Fig. 4.3 (Dallapiazza et al., 2018; Lee et al., 2017; Li et al., 2016; Mehić et al., 2014; Min et al., 2011a; Yang et al., 2012; Yoo et al., 2011a). Work in disease models for neurodegenerative diseases has also not shown any damage due to low-intensity US in control groups as well as offering a neuroprotective benefit following toxin exposure reducing oxidative stress (Zhao

et al., 2017), myelin loss and apoptosis (Yang et al., 2015) resulting in increased cell viability.

Out of the 54 CNS studies reviewed, only 2 reported damage associated with US stimulation. In rats, one animal exhibited several areas containing hemosiderin indicating the potential of local bleeding (Kim et al., 2014a). The parameters used were an US frequency of 0.35 MHz at an I_{SPPA} = 22.4 W/cm^2, MI = 1.38 and BI = 2 s. The second study, in sheep, showed that repeated stimulations (more than 500 trials) delivered at short BIs of 1 s resulted in small micro-haemorrhages (Lee et al., 2016c). However, at 5 s BIs, no damage was observed. These studies highlight the need to design US sequences that are away from any possible damaging levels by limiting the maximum intensities used and ensuring sufficient rest periods between pulses.

In terms of mechanical safety concerns, to our knowledge, no CNS study has detected direct evidence of cavitation during US stimulation. At the pressures utilised in human studies (<600 kPa) it is unlikely to lead to large blood-vessel rupture. Although limited data have been published on the cavitation thresholds in brain tissue in the absence of UCAs, a study in sheep at 0.66 MHz with short, 2-cycle pulses required peak negative pressures of 12.7 MPa to induce bubble nucleation (Gateau et al., 2011). Using 20 s duration pulses at 220 kHz, cavitation was detected for source powers of 300 W and above (Xu et al., 2015) which resulted in a detectable lesion. These pulses also led to significant temperature rises (> 10 °C) and consequently are far removed from the parameters utilised in ultrasonic neuromodulation.

Whilst histology in humans has clearly not been viable, neurological examinations and MRI follow-ups have not reported any adverse findings in any of the human studies up to an I_{SPPA} of 11.6 W/cm^2 (Lee et al., 2015, 2016b; Legon et al., 2014). The most severe complication was a headache experienced by one subject which quickly resolved (Hameroff et al., 2013).

4.5.2 Peripheral nervous system

Typically, US intensities for PNS stimulation have been higher than those required for neuromodulation in the CNS. Reversible CAP effects have not been associated with any damage in animals or humans. However, following prolonged US exposure, nerve damage has been detected and is linked with irreversible activity suppression (Colucci et al., 2009; Foley et al., 2008; Lele, 1963). In ex vivo crab nerve preparations, afterdischarge was observed at high intensities, 230 $\mathrm{W/cm^2}$ that resulted in reduced CAPs (Wright et al., 2017). This was associated with significant cavitational activity and therefore probably arose as a result of membrane rupture.

In mice, damage was only observed in a positive control group using pressures of 5.4 MPa at 3.57 MPa and a 90 % BDC, 0.5 s pulse length (Downs et al., 2018). For lower pressures (0.53 MPa) at 350 kHz, no tissue damage or BBB disruption was detected (Kim et al., 2012). No damage was detected in human fingertip vibrotactile experiments (Dickey et al., 2012; Lee et al., 2014). Again, any damage parameters are highlighted in Fig. 4.4.

4.5.3 Review of acoustic parameters

The tables in Appendix B list the studies in the literature where US was used for neuromodulation in the CNS and PNS, respectively, without any additional exogenous agents, highlighting the key findings along with any reported safety information. The literature search was carried out using the the keywords “ultrasound” and “neuromodulation” or “brain stimulation” or “LIFU” on the PubMed, ScienceDirect and Google Scholar databases. Any studies that used additional agents (for example: UCAs or nano-particles) or caused thermal ablation were neglected. In total 77 studies were identified that used US to modulate the nervous system. For each study the acoustic parameters were extracted or, if not given, then determined from the quoted parameters. The full US parameter sets can be found in Appendix C.

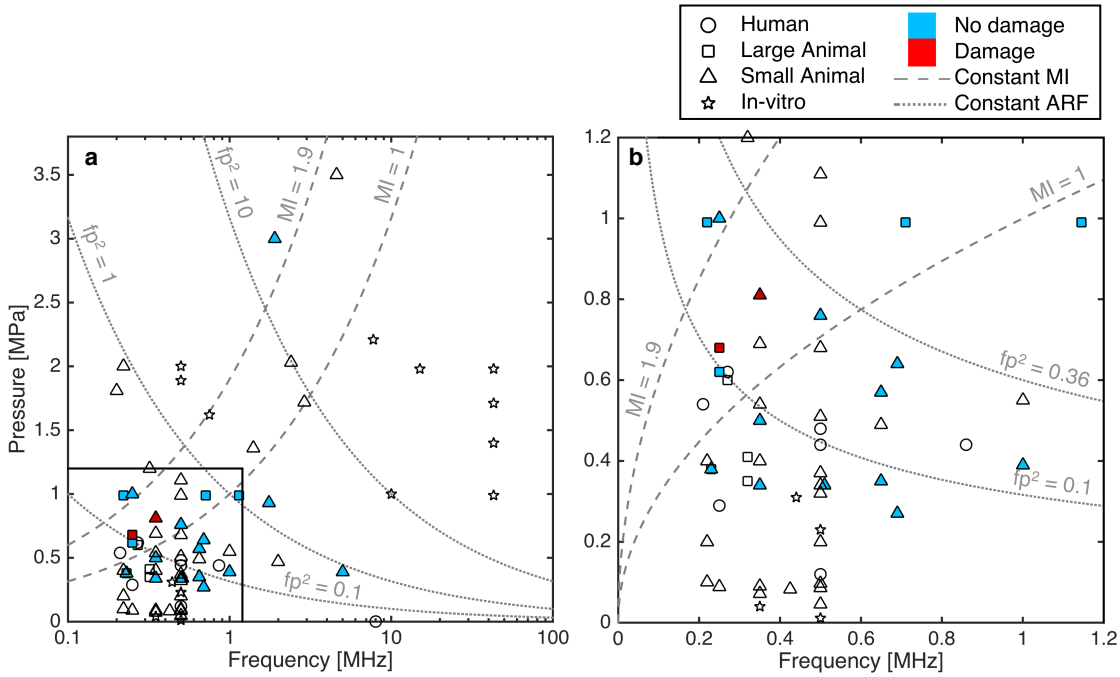


Fig. 4.2: Parameter analysis of central nervous system (CNS) studies: instantaneous peak pressure (p) against driving frequency (f). The studies are split into human, large animal, small animal and in-vitro work. Any studies that conduct histological analysis and report no damage are filled in blue and those that report damage are filled in red. Lines of constant mechanical index (MI) and fp^2, a measure of acoustic radiation force (ARF) are also displayed. **a** Full parameter space (log scale). **b** Subset of parameters applicable to transcranial human delivery (linear scale, $p < 1.2$ MPa, $f < 1.2$ MHz).

Fig. 4.2 displays the peak instantaneous pressure against driving frequency for all of the CNS studies. Here, only the maximum pressure used in each experiment or study has been extracted in order to focus on safety and establishing an upper bound on safe parameters. Successful stimulation may therefore have occured at lower thresholds. The data have been split into four categories: human, large animal, small animal and in vitro work. Where histological analysis has been conducted, the markers are filled with blue, indicating no damage, or red to indicate damage. Contours lines of MI = 1.0 and MI = 1.9 are plotted in order to place data relative to the safety metrics. Also shown are lines of constant fp^2 which correspond to a constant ARF as shown in Eq. (4.1). It is noted, that this expression takes a similar form to the heating rate $(\frac{dT}{dt})$ where c_p is the specific heat capacity of the tissue. For $fp^2 = 1$, this results in a heating rate of approximately 1 °C per second. Fig. 4.2a

shows the data on a logarithmic frequency scale spanning almost three orders of magnitude. The majority of the studies have been conducted in the sub-megahertz region, typically at pressures below 1 MPa. This subset of the full parameter space also corresponds to the likely range of viable parameters for transcranial human applicability from both a delivery and ultimately a safety perspective. It can be see that the human studies fall within the FDA US imaging guidelines with an MI of below 1.9 and I_{SPPA} below 190 W/cm^2 (the exact values can be found in the Appendix C). This region is zoomed in on in Fig. 4.2b. It can be seen that the two reports of damage occur towards the upper end of the pressure scale ($p > 0.65$ MPa) and the lower end of the frequency spectrum (250–350 kHz) for this cluster of points correlated with higher MI values. Although it is also noted that there have been studies both in a large animal and small animals that that report no damage at similar frequencies but at higher pressures, up to 1.2 MPa.

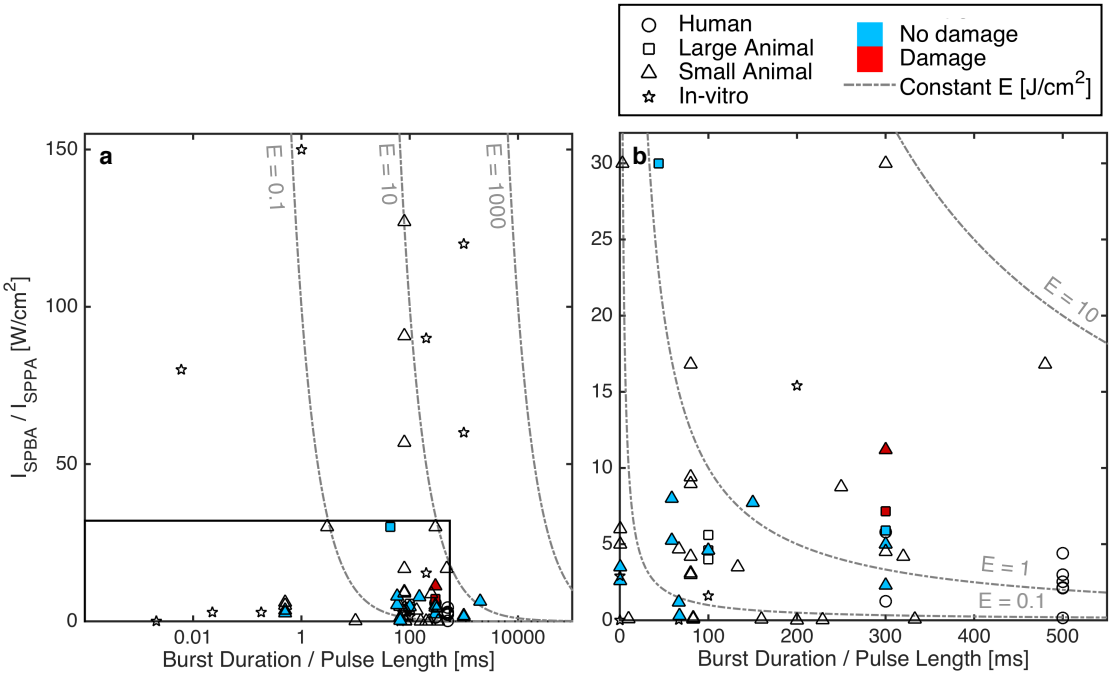


Fig. 4.3: Parameter analysis of central nervous system (CNS) studies: intensity versus duration. For burst wave: burst-averaged intensity (I_{SPBA}) versus burst duration (BD). For continuous wave: pulse-averaged intensity (I_{SPPA}) against pulse length (PL). The studies are split into human, small animal and in-vitro work. Any studies that conduct histological analysis and report no damage are filled in blue and those that report damage are filled in red. Lines of constant energy density ($E=I_{SPBA}\times BD$ or $E=I_{SPPA}\times PL$) are also displayed. **a** Full parameter space (log scale). **a** Subset of parameters (linear scale, $I_{SPBA}/I_{SPPA} < 30\,W/cm^2$, BD/PL < 500 ms).

The same data but plotted as the I_{SPBA} versus burst duration (burst wave) or I_{SPPA} versus pulse length (continuous wave) are shown in Fig. 4.3. Contours of constant energy per unit area are also displayed; that is, either $I_{SPBA} \times BD$ or $I_{SPPA} \times PL$ for CW. The wide span of different parameters is again evident in Fig. 4.3a with pulse lengths ranging from hundreds of nanoseconds to the order of seconds. The majority of the data are clumped in one region between 20 and 550 ms and at intensities less than 30 W/cm^2 and shown in more detail in Fig. 4.3b. On this axis, the damage parameters are slightly separated from those that reported no damage and are correlated with higher energy density levels. Unfortunately, in general, insufficient data were available to calculate the total cumulative energy (energy delivered in one burst (pulse) multiplied by the total number of bursts (pulses)) for each study to calculate a total energy dose. This may have further separated the data as for the sheep study only repeated application of more than 500 trials resulted in microhaemorrhage (Lee et al., 2016c). That said, the other report of damage only applied three repeated trials but with a higher energy density per burst (Kim et al., 2014b).

For the PNS, the data do not exhibit clusters as for the CNS literature. For both plots, pressure versus frequency (Fig. 4.4a) and intensity versus pulse length (Fig. 4.4b), large variations in the acoustic parameters between studies are observed. There are also more reports of damage following the trend described in Sec. 1.3.2, where initially reversible effects without damage are observed followed by irreversible changes linked with nerve damage. However, again, insufficient data were available in order to plot the data against a total cumulative energy measure. Some of the irreversible effects are likely due to thermal damage due to the higher intensities and longer exposures used in PNS stimulation but for shorter pulses, cavitation has also been linked to damage through nerve rupture (Wright et al., 2017).

Comparing the CNS and PNS parameters, it is clear that the pressures and inten-

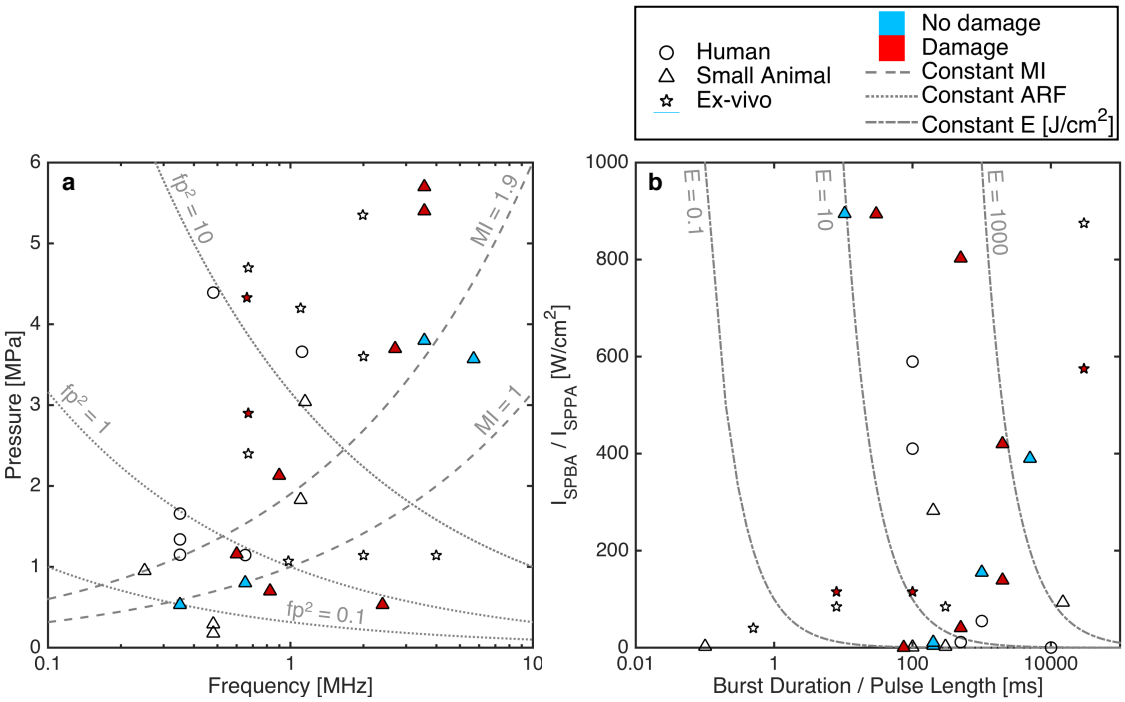


Fig. 4.4: Parameter analysis of peripheral nervous system (PNS) studies. a Instantaneous peak pressure (p) against driving frequency (f) with lines onstant mechanical index (MI) and fp^2, a measure of acoustic radiation force (ARF) (log scale). **b** For burst wave: burst-averaged intensity (I_{SPBA}) versus burst duration (BD). For continuous wave: pulse-averaged intensity (I_{SPPA}) against pulse length (PL). Lines of constant energy density ($E=I_{SPBA}\times BD$ or $E=I_{SPPA}\times PL$) are also displayed (log scale). The studies are split into human, small animal and ex-vivo work. Any studies that conduct histological analysis and report no damage are filled in blue and those that report damage are filled in red.

sities used for PNS modulation tend to be higher than for the CNS as shown in Fig. 4.5. Whilst these plots only depict the maximum parameters, a similar trend is also observed for success thresholds indicating more energy is required to elicit responses in peripheral nerves. This may be attributed to numerous factors including differences in cell morphology, axonal bundle sizes and nerve myelination and therefore potentially requiring different mechanisms to stimulate them.

4.5.4 Thermal effects

Thermal effects are clearly involved in some of the peripheral nervous studies with effects replicated in temperature controlled water baths (Lele, 1963) and temperature changes can affect neural function as described in the Sec. 1.3.3. However, for most of the recent brain studies, expected temperature rises are typically less than

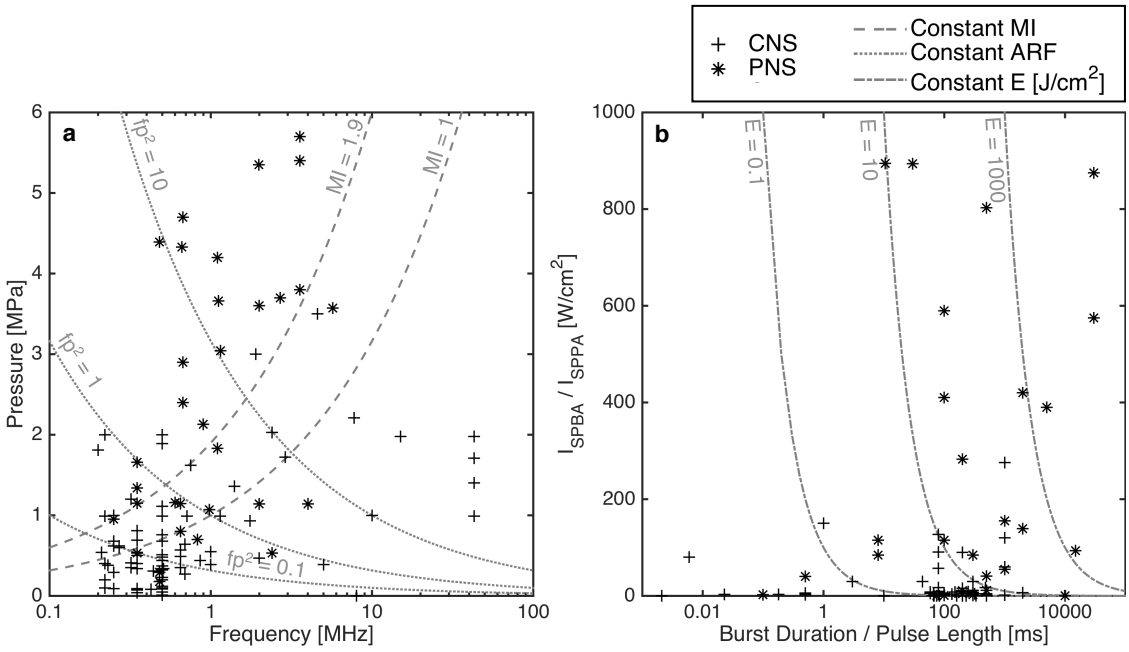


Fig. 4.5: Comparison of parameters employed in the central nervous system (CNS, cross) and the peripheral nervous system (PNS, star). a Instantaneous peak pressure (p) against driving frequency (f) with lines of constant mechanical index (MI) and fp^2, a measure of acoustic radiation force (ARF) (log scale). **b** For continuous wave: pulse-averaged intensity (I_{SPPA}) against pulse length (PL). Lines of constant energy density ($E{=}I_{SPBA}{\times}BD$ or $E{=}I_{SPPA}{\times}PL$) are also displayed (log scale).

a tenth of a degree, which should be negligible (Khraiche et al., 2008; Lee et al., 2016b,c; Tufail et al., 2010) and consequently thermal effects are not considered to contribute to neurostimulation responses.

Retrospective temperature simulations in several rodent setups (Constans et al., 2018) revealed that in general, temperature effects could be neglected, but in one study (Kamimura et al., 2016), a temperature rise of 7 °C was reported as a result of thermal diffusion from the skull bone into the brain. Therefore, care must be taken to ensure off-target temperature rises do not occur through skull-induced heating potentially resulting in thermal modulation.

4.6 Discussion

It is apparent that a very diverse set of US parameters has been employed to induce neuromodulatory effects spanning over two orders of magnitude in frequency (0.2–

43 MHz), combined with almost every conceivable pulse length and burst sequence, with pressures ranging from as low as 11 kPa through to 3.5 MPa in the CNS and up to 5.7 MPa in the PNS. From a mechanistic and a safety perspective, it is therefore highly likely that multiple bioeffects are relevant for different frequencies and time scales.

The US parameters that the community seems to be settling for CNS stimulation on are a frequency of ∼200-500 kHz delivered as a 300–500 ms burst of ∼0.5 ms pulses at a PRF of ∼1 kHz with pressure amplitudes on the order of 0.1–0.6 MPa in the brain. We carried out an analysis of the safety metrics developed for diagnostic US imaging for the US parameters used in the brain and found that the US parameters employed in the human trials would be considered safe from a imaging regulatory view. Although we note that the pulsing paradigm used in US stimulation studies involves longer pulses than used in US imaging and this may have an impact on cavitation thresholds which should be considered further.

In terms of safety in the CNS, the data reveal that caution should be applied for frequencies below 500 kHz at pressures above 0.65 MPa as well as for highly repetitive stimulation. Current human trials have only used pressures up to 0.6 MPa and have not led to any reported injuries. At present for human subjects, we therefore recommend to stay within this pressure range as well as limiting the minimum ISI and the number of sonications for a single brain location. We anticipate that further work in the safety area could allow a larger range of acoustic parameters to be employed than has been used to date.

US seems to be well tolerated in humans with the most severe complication across all participants being one headache that quickly resolved (Hameroff et al., 2013) in comparison to other NIBS methods where, for example, TMS stimulation can induce pain, discomfort and headaches occurring in up to 40 % of participants, particularly for repetitive protocols (Rossi et al., 2009). However, this is countered by additional

complications associated with the coupling of the transducer to the scalp requiring US gel to be applied as well as potential discomfort from the contact of the coupling cone to the scalp for long periods of time.

In summary, US is emerging as an exciting NIBS method that has been demonstrated to safely and reversibly modulate the nervous system. One goal for the community would be to develop appropriate guidelines for the use of ultrasonic neuromodulation in both research and clinical settings, as has been done for TMS (Rossi et al., 2009) and tCDS (Nitsche et al., 2008).

5

Human pilot study

This final research chapter presents the setup, implementation and results of a human pilot study using US to stimulate areas of the visual cortex. The study is the culmination of the work in the previous chapters which aimed to address safety and delivery concerns. Three visual areas in the right hemisphere were targeted with US with stimulation applied in a randomised trial design. Subject-specific modelling informed source locations and amplitudes with real-time alignment achieved through a neuronavigational system. During the behavioural tasks, simultaneous EEG data were recorded to assess changes in brain activity. US resulted in strong auditory activation and so an audio mask was designed to conceal the US burst. Behavioural and preliminary electrophysiological results are presented although EEG analysis is still in progress. Ultimately, the study confirms evidence in animal models that US bursts lead to direct auditory activation which may confound neuromodulation studies.

5.1 Introduction

US neuromodulation in humans has primarily been confined to cortical brain sites close to the brain surface which can be focused to using single-element transducers. Stimulation of the primary visual cortex (V1) has resulted in phosphenes (Lee et al., 2016b) and of the primary and secondary somatosensory cortices (S1, S2) in sensations felt in the hands (Lee et al., 2016a, 2015). The elicitation of US-evoked potentials has been reported through stimulation of V1 (Lee et al., 2016b) and S1 (Lee et al., 2015) as well as the modulation of SEPs induced by median nerve stimulation through the stimulation of S1 (Legon et al., 2014) and the thalamus (Legon et al., 2018a); and MEPs triggered by TMS as a result of primary motor cortex (M1) stimulation (Legon et al., 2018b). BOLD fMRI maps confirmed activation of V1 and associated visual pathways (Lee et al., 2016b) and increased the activation volume of the M1 thumb representation although in this instance without activating connected regions (Ai et al., 2018).

These studies are encouraging for use of US as a NIBS tool for modulation of the human brain offering increased spatial selectivity and depth penetration over existing electrically-based modalities. However, they also highlight the need for participant-specific modelling to ensure co-alignment of the target and US focus (Lee et al., 2015, 2016b) and work in animal models showing widespread auditory activation (Guo et al., 2018; Sato et al., 2018) demands careful attention to sham sites and experimental controls.

The aim of this pilot study was therefore to replicate previous work targeting V1 to look for phosphenes as well as to extend US stimulation to other visual areas: the middle temporal (MT) area which plays a major role in motion perception (Born and Bradley, 2005), and a deeper target, the face fusiform area (FFA), involved in facial processing (Kanwisher and Yovel, 2006). The study was a collaboration

between Engineering Science and the Nuffield Department for Clinical Neuroscience (Dr. Verena Braun and Dr. Chris R Butler).

Subject-specific modelling was performed using structural and functional MRI data following close agreement between stimulations using maps obtained from each modality as outlined in Sec. 3.6.2, and owing to the difficulty in acquiring approval for conducting CT scans in healthy volunteers. An fMRI localiser was used to obtain specific anatomical sites for each brain target. A total of 200 trials at V1 and 500 trials at MT and FFA were performed, 50 % of which were stimulation trials and 50 % without stimulation delivered in a randomised sequence. A sham site for MT was also defined, 15–20 mm from the real MT location posteriorly but at a similar depth into the brain in the same transverse plane.

Following preliminary tests, it was evident that the US burst sequence (300 ms BD, 50 % BDC) produced an audible tone to the participant although this sound was not discernible to anyone else in the room. It was therefore hypothesised that this sound was due to an US-induced flexural wave propagating through the skull bone that directly activated the cochlear as has been suggested previously (Guo et al., 2018). This is discussed in more detail in Sec. 5.3.3. In keeping with the bone conduction hypothesis, which would result in the generation of a square wave at the PRF of 1 kHz in the skull, an audio tone was generated to mimic this waveform for 700 ms and played through a set of earphones to mask the US-induced sound which was embedded within the tone. An initial block of 100 randomised trials was conducted to determine whether the subject could detect when the stimulation was applied at each target site. Behavioural tasks were then executed with the mask employed throughout. Simultaneous EEG acquisition was performed during all tasks to determine any changes in brain activity. The total experimental time ranged from 6–10 h including EEG cap setup, the running of the tasks and break periods.

5.2 Methods

5.2.1 Subjects

All experiments were conducted with the approval of the University of Oxford Medical Sciences Interdivisional Research Ethics Committee. A total of 21 healthy volunteers were tested: 13 female and 8 male, aged 20–51 with a mean age of 27.2 ± 8.6 (standard deviation). Each volunteer provided informed written consent to participate in the study. Two subjects reported as being left-hand dominated, and none of the subjects reported any contraindications to NIBS as outlined by the TMS protocol (Rossi et al., 2009). The study was split into three parts: a pre-stimulation MRI session to determine a participant's structural and functional anatomy to inform the modelling, a behavioural task session where US stimulation was conducted, and a post-stimulation MRI session to check for any long-term brain changes as a result of the stimulation.

5.2.2 Magnetic resonance imaging (MRI)

Scans were performed in a 3-Tesla Siemens TIM Trio MR scanner (Siemens Medical Solutions, Erlangen, Germany). T1-weighted images were acquired and used for tissue segmentation as described in Sec. 5.2.4. From a safety perspective, susceptibility-weighted imaging (SWI) (Haacke et al., 2009) was also performed both pre- and post-sonication. SWI MR imaging is sensitive to deoxygenated blood and hemosiderin (Haacke et al., 2009) and thus can be used to detect any induced microbleeds.

fMRI localisers were conducted to determine participant-specific target locations for V1, MT and FFA. In each case, subjects were shown images in the MRI scanner to activate the different visual areas. The V1 location was identified visually based on the structural scans but for MT and FFA, subtractions between the averaged activation maps obtained from the presentation of different images was used to

locate each site. For MT the subtraction was the activation of stationary dots from moving dots and for FFA, houses from faces. Finally, the site of peak activation in the right hemisphere was extracted from each map and defined as the target location.

5.2.3 Ultrasound parameters & delivery

US stimulation was delivered through a 500 kHz single-element geometrically-focused transducer (H-107, Sonic Concepts Inc, Bothell, WA, USA). One stimulation trial consisted of a 300 ms burst applied at a 1 kHz PRF and 50 % BDC as shown in Fig. 5.1.

The transducer was connected through a 55 dB broadband amplifier (1140LA, E&I, Rochester, NY, USA) and a matching network and driven by the arbitrary waveform generator of a USB oscilloscope (Handyscope HS5, TiePie, WL Sneek, The Netherlands).

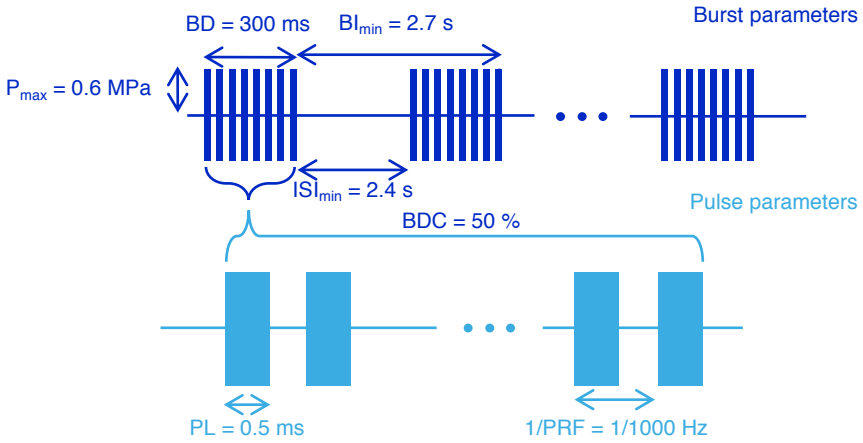


Fig. 5.1: US sequence parameters. One sonication trial consisted of a 300 ms US burst at a burst duty cycle (BDC) of 50 %, that is 0.5 ms pulses at a pulse repetition frequency (PRF) of 1 kHz. The maximum modelled peak positive pressure was 0.6 MPa and a minimum interstimulation interval (ISI) of 2.4 s ensured the spatial-peak, time-averaged intensity (I_{SPTA}) was below the 720 mW/cm^2 FDA output display standard limit.

Based on the literature analysis presented in Chapter 4, the following safety limits and constraints were implemented:

1. Maximum peak modelled pressure in CSF or brain tissue = 0.6 MPa.
2. Maximum number of stimulation trials per target = 250.
3. Minimum inter-stimulation interval (ISI) = 2.4 s.
4. Maximum temperature rise in skull bone = 3 °C.
5. Maximum temperature rise in brain tissue = 1 °C.

The maximum intensity is based on the highest in situ intensity that has been previously used in humans (Lee et al., 2016b), although in that study the US source was at 270 kHz which increased the likelihood of cavitation activity. The constraints on the maximum number of trials and minimum time between trials were in response to the results of the ovine study (Lee et al., 2016c) where highly repetitive stimulation at short ISIs led to some microhaemorrhages. The minimum ISI also ensures the time-averaged intensities fall within the FDA output display standard (ODS) limit. The ODS pathway for device approval allows the cephalic limit on the time-averaged intensity of 94 mW/cm^2 to be raised to the general limit of 720 mW/cm^2 in exchange for real-time display of the TI and MI indices. Whilst these metrics were not displayed during the trial, given that transducer was only used at one amplitude setting for each target based on prior subject-specific modelling effectively fixing the TI and MI, it was deemed acceptable to use the higher limit.

Coupling cone

The transducer was coupled to the scalp using a flexible polyurethane membrane from a shock wave source (MINILITH SL1, Storz Medical, Tägerwilen, Switzerland). This was fixed around the edges of the transducer using a custom mount with an o-ring seal. The cone was filled with degassed water through syringe connections on a back plate over the central circular transducer cut-out. The depth of the coupling

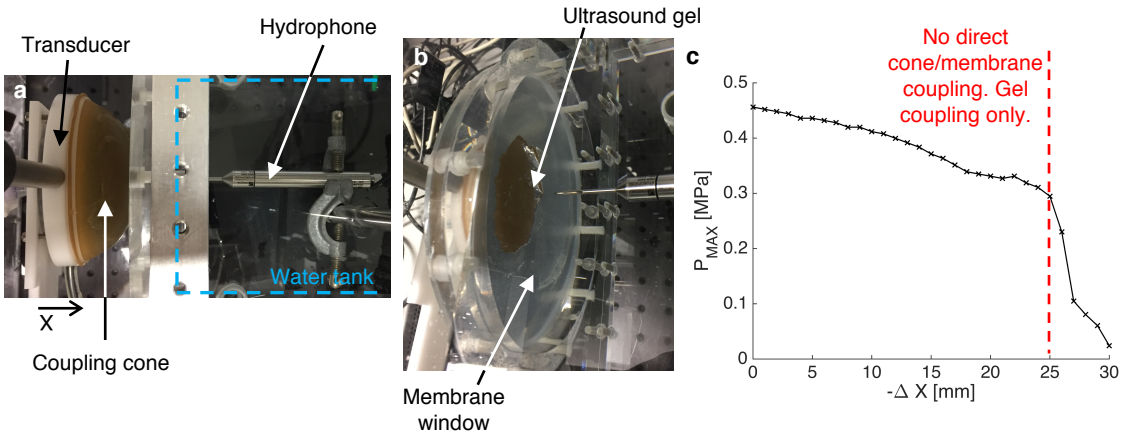


Fig. 5.2: H107 expandable membrane coupling cone contact test. a, b Images of the experimental setup: the expanded coupling cone, filled with degassed water, was connected to a water tank via a membrane window with ultrasound gel applied between the two surfaces. Both the transducer and needle hydrophone were attached to positioning stages. Starting with the coupling cone strongly coupled to the membrane (**b**), both the transducer and hydrophone were moved in unison in the negative X, axial direction reducing the coupling to the tank, in steps of 1 mm. **c** Maximum pressure (p_{MAX}) as a function of distance (ΔX). The red dashed line indicates where there was no direct coupling between the two surfaces with a connection made only through the ultrasound gel. The freefield pressure was 0.5 MPa

cone was then simply adjusted according to the volume of water injected allowing it to be easily modified for varying depth brain targets without the need to change cones.

To test the effect of contact surface area between the cone and scalp on the transmitted pressure amplitudes, an experiment was conducted using a water tank with a membrane window allowing the coupling cone to be connected externally with a hydrophone (HNA needle hydrophone, 400 µm, ONDA, Sunnyvale, CA, US) positioned inside the tank at the US focus as shown in Fig. 5.2a, b. US gel was applied between the cone and tank membranes. Both the transducer and hydrophone were connected to positioning systems allowing them to be moved together axially in steps of 1 mm, starting with the cone pressed tightly up to the tank window and then reducing the coupling surface area. The focal pressures are displayed in Fig. 5.2c. For maximum coupling ($\Delta X = 0$), a drop in pressure amplitude of 10 % is observed relative to freefield although the exact loss contribution of the two membranes and the coupling is undifferentiable. An approximately linear decline in amplitude is

observed from this point until there was no direct contact between the two membranes with only gel connecting the two, where a large drop in magnitude occurred. At this location, indicated by the red dashed line, the pressure dropped by 33 % in comparison to the maximum contact measurement. Consequently, whilst the H-107 calibration in Sec. 2.4.3 was conducted with the coupling cone attached accounting for the membrane losses, the in situ pressure fields will be contact-dependent with a reduction in amplitude of up to 40 %. However, these coupling consequences or any additional losses as a result of hair or trapped air bubbles in the acoustic path were not considered in the determination of source amplitudes as per Sec. 5.2.4. As such, these losses act as an additional safety buffer.

5.2.4 Subject-specific modelling

Both acoustic and thermal participant-specific modelling was carried out to determine appropriate source locations and amplitudes in order to focus to the intended targets as well as satisfy the safety constraints outlined in the previous section. Tissue maps and brain coordinates for each subject were obtained from MRI scans as described in Sec. 5.2.2. Segmentation of the T1-weighted scans was carried out using the MARS (Morphologically and Anatomically accuRate Segmentation) toolbox (Huang and Parra, 2015) to assign the following tissue types: scalp tissue, skull bone, CSF, white and grey matter. Acoustic properties were designated according to Table 5.1. Coupling of the source to the scalp was assumed to be perfect and hence the head was modelled as immersed in water. The lateral resolution of the MRI scans was 0.5 mm and so k-Wave simulations in this section were performed at the same grid spacing (5.95 PPW in water).

To determine the optimal transducer placement for each target, the same computational framework as detailed in Sec. 3.2.3 was employed with the inclusion of the soft tissues. This is illustrated in Fig. 5.3 and is briefly recapped here:

		Acoustic		Thermal	
Material	Density, ρ_0 [kg/m^3]	Sound speed, c_0 [m/s]	Attenuation, α [dB/cm]	Thermal conductivity, κ [W/(m K)]	Specific heat capacity, c_p [J/(kg K)]
Water[1]	1000	1488	0	0.6	4178
Scalp[2,3]	1000	1500	0.15	0.528	3600
Skull[1,4]	1732	2820	3.28	0.32	1313
CSF[1]	1007	1504.5	0.004	0.57	4096
White matter[1]	1041	1552.5	0.29	0.48	3583
Grey matter[1]	1045	1500	0.05	0.55	3696

Table 5.1: Acoustic and thermal properties of different tissue types. Compressional acoustic properties only. Attenuation values calculated for a frequency of 500 kHz based on the relevant power-law exponent, n in $\alpha = \alpha_0 f^n$. [1]Hasgall et al. (2018), [2]Duck (2007), [3]Constans et al. (2018), [4]Treeby and Cox (2014).

a T1-weighted structural and functional localiser MRI scans are performed.

b Tissue types are segmented from the structural MRI scan using the MARS toolbox. Target brain sites are defined as the peak activation sites from fMRI localiser maps.

c Acoustic waves from a numerical point source located at the target site are propagated out through the skull to a spherical surface which corresponds to a sphere of radius equal to the focal length of the transducer. This spherical surface therefore represents the set of all possible transducer locations to refocus to the target location.

d The steady state phase distribution is extracted over the spherical surface. Multiple transducer locations are then selected based on visual inspection of the phase field.

e The forward simulation for each transducer location was computed and the in situ pressure fields and amplitudes assessed to determine the optimal transducer location for each target. Locations that produced tighter focal spots and higher pressure amplitudes at the target were selected. Targets were defined as 2 mm radius spheres around the site of peak activation.

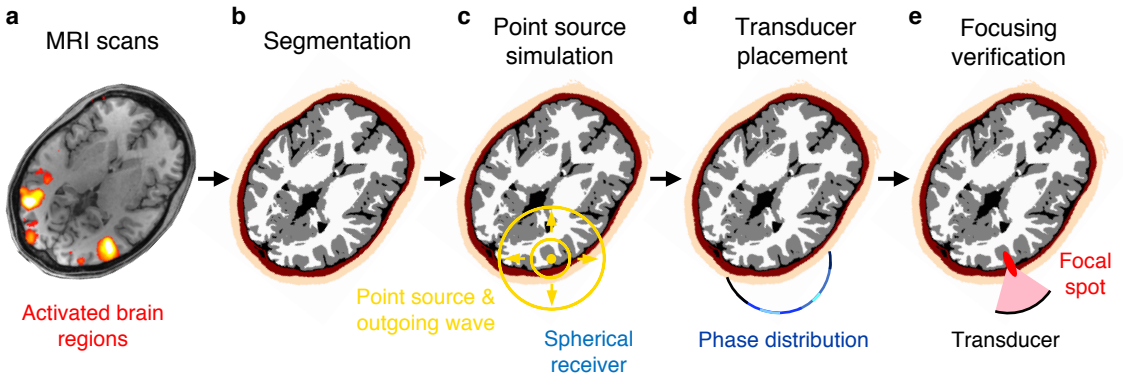


Fig. 5.3: Proposed modelling pipeline for determining single-element transducer position for human pilot study. **a** T1-weighted structural scan and fMRI localiser to determine activated brain regions. **b** Segmentation of structural information into tissue types, and extraction of peak activation brain site. **c** Acoustic point source placed at target location (location of peak brain activation) and wave propagated outwards through the skull to a spherical receiver of radius equal to the focal length of the transducer, corresponding to the set of all possible transducer positions to refocus to the target site. **d** The steady state phase distribution is extracted on this surface informing the manual selection of transducer placement. Multiple locations were selected. **e** The resultant in situ pressure fields for each transducer location were compared in order to determine the optimal source position.

Once the optimal transducer location was selected for each target, the function generator voltage required to achieve 0.6 MPa in the brain was determined from the calibrations in Sec. 2.4.3, and the amplifier gain.

An additional sham brain site for MT was defined 15–20 mm laterally and posteriorly at a similar cortical depth in the same transverse plane. The optimal transducer location was determined following the same modelling protocol in Fig. 5.3, after which the −12 dB acoustic field was overlaid with the fMRI brain activation map to ensure there was no overlap between the pressure field for MT sham and the activated MT brain region. If there was overlap, the location was shifted further from the real MT site and the process repeated. The source amplitude was scaled to match the target pressure for the real MT location.

Finally, thermal simulations were performed using the resultant pressure fields, scaled to a maximum of 0.6 MPa inside the brain to determine the input heating rate, q. Tissue specific properties were defined as given in Table 5.1 and blood perfusion properties defined in Eq. (2.28) were defined as: $w = 0.008/\mathrm{s}$, $\rho_b = 1030\,\mathrm{kg/m^2}$,

$c_{p,b} = 3620\,\mathrm{J/(kg\,K)}$, and $T_a = 37\,^{\circ}\mathrm{C}$ (Constans et al., 2018; Pulkkinen et al., 2011). It is noted that the absorption values in Eq. (2.28) were entered as the attenuation values from Table 5.1. However, for skull bone the majority of the attenuation may actually be due to reflection, scattering and mode conversion rather than absorption (Pinton et al., 2012a) and thus the predicted temperature rises calculated here are likely overestimated. The specifics of the timings for the thermal simulations are discussed in Sec. 5.3.1.

5.2.5 Electroencephalography (EEG)

EEG data were acquired using the BrainProducts 64-electrode EasyCap system in conjunction with a BrainAmp amplifier (BrainProducts GmbH, Gilching, Germany). The electrodes were Ag/AgCl sintered ring electrodes of which 8 were removed (Oz, O2, PO4, PO8, P6, P8, TP8, TP10) and a hole cut in the cap in order to allow room for the transducer to be coupled. A sampling rate of 500 Hz allowed EEG signals in the frequency range 0.1–250 Hz to be recorded within an amplitude range of $\pm 16.384\,\mathrm{mV}$.

Pre-processing of the EEG recordings was performed as follows: trials with eye movement artefacts were removed, signals were divided into 2.5 s epochs starting 1 s before stimulation onset and then low-pass filtered at 30 Hz using a Butterworth filter. Finally, signals were baseline corrected using the first 500 ms of each epoch.

5.2.6 Stereotactic neuronavigation

Alignment of the US transducer to correctly focus to the intended target was achieved using a neuronavigational system (BrainSight, Rogue Resolutions, Montreal, Canada). Optical trackers were fitted to the participant via a set of glasses and fixed to the transducer allowing real-time tracking via triangulation of three reflective silver globes. Individual subject scans were registered to the participant

using anatomical points (the nasion, left and right pre-auricular and, where possible, the tip of the nose). Transducer locations were entered as the centre point of the back of the transducer but a modified calibration mount applied the required focal offset to track the focal point. This point, along with the required trajectory of the transducer, were then used to align the source with respect to the subject. During the tasks, the participant rested on a chin support to minimise head movements although given the length of the tasks, some movement was unavoidable. Therefore, an observer adjusted the transducer position in real-time to correct for any small movements that did occur based on the tracking information from the neuronavigation readout as shown in Fig. 5.4.

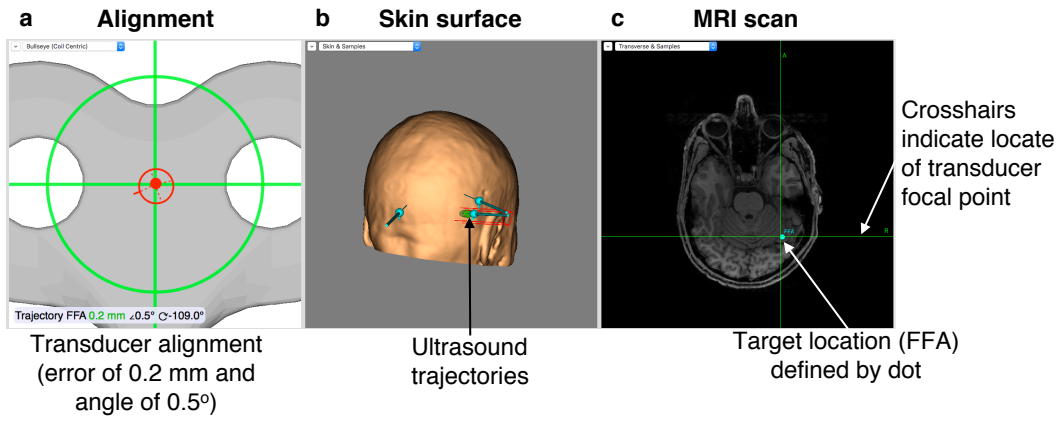


Fig. 5.4: BrainSight neuronavigation system. **a** Alignment window: translational and rotational errors displayed. Alignment achieved by matching target (red dot) and transducer focus (green crosshairs) along with correct trajectory (indicated by red circle). **b** Skin surface reconstruction: 3D visualisation with the required transducer trajectories overlaid. **c** Position of US focus (green crosshairs) overlaid on to structural MRI scan. Target location denoted by blue circle.

5.2.7 Combined setup

The integrated setup of the US, EEG and tracking system is shown in Fig. 5.5. Subjects were seated in an office chair at a desk with a monitor for displaying the behavioural tasks located 50 cm from the head which was supported by a chin rest. The transducer itself was attached to a computer monitor arm (M2 monitor arm, Humanscale, CO, USA) which was mounted on to a vertical jack and a lateral

positioning stage. The whole unit was then bolted to a moveable trolley in order to allow movement in as many degrees of freedom as possible.

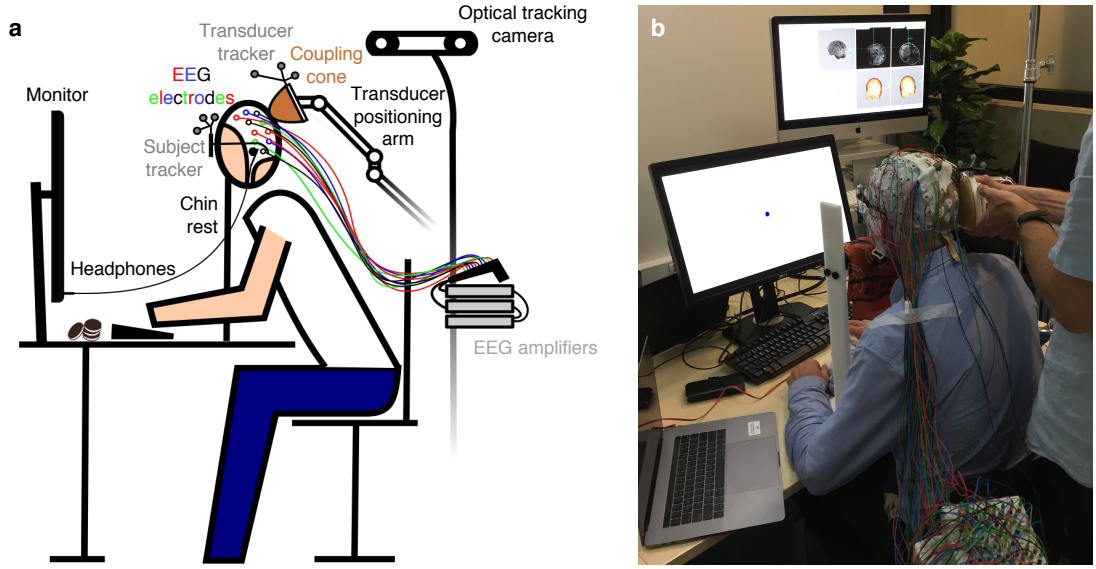


Fig. 5.5: Human pilot study experimental setup a. Schematic. **b** Image. The participant is seated at a desk at a specified distance of 50 cm from the monitor display where the behavioural tasks are displayed. Responses are logged via the right/left arrows keys on the keyboard. A 64-electrode EEG cap, with a cut-out over the posterior right hemisphere for transducer coupling, is fitted to the head. Alignment of the transducer is achieved through the BrainSight neuronavigational system which uses an infrared camera to track both the subject and the transducer. Brain targets are added to the structural MRI scan and this is registered to the subject via selection of anatomical points (the nasion, right pre-auricular, left pre-auricular and where possible, the tip of the nose) using a pointer. The position of the trackers and pointer is determined via triangulation of three reflective silver globes. Attachment of these reflectors is through direct fixation to the transducer cone base and on a set of glasses for the participant. The transducer coupling cone is made from a polyurethane membrane and thus can be expanded through the addition of degassed water to adjust its depth. Ultrasound gel is applied to the hair to couple the cone to the scalp.

A schematic of the signal paths is given in Fig. 5.6. Triggering of the US stimulation was achieved using the USB oscilloscope which sent timestamps using a digital output to a spare EEG channel in order to denote when each trial began. The output voltage of the amplifier was also fed back into the oscilloscope via an attenuation probe and the amplitudes checked for each target in each participant prior to the start of the session. During the tasks, the output voltages were constantly monitored with the system set to automatically exit if the values exceeded the limit set at 10 % above the required value.

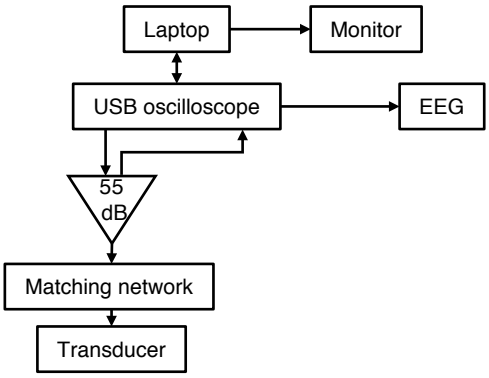


Fig. 5.6: Signal paths for human pilot study. A laptop running MATLAB controlled the timings and displayed the tasks on a monitor for the participant to see. The laptop controlled the output of the USB oscilloscope which triggered the transducer via a 55 dB amplifier and a matching network and sent a digital pulse to a spare EEG channel. Amplifier voltages were also fed back through the oscilloscope.

5.2.8 Behavioural tasks

Behavioural tasks were all designed in MATLAB, using the Psychophysics Toolbox extensions (Brainard, 1997; Kleiner et al., 2007).

Stimulation detection

Stimulation detection was performed at each target location to determine if a participant could correctly identify when US stimulation was delivered. For V1 this was done with and without the audio mask but for the subsequent MT and FFA locations, only with the mask. Each stimulation detection block comprised 100 trials, of which 50 were accompanied by US stimulation in a randomised sequence. For each trial, the participant fixated on a white cross in the centre of the screen and was instructed to indicate whether they thought they had been stimulated during a response period 0.5–1.4 s after the cessation of stimulation.

There was no behavioural task at V1. Participants were simply asked whether they perceived any visual, or other sensory, sensations during the stimulation detection tasks.

MT

For MT, the behavioural task centred around identifying the overall global direction of a cloud of moving dots, either to the left or to the right. Whilst for 100 % of the dots moving in the same direction the answer is trivial, the task is complicated by reducing the number of dots moving in a coherent manner with the others moving stochastically. An initial block of the task was conducted without any US stimulation, first to familiarise the participant with the task with feedback given and then to determine their threshold, without feedback, using the Psychtoolbox Quest functions. The threshold was defined as the minimum percentage of coherently moving dots in order to attain a 70 % success rate. As MT is thought to be lateralised, stimuli (dots) were presented to either the left or right visual fields with the participant instructed to retain their attention on the central fixation cross. Consequently, independent thresholds for the left and right visual fields were obtained.

The timings of each trial are indicated in Fig. 5.7a and were as follows: a 1.5–2.5 s fixation period, 0.3 s stimulus presentation to either the left or right visual field, a further 0.5–1.4 s fixation interval and a response period of 0.7–1.2 s. If US stimulation was applied, the 300 ms burst coincided exactly with the stimulus presentation. The audio mask started ∼110 ms before the stimulus onset and lasted for 0.7 s. The reason for variable length fixation periods was to reduce expectancy effects and associated preparation brain activity.

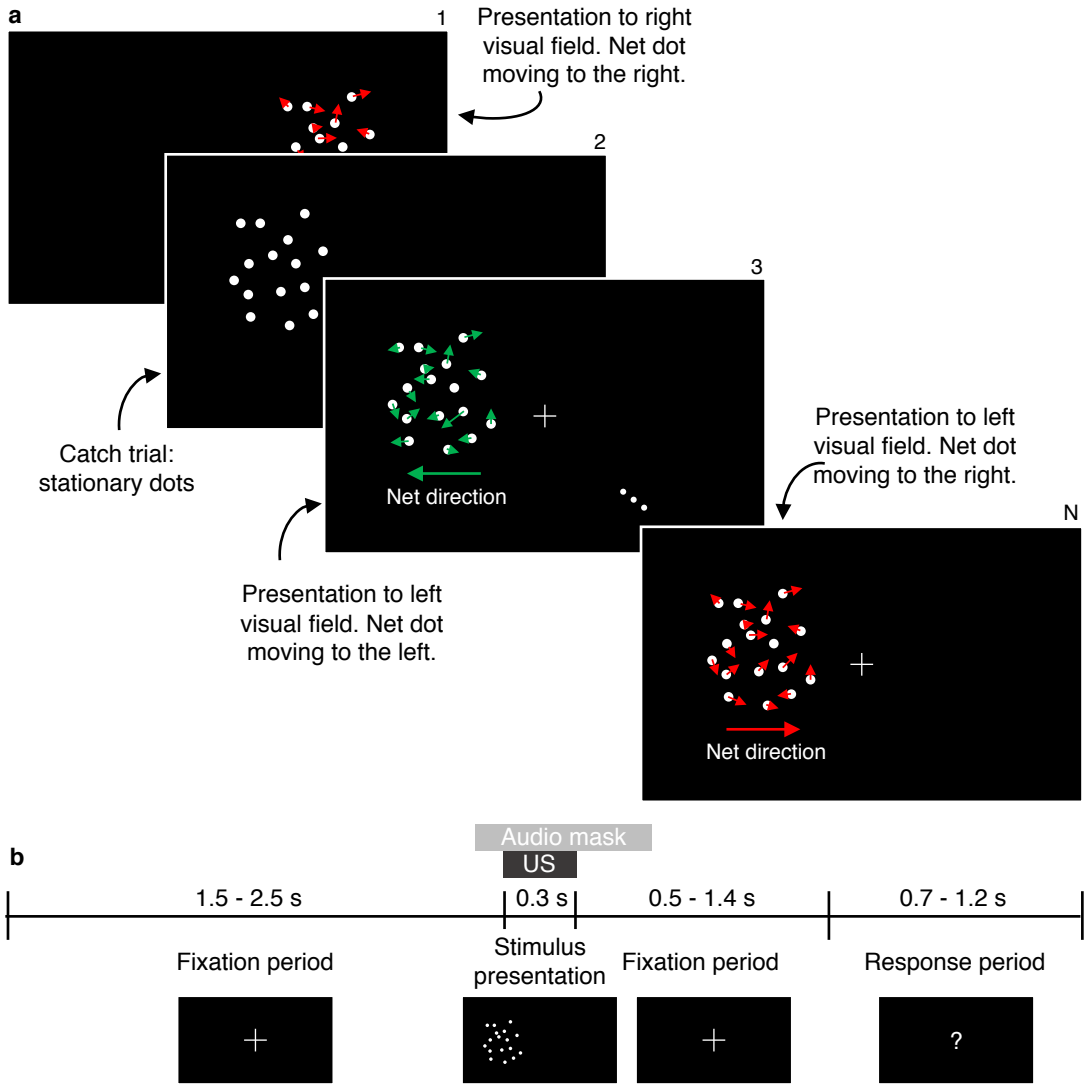


Fig. 5.7: MT dots behavioural task. a Moving dots were presented to either the left or right visual field while the participant fixated on a central cross. Participants were asked to indicate whether they perceived the dots to be moving to the left or to the right. The percentage of coherently moving dots was varied ± 4 standard deviations either side of their threshold (as previously determined using the Psychtoolbox Quest functions). Catch trials consisting of stationary dots were also randomly presented requiring the subject to respond with a different key in order to measure attentiveness. **b** Timing sequence: 1.5–2.5 s fixation period, 0.3 s stimulus presentation to either the left or right visual field, a further 0.5–1.4 s fixation interval and a response period of 0.7–1.2 s. If US was delivered, the 0.3 s burst coincided exactly with stimulus presentation. The audio mask started ~110 ms before the stimulus onset and lasted for 0.7 s.

The task in conjunction with randomised US stimulation was then conducted for a total of 200 stimulation and 200 no stimulation trials. 40 catch trials (without stimulation) were also randomly inserted where stationary dots were displayed requiring the participant to respond with a different key in order to monitor the attentiveness

and alertness of the subjects over the duration of the task. The difficulty of the task was varied for each trial but was always set to be within four standard deviations of the mean (threshold) in order to be in the most sensitive range such that any effect of stimulation would have the highest change of manifesting in a behavioural change. The total running time of the task took approximately 40 min to run but it was split into 4 blocks to allow short breaks in between each segment.

The same protocol (minus the thresholding) was also conducted for the sham MT site. Whether MT real or MT sham was tested first was varied for each participant and thus counterbalanced across the whole group. If FFA could be targeted, this was completed in between the two sets of the dots task.

FFA

For FFA, the behavioural task involved facial processing. Participants were initially given some time to gain familiarity with two faces, Sarah and Jane, as shown in Fig. 5.8. The names corresponding to each face were swapped for each subject. The faces were then morphed with another face (neither Sarah nor Jane) to different degrees and the participant required to determine whether the face most resembled Sarah or Jane. A similar block of Quest thresholding was again run as described in the previous section although, as the stimulus (face) presentation was centralised, individual left/right visual field thresholds were not determined. The task combined with US stimulation followed an identical layout to the MT tasks except catch trials comprised a pixelated face rather than stationary dots. The timings and number of trials were the same but there was no sham site for FFA.

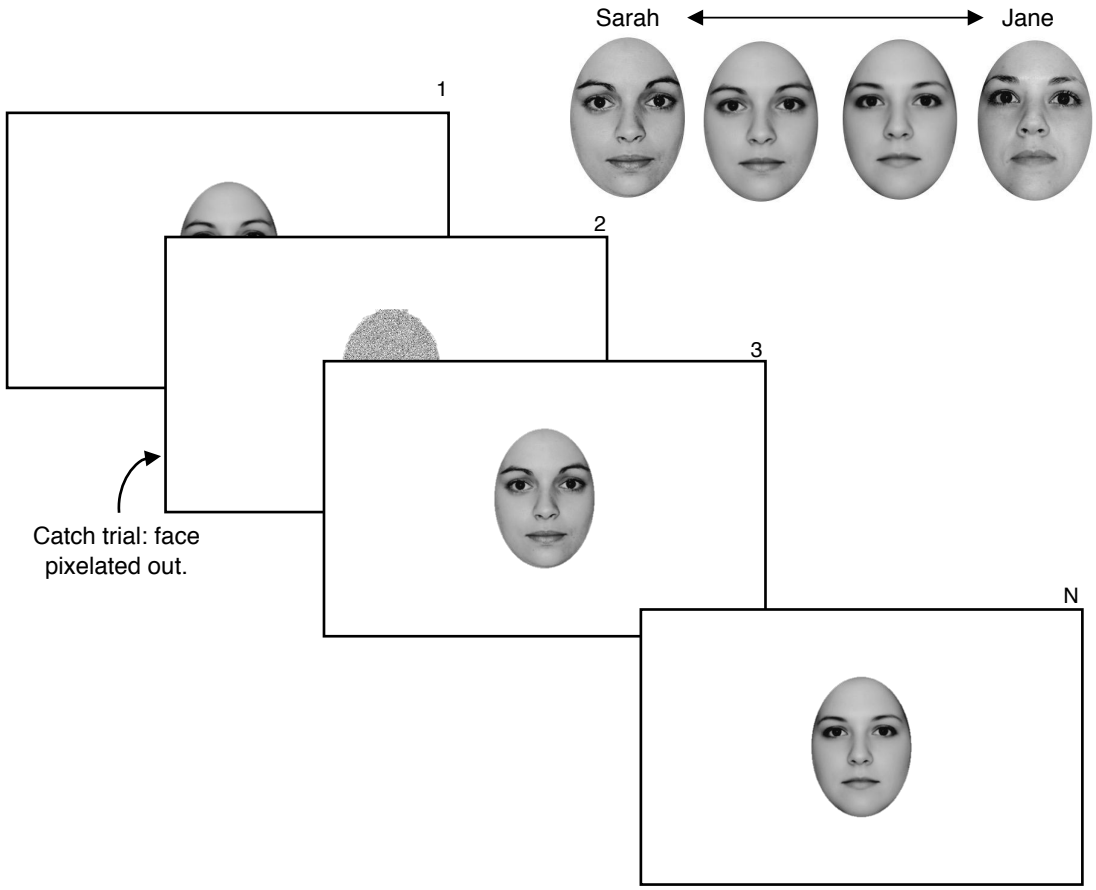


Fig. 5.8: FFA faces behavioural task. Morphed faces were presented centrally. Participants were asked to indicate whether the face most resembled Sarah or Jane. The degree to which faces were merged was varied ±4 standard deviations either side of their threshold as previously determined using the Psychtoolbox Quest functions. Catch trials consisting of a pixelated face were also randomly presented requiring the subject to respond with a different key in order to measure attentiveness.

5.3 Results

5.3.1 Predicted acoustic and thermal fields

The estimated pressures and temperature rises at the target site (defined as a 2 mm radius sphere around the peak activation location) are shown for each participant in Table 5.2. In each case, the maximum pressure inside the skull (anywhere in the CSF, white or grey matter) was limited to 0.6 MPa. The pressures were reduced for V1 in participants 4 and 18 in order to ensure the maximum thermal rise in the skull was less than 3 °C and so for these cases the maximum brain pressure was less

than 0.6 MPa. For real and sham MT, the target pressures were matched and thus some reductions in the maximum pressure for one of the targets was also necessary.

The amplitudes followed a similar trend to those measured inside the the ex vivo skull presented in Chapter 3, with the highest pressures achieved at V1, then MT and finally FFA. In general, ellipsoidal focal contours around the target where observed for V1 and both of the MT sites. Targeting of MT sham was typically slightly improved compared to MT real as it was located more posteriorly where the skull bone is more uniform. Consequently, in the majority of cases, the source amplitude was reduced for MT sham from the maximum allowable, based on the 0.6 MPa limit, in order to match the MT real target pressure. There were some exceptions to this where the reverse was true: the amplitude of MT real was reduced to match MT sham.

Targeting of FFA was much more difficult and the field often fragmented, as was also shown in Chapter 3, with the main hotspot steered away from the intended site. Therefore, the FFA task was only conducted if a reasonable pressure amplitude was delivered to the target. Practical reasons also prevented FFA from being ultrasonically accessible: for example, an acoustic path that collided with the pinna of the ear. This was especially the case for subjects with FFA anatomical locations further forward in the brain. Consequently, 10 out of the 21 participants tested did not undergo FFA stimulation as indicated by dashes in Table 5.2.

The thermal simulations for each subject were computed assuming an ISI of 2.4 s in between the presentation of each 300 ms stimulus, with US applied every other trial for a total of 200 trials (100 US stimulations). In reality, the duration of each trial was longer, 3–5.4 s, in accordance with the timings described in Sec. 5.2.8, and so the predicted thermal fields are likely an overestimate. Trials featuring US stimulation were also randomised rather than periodic as assumed here. An example of the

Participant ID	P_{V1} [MPa]	P_{MT} [MPa]	P_{FFA} [MPa]	ΔT_{V1} [°C]	$\Delta T_{MT\ (Real)}$ [°C]	$\Delta T_{MT\ (Sham)}$ [°C]	ΔT_{FFA} [°C]
1	0.50	0.47	0.30	0.12	0.17	0.11	0.01
2	0.57	0.30	0.22	0.10	0.04	0.07	0.00
3	0.32	0.29	0.34	0.06	0.02	0.11	0.01
4	0.36	0.44	-	0.08	0.04	0.05	-
5	0.34	0.52	0.25	0.10	0.03	0.07	0.02
6	0.41	0.28	0.24	0.11	0.03	0.07	0.01
7	0.59	0.24	0.19	0.07	0.02	0.01	0.01
8	0.30	0.34	-	0.02	0.08	0.05	-
9	0.44	0.42	0.6	0.08	0.03	0.02	0.02
10	0.59	0.42	-	0.11	0.02	0.03	-
11	0.51	0.49	0.42	0.01	0.02	0.06	0.02
12	0.60	0.51	-	0.01	0.03	0.04	-
13	0.58	0.51	0.41	0.11	0.03	0.04	0.02
14	0.47	0.57	0.39	0.12	0.18	0.16	0.02
15	0.54	0.52	-	0.09	0.04	0.04	-
17	0.57	0.54	-	0.13	0.15	0.05	-
18	0.50	0.48	-	0.15	0.03	0.01	-
19	0.60	0.58	-	0.08	0.04	0.04	-
20	0.45	0.45	0.36	0.02	0.05	0.03	0.01
21	0.41	0.60	-	0.02	0.08	0.08	-
22	0.41	0.43	-	0.06	0.03	0.05	-
Mean	0.48	0.45	0.34	0.08	0.06	0.06	0.01
Standard deviation	0.10	0.10	0.12	0.04	0.05	0.04	0.01

Table 5.2: Predicted pressure amplitudes and temperature elevations at the target sites. Data shown for each target for each participant along with the mean and standard deviations. Dashes indicate that the target was not stimulated.

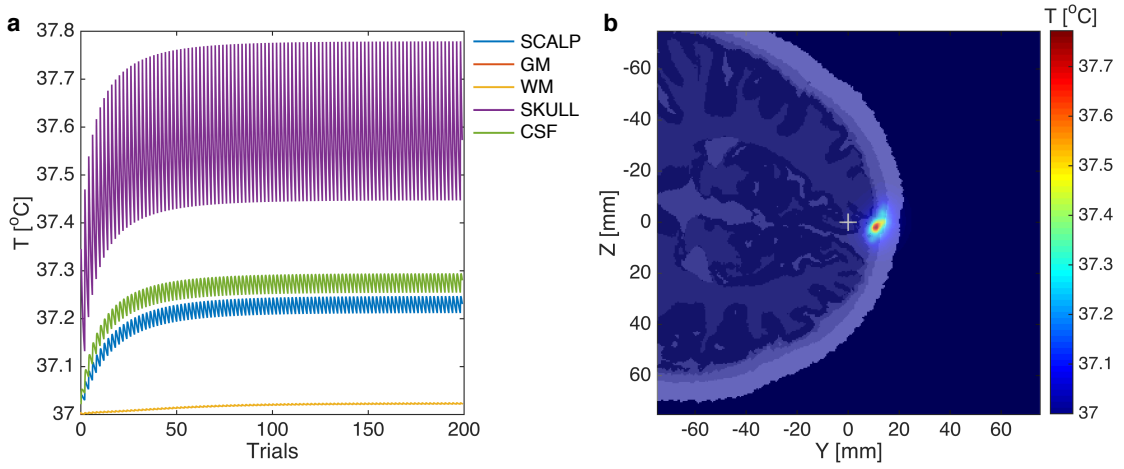


Fig. 5.9: Thermal simulation modelling at V1. **a** Thermal evolution over time as a function of trial number. Each trial was simulated as lasting for 2.7 s with a 300 ms US burst applied every other trial. The maximum temperature evolution in each tissue type is plotted (WM = white matter, GM = grey matter). N.B. The WM and GM curves are identical. **b** Maximum steady state spatial temperature field in the transverse plane through the target centre, indicated by the white cross, overlaid on to the segmented tissue map.

thermal modelling is illustrated in Fig. 5.9 showing the temperature evolution as a function of number of trials for the site of maximal heating in each tissue type. The final steady state temperature field, which had been established at approximately 100 trials (50 US bursts), is displayed in Fig. 5.9b with the main hotspot occurring in the skull bone layer.

For the temperature elevations in Table 5.2 MT real and MT sham are included as separate columns as although the target pressures matched, differences in anatomical and acoustic field topology led to differing thermal fields. The maximum target temperature rise across all subjects was 0.18 °C with higher temperatures observed for V1, consistent with higher pressures and increased proximity to the skull bone, and the lowest for FFA, agreeing with the lesser pressure amplitudes further from the skull interface. The maximal thermal elevations in the skull bone were typically 1–2 °C with a maximum across all subjects of 2.71 °C. The shape of the hotspots in the bone tended to be tighter for V1 and more diffuse for FFA roughly corresponding to the lateral spread of the incident radiation cone which differed for the two locations due to the increased depth for FFA. However, despite these general tendencies,

strong local differences in both the morphology and amplitudes of the thermal fields were evident for each subject.

5.3.2 Phosphene perception

Following the stimulation detection tasks conducted at V1, participants were asked to report any sensations they experienced. In general, apart from the induced sound (discussed in Sec. 5.3.3), only a few other sensations in a small subset of individuals were identified: some tingling in the back and legs and some blurred vision. However, this was not time-locked to the US stimulation and more likely a consequence of simply staring at a monitor for a long time. The only semi-convincing report of a phosphene was in one individual who perceived intermittent dots and ripples in the left visual field which made intuitive sense given that the stimulation was applied to the right hemisphere although the sensations were sporadic and inconsistent.

5.3.3 Auditory effects

Without audio masking through a set of earphones, all participants heard a sound as a result of the US stimulation. However, the directionality of the sound varied between participants and was not always perceived to emanate from the location of the US transducer. This was not audible to other observers in the room although some sporadic chirping sounds were noticed emanating from the back of the transducer possibly due to gas bubbles trapped in the back of the coupling cone.

In order to mask the tone associated with US stimulation, a 1 kHz square wave tone was generated in MATLAB and played through a set of earphones for 700 ms commencing ∼110 ms before stimulus presentation. The stimulation detection task was performed both with and without the mask. The results in terms of hit rate (the ratio of correctly identified stimulation trials to incorrectly identified) is presented in Fig. 5.10. A statistically significant reduction in the subject's ability to distinguish

stimulation trials was observed when the mask was applied from 0.77 ± 0.07 (mean $\pm$ SEM) to 0.46 ± 0.07 which is close to chance (paired t-test, $t(16) = 3.364, p = 0.004$).

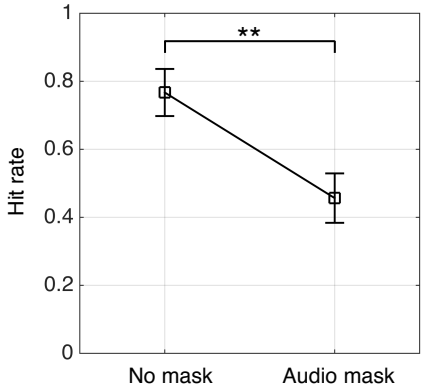


Fig. 5.10: V1 stimulation detection responses. Mean $\pm$ standard error of the mean (SEM) hit rates with and without audio masking through a set of earphones. The audio mask produced a significant decrease in the participant's ability to differentiate between stimulation and no stimulation trials (paired t-test, $t(16) = 3.364, p = 0.004$).

Despite effectively masking the US tone for the majority of subjects, 3 participants were still able to distinguish between trials with and without US even with the mask employed. They described the US as an additional slightly higher pitched tone during the longer audio masking sound although it was generally a subtle difference only evident when specifically listening for it.

EEG recordings confirmed strong auditory activation. The grand average across all participants $\pm$ SEM for the unmasked, and masked, with and without US stimulation, conditions are displayed in Fig. 5.11a. The signals were averaged over 9 central electrodes as indicated in Fig. 5.11b. The timings of the US burst and audio mask are denoted by the black and grey bars, respectively. For the unmasked condition, an auditory event-related potential (ERP) was observed shortly after the onset of the US burst. Subsequent masking shifted this ERP earlier, coinciding with the start of the audio tone, $\sim$110 ms prior to the start of the US, with increased magnitudes of both the main positive and negative components with respect to the unmasked ERP. No differences were observed between the grand-averaged masked

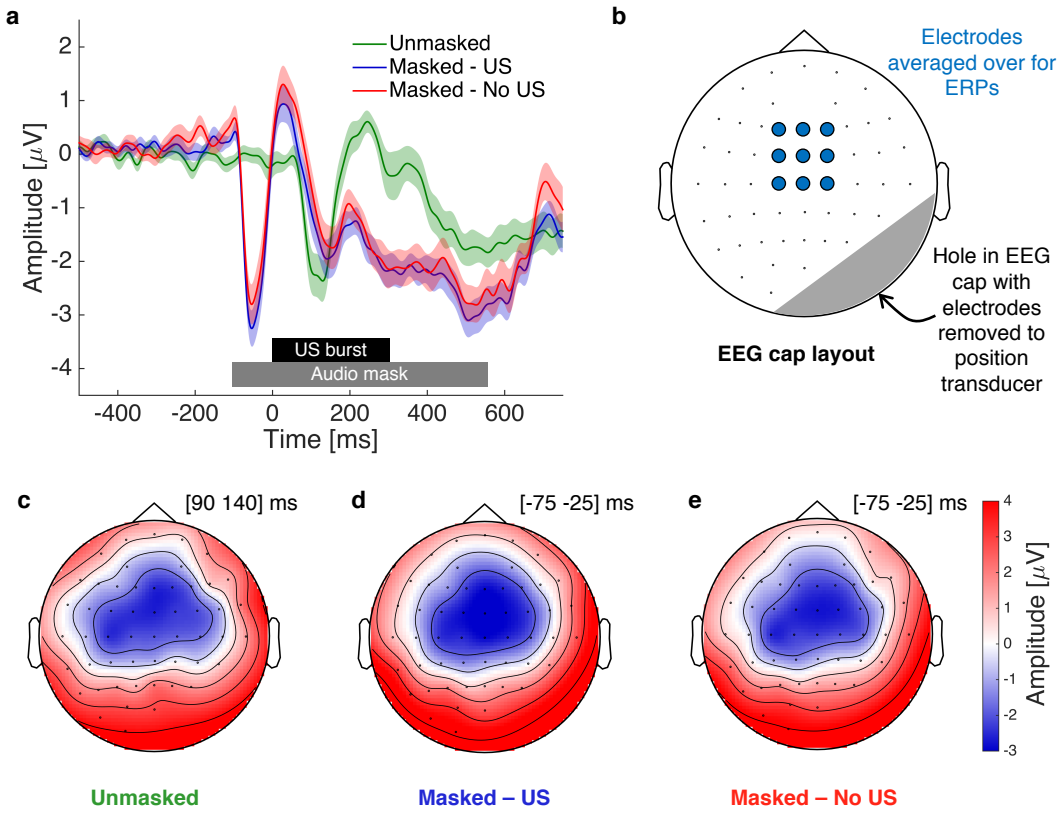


Fig. 5.11: Induced auditory event-related potentials (ERPs) and the effect of auditory masking. **a** Grand average ± standard error of the mean EEG traces over 9 central electrodes (F1, Fz, F2, FC1, FCz, FC2, C1, Cz and C2). Traces are shown for unmasked US stimulation and for auditory masking with and without US stimulation. The timings of the 300 ms US burst and 700 ms audio mask are indicated by the black and grey bars. **b** EEG cap layout with the region of removed electrodes to couple the transducer indicated in grey. The electrodes over which the ERPs were averaged in **a** are highlighted in blue. **c, d, e** Topographic distributions over all electrodes for each condition; the averaged potential over the specified time windows in ms, corresponding to the main negative ERP component, are displayed.

ERPs generated with and without US stimulation. To confirm the spatial origin of the ERPs, topographic maps over the entire EEG cap for each condition are shown in Fig. 5.11c–e corresponding to the averaged potential over the designated 50 ms time windows for the main negative ERP component. Aside from some small differences in amplitude, the maps show strong agreement between all 3 groups further affirming the strong auditory activation as a result of coupled bursts of US.

ex vivo skull recordings

To investigate the mechanism through which US results in auditory activation, further experiments were carried out using the same ex vivo human skull used to obtain hydrophone measurements in Chapter 3. In this instance, the transducer was connected to the skull via a coupling cone and US gel outside of the tank and a small piezo speaker (SPS-2220-03, Sonitron, Sint-Niklass, Belgium) with a bandwidth of 700 Hz to 20 kHz coupled to the skull close to the ear would have been located (Fig. 5.12a). All incident US bursts were 300 ms in length at a 50 % BDC and a PRF of 500 Hz (note this is different to the 1000 Hz PRF rate used in the human behavioural study) except in Fig. 5.12g where the PRF was increased in steps of 250 Hz up to 10 kHz.

The recorded frequency power spectra in dB for US bursts with the cone uncoupled, coupled and pushed into firmer contact with the skull are shown in Fig. 5.12b. Peaks at 500 Hz, 1500 Hz and 2500 Hz are present only when the transducer is coupled to the skull, consistent with the FT of a 500 Hz square providing indirect evidence of a flexural wave propagating through the skull. Close ups over each of these harmonics are displayed in Fig. 5.12c–e. Interestingly, the peaks are split in two at each harmonic approximately 10 Hz either side of the nominal frequency. To date, an explanation for this phenomena has not been elucidated. It is also noted that there was a strong peak at 1090 Hz, the origin of which is not clear; however, it was present for all conditions and so not deemed to be the product of wave transmission through the skull.

Although there is little difference between the power spectra for the two couplings with and without added contact pressure applied, for ipsilateral versus contralateral receiver positions, the amplitudes did differ suggesting that skull topology may be important in the transmission of the flexural wave. This may explain why subjects

reported the origin of the sound to be from different directions.

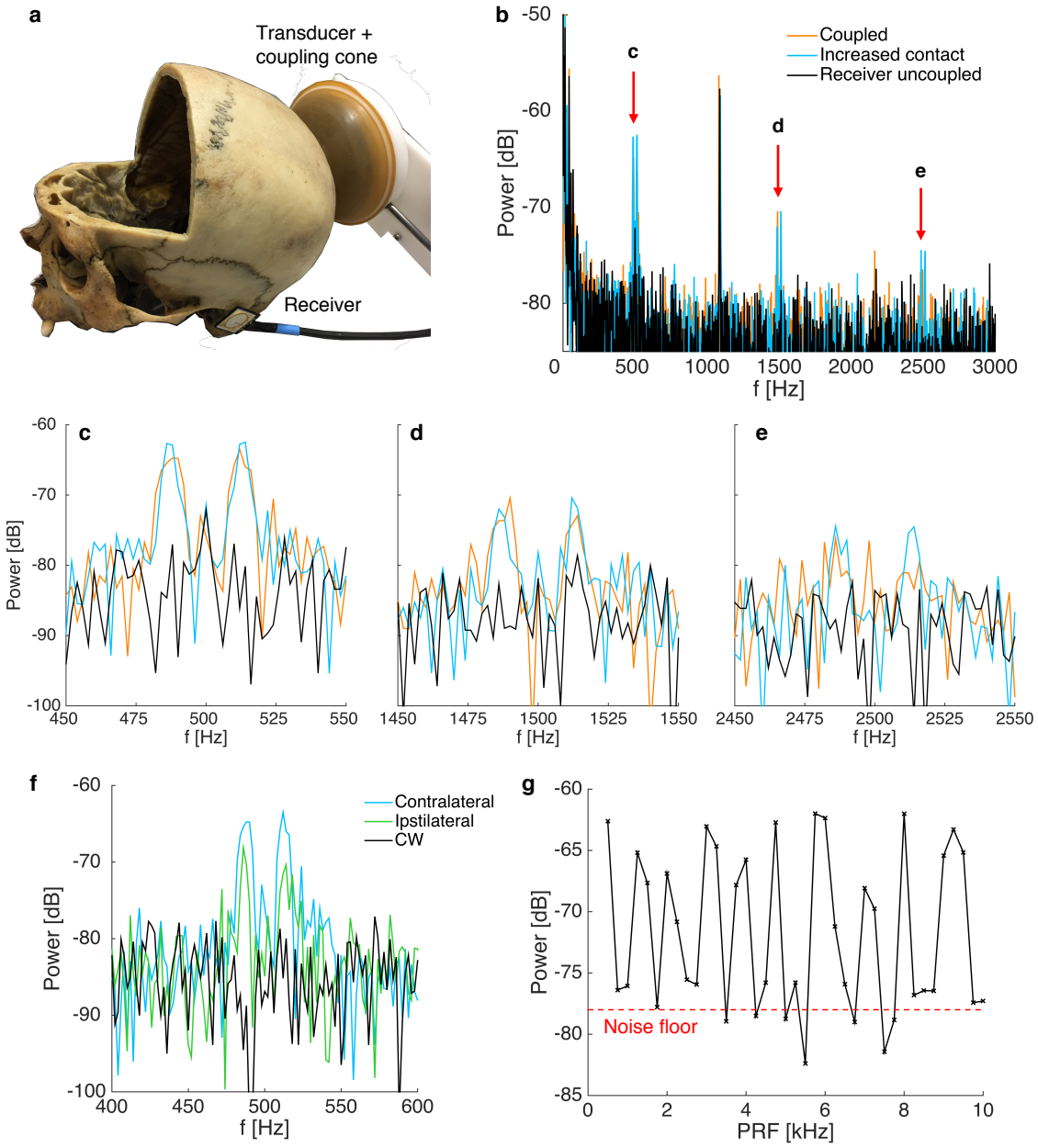


Fig. 5.12: ex vivo skull auditory recordings. **a** Image of setup: coupling cone and ultrasound (US) gel used to couple transducer to skull with receiver placed near the ear on the contralateral side. **b** Power spectra for the received waveform with the transducer uncoupled, coupled, and with increased coupling contact achieved by pushing the transducer on to the skull when sonicated. US waveform was a 300 ms burst at a 50 % duty cycle and 500 Hz pulse repetition frequency (PRF). **c, d, e** Close ups at 500 Hz, 1500 Hz and 2500 Hz as indicated by the red arrows in **b**. **f** Effect of receiver position located contralateral or ipsilateral with respect to the transducer and the spectra from a continuous wave 300 ms US pulse. **g** Effect of PRF on power spectra amplitudes. Maximum power in a 40 Hz window around the nominal PRF displayed as the PRF was swept from 500 Hz to 10 kHz in steps of 250 Hz. Amplitude of the noise floor indicated by the red dashed line.

The amplitude of the modulation signal was measured as a function of PRF and the data (maximum amplitude over a 40 Hz window around the nominal PRF) is shown in Fig. 5.12g. It can be seen that the amplitudes vary substantially implying that adjustment of the PRF may reduce the amplitude of the induced wave, possibly dependent on the resonant modes of the skull structure. A minimum occurred at 1 kHz which matched the preliminary finding from the pilot study that the induced tone was less obvious to participants at this frequency than at 500 Hz hence why the behavioural study was conducted at this PRF rate. However, it is possible that the amplitudes at different PRFs are both skull and location specific.

5.3.4 Behaviour

Behavioural data for the MT dots task is depicted in Fig. 5.13 for the MT real, MT sham and combined targets. 2 participants had to be removed due to excessive eye movements as detected by EEG. The mean and SEM across all participants is plotted on top of each individual's data points. A repeated measures ANOVA between target, visual field and stimulation conditions revealed a significant interaction between stimulation and visual field independent of the target location ($F(1, 18) = 4.948, p = 0.039$). A paired samples t-test showed that this was only significant for the right visual field when the targets were combined with US serving to impair a participant's performance ($t(18) = -2.211, p = 0.04$, Fig. 5.13c).

Whilst this result suggests US may be affecting behavioural outcomes, the underlying explanation as to why only the right visual field is sensitive to US stimulation is unclear especially given that one would expect modulation of the left visual field, given that stimulation was applied to the right hemisphere. In addition, there was no difference between stimulation of real and sham MT targets suggesting a non-specific origin of the response. There is also a wide spread in data points with no consistent trend among individuals pointing to inherent intersubject variability, a

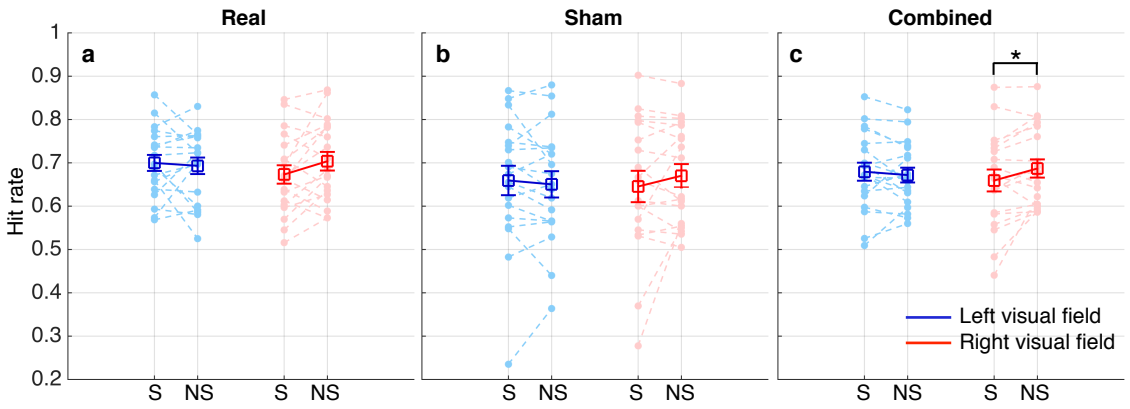


Fig. 5.13: MT behavioural data. Hit rates for **a** Real MT, **b** Sham MT, and **c** Combined MT locations for the left (blue) and right (red) visual fields between US stimulation (S) and no US stimulation (NS) trials. Averaged data over all participants ± the standard error of the mean are overlaid on to individual subject results. A repeated measures ANOVA found a statistically significant interaction between the visual field and stimulation ($F(1, 18) = 4.948, p = 0.039$) but it was only significant for the right visual field (paired samples t-test, $t(18) = -2.211, p = 0.04$).

problem encountered for all NIBS techniques.

For the FFA faces protocol, there was no statistical difference between stimulation and no stimulation trials (paired t-test, $t(10) = -1.168, p = 0.27$, Fig. 5.14).

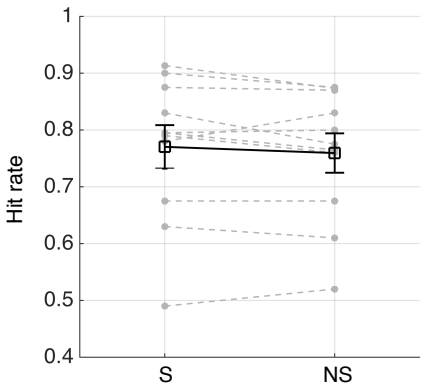


Fig. 5.14: FFA behavioural data. Hit rates for US stimulation (S) and no US stimulation (NS) trials. Averaged data over all participants ± the standard error of the mean are overlaid on to individual subject results. There was no statistical difference between the two groups (paired t-test, $t(10) = -1.168, p = 0.27$).

5.3.5 EEG

The collected EEG traces form a large dataset that can be analysed in many different ways across a multitude of different groups, time frames and locations. Data analysis is still ongoing by my colleague, Dr. Verena Braun, and so no data is presented here beyond the auditory ERPs shown in Fig. 5.11. As of the time of writing, only subtle differences have been observed in the processed EEG data.

5.3.6 Safety

The post-sonication SWI scans are still being conducted to compare with the scans before stimulation in order to check for any damage and so the full results cannot yet be analysed. For participant 2, both scans have been completed and images of a transverse slice through the visual cortex are shown in Fig. 5.15. The red ellipses specify where sonications were performed. The scans were checked by a neurologist and no differences were found between the two indicating that no damage was incurred. No participants reported any side effects from the trial.

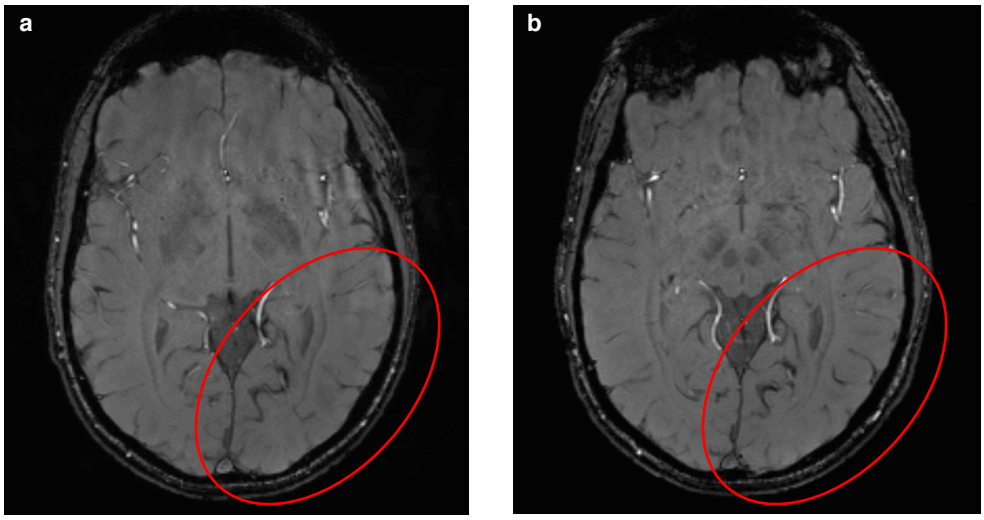


Fig. 5.15: Susceptibility-weighted imaging safety scans. **a** Pre-sonciation. **b** Post-sonication. Transverse slices through the visual cortex. Red ellipses indicate the regions over which stimulation was performed.

5.4 Discussion

In this chapter, the planning and implementation of a human pilot study using US to modulate areas of the visual cortex was presented along with some preliminary results. To control for intersubject anatomical variations, fMRI localisers and structural MRI scans were used to obtain tissues maps and brain targets for each participant which were used to carry out subject-specific acoustic and thermal modelling. The reason for this was two-fold: to determine the optimal transducer location and appropriate source pressures and to satisfy a number of safety constraints developed from analysis of the CNS neuromodulation literature (Chapter 4). A neuronavigation system was used throughout the trials to ensure alignment and track head movements in real-time. Coupling of the transducer to the head was achieved using a coupling cone created from a lithotripter membrane to allow for an expandable surface and hence the sonication of varying depth targets without the need to change coupling cones.

Acoustic modelling mirrored the findings in Chapter 3 in the sense that for V1 and MT, a coherent focus could be achieved at the target that was spatially confined whereas the fields for FFA were more diffuse often with hotspots located away from the intended site. Consequently, the faces task was only conducted for a subset of the volunteers where a reasonable pressure was delivered to the target site. The required source pressures varied substantially between subjects highlighting the need for participant-specific modelling.

An important outcome of the study is direct evidence of non-specific auditory activation following bursts of US sonication; similar audible sounds are also generated during TMS stimulation (Rossi et al., 2009). This therefore demands that attention is given to the design of appropriate sham controls to mitigate any effects of the auditory confound. Whilst some of the previous studies have reported chirping

sounds from the transducer (Legon et al., 2014), in general, auditory effects have not been considered to play a major role until the publication of two animal studies demonstrating coupling into the auditory pathway independent of the sonication site (Guo et al., 2018; Sato et al., 2018). Here, auditory ERPs were recorded in humans over a large number of central electrodes confirming widespread auditory activation. To mask the effects of the induced auditory responses, an audio waveform was played through earphones which had the same waveform as the envelope of the US burst. The level of the audio signal was adjusted until the ability of the participants to detect the US signal was down to chance levels. In 3 participants we were unable to mask the US burst for the audio levels used. It is unclear why the US burst was still discernible to these individuals although they all commented that they perceived the sound due to the US at a higher pitch. One theory is simply that some subjects have heightened auditory sensitivity that is capable of detecting the differences between the US burst and the mask.

At V1, we were unable to induce phosphene perception at odds with a previous study targeting the primary visual cortex (Lee et al., 2016b). One subject did report ripples in the left visual field which was consistent with phosphene perception but very sporadic and ultimately, it was not clear whether this was a direct result of US stimulation or merely an artefact of fixating on a monitor. Conversely, Lee *et al.* reported phosphenes in 11/19 participants described as a "*diffuse, amorphous, non-colored brightening of the central visual fields that recurred intermittently*".

In terms of behavioural modulation, a small yet significant interaction was observed for the dots paradigm between stimulation and the right visual field with US serving reduce a participant's performance. However the effect was independent of the target (real or sham MT) with high variability in the results between subjects. Consequently, the underlying explanation for this effect is not clear especially given that stimulation was applied to the right hemisphere and so one would expect a

response for the left visual field rather than the right. One theory is that US sonication also stimulated the temporoparietal junction (TPJ) which is located close to MT leading to shifts in attention biased towards the left visual field thus reducing a participant's ability to discern motion in the right visual field. This may be akin to findings in stroke patients where damage to the right temporoparietal junction (TPJ) results in left-hemisphere neglect (Saxe, 2010) except in this scenario stimulation activated the TPJ, shifting attention in the opposite direction to the left visual field (right-hemisphere neglect). FFA showed no significant change in behaviour.

The EEG analysis is ongoing and was not reported here. However, it is worth noting that so far, very few significant differences have been found between stimulation and no stimulation trials. There are numerous explanations as to why this might be; the simplest being that the pressures were below the threshold required to elicit effects with the behavioural effect ultimately the result of a different cause. The contact test conducted showed that losses of up to 40 % could be introduced through coupling alone before the losses accounting for transmission through the hair are added. Consequently, the in situ amplitudes may have been insufficient to evoke a response. In addition to that, if lower frequencies are more effective at modulating activity as has been shown in animal models (Kim et al., 2014b; King et al., 2013; Tufail et al., 2010; Ye et al., 2015), this may explain why we were unable to replicate phosphene perception which was reported following 270 kHz sonications at similar intensities. The other difference between the US waveforms was the PRF: 1000 Hz with pulses of 0.5 ms in our study versus 500 Hz in 1 ms pulses for Lee *et al.*, both resulting in a BDC of 50 %. On the other hand, human brain modulation has been demonstrated at 500 kHz at pressures of 120 kPa (Legon et al., 2018b). An alternative hypothesis is that the auditory-evoked ERPs simply dominated any subtler US-induced effects and hence they could be not extracted from the EEG data.

In terms of safety, pre- and post-sonication SWI scans showed no changes for one

participant indicating that no damage occurred as a result of the US exposure. The post-stimulation scans for the other participants are currently underway.

Ultimately, further work is clearly required to understand the auditory phenomena and how this impacts on neuromodulatory outcomes. The aim of this human pilot study was to replicate previous findings of phosphenes and then extend the technique to other, deeper, visual areas. However, given that the modulatory effects at V1 could not be repeated, moving to another well-characterised primary area might be a sensible approach moving forwards. M1 would be one such target that has been extensively studied using TMS with US shown to modulate TMS-evoked potentials (Legon et al., 2018b). Another option would be to try and modulate visual-evoked potentials at V1 at different US frequencies and parameters. However, as demonstrated in the Chapter 4, caution should be applied when utilising lower driving frequencies below 500 kHz and at increased pressure amplitudes.

6

Conclusions & future work

This chapter summarises the main findings detailed in this thesis as well as discussing the impact of the work. Possible future directions are considered before the final conclusions are drawn.

6.1 Summary

In this thesis, the key practical challenges for human translation of human neuromodulation have been highlighted and explored. In Chapter 1, the work of the past several decades demonstrating the ability of US to modulate neural activity in both the central and peripheral nervous systems is summarised. The highlights of the current work that ranges from cell cultures to human subjects are as follows. At the cell level, fluorescence imaging and patch clamp recordings showed transient Na^+ and Ca^{2+} ion currents in response to US (Tyler et al., 2008). These ionic currents likely result from the incident US energy interacting with cell membranes; potentially through conformational changes in the lipids in the membrane or by mechanosensitive ion channels. In rodents, US has been shown to affect both the motor cortex and the visual system (Kamimura et al., 2016; Kim et al., 2015; King et al., 2013; Tufail et al., 2010; Younan et al., 2013). In the latter case VEPs could be suppressed or enhanced (Kim et al., 2015), consistent with what was observed at a cell level. For large animals, evoked potentials have been reported in the motor and visual pathways (Dallapiazza et al., 2018; Lee et al., 2016c) and in non-human primates, modulation of latencies in the visual system confirmed the ability to modulate high-level cognitive behaviour (Deffieux et al., 2013; Wattiez et al., 2017). In humans, stimulation of the visual system has resulted in phosphenes (Lee et al., 2016b), of the somatosensory system in sensations felt in the hands (Lee et al., 2016a, 2015), and of the motor cortex in the suppression of MEPs (Legon et al., 2018b).

These data provide compelling evidence that neural systems can be stimulated by US over a range of length scales with a multitude of electrophysiological methodologies and techniques employed to record the responses. However, a number of outstanding questions remain before US can be considered a viable neuromodulatory tool including: accurate modelling to predict transcranial pressure distributions; safe US

sequences for use in the brain; elucidation of the fundamental mechanistic underpinnings; and monitoring of the approach to confirm US focus alignment as well as to detect neural modulation effects. We addressed two of these concerns in detail: the transcranial delivery of US to a specific brain site (Chapter 3) and the safety of the approach from both a thermal and mechanical viewpoint (Chapter 4).

From a delivery perspective, we have shown that the targeting of many brain sites can be achieved using single-element, geometrically-focused transducers by adjustment of the source position alone. To that end, a modelling pipeline was designed to determine the optimal placement of a transducer given a subject's anatomical dataset. Although the data highlight the need for subject-specific modelling to uniquely define source positions and amplitudes for each individual, a number of trends were observed which are likely beneficial when planning further human neuromodulation studies. Firstly, the plausibility of targeting a particular brain region is strongly dependent on the structure of the overlying skull bone with more uniform profiles associated with effective focusing and heterogeneous structures (for example, anatomical features including the inion and petrous ridge) presenting more of a challenge through shifting and fragmentation of the focus. In general, normally incident locations, with respect to the skull bone, are preferable as, with increased incident angles, the sensitivity of the models to acoustic property errors is increased and could lead to overexposure increasing safety concerns or underexposure resulting in the absence of an effect.

We showed that fluid-based simulations with homogeneous acoustic property assignment that can be computed in $\sim$4 min are able to effectively predict in situ pressure fields as validated by hydrophone measurements in ex vivo human skulls. That said, for targeting FFA, or through other complex skull structures, the accuracy of the models was reduced indicating finer resolution simulations or more accurate property allocation may be required to capture all of the fragmentation effects. For such

targets, more sophisticated source strategies, for instance a lens (Maimbourg et al., 2018) or an array (Hynynen and Sun, 1999; Marquet et al., 2009), will be required to correct for the induced aberrations. In addition, for some targets, simulations using time reversal to correct the source amplitudes and phases suggested that larger apertures than that of the single-element employed in this thesis may be required which will in turn need more advanced coupled strategies that those currently used for behavioural human trials.

The US parameters that the community seems to be settling on for CNS stimulation are a frequency of ∼200–500 kHz delivered as a 300–500 ms burst of ∼0.5 ms pulses at a PRF of ∼1 kHz with pressure amplitudes on the order of 0.1–0.6 MPa in the brain. We carried out an analysis of the safety metrics developed for diagnostic US imaging for the US parameters used in the neuromodulation studies and found that the US parameters employed in the human trials would be considered safe from a imaging regulatory view. Although we note that the pulsing paradigm used in US stimulation studies involves longer pulses than used in US imaging and this may have an impact on cavitation thresholds which should be considered further.

Inspection of the safety data revealed that caution should be taken when utilising frequencies below 500 kHz at pressures above 0.65 MPa as well as for highly repetitive stimulation as some damage has been observed for this parameter space (Kim et al., 2014b; Lee et al., 2016c). For future human studies, we therefore recommend placing limits on the maximum pressure, inter-stimulation interval and number of sonications per target. We anticipate that further work in the safety area may allow a larger range of acoustic parameters to be employed than has been used to date. Ultimately, a useful goal for the community would be to develop guidelines for the use of US as a neuromodulatory tool accounting for the longer pulse lengths.

Following this groundwork into transcranial US delivery and the selection of appropriate US parameters, we carried out a human pilot study utilising US to modulate

areas of the visual cortex in 21 healthy subjects. Participant-specific modelling was conducted for each subject to define source positions and amplitudes and a neuronavigational system was used to ensure correct alignment. One key finding was that subjects could hear a tone during US sonication which appeared to be the 1 kHz PRF envelope being converted into a wave in the skull which conducted to the cochlea. This was confirmed by the measurement of ERPs over the auditory cortex consistent with recent animal studies demonstrating auditory responses (Guo et al., 2018; Sato et al., 2018). Given that all subjects were able to detect the sound, we were surprised that this has not been paid much attention in past human studies especially as this can confound electrophysiological recordings. In fact, auditory sensations in humans as a result of amplitude-modulated US has been well studied in the past (1970s-80s) with the transmission of more complicated auditory waveforms such as music or speech possible. Moreover, the site of US application was varied over the head, neck, and torso and although the strength of the auditory sensation was altered, the same tone was generated regardless of the location. These findings, and others, are summarised by Gavrilov and Tsirulnikov (2012) and may prove a useful resource for the design of US sequences to minimise auditory effects. In our pilot study, to counter the auditory sensations, we applied an audio mask to conceal the US burst and showed very similar grand-averaged ERPs between masked trials with and without US as well as a significant decrease in the participant's ability to detect the US, down to chance. Despite this, 3 individuals were still able to distinguish between stimulation and no stimulation trials.

In total, three different visual targets were stimulated: V1, MT and FFA. At V1, we were unable to replicate previous work in humans generating phosphene perception (Lee et al., 2016b). The only notable difference between the US sequences was the driving frequency (we used 500 kHz compared to 270 kHz previously) and so one possible explanation is an increasing threshold at higher frequencies as suggested in animal models (Kim et al., 2014b; King et al., 2013; Tufail et al., 2010; Ye et al.,

2015). One the other hand, 500 kHz US has already been shown to effectively modulate the human brain at similar intensities to those employed in this pilot study (Legon et al., 2018a,b, 2014) and so the reason for the lack of phosphene induction is uncertain. It is also noted that there have been a number of anecdotal reports of the inability to generate phosphenes.

At MT, a further sham site was tested in addition to the real location. A significant decrease in performance to detect the motion of moving dots was shown, albeit independent of target location and only for the right visual field. At FFA, there was no behavioural change. In both instances, there was a wide spread in individual data points with no consistent trend across all subjects. Although the performance of discrimination tasks has been shown to be modulated through US stimulation (Legon et al., 2018a, 2014), behavioural manifestations undoubtedly require strong alterations of brain activity and so it was not unexpected to only see minimal or no changes. The extent to which MT and FFA are lateralised is also not entirely clear and so it is possible that the brain location in the opposite hemisphere compensated for any effects at the targeted site. Therefore, to see even a small behavioural change is encouraging although the underlying explanation for the interaction between the right visual field and stimulation, independent of the MT sonication site (real or sham), remains an open question. One theory is that the TPJ was stimulated resulting in attentional shifts biased towards the left visual field diminishing a participant's ability to detect motion in the right visual field although this is still unproven.

In terms of the electrophysiological data, analysis is still ongoing but initial results also suggest minimal differences between stimulation and no stimulation trials. The fundamental reasons for the lack of a response could be due to many factors such as, the behavioural effect was driven by a different phenomena and we were actually below the threshold for US neuromodulation or the auditory ERP was so strong that

it overshadowed more subtle US-induced changes. Furthermore, although we tried to mitigate intersubject anatomical variability through the use of fMRI localisers, neuronavigation and participant-specific modelling, it is possible this still had an impact on the study along with other inherent variabilities as with all forms of NIBS, such as cognitive state.

6.2 Future work

In terms of parameter selection and whether continuous wave US is as effective as bursts of US, further parametrisation studies in model systems may be useful but ultimately, determining the mechanistic underpinning behind US neuromodulation is key to effectively planning protocols. This will likely also come from in vitro work where individual cells and brain architectures can be isolated and combined with precise electrophysiological recordings. We anticipate this will be a gradual process as illuminating the underlying mechanisms in brain will invariably be multi-faceted as evidenced by the electrically-based NIBS literature (Cirillo et al., 2016; Gellner et al., 2016; Giordano et al., 2017; Herrmann et al., 2013; Klomjai et al., 2015). However, one more attainable objective would be to combine acoustic and optical systems to determine whether cavitation signatures are detected during US brain stimulation. We attempted to study US stimulation of murine hippocampal slices using optics to monitor the responses (Appendix A) but due to limited time and numerous complications were unable to complete this goal. Continuation of this work could have a large impact on the field and provide evidence of the role of cavitation in US neuromodulation in the CNS, which is so far lacking. A word of caution with these in vitro setups is that the local environment may be very different from that experienced by neurons in vivo; both biologically in that cells are in artificial environments but also because of acoustically reflective surfaces (e.g., cover-slips, patch pipettes, air interfaces), the acoustic field, and hence stimulus, will

be affected. Understanding the limitations of artefacts associated with the in vitro system is something that should be appreciated in interpreting the data.

Another avenue that clearly requires further consideration is the impact of widespread auditory activation on US-induced neuromodulatory outcomes. Our results, and previous animal work (Guo et al., 2018; Sato et al., 2018), provide compelling evidence of the activation of the auditory system which might confound neuromodulation studies. Future human trials should be aware of this and design appropriate sham and control groups to ensure effects are due to the specific stimulation of the intended site. The modification of US waveforms through the use of ramps and pulse shaping may also be useful to attenuate the auditory response. Indeed, previous work demonstrating modulation of saccadic behaviours and changes in neuronal activity recorded in the medial frontal cortex following US over the frontal eye field (Deffieux et al., 2013; Wattiez et al., 2017) is unlikely to be auditory-mediated given the use of smoothed US waveforms.

From a safety standpoint, more studies are required to determine appropriate pulse sequences to safely modulate the nervous system over the full US parameter space. In particular, data on the effects of different target pressures and repetitive stimulation as well as on any longer term outcomes would be beneficial. This data will likely be crucial in the development of suitable guidelines specifically for neuromodulation applications to ensure its safe usage as more research groups become interested in the technique.

Finally, in terms of US delivery, further development of acoustic lenses (Maimbourg et al., 2018) and smaller, portable arrays may increase the accessibility to more areas in the brain as well as improving specificity. Computational models will be important regardless of the chosen source and so further attempts to increase the accuracy of transcranial acoustic propagation simulations should be investigated including the determination of the most applicable model for skull bone, for example, fluid,

elastic or porous. A useful technique may be the development of adaptive sound speed estimation using US in order to determine participant-specific sound speed values as well as to extract the skull bone profile (Hajian et al., 2017). Moreover, improvement of MRI sequences and segmentation algorithms specifically to obtain the skull bone contours should be considered, particularly as getting ethical approval for CT scans in healthy volunteers is difficult to obtain.

6.3 Conclusions

There is now a body of evidence which runs the gamut from isolated cells to cognitive response in humans, that US does result in neurostimulation. The data show that US has the potential to enhance or suppress nerve firing depending on the US parameters although, at the network level, whether a stimulation results in excitatory or inhibitory behavioural outcomes will also depend on the connectivity of the neurons. The ability to use low intensity focused US for non-invasive, anatomically precise neuromodulation in humans has therefore generated much excitement due to its potential both for understanding normal brain function and for diagnostic and therapeutic applications in disease.

We have shown how single-element transducers can be effectively targeted to many areas of the brain without requiring correction methods and investigated appropriate parameters for the safe use of US in the human brain. We then conducted a human pilot study to determine whether US could modulate behaviour as well as alter electrophysiological signals through stimulation of areas of the visual cortex. Whilst the results of the study are inconclusive as to the direct effects of US on specific brain nuclei, they provide compelling evidence of widespread, non-specific auditory activation most likely through bone conduction in the skull.

In conclusion, US is emerging as an intriguing and exciting NIBS method that is

rapidly gaining interest in both the US and neuroscience communities. Whilst US has been demonstrated to safely and reversibly modulate the nervous system, more work is needed to fully explore the US parameter space from both a safety and a mechanistic perspective and to understand the influence of widespread auditory activation on neuromodulatory outcomes before US can be considered as a viable US tool for utility in research as well as therapeutically.

A

Mechanisms

This appendix details the in vitro work undertaken to study US-induced neuromodulation mechanisms. Whilst multiple problems were encountered with the setups, this serves as a reference outlining the basis of the work along with the limitations.

A.1 Introduction

Although numerous neuromodulatory effects have been reported as a result of US sonication, the underlying mechanisms that couple the acoustic perturbations into neural modulation remain unclear. This in vitro work was conducted with a view to providing some insight into the conditions required to elicit effects. Multiple mechanistic underpinnings have been postulated (see Blackmore et al. (2019) for a full review) but of primary importance is establishing which bioeffect, the ARF or cavitation, or both, or neither, ultimately leads to nervous system modulation. This was therefore one of the primary objectives of the study along with determining more effective stimulation parameters utilising the same source from the pilot study

(Sonic Concepts H-107 500 kHz single-element transducer).

A.2 Methods

A.2.1 Organotypic slices

Hippocampal slices were used as the model system. These cultured slice preparations are more representative of real brain networks than dissociate neuronal cell cultures as they retain the in vivo architecture including the extracellular matrix and non-neuronal supporting cells, such as glial cells. Transverse sections of the hippocampus were prepared from 7-day postnatal rat pups and incubated (37 °C, 5 % CO_2) on Millicell culture inserts for 1-2 weeks in culture medium before use. The organotypic cultures were approximately 2–3 mm in diameter and 350 µm thick. Media was replaced twice weekly. During the experiments, slices were transferred to a chamber containing artificial cerebrospinal fluid (aCSF). Full details of the culture media, aCSF and references for the prepartation of the organotypic slices can be found in Haslehurst et al. (2018).

A.2.2 Microscope setup

Two different microscope configurations were used for different sets of experiments: (1) a confocal microscope and (2) an epifluorescence microscope. The confocal setup allows illumination of planes at any depth though the tissue and the ability to resolve specific cells, axons and dendrites. Patch clamp techniques can also be incorporated into the system for electrical membrane measurements and to fill individual neurons with membrane impermeable fluorescent dyes. However, the microscope condenser and light source did not allow enough room to co-align the transducer and microscope foci. Furthermore, with the transducer orientated vertically, substantial standing wave effects would have inevitably occured making estimation of the acoustic field almost impossible. A passive cavitation device (PCD) could also

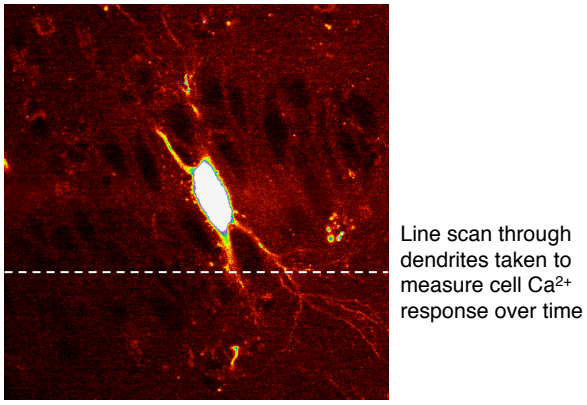


Fig. A.1: Hippocampal slice CA1 pyramidal neuron filled with membrane impermeable OGB-1 Ca^{2+} fluorescent dye. White dashed line indicates an example of where line scans where performed to measure the cell response over time.

not be fitted due to space constraints. In the epifluorescence setup, much more space was available and hence a small water tank could be fitted below the objective with the transducer angled to try and minimise standing wave effects. This more desirable acoustics setup was offset by reduced optics capabilities preventing the ability to resolve single cells and thus having to rely fluorescent intensity measurements from the surface of the slice. Furthermore, there was no method to check cell viability and neuronal cell health during the experiments.

A.2.3 Electrophysiological recordings

In the confocal setup, patch-clamp techniques were initially attempted to provide electrical measurements of the cell membrane. However, even at very low pressures, the patch seal was disrupted due to mechanical vibrations making this technique intractable. Therefore, the patch pipette was used to load a single cell with membrane impermeable OGB-1 Ca^{2+} dye as shown in Fig. A.1, and then retracted prior to sonication. The back-propagating Ca^{2+} wave can then be recorded in the dendrites following AP generation (Ross and Manita, 2012).

For the epifluorescent configuration, the slices were bathed for 30 min in the membrane permeable (AM) version of the OGB-1 or Fluo-3 Ca^{2+} dyes following the

loading protocol as set out by Tyler et al. (2008).

A.2.4 Sonication parameters

Initially, the bursting sequences utilised by Tyler et al. (2008) were replicated, followed by a range of different US sequences over a range of pressures and time scales. Unfortunately, due to the complexity and numerous interfaces in the microscope setups, it was not possible to estimate the pressures achieved in the slice.

A.3 Results

In the confocal setup, only sporadic responses could be generated regardless of the sonication parameters. Time-locked activity corresponding to the onset of the US burst was produced multiple times, although not every time, and only for the first burst application. Subsequent US bursts did not stimulate any activity. Examples of the AP firing, as evidenced by the back-propagating Ca^{2+} wave into the dendrites, are shown in Fig. A.2 with similar responses generated for 5 s (Fig. A.2a) and 200 ms (Fig. A.2b) burst lengths both consisting of 100 cycle pulses at a 50 Hz PRF. On a couple of occasions, activity was observed several seconds into the US exposure as displayed in the right hand plot in Fig. A.2b but it was unclear if this was a direct result of the US or just a spontaneous event. On another occasion, the initial activity was followed by a stronger bout of spiking as illustrated in the image on the right of Fig. A.2a. In all cases, the cells were perfectly electrically excitable and looked normal under the microscope after US exposure thus ruling out damage to the cells as the reason for the inability to re-stimulate them with US. Moreover, rest periods of 30 min to 1 h, the use of older, more excitable cells, the addition of potassium to alter the resting membrane potential and whether aCSF was flowed or stationary also did not have any effect on the outcomes. The only thing that increased the likelihood of a response was re-setting all the equipment including taking it all out

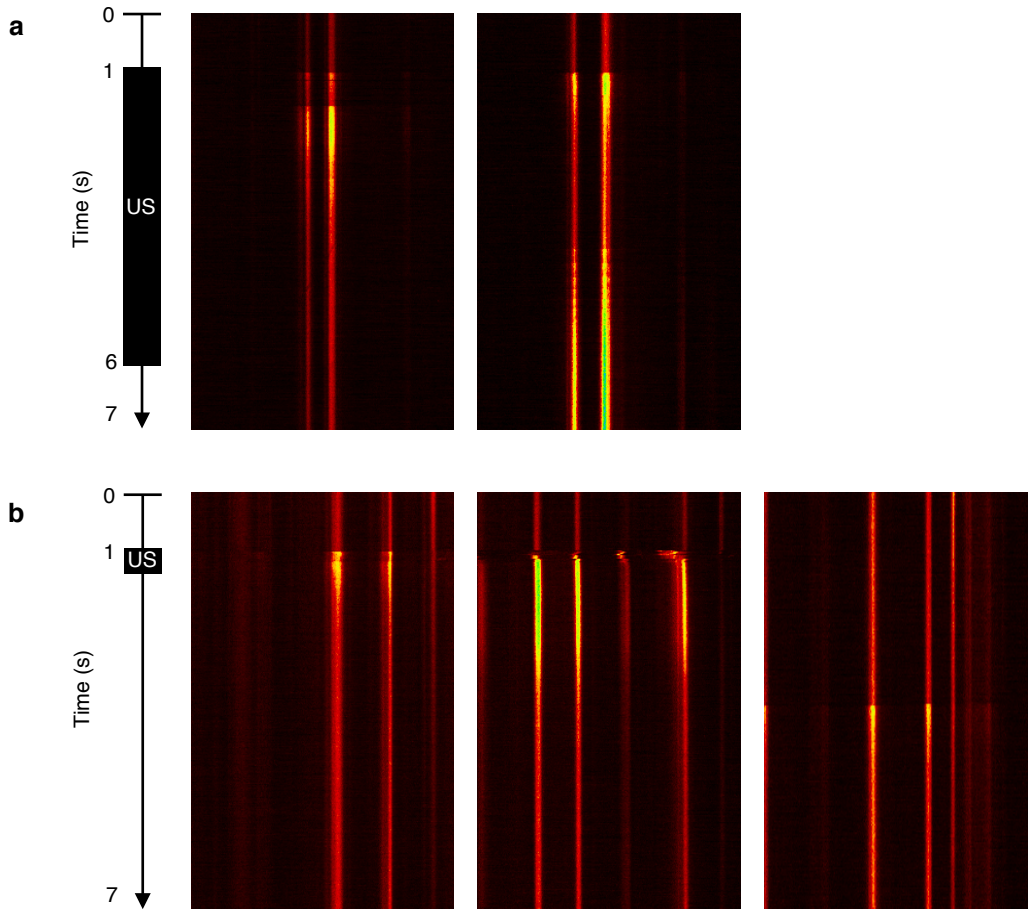


Fig. A.2: Visualisation of back-propagating Ca^{2+} wave over the dendrites of a CA1 pyramidal neuron following US exposure. **a** 5 s and **b** 200 ms US bursts, 100 cycle pulses at 50 Hz PRF. Bars indicate timings of US sonication.

and then replacing it. One possible explanation for this was that small trapped air bubbles were driving the response; these were then used up by the first burst and so no further activity could be generated until the aCSF solution was replaced. However, it is noted that just changing the aCSF alone did not allow subsequent bursts to trigger responses. Unfortunately, the cavitation hypothesis could not be tested in this rig as there was no space to incorporate a PCD.

A switch was therefore made to the epiflourescence setup in order to incorporate a PCD and determine whether cavitation signals were detected and correlated with network activity. However, the limitation of the epiflourescent microscope is that it only allows the surface of the slice to be visualised and so averaged fluorescence

intensity values over a large portion of the slice was the best that could be achieved. Two different wavelengths were measured in order to subtract out any movement artefacts. Unfortunately, although some signals initially looked like the result of network activity, upon subtraction, it was evident they were indeed the result of movement of the slice. Reduction of the amplitudes and pulse lengths to prevent any movement did not produce any effects.

A.4 Discussion

Ultimately, this mechanistic study required more time than I was able to allocate. Ideally, a dedicated setup incorporating both acoustics and optics, preferably within a confocal microscope allowing the use of additional electrophysiological techniques beyond fluorescent dyes (e.g. stimulating electrodes) would make for a powerful tool for unpicking the mechanistic underpinnings of US neuromodulation and would likely have a large impact on the field.

B

US neuromodulation literature synopsis

B.1 CNS studies

Study	Organism & Target	Key Findings	Safety
Legon et al. (2018b)	Human (M1)	Combined US and magnetic stimulation. US inhibits amplitude of single-pulse TMS-induced MEPs and reduces reaction times during stimulus response task.	-
Legon et al. (2018a)	Human (Thalamus)	Modulation of sub-cortical nuclei. Attenuation of P14 SEP amplitude. Reduction in performance of discrimination task.	-
Lee et al. (2016b)	Human (V1)	Phosphene perception. fMRI: activation of V1, visual pathways & cognitive processes. Modulation of VEPs.	Neurological examination, MRI follow-up (0,2,4 weeks) and follow-up interviews (2 months): no abnormal findings across all participants.
Lee et al. (2016a)	Human (S1, S2)	Elicitation of tactile sensations on hand and arm. Simultaneous S1/S2 stimulation.	No adverse changes or discomfort in mental/physical status across all individuals.

Ai et al. (2016)	Human (M1, S1, caudate)	fMRI responses in sensorimotor & caudate regions.	-
Lee et al. (2015)	Human (S1)	Elicitation of peripheral sensations on hand and arm. Modulation of SEPs.	Neurological and neuroradiological assessment did not show any safety concerns.
Mueller et al. (2014)	Human (S1)	Modulation of EEG dynamics including phase and phase rate in beta and gamma bands.	-
Legon et al. (2014)	Human (S1)	Modulation of SEPs and alpha, beta and gamma frequency bands. Improvement in discrimination tasks.	-
Hameroff et al. (2013)*	Human (Posterior frontal cortex)	Improvement in mood scores. Small pain reduction but not significant.	One subject experienced a headache which quickly resolved. No other side effects up to 4 months after the study.
Kubanek et al. (2017a)	Monkey (FEF)	US stimulation to left (right) FEF shifted animal's choices to rightward (leftward) target.	No long term bias in animals choices after 8 days of stimulation of each region.
Wattiez et al. (2017)	Monkey (FEF)	Single neuron recordings in SEF: activity changes following US stimulation of FEF. ∼40 % of neurons modulated.	-
Deffieux et al. (2013)	Monkey (FEF)	Increased latencies in antisaccade task.	Stimulation effect was transient (no significant effects observed on the following control trials).
Dallapiazza et al. (2018)	Pig (Thalamus)	Reversible suppression of SEPs. Selective activation of sub-nuclei within somatosensory thalamus.	Histology: no gross or microscopic tissue damage.
Daniels et al. (2018)	Pig (AC)	AEP suppression.	-
	Rat (Inferior colliculus region)	AEP supression.	Histology (H&E): no damage. No sign of inflammatory response or structural changes. AEP amplitude recovery 1 h – 1 month.

Lee et al. (2016c)	Sheep (SM1, V1)	SM1: EMG response of contralateral hind leg. V1: VEPs.	Histology: small microhaemorrhage for repetitive stimulation ($\geq$ 500 stimulations delivered at 1 s intervals). Damage not seen at longer ISIs. Post-sonication behaviour normal.
Fisher and Gumenchuk (2018)	Mouse (Cortex)	Reduction in latency and increased Ca^{2+} response following electrical stimulation with US pre-treatment.	Histology: no changes in distribution of glial fibrillary acidic protein or evans blue – no neural injury or BBB opening.
Han et al. (201)	Rat (Motor cortex) & Cell cultures	Response robustness increased with intensity and linked with shorter latencies. Ketamine reduced Ca^{2+} transients in dose-dependent manner by up to 82 %.	Histology (H&E): no obvious damage, morphological changes, tissue bleeding or cytoplasmic swelling.
Guo et al. (2018)	Guinea Pig (Various inc. A1, S1)	US response due to indirect cochlear fluid pathway rather than direct activation. Similar activity in A1, SC1 recorded irrespective of target location. US-evoked activity eliminated by removal of cochlear fluid.	-
Sato et al. (2018)	Mouse (Visual cortex)	Widespread neural activation through indirect auditory mechanism. Contralateral visual cortex had similar response kinetics to targeted side but auditory cortex showed contralateral bias. Chemical deafening greatly reduced motor outputs.	-
Gulick et al. (2017)	Rat (Motor cortex)	Long-term modulation of electrical stimulation: reduced hindlimb responses. Direct motor response had 3 s refractory period.	No behavioural changes observed following stimulation.
Lee et al. (2017)	Rat	-	Histology (H&E, TUNEL assay): no cell necrosis.
Li et al. (2016)	Mouse (Motor cortex)	Increased specificity and decreased latencies at 5 MHz compared to 1 MHz.	Histology (H&E): no evidence of tissue bleeding or cell necrosis.

Kamimura et al. (2015, 2016)	Mouse (Motor & cognitive areas)	Limb movement and eyeball dilation.	Histology (H&E): no damage.
Darvas et al. (2016)	Rat	EEG signal at the frequency of the US PRF was induced along with demodulated activity in gamma & beta bands: potential use of US to tag deep regions for EEG-based mapping.	-
Yu et al. (2016)	Rat	Localisation of induced brain activity using electrophysiological source imaging.	-
Moore et al. (2015)	Mouse (Somatosensory cortex)	US and optogenetic responses have similar form for pyramidal neurons but not interneurons but amplitudes 10–20 fold lower for US.	-
Ye et al. (2015)	Mouse (Motor cortex)	Success rate decreases with frequency for given intensity. Focal spot size did not have consistent effect on success rates; most of variance can be explained by frequency. Success strongly correlated with cavitation index and particle displacement but not ARF.	-
Kim et al. (2015)	Rat (Visual cortex)	VEP magnitude suppression/enhancement dependent on intensity and BD. Threshold intensity to elicit response.	-
King et al. (2014)	Mouse (Motor cortex)	Differences in EMG response (magnitude and latency) following rostral or caudal stimulation.	-
Kim et al. (2014a)	Rat (Motor cortex)	Pulsed US more effective at stimulating tail twitches than CW. 50 % BDC, 300 ms BD, 2 ms PL most effective. Reduction of PL, change in BDC and BD all increased required intensity for successful stimulation.	Histology (H&E) did not reveal any tissue damage or haemorrhage. One animal at a higher intensity (I_{sppa} = 22.4 W/cm^2) did exhibit several areas containing hemosiderin, indicating the potential of local bleeding.

Kim et al. (2014b)	Rat (Unilateral thalamic area)	Neuromodulatory site detected by glucose uptake PET imaging: corresponds to full width at 90 % maximum US field (much smaller than FWHM).	-
Mehić et al. (2014)	Rat (Motor cortex)	Comparison of planar, focused and modulated focused source using 1.75 and 2.25 MHz to generate a 0.5 MHz difference frequency. Large variance in responses. Robustness of motor movement scaled with I_{SPTA}.	All histology samples showed no damage to brain tissue.
Younan et al. (2013)	Rat	Motor responses: tail, fore and hind limbs, eye, single whisker. Pressure threshold for response dependent on anaesthesia levels. Rat skull distributes field across whole brain and introduces pressure hot spots due to reverberations.	No change in behaviour or weight was observed.
King et al. (2013)	Mouse (Motor cortex)	EMG motor responses. Anaesthesia levels important. CW as effective as pulsed US. All or nothing responses. Responses occur due to stimulus onset (within 30–100 ms). Required intensity increases with frequency. Success rate increases with PRF from 100–3000 Hz. Key variable appears to be integral of amplitude over a time interval of 50 to 150 ms.	-
Yang et al. (2012)	Rat (Thalamus)	Reduction in extracellular GABA for at least 2 h following sonication. No change in glutamate levels.	Histology showed no abnormal findings at either the focus or along the beam path.
Yoo et al. (2011a)	Rabbit (Somatomotor & visual areas)	Bimodal modulation: excitation of motor response and suppression of p30 VEP component. EEG signals confirmed by BOLD fMRI.	Histology did not reveal any tissue damage. No TUNEL positive apoptotic cells or VAF positive ischemic cells were found. No increase in Gadolinium signal suggesting no BBB disruption.
Yoo et al. (2011b)	Rat (Thalamus)	Reduction in anaethesia times following FUS (up to 20 min).	-

Min et al. (2011a)	Rat (Thalamus)	Reduction in EEG theta bursts after epileptic seizure induction.	Histology: no tissue damage (H&E) or DNA fragmentation (TUNEL).
Min et al. (2011b)	Rat (Thalamus)	Increase in extracellular dopamine and serotonin levels for at least 2 h post sonication.	-
Tufail et al. (2010)	Mouse (Motor cortex & hippocampus)	Increased cortical spiking. TTX blocked US-evoked activity. Mean failure rate increased from 0.25–5 MHz. Lower frequencies & I_{sppa}s give more robust EMG responses. Evoked potentials in hippocampus followed by 3 s afterdischarge containing gamma, sharp wave ripple oscillations and increase in spike frequency. Increase in BDNF.	No evidence of BBB opening. No change in density of apoptotic glial cells or neurons. No differences in synapse density or cortical neuropil ultra-structure. No neurological abnormalities during rotorod and wire-hanging tasks.
Koroleva et al. (1986)	Rat (Cerebral cortex & hippocampus)	Direct current potential changes and spreading depression waves.	-
Ballantine et al. (1960)	Cat (Edinger-Westphal nucleus)	Temporary dilation of eye.	No lesions observed.
Fry et al. (1958)	Cat (LGN)	Reversible suppression of VEPs.	No histologically detectable lesions.
Prieto et al. (2018)	Cull cultures	Patch clamp recordings: activation of Piezo1 but not $Na_V1.2$ through membrane stress as a result of acoustic streaming.	-
Kubanek et al. (2018)	C. Elegans	MEC-4, a pore-forming subunit expressed in touch receptor neurons required for US-evoked behaviours. TRP-4 response due to background genetic mutation. 50% DC and 300–1000 Hz PRF produce optimal response rates.	-
Menz et al. (2017)	in vitro: Isolated salamander retina	US stimulation results in micron-scale displacements. Efficacy increased with frequency consistent with an ARF-mediated mechanism.	-

Kim et al. (2017b)	in vitro: Hippocampal slice	MEA: region and threshold-specific increased spike activity during and after US stimulation.	-
Menz et al. (2013)	in vitro: Isolated salamander retina	US evoked strong response similar to visual response but with shorter latencies. US activated other cells beyond photoreceptors. PRF 15 Hz – 1 MHz had no effect on responses; only temporal-averaged power important.	-
Choi et al. (2013)	in vitro: Rat hippocampal neurons	MEA: increased spiking and bursting. Effect observed post exposure. Largest firing rate at 0.8 MPa, decreased at higher pressures.	-
Tyler et al. (2008)	in vitro: Hippocampal slices and isolated mouse brain	US-induced APs during whole-cell current clamp recordings in CA1 pyramidal neurons. Triggering of voltage-gated Na^+ and Ca^{2+} channels, vesicle exocytosis and synaptic transmission. Addition of TTX and Cd^{2+} blocked Na^+ and Ca^{2+} transients respectively.	Repeated stimulation (36 — 48 h) did not alter fine membrane structure.
Khraiche et al. (2008)	in vitro: Hippocampal slices	MEA: US can excite neurons and increase firing rates.	-
Bachtold et al. (1998)	in vitro: Hippocampal slices	Enhancement and depression of electrically evoked potentials.	-
Rinaldi et al. (1991)	in-vitro: Hippocampal slices	Depression of electrically evoked potentials.	-

Table B.1: Synopsis of central nervous system studies. A1 – primary auditory cortex, AC – auditory cortex, AEP – auditory evoked potential, AP – action potential, ARF – acoustic radiation force, BBB – blood brain barrier, BOLD – blood oxygen level dependent, CW – continuous wave, EEG – electroencephalography, EMG – electromyography, FEF – frontal eye field, H&E – hematoxylin and eosin (staining), M1 – primary motor cortex, MEA – multi electrode array, MEP – motor evoked potential, MRI – magnetic resonance imaging, LGN – lateral geniculate nucleus, SEF – supplementary eye field, SEP – somatosensory evoked potential, SM1 - primary sensorimotor area, S1 – primary somatosensory cortex, S2 – secondary somatosensory cortex, TMS – transcranial magnetic simulation, V1 – primary visual cortex, VEP – visual evoked potential.

* GE LOGIQe US scanner with 12L-RS imaging probe.

B.2 PNS studies

Study	Organism & Target	Key Findings	Safety
Lee et al. (2014)	Human (Fingertip)	Induction of different peripheral sensations (thermal, vibrotactile, nociception) depending on US parameters. CW did not induce sensations. Thermal responses maximum over a band of intensities (I_{sppa} = 10–30 W/cm^2) whereas for vibrotactile and nociception, response rate increased with intensity. Greater response rate at 350 kHz than 650 kHz.	No short-term or long-term tissue damage to insonified finger.
Legon et al. (2012)	Human (Fingertip)	US induced evoked potentials similar to other stimulus modalities. The waveform can be adjusted to preferentially stimulate different fibres ($A\beta$, Aδ and C) and the subsequent somatosensory neural circuits as confirmed by fMRI.	-
Dickey et al. (2012)	Human (Fingertip)	Sigmoidal response rate with increasing intensity. High specificity (participants ability to determine when US applied) indicates unique tactile sensations induced by US. Response correlates with density of mechanoreceptors.	No psychological or physiological changes (assessed by questionnaire).
Gavrilov et al. (1977a)	Human (Hand, forearm)	Increasing intensity: tactile, temperature and finally pain sensations. At deeper targets, only pain elicited. Longer stimuli (>100 ms), sensations present at start and end of waveform. Temperature sensations dependent on temperature of water bath that hand immersed in. Cavitation detected before onset of pain sensations.	-

Downs et al. (2018)	Mouse (Sciatic nerve)	EMG activity and visible muscle activation for p > 3.2 MPa and BDC > 35 %. A break period of 20–30 s improved the next stimulation success rate to 92 %. Latencies similiar to electrical stimulation.	Histology: no damage detected for successful US stimulation parameters or negative control groups. Damage observed for positive control (5.4 MPa, 90 % BDC, 1kHz PRF, 0.5 s BD) and for PL > 30 ms at 5.7 MPa.
Casella et al. (2017)	Rat (Posterior tibial nerve)	Inhibition of rhythmic bladder contractions. Longer latency and refractory periods compared to electrical stimulation.	-
Ni et al. (2016)	Rat (Sciatic nerve)	Improved regeneration and functional recovery following crush injury. BDNF levels increased for first 2 weeks following treatment.	-
Juan et al. (2014)	Rat (Vagus nerve)	Decrease in electrically-evoked CAPs, effect increased in magnitude with I_{spta}. Decrease in conduction velocities.	-
Tych et al. (2013)	Rat (Sciatic nerve)	US threshold for paw withdrawal reduced for neuropathic tissue compared with sham surgery tissue.	-
Kim et al. (2012)	Rat (Abducens nerve)	Eyeball movement.	Histology (H&E, trypan blue): no damage or BBB disruption.
Foley et al. (2008)	Rat (Sciatic nerve)	Increased reduction in CMAPs with intensity. CMAP amplitude recovered by 28 days in all but highest intensity which showed no recovery.	Histology: increased levels of damage as intensity increased up to complete axonal degeneration and necrosis.
Ellisman et al. (1987)	Rat (Dorsal nerve roots)	Electron microscope: morphological changes in rats at myelination development stage (3–5 days old) – enlargement of periaxonal space, abnormal morphology of nodes of Ranvier and demyelination.	See results.

Gavrilov (1984)	Various	Human: skin receptors, threshold value dependent on density of receptors distributed on skin surface. Perception of 400 ms pulse the same as two spaced 10 ms pulses. Use of US for diagnosis of neurological diseases based on tactile sensation response. Skate fish: stimulation of electroreceptors only achieved with pulsed US and not CW.	-
Gavrilov et al. (1977b)	Cat (Pacinian corpuscle), Frog (Ear labyrinth)	APs induced in Pacician corpuscle for intensities in range 0.1–4.2 W/cm^2. Amplitude of receptor potentials increased with intensity. Evoked potentials in frog auditory brain at intensities as low as 0.01 W/cm^2 similar in shape to sonic stimuli.	-
Lele (1963)	Cat, Monkey, Human, Earthworm.	Progressive US dose leads to initial AP amplitude enhancement, then reversible and finally irreversible depression. Conduction velocities increase with dose. Physiological effects reproduced by heat application.	Enhancement/reversible depression: undistinguishable from unirradiated nerves. Irreversible depression: nodularity, fragmentation of axis cylinders restricted to irradiated section of nerve (indistinguishable from heat damage). Prolonged, intense US irradiation without rise in nerve surface temperature without apparent physiological and anatomical effects.
Young and Henneman (1961)	Cat (Saphenous nerve)	Differential blocking of mammalian nerves. C-fibres most responsive. A-α least sensitive. Reversible and then permanent block with increasing US dose.	-
Wahab et al. (2012)	Earthworm (Giant Axon)	Cumulative ARF negatively correlated to reduction in conduction velocity and AP amplitude. At low impulses, enhancement in amplitude before dropping at longer exposure times. Final changes semi-permanent: no recovery within 15 minutes.	Semi-permanent effects in reduction of AP amplitudes following repeated single pulse sonications 100 times a second for over 200 s.

Wright et al. (2017, 2015)	ex vivo: Crab (Leg nerve axon)	Unpredictable responses with slight preference for first stimulus. Lowest intensity for successful stimulation was 100 W/cm^2 (1.8 MPa) at 0.67 MHz. No responses at 1.1 or 2 MHz. Cavitation signals detected for all successful stimuli.	Afterdischarge at 230 W/cm^2 resulting in reduced CAPs. Probably due to cavitation-induced membrane rupture.
Colucci et al. (2009)	ex vivo: Bullfrog (Sciatic nerve)	1.986 MHz: reduction in CAP amplitude, thermal effect matched by experiments varying water bath temperature. 0.661 MHz: discrepancy with thermal effects. Pulsed US: initial small increase in CAP then reduction.	Histology (H&E): 1.986 MHz, little or no damage consistent with thermal effects. 0.661 MHz, varying levels of damage depending on intensity. At higher intensities evidence of cavitation.
Tsui et al. (2005)	ex vivo: Bullfrog (Sciatic nerve)	Increased conduction velocity with power. Amplitude increased by 9 % at 1 W but then decreased at higher powers.	-
Schelling et al. (1994)*	ex vivo: Frog (Sciatic nerve)	CAPs generated similar in shape but lower in amplitude than electrically-induced CAPs. Movement away from the focus prevented CAP generation until air bubbles where added.	-
Mihran et al. (1990)	ex vivo: Frog (Sciatic nerve)	Latency of applied US results in different responses: enhancement or suppression of electrically-induced CAP. Required BD to induce response reduced as intensity increases.	-
Fry et al. (1950)	ex vivo: Crayfish (Ventral nerve)	Increased spiking and then reversible depression of spontaneous activity.	-

Table B.2: Synopsis of peripheral nervous system studies. AP – action potential, ARF – acoustic radiation force, BDNF – brain derived neurotrophic factor, CAP – compound action potential, CMAP – compound muscle action potential, CW – continuous wave, EMG – electromyography.

* Shock wave source.

C

US neuromodulation parameters

This appendix contains the tabulated data extracted from the CNS and PNS ultrasonic neuromodulation studies, respectively. Where possible, parameters were directly taken from the literature and these are marked in the tables in black. If additional parameters could be calculated from the published parameters, this was done and these parameters are marked in red. Studies have been split into multiple rows where necessary in order to account for different experiments and US sequences. If continuous wave US was used, the burst parameters are undefined and therefore marked with a dash.

The majority of calculations where converting between intensities and pressures. We did this using the following equation assuming a plane time-harmonic wave,

$$I = \frac{p^2}{2\rho_0 c_0}, \tag{C.1}$$

where p is the pressure amplitude, ρ_0 was taken to be $1046\,\mathrm{kg/m^3}$ (Hasgall et al., 2018) and c_0 was $1562\,\mathrm{m/s}$ (Duck, 1990). We also converted between intensities over different time scales (temporal-averaged, burst-averaged and pulse-averaged) using the duty cycle information given in the reference.

Study	Category	Organism	f (MHz)	I_SPTA (mW/cm2)	I_SPBA (W/cm2)	I_SPPA (W/cm2)	p (MPa)	BD (ms)	BI (s)	PL (ms)	PRF (Hz)	BDC (%)	TDC (%)	N	TL (s)	MI	Histology	Damage	Notes
Legon et al., 2018	H	Human (M1)	0.5		0.16	0.44	0.12	500	8-10	0.36	1000	36		100					
Legon et al., 2018	H	Human (Thalamus)	0.5		2.53	7.03	0.48	500	4	0.36	1000	36		300		0.56			
Lee et al., 2016a	H	Human (V1)	0.27		0.85-5.8	1.7-11.6	0.24-0.62	300	2.5, 13	1	500	50		50		0.2-1.2			
Lee et al., 2016b	H	Human (S1, S2)	0.21		3.5-4.4	7-8.8	0.48-0.54	500	7	1	500	50						×	Dual single-element transducers.
Ai et al., 2016	H	Human (S1)	0.5		2.16	6	0.44	500	12.0-14	0.36	1000	36		90				×	
	H	Human(S1)	0.86		3	6	0.44	500		0.5	1000	50						×	
Lee et al., 2015	H	Human (S1)	0.25		0.25-1.25	0.5-2.5	0.13-0.29	300	3	1	500	50						×	
Mueller et al., 2014	H	Human (S1)	0.5		2.12	5.9	0.44	500	6	0.36	1000	36		120				×	
Legon et al., 2014	H	Human (S1)	0.5		2.12	5.9	0.44	500	6	0.36	1000	36		120				×	
Hameroff et al., 2013	H	Human (Posterior Frontal Cortex)	8	152		8.00E-06	5.00E-04								15	0.7		×	LOGIQe imaging probe.p, ISPPA estimated from MI value, derating and accounting for skull.
Kubanek et al., 2017	L	Monkey (Frontal Eye Field)	0.27				0.6	300										×	
Wattiez et al., 2017	L	Monkey (Frontal Eye Field)	0.32		-	1.9,5.6	0.24,0.41	-		100		-		386, 400				×	
Deffieux et al., 2013	L	Monkey (Frontal Eye Field)	0.32	13.5	-	4	0.35	-		100		-				0.6		×	
Dallapiazza et al., 2016	L	Pigs (Thalamus)	0.22		-	30	0.99	-		43.7	10	-			40		✓	×	Assuming ISPPA = ISA.
	L	Pigs (Thalamus)	0.71		-	30	0.99	-		43.7	10	-			40		✓	×	Assuming ISPPA = ISA.
	L	Pigs (Thalamus)	1.145		-	30	0.99	-		43.7	10	-			40		✓	×	Assuming ISPPA = ISA.
Daniels et al., 2018	L	Pig	0.23		-	4.6	0.38	-	3	100		-			52				Quoted pressures do not correspond with intensities. Assumed quoted intensity correct.
	S	Rat	0.23		-	2.3-4.6	0.27-0.38	-	3	100		-			52		✓	×	Quoted pressures do not correspond with intensities. Assumed quoted intensity correct.
Lee et al., 2016	L	Sheep (SM1)	0.25		1.7-5.9	3.4-11.8	0.33-0.62	300	5	1	500	50		100			✓	×	
	L	Sheep (V1)	0.25		0.85-7.15	1.7-14.3	0.24-0.68	300	1	1	500	50		100-600			✓	✓	Damage >500 times every second at moderate (ISPPA 6.6–10.5 W/cm2, MI=0.9–1.2).
Fisher et al., 2018	S	Mouse (Cortex)	0.51			0.69-3.5	0.17	1000		0.5	1000	50					✓	×	
Han et al., 2017	S	Rat (Motor Cortex)	0.35		0.4-4.67	1.16-13.55	0.06-0.69	66.67	2	0.23	1500	34.5							
	S	Rat (Motor Cortex)	0.35		1.19	3.46	0.34	66.67	2	0.23	1500	34.5			20 min		✓	×	
	I	Cortical cell cultures	0.35		0.02	0.056	0.04	66.67	2	0.23	1500	34.5							
Guo et al., 2017	S	Guinea Pig (A1, S1)	0.22			0.33	0.1	500		0.1-10									A1 activation.
	S	Guinea Pig (A1, S1)	0.22		0.73	1.22	0.2			0.1-10	10-1500								First spike latency experiment.
	S	Guinea Pig (A1, S1)	0.22			122	2	10											Auditory nerve transection.
	S	Guinea Pig (A1, S1)	0.22			1.22	0.2	1-6 s		0.5	1000-16000								Indirect somatosensory activation.
	S	Guinea Pig (A1, S1)	0.22			4.89	0.05-0.4	0.5-6 s		0.5-10									Cochlear fluid removed.
Sato et al., 2017	S	Mouse (Visual Cortex)	0.5		0.034-4.2	14	0.68	80		0.2	1500	30							
Gulick et al., 2017	S	Rat (Motor Cortex)	0.2	4500	30	60 (ISPTP = 100)	1.81	300	1-10	0.5	1000	50				3.1		×	US/ECS interaction. ISPPA calculated from quoted table.
	S	Rat (Motor Cortex)	0.2	9	30	60 (ISPTP = 100)	1.81	3	10	0.5	1000	50				3.1		×	EMG latency. ISPPA calculated from quoted table.
Lee et al., 2017	S	Rat	0.25			0.5-11	0.1-1										✓	×	
Li et al., 2016	S	Mouse (Motor Cortex)	1	130-230	2.3	4.6	0.39	300	3	0.5	1000	50	5		60		✓	×	
	S	Mouse (Motor Cortex)	5	130-230	2.3	4.6	0.39	300	3	0.5	1000	50	5		60		✓	×	
Kamimura et al., 2016	S	Mouse (Motor Cortex & Cognitive Areas)	1.9		44.1-275.4	22-137.7	1.2-3	1000	2	1	1000	50		10	20		✓	×	
Darvas et al., 2016	S	Rat	2		1.4	6.8	0.47	1000	2	0.2	1050	21		100	200				Assuming quoted ISPTA is averaged over the burst.
Yu et al., 2016	S	Rat	0.5		0.1-0.6 mW/cm2	0.7-4.6 mW/cm2	18.3-45.9 kPa	5-200	3	0.07	2000	14							38-252 mW/cm2 ISPTP, ring down pulse.
Moore et al., 2015	S	Mouse	0.35		0.03-0.1	0.07-0.23	0.09	10	0.14	0.214	2000	42.8			10 min				
Ye et al., 2015	S	Mouse (Motor Cortex)	0.3,0.4,0.5,0.6		-	0.1-3.5	0.06-0.34	-		66.7-133.3		-							A (planar)
	S	Mouse (Motor Cortex)	0.6,1,1.4		-	0.02-9.4	0.03-0.55	-		80		-							B
	S	Mouse (Motor Cortex)	1.4, 1.9, 2.4, 2.9		-	1.1-127	0.19-2.03	-		80		-							C
	S	Mouse (Motor Cortex)	0.3,0.4,0.5,0.6		-	0.04-3.1	0.04-0.32	-		80		-							D
	S	Mouse (Motor Cortex)	1.4		-	56.9	1.36	-		80		-							E
	S	Mouse (Motor Cortex)	2.9		-	90.7	1.72	-		80		-							E
Kim et al., 2015	S	Rat (Visual Cortex)	0.35	50-250	-	1-5	0.4	-		0.5	20-166	-	1-8.3		150				
King et al., 2014	S	Mouse (Motor Cortex)	0.5		-	3	0.2	-		80		-							
Kim et al., 2014a	S	Rat (Motor Cortex)	0.35		2.45-11.2	4.91-22.4	0.4-0.81	200-400	2	0.25-5	60-2800	30-70			1.38		✓	✓	Damage at 22.4 W/cm2 ISPPA, 300 ms, 3 bursts.
	S	Rat (Motor Cortex)	0.35		-	7.73	0.5	-		150		-					✓	×	
	S	Rat (Motor Cortex)	0.65		3.5-5	7-10	0.48-0.57	300		0.5-5	100-1000	50					✓	×	
Kim et al., 2014b	S	Rat (Thalamus)	0.35		3.5-4.5	7-9	0.48-0.54	300	2	0.5	1000	50			40 min				
	S	Rat (Thalamus)	0.35		3.5-4.5			300		0.25-5		30-70			40 min				PL and PDC variation.
Mehic et al., 2014	S	Rat (Motor Cortex)	0.5		0.15 - 5.25	0.5-17.5	0.13-0.76	58.7	1	0.2	1500	30		10	10		✓	×	Planar transducer.
	S	Rat (Motor Cortex)	1.75 & 2.25		1-8	3.3-26.7	0.18-0.93	14.7-58.7		0.1-0.2	1500	15-30		10	10		✓	×	mFU: two frequencies separated by 500 kHz.
Younan et al., 2013	S	Rat (Motor Cortex)	0.32		8.75	17.5	1.2	250		0.23	2000	50				2.2		×	Incorporates correction factor for standing waves.
King et al., 2013	S	Mouse (Motor Cortex)	0.5		-	0-16.8	0-0.51	-	>5	80		-							Acoustic intensity sweep.
	S	Mouse (Motor Cortex)	0.5		-	4.2	0.37	-		0-320		-							Sonication duration.
	S	Mouse (Motor Cortex)	0.25-0.6		-			-		40,000 cycles		-							Frequency sweep.
	S	Mouse (Motor Cortex)	0.5		23.7	0-79.02	0.03-1.11			0.2	1500								Pulsed v. CW.
	S	Mouse (Motor Cortex)	0.5		8.97	4.2-29.9	0.37-0.99	80		0.2	11-3000	30							Pulsed.
	S	Mouse (Motor Cortex)	0.5		-	0-16.8	0-0.51	-		0-480		-							Full CW parameter sweep.
Yang et al., 2012	S	Rat (Thalamus)	0.65	175	-	3.5	0.35	-		0.5	100	-			20 min		✓	×	
Yoo et al., 2011a	S	Rabbit (Somatomotor & Visual Areas)	0.69		1.6-6.3	3.3-12.6	0.64	0.5-2		0.05-50	10-1000	50					✓	×	
Yoo et al., 2011b	S	Rat (Thalamus)	0.65	300	-	6	0.49	-		0.5	100	-			20 min	0.61			
Min et al., 2011a	S	Rat (Thalamus)	0.69	130	-	2.6	0.27	-		0.5	100	-	5		2x3 min	0.33	✓	×	
Min et al., 2011b	S	Rat (Thalamus)	0.65	175	-	3.5	0.35	-		0.5	100	-	5		20 min	0.2			
Tufail et al., 2010	S	Mouse (Motor Cortex)	0.35		0.0362			229			1500								Initial LFP recordings and MUA in M1.
	S	Mouse (Motor Cortex)	0.5		0.06453	0.228	0.086	160			1500								Bilateral M1 stimuation.
	S	Mouse (Motor Cortex)	0.25		0.061-0.123	0.242	0.089	53-83		0.32-0.48	1200-1500	38.4-72				0.18			M1 parameter sweep.
	S	Mouse (Motor Cortex)	0.35		0.021-0.066	0.159	0.072	27-83		0.229-0.571	1200-2500	27.5-85.7				0.12			M1 parameter sweep.
	S	Mouse (Motor Cortex)	0.425		0.029-0.075	0.211	0.083	50-333		0.188-0.235	1500-3000	28.2-70.5				0.13			M1 parameter sweep.
	S	Mouse (Motor Cortex)	0.5		0.041-0.163	0.259-0.288	0.092-0.097	27-83		0.16-0.45	1200-2500	19.2-75				0.13-0.14			M1 parameter sweep.
	S	Mouse (Motor Cortex)	0.5		0.142-0.3			67.2	10	0.45	1500				30 min		✓	×	BBB disruption check.
	S	Mouse (Hippocampus)	0.25		0.084					0.16	2000								
Koroleva et al., 1986	S	Rat (Various)	4.6		-	5-100 V/cm2	0.9-3.5	-		10-100	5-10	-			10-40				BBB disruption.
Ballantine et al., 1960	S	Cat (Edinger-Westphal Nucleus)	2.7		-	1700	7.45		3	140	0.33			1-59			✓	✓	Lesions in 14 Cats (N=1-59) and not in 6 others (N=1-13).

Study	Category	Organism	f (MHz)	I_SPTA (mW/cm2)	I_SPBA (W/cm2)	I_SPPA (W/cm2)	p (MPa)	BD (ms)	BI (s)	PL (ms)	PRF (Hz)	BDC (%)	TDC (%)	N	TL (s)	MI	Histology	Damage	Notes
Legon et al., 2018	H	Human (M1)	0.5		0.16	0.44	0.12	500	8-10	0.36	1000	36		100					
Legon et al., 2018	H	Human (Thalamus)	0.5		2.53	7.03	0.48	500	4	0.36	1000	36		300		0.56			
Lee et al., 2016a	H	Human (V1)	0.27		0.85-5.8	1.7-11.6	0.24-0.62	300	2.5, 13	1	500	50		50		0.2-1.2			
Lee et al., 2016b	H	Human (S1, S2)	0.21		3.5-4.4	7-8.8	0.48-0.54	500	7	1	500	50						×	Dual single-element transducers.
Ai et al., 2016	H	Human (S1)	0.5		2.16	6	0.44	500	12.0-14	0.36	1000	36		90				×	
	H	Human(S1)	0.86		3	6	0.44	500		0.5	1000	50						×	
Lee et al., 2015	H	Human (S1)	0.25		0.25-1.25	0.5-2.5	0.13-0.29	300	3	1	500	50						×	
Mueller et al., 2014	H	Human (S1)	0.5		2.12	5.9	0.44	500	6	0.36	1000	36		120				×	
Legon et al., 2014	H	Human (S1)	0.5		2.12	5.9	0.44	500	6	0.36	1000	36		120				×	
Hameroff et al., 2013	H	Human (Posterior Frontal Cortex)	8	152		8.00E-06	5.00E-04								15	0.7		×	LOGIQe imaging probe.p, ISPPA estimated from MI value, derating and accounting for skull.
Kubanek et al., 2017	L	Monkey (Frontal Eye Field)	0.27				0.6	300										×	
Wattiez et al., 2017	L	Monkey (Frontal Eye Field)	0.32		-	1.9,5.6	0.24,0.41	-		100		-		386, 400				×	
Deffieux et al., 2013	L	Monkey (Frontal Eye Field)	0.32	13.5	-	4	0.35	-		100		-				0.6		×	
Dallapiazza et al., 2016	L	Pigs (Thalamus)	0.22		-	30	0.99	-		43.7	10	-			40		✓	×	Assuming ISPPA = ISA.
	L	Pigs (Thalamus)	0.71		-	30	0.99	-		43.7	10	-			40		✓	×	Assuming ISPPA = ISA.
	L	Pigs (Thalamus)	1.145		-	30	0.99	-		43.7	10	-			40		✓	×	Assuming ISPPA = ISA.
Daniels et al., 2018	L	Pig	0.23		-	4.6	0.38	-	3	100		-			52				Quoted pressures do not correspond with intensities. Assumed quoted intensity correct.
	S	Rat	0.23		-	2.3-4.6	0.27-0.38	-	3	100		-			52		✓	×	Quoted pressures do not correspond with intensities. Assumed quoted intensity correct.
Lee et al., 2016	L	Sheep (SM1)	0.25		1.7-5.9	3.4-11.8	0.33-0.62	300	5	1	500	50		100			✓	×	
	L	Sheep (V1)	0.25		0.85-7.15	1.7-14.3	0.24-0.68	300	1	1	500	50		100-600			✓	✓	Damage >500 times every second at moderate (ISPPA 6.6–10.5 W/cm2, MI=0.9–1.2).
Fisher et al., 2018	S	Mouse (Cortex)	0.51			0.69-3.5	0.17	1000		0.5	1000	50					✓	×	
Han et al., 2017	S	Rat (Motor Cortex)	0.35		0.4-4.67	1.16-13.55	0.06-0.69	66.67	2	0.23	1500	34.5							
	S	Rat (Motor Cortex)	0.35		1.19	3.46	0.34	66.67	2	0.23	1500	34.5			20 min		✓	×	
	I	Cortical cell cultures	0.35		0.02	0.056	0.04	66.67	2	0.23	1500	34.5							
Guo et al., 2017	S	Guinea Pig (A1, S1)	0.22			0.33	0.1	500		0.1-10									A1 activation.
	S	Guinea Pig (A1, S1)	0.22		0.73	1.22	0.2			0.1-10	10-1500								First spike latency experiment.
	S	Guinea Pig (A1, S1)	0.22			122	2	10											Auditory nerve transection.
	S	Guinea Pig (A1, S1)	0.22			1.22	0.2	1-6 s		0.5	1000-16000								Indirect somatosensory activation.
	S	Guinea Pig (A1, S1)	0.22			4.89	0.05-0.4	0.5-6 s		0.5-10									Cochlear fluid removed.
Sato et al., 2017	S	Mouse (Visual Cortex)	0.5		0.034-4.2	14	0.68	80		0.2	1500	30							
Gulick et al., 2017	S	Rat (Motor Cortex)	0.2	4500	30	60 (ISPTP = 100)	1.81	300	1-10	0.5	1000	50				3.1		×	US/ECS interaction. ISPPA calculated from quoted table.
	S	Rat (Motor Cortex)	0.2	9	30	60 (ISPTP = 100)	1.81	3	10	0.5	1000	50				3.1		×	EMG latency. ISPPA calculated from quoted table.
Lee et al., 2017	S	Rat	0.25			0.5-11	0.1-1										✓	×	
Li et al., 2016	S	Mouse (Motor Cortex)	1	130-230	2.3	4.6	0.39	300	3	0.5	1000	50	5		60		✓	×	
	S	Mouse (Motor Cortex)	5	130-230	2.3	4.6	0.39	300	3	0.5	1000	50	5		60		✓	×	
Kamimura et al., 2016	S	Mouse (Motor Cortex & Cognitive Areas)	1.9		44.1-275.4	22-137.7	1.2-3	1000	2	1	1000	50		10	20		✓	×	
Darvas et al., 2016	S	Rat	2		1.4	6.8	0.47	1000	2	0.2	1050	21		100	200				Assuming quoted ISPTA is averaged over the burst.
Yu et al., 2016	S	Rat	0.5		0.1-0.6 mW/cm2	0.7-4.6 mW/cm2	18.3-45.9 kPa	5-200	3	0.07	2000	14							38-252 mW/cm2 ISPTP, ring down pulse.
Moore et al., 2015	S	Mouse	0.35		0.03-0.1	0.07-0.23	0.09	10	0.14	0.214	2000	42.8			10 min				
Ye et al., 2015	S	Mouse (Motor Cortex)	0.3,0.4,0.5,0.6		-	0.1-3.5	0.06-0.34	-		66.7-133.3		-							A (planar)
	S	Mouse (Motor Cortex)	0.6,1,1.4		-	0.02-9.4	0.03-0.55	-		80		-							B
	S	Mouse (Motor Cortex)	1.4, 1.9, 2.4, 2.9		-	1.1-127	0.19-2.03	-		80		-							C
	S	Mouse (Motor Cortex)	0.3,0.4,0.5,0.6		-	0.04-3.1	0.04-0.32	-		80		-							D
	S	Mouse (Motor Cortex)	1.4		-	56.9	1.36	-		80		-							E
	S	Mouse (Motor Cortex)	2.9		-	90.7	1.72	-		80		-							E
Kim et al., 2015	S	Rat (Visual Cortex)	0.35	50-250	-	1-5	0.4	-		0.5	20-166	-	1-8.3		150				
King et al., 2014	S	Mouse (Motor Cortex)	0.5		-	3	0.2	-		80		-							
Kim et al., 2014a	S	Rat (Motor Cortex)	0.35		2.45-11.2	4.91-22.4	0.4-0.81	200-400	2	0.25-5	60-2800	30-70			1.38		✓	✓	Damage at 22.4 W/cm2 ISPPA, 300 ms, 3 bursts.
	S	Rat (Motor Cortex)	0.35		-	7.73	0.5	-		150		-					✓	×	
	S	Rat (Motor Cortex)	0.65		3.5-5	7-10	0.48-0.57	300		0.5-5	100-1000	50					✓	×	
Kim et al., 2014b	S	Rat (Thalamus)	0.35		3.5-4.5	7-9	0.48-0.54	300	2	0.5	1000	50			40 min				
	S	Rat (Thalamus)	0.35		3.5-4.5			300		0.25-5		30-70			40 min				PL and PDC variation.
Mehic et al., 2014	S	Rat (Motor Cortex)	0.5		0.15 - 5.25	0.5-17.5	0.13-0.76	58.7	1	0.2	1500	30		10	10		✓	×	Planar transducer.
	S	Rat (Motor Cortex)	1.75 & 2.25		1-8	3.3-26.7	0.18-0.93	14.7-58.7		0.1-0.2	1500	15-30		10	10		✓	×	mFU: two frequencies separated by 500 kHz.
Younan et al., 2013	S	Rat (Motor Cortex)	0.32		8.75	17.5	1.2	250		0.23	2000	50				2.2		×	Incorporates correction factor for standing waves.
King et al., 2013	S	Mouse (Motor Cortex)	0.5		-	0-16.8	0-0.51	-	>5	80		-							Acoustic intensity sweep.
	S	Mouse (Motor Cortex)	0.5		-	4.2	0.37	-		0-320		-							Sonication duration.
	S	Mouse (Motor Cortex)	0.25-0.6		-			-		40,000 cycles		-							Frequency sweep.
	S	Mouse (Motor Cortex)	0.5		23.7	0-79.02	0.03-1.11			0.2	1500								Pulsed v. CW.
	S	Mouse (Motor Cortex)	0.5		8.97	4.2-29.9	0.37-0.99	80		0.2	11-3000	30							Pulsed.
	S	Mouse (Motor Cortex)	0.5		-	0-16.8	0-0.51	-		0-480		-							Full CW parameter sweep.
Yang et al., 2012	S	Rat (Thalamus)	0.65	175	-	3.5	0.35	-		0.5	100	-			20 min		✓	×	
Yoo et al., 2011a	S	Rabbit (Somatomotor & Visual Areas)	0.69		1.6-6.3	3.3-12.6	0.64	0.5-2		0.05-50	10-1000	50					✓	×	
Yoo et al., 2011b	S	Rat (Thalamus)	0.65	300	-	6	0.49	-		0.5	100	-			20 min	0.61			
Min et al., 2011a	S	Rat (Thalamus)	0.69	130	-	2.6	0.27	-		0.5	100	-	5		2x3 min	0.33	✓	×	
Min et al., 2011b	S	Rat (Thalamus)	0.65	175	-	3.5	0.35	-		0.5	100	-	5		20 min	0.2			
Tufail et al., 2010	S	Mouse (Motor Cortex)	0.35		0.0362			229			1500								Initial LFP recordings and MUA in M1.
	S	Mouse (Motor Cortex)	0.5		0.06453	0.228	0.086	160			1500								Bilateral M1 stimuation.
	S	Mouse (Motor Cortex)	0.25		0.061-0.123	0.242	0.089	53-83		0.32-0.48	1200-1500	38.4-72				0.18			M1 parameter sweep.
	S	Mouse (Motor Cortex)	0.35		0.021-0.066	0.159	0.072	27-83		0.229-0.571	1200-2500	27.5-85.7				0.12			M1 parameter sweep.
	S	Mouse (Motor Cortex)	0.425		0.029-0.075	0.211	0.083	50-333		0.188-0.235	1500-3000	28.2-70.5				0.13			M1 parameter sweep.
	S	Mouse (Motor Cortex)	0.5		0.041-0.163	0.259-0.288	0.092-0.097	27-83		0.16-0.45	1200-2500	19.2-75				0.13-0.14			M1 parameter sweep.
	S	Mouse (Motor Cortex)	0.5		0.142-0.3			67.2	10	0.45	1500				30 min		✓	×	BBB disruption check.
	S	Mouse (Hippocampus)	0.25		0.084					0.16	2000								
Koroleva et al., 1986	S	Rat (Various)	4.6		-	5-100 V/cm2	0.9-3.5	-		10-100	5-10	-			10-40				BBB disruption.
Ballantine et al., 1960	S	Cat (Edinger-Westphal Nucleus)	2.7		-	1700	7.45		3	140	0.33			1-59			✓	✓	Lesions in 14 Cats (N=1-59) and not in 6 others (N=1-13).

Study	Category	Organism	f (MHz)	I_SPTA (mW/cm2)	I_SPBA (W/cm2)	I_SPPA (W/cm2)	p (MPa)	BD (ms)	BI (s)	PL (ms)	PRF (Hz)	BDC (%)	TDC (%)	N	TL (s)	MI	Histology	Damage	Notes
Lee et al., 2014	H	Human (Fingertip)	0.35	3-100	0.003-0.1	0.3-10	0.118-1.148	10 s		0.1-1	10-100	1				0.1-0.97		×	
	H	Human (Fingertip)	0.65	3-100	0.003-0.1	0.3-10	0.21-1.145	10 s		0.1-1	10-100	1				0.13-0.71		×	
Legon et al., 2012	H	Human (Fingertip)	0.35		11.8	84.3	1.66	500	12	2	70	14	3x50						
	H	Human (Fingertip)	0.35		54.8	54.8	1.34	1000	12	10	100	100	3x50						
Dickey et al., 2012	H	Human (Fingertip)	1.117		-	0-410	3.66	-		100		-						×	
Gavrilov et al., 1977a	H	Human (Hand, forearm)	0.48		-	0-590	0-4.39	-		1-100		-						×	Pain thresholds
	H	Human (Hand, forearm)	0.887		-	0-8000	0-16.17	-		1-100		-						×	Pain thresholds
	H	Human (Hand, forearm)	2.67		-	0-30000	0-31.3	-		1-100		-						×	Pain thresholds
Downs et al., 2018	S	Mouse (Sciatic Nerve)	3.57		348-994	207-994	2.6-5.7	0.8-10.5			1000	35-100					✓	×	Successful parameters for EMG activity
	S	Mouse (Sciatic Nerve)	3.57		42.7-155	122-442	2-3.8	1			1000	35					✓	×	
	S	Mouse (Sciatic Nerve)	3.57		894	994	5.7	30			1000	90					✓	✓	
	S	Mouse (Sciatic Nerve)	3.57		803	892	5.4	500			1000	90					✓	✓	Positive control
Casella et al., 2017	S	Rat (Micturition Reflex)	0.25		2.1	28	0.95	300	2	0.252	2000				5-15 min				
Ni et al., 2016	S	Rat (Sciatic Nerve)	1	0.2											1 min/day				
Juan et al., 2014	S	Rat (Vagus Nerve)	1.1		13.6-93.4	74.8-102.8	1.83	15 s			200-1000	18.2-90.9				1.43-1.67			
Tych et al., 2013	S	Rat (Sciatic Nerve)	1.15		-	50-283	3.04	-		200		-							
Kim et al., 2012	S	Rat (Abducens Nerve)	0.35		4.6	8.6	0.53	200	1	0.36	1500	54		10			✓	×	8.6W/cm2 min for response.
	S	Rat (Abducens Nerve)	0.65		0.27-10.8	0.5-20	0.8	200	1	0.36	1500	54		10			✓	×	No responses.
Foley et al., 2008	S	Rat (Sciatic Nerve)	5.7		-	390	3.57	-		5 s		-					✓	×	
	S	Rat (Sciatic Nerve)	5.7		-	2255-7890	16.1	-		5 s		-					✓	✓	
Ellisman et al., 1987	S	Rat (Dorsal Nerve Roots)	2.4			1.9 (ISPTP=8.7)	0.53										✓	✓	Nerves in developing myelination stage
Gavrilov et al., 1977b	S	Cat (Pacinian Corpuscle)	0.48		-	0.4-2.5	0.11-0.29	-		0.1		-							
	S	Frog (Ear labyrinth)	0.48		-	0.01-1	0.02-0.18	-		1-100		-							
Lele et al., 1963	S	Earthworm (Giant Axon)	0.6		-	41	1.16	-	1	500		-					✓	✓	Damage for longer durations/intensities
	S	Earthworm (Giant Axon)	0.9		-	139.2	2.13	-	3	1400-2000		-					✓	✓	
	S	Earthworm (Giant Axon)	2.7		-	420	3.7	-		100-2000		-					✓	✓	
Young & Henneman, 1961	S	Cat (Saphenous Nerve)			-	700-800 V		-	2-3	400-900		-							
Wahab et al., 2012	S	Earthworm (Giant Axon)	0.825			0.1-15	0.1-0.7	15-75		50 us	100	0.5						✓	
Wright et al., 2017	I	Crab Leg Nerve Axon	0.67		10-84.5	20-169	1.8-2.4	8			10000	50			22 min			×	
	I	Crab Leg Nerve Axon	0.67		115-281	230-562	2.9-4.7	8			10000	50						✓	
	I	Crab Leg Nerve Axon	0.67		10-281	20-562	2.4-4.7	100			10000	50						✓	
	I	Crab Leg Nerve Axon	0.67		84.5	169	2.4-4.7	300		1	500	50						×	Lee et al., 2016 parameter replication
	I	Crab Leg Nerve Axon	1.1			17-475	0.7-4.2								22 min			×	No responses
	I	Crab Leg Nerve Axon	2			12-343	0.5-3.6								22 min			×	No responses
Colucci et al., 2009	I	Bullfrog (Sciatic Nerve)	0.661		-	100-575	1.81-4.33	-	1.5	30 s		-					✓	✓	Damage at higher intensities
	I	Bullfrog (Sciatic Nerve)	1.986		-	100-875	1.81-5.35	-	1.5	30 s		-							
	I	Bullfrog (Sciatic Nerve)	0.661					30 s	1.5	1-10	10-20								
	I	Bullfrog (Sciatic Nerve)	1.986					30 s	1.5	1-10	10-20								
Tsui et al., 2005	I	Bullfrog (Sciatic Nerve)	3.5		-	1-3 W		-		5 min		-							
Mihran et al., 1990	I	Frog (Sciatic Nerve)	2		-	0-40	0-1.14	-		0.5		-							
	I	Frog (Sciatic Nerve)	4		-	0-40	0-1.14	-		0.5		-							
Fry et al., 1950	I	Crayfish (Ventral Nerve)	0.98		35		1.07	2.8-43.5		0.5 - CW									

Bibliography

Society Guidelines for the safe use of diagnostic ultrasound equipment. *The British Medical Ultrasound Society*, 2010.

Ai, L., Bansal, P., Mueller, J.K., and Legon, W. Effects of transcranial focused ultrasound on human primary motor cortex using 7T fMRI : a pilot study. *BMC Neuroscience*, 19(56):1–10, 2018.

Ai, L., Mueller, J.K., Grant, A., Eryaman, Y., and Legon, W. Transcranial focused ultrasound for BOLD fMRI signal modulation in humans. *Proceedings of the 38th Annual International Conference of the IEEE Engineering in Medicine and Biology Society*, 1758–1761, 2016.

Airan, R.D., Meyer, R.A., Ellens, N.P., Rhodes, K.R., Farahani, K., et al. Noninvasive Targeted Transcranial Neuromodulation via Focused Ultrasound Gated Drug Release from Nanoemulsions. *Nano Letters*, 17(2):652–659, 2017.

Alonso, A., Reinz, E., Leuchs, B., Kleinschmidt, J., Fatar, M., et al. Focal delivery of AAV2/1-transgenes into the rat brain by localized ultrasound-induced BBB Opening. *Molecular Therapy-Nucleic Acids*, 2:e73, 2013.

Amiez, C., Joseph, J.P., and Procyk, E. Reward encoding in the monkey anterior cingulate cortex. *Cerebral Cortex*, 16(7):1040–1055, 2006.

Apfel, R.E. and Holland, C.K. Gauging the likelihood of cavitation from short-pulse, low-duty cycle diagnostic ultrasound. *Ultrasound in Medicine and Biology*, 17(2):179–185, 1991.

Ashkan, K., Rogers, P., Bergman, H., and Ughratdar, I. Insights into the mechanisms of deep brain stimulation. *Nature Reviews Neurology*, 13(9):548–554, 2017.

Aubry, J.F., Tanter, M., Pernot, M., Thomas, J.L., and Fink, M. Experimental demonstration of noninvasive transskull adaptive focusing based on prior computed tomography scans. *The Journal of the Acoustical Society of America*, 113(1):84–93, 2003.

Bachtold, M.R., Rinaldi, P.C., Jones, J.P., Reines, F., and Price, L.R. Focused Ultrasound Modifications of Neural Circuit Activity in a Mammalian Brain. *Ultrasound in Medicine and Biology*, 24(4):557–565, 1998.

Bader, K.B. and Holland, C.K. Gauging the likelihood of stable cavitation from ultrasound contrast agents. *Physics in Medicine and Biology*, 58(1):127–144, 2013.

Ballantine, H.T., Bell, E., and Manlapaz, J. Progress and problems in the neurological applications of focused ultrasound. *Journal of Neurosurgery*, 17:858–876, 1960.

Blackmore, J., Cleveland, R.O., and Mobley, J. Spatial filters suppress ripple artifacts in the computation of acoustic fields with the angular spectrum method. *The Journal of the Acoustical Society of America*, 144(5):2947–2951, 2018.

Blackmore, J., Shrivastava, S., Sallet, J., Butler, C.R., and Cleveland, R.O. Ultrasound neuromodulation; a review of results, mechanisms and safety. *Ultrasound in Medicine and Biology*, In press, 2019.

Blackstock, D.T. *Fundamentals of Physical Acoustics*. John Wiley & Sons, 2000.

Bootman, M.D., Rietdorf, K., Collins, T., Walker, S., and Sanderson, M. Ca2+-sensitive fluorescent dyes and intracellular Ca2+ imaging. *Cold Spring Harbor protocols*, 2013(2):83–99, 2013.

Born, R. and Bradley, D. Structure and Function of Visual Area MT. *Annual Review of Neuroscience*, 28(1):157–189, 2005.

Boyden, E. A history of optogenetics: the development of tools for controlling brain circuits with light. *F1000 Biology Reports*, 3(May):1–12, 2011.

Brainard, D.H. The Psychophysics Toolbox. *Spatial Vision*, 10:433–436, 1997.

Brette, R. and Destexhe, A. Intracellular Recording. *Handbook of Neural Activity Handbook*, 44–91. 2012.

Brohawn, S.G. How ion channels sense mechanical force: Insights from mechanosensitive K2P channels TRAAK, TREK1, and TREK2. *Annals of the New York Academy of Sciences*, 1352(1):20–32, 2015.

Bulychev, A.A., Kamzolkina, N.A., Luengviriya, J., Rubin, A.B., and Müller, S.C. Effect of a single excitation stimulus on photosynthetic activity and light-dependent pH banding in Chara cells. *Journal of Membrane Biology*, 202(1):11–19, 2004.

Buzsáki, G., Anastassiou, C.A., and Koch, C. The origin of extracellular fields and currents – EEG, ECoG, LFP and spikes. *Nature Reviews Neuroscience*, 13(6):407–420, 2012.

Carter, D.R. and Hayes, W.C.. The Compressive Behavior Porous of Bone Structure as a Two-Phase. *The Journal of Bone and Joint Surgery*, 59(7):954–962, 1977.

Casella, D.P., Dudley, A.G., Clayton, D.B., Pope, J.C., Tanaka, S.T., et al. Modulation of the rat micturition reflex with transcutaneous ultrasound. *Neurourology and Urodynamics*, 36(8):1996–2002, 2017.

Cesare, P., Moriondo, A., Vellani, V., and McNaughton, P.A. Ion channels gated by heat. *Proceedings of the National Academy of Sciences*, 96(14):7658–7663, 1999.

Chaffaï, S., Padilla, F., Berger, G., and Laugier, P. In vitro measurement of the frequency-dependent attenuation in cancellous bone between 0.2 and 2 MHz. *The Journal of the Acoustical Society of America*, 108(3):1281–1289, 2000.

Chapman, R. Dependence on temperature of the conduction velocity of the action potential of the squid giant axon. *Nature*, 213(5081):1143–1144, 1967.

Chauvet, D., Marsac, L., Pernot, M., Boch, A.L., Guillevin, R., et al. Targeting accuracy of transcranial magnetic resonance–guided high-intensity focused ultrasound brain therapy: a fresh cadaver model. *Journal of Neurosurgery*, 118:1046–1052, 2013.

Chen, X., Schwarz, K.Q., and Parker, K.J. Radiation pattern of a focused transducer: a numerically convergent solution. *The Journal of the Acoustical Society of America*, 94(5):2979–2991, 1993.

Chernov, M. and Roe, A.W. Infrared neural stimulation: a new stimulation tool for central nervous system applications. *Neurophotonics*, 1(1):011011, 2014.

Chesler, M. Regulation and Modulation of pH in the Brain. *Physiological Reviews*, 83(4):1183–1221, 2003.

Choi, J.B., Lim, S.H., Cho, K.W., Kim, D.H., Jang, D.P., et al. The effect of focused ultrasonic stimulation on the activity of hippocampal neurons in multichannel electrode. *International IEEE/EMBS Conference on Neural Engineering*, 731–734. 2013.

Chu, P.C., Liu, H.L., Lai, H.Y., Lin, C.Y., Tsai, H.C., et al. Neuromodulation accompanying focused ultrasound-induced blood-brain barrier opening. *Scientific Reports*, 5:15477, 2015.

Church, C.C., Labuda, C., and Nightingale, K. A theoretical study of inertial cavitation from acoustic radiation force impulse (ARFI) imaging and implications for the mechanical index. *Ultrasound in Medicine and Biology*, 41(2):472–485, 2015.

Cirillo, G., Di Pino, G., Capone, F., Ranieri, F., Florio, L., et al. Neurobiological after-effects of non-invasive brain stimulation. *Brain Stimulation*, 10(1):1–18, 2016.

Clement, G.T. and Hynynen, K. A non-invasive method for focusing ultrasound through the human skull. *Physics in Medicine and Biology*, 47:1219–1236, 2002a.

Clement, G.T. and Hynynen, K. Correlation of ultrasound phase with physical skull properties. *Ultrasound in Medicine and Biology*, 28(5):617–624, 2002b.

Clement, G.T. and Hynynen, K. Micro-receiver guided transcranial beam steer-

ing. *IEEE Transactions on Ultrasonics, Ferroelectrics, and Frequency Control*, 49(4):447–453, 2002c.

Clement, G.T., White, P.J., and Hynynen, K. Enhanced ultrasound transmission through the human skull using shear mode conversion. *The Journal of the Acoustical Society of America*, 115(3):1356–1364, 2004.

Colucci, V., Strichartz, G., Jolesz, F., Vykhodtseva, N., and Hynynen, K. Focused Ultrasound Effects on Nerve Action Potential in vitro. *Ultrasound in Medicine and Biology*, 35(10):1737–1747, 2009.

Constans, C., Deffieux, T., Pouget, P., Tanter, M., and Aubry, J.F. A 200-1380-kHz Quadrifrequency Focused Ultrasound Transducer for Neurostimulation in Rodents and Primates: Transcranial in Vitro Calibration and Numerical Study of the Influence of Skull Cavity. *IEEE Transactions on Ultrasonics, Ferroelectrics, and Frequency Control*, 64(4):717–724, 2017.

Constans, C., Mateo, P., Tanter, M., and Aubry, J.F. Potential impact of thermal effects during ultrasonic neurostimulation : retrospective numerical estimation of temperature elevation in seven rodent setups. *Physics in Medicine and Biology*, 63(2):025003, 2018.

Coussios, C.C. and Roy, R.A. Applications of Acoustics and Cavitation to Noninvasive Therapy and Drug Delivery. *Annual Review of Fluid Mechanics*, 40(1):395–420, 2008.

Cox, B.T., Kara, S., Arridge, S.R., and Beard, P.C. k-space propagation models for acoustically heterogeneous media: Application to biomedical photoacoustics. *The Journal of the Acoustical Society of America*, 121(6):3453–3464, 2007.

Dalecki, D. Mechanical Bioeffects of Ultrasound. *Annual Review of Biomedical Engineering*, 6(1):229–248, 2004.

Dallapiazza, R.F., Timbie, K.F., Holmsberg, S., Gatesman, J., Lopes, M.B., et al. Noninvasive neuromodulation and thalamic mapping with low-intensity focused ultrasound. *Journal of Neurosurgery*, 128:875–884, 2018.

Daniels, D., Sharabi, S., Last, D., Guez, D., Salomon, S., et al. Focused Ultrasound-Induced Suppression of Auditory Evoked Potentials in Vivo. *Ultrasound in Medicine and Biology*, 44(5):1022–1030, 2018.

Darvas, F., Mehić, E., Caler, C.J., Ojemann, J.G., and Mourad, P.D. Toward Deep Brain Monitoring with Superficial EEG Sensors Plus Neuromodulatory Focused Ultrasound. *Ultrasound in Medicine and Biology*, 42(8):1834–1847, 2016.

Deffieux, T., Younan, Y., Wattiez, N., Tanter, M., Pouget, P., et al. Low-intensity focused ultrasound modulates monkey visuomotor behavior. *Current Biology*, 23(23):2430–2433, 2013.

Deng, Z.D., Lisanby, S.H., and Peterchev, A.V. Electric field depth–focality tradeoff in transcranial magnetic stimulation: simulation comparison of 50 coil designs. *Brain Stimulation*, 6(1):1–13, 2013.

Dickey, T.C., Tych, R., Kliot, M., Loeser, J.D., Pederson, K., et al. Intense Focused Ultrasound Can Reliably Induce Sensations in Human Test Subjects in a Manner Correlated With the Density of Their Mechanoreceptors. *Ultrasound in Medicine and Biology*, 38(1):85–90, 2012.

Downs, M.E., Buch, A., Karakatsani, M.E., Konofagou, E.E., and Ferrera, V.P. Blood-Brain Barrier Opening in Behaving Non-Human Primates via Focused Ultrasound with Systemically Administered Microbubbles. *Scientific Reports*, 5:15076, 2015.

Downs, M.E., Lee, S.A., Yang, G., Kim, S., Wang, Q., et al. Non-invasive peripheral nerve stimulation via focused ultrasound in vivo. *Physics in Medicine and Biology*, 63(3):035011, 2018.

Duck, F.A. *Physical properties of tissues: a comprehensive reference book*. 1990.

Duck, F.A. Medical and non-medical protection standards for ultrasound and infrasound. *Progress in Biophysics and Molecular Biology*, 93(1-3):176–191, 2007.

Duck, F.A. Hazards, risks and safety of diagnostic ultrasound. *Medical Engineering and Physics*, 30(10):1338–1348, 2008.

Eames, M.D., Hananel, A., Snell, J.W., Kassell, N.F., and Aubry, J.F. Trans-cranial focused ultrasound without hair shaving: feasibility study in an ex vivo cadaver model. *Journal of Therapeutic Ultrasound*, 1(24), 2013.

El Hady, A. and Machta, B.B. Mechanical surface waves accompany action potential propagation. *Nature Communications*, 6:1–7, 2015.

Elias, W.J., Huss, D., Voss, T., Loomba, J., Khaled, M., et al. A pilot study of focused ultrasound thalamotomy for essential tremor. *The New England Journal of Medicine*, 369(7):640–648, 2013.

Ellisman, M.H., Palmer, D.E., and André, M.P. Diagnostic levels of ultrasound may disrupt myelination. *Experimental Neurology*, 98(1):78–92, 1987.

Falleroni, F., Torre, V., and Cojoc, D. Cell Mechanotransduction With Piconewton Forces Applied by Optical Tweezers. *Frontiers in Cellular Neuroscience*, 12(May):1–11, 2018.

Faria, P., Hallett, M., and Miranda, P.C. A finite element analysis of the effect of electrode area and inter- electrode distance on the spatial distribution of the current density in tDCS. *Journal of Neural Rngineering*, 8(6):1–24, 2012.

Fellah, Z.E.A., Chapelon, J.Y., Berger, S., Lauriks, W., and Depollier, C. Ultrasonic wave propagation in human cancellous bone : Application of Biot theory. *Journal of the Acoustical Society of America*, 116(1):61–73, 2004.

Fenno, L., Yizhar, O., and Deisseroth, K. The Development and Application of Optogenetics. *Annual Review of Neuroscience*, 34(1):389–412, 2011.

Fields, R.D. A new mechanism of nervous system plasticity: Activity-dependent myelination. *Nature Reviews Neuroscience*, 16(12):756–767, 2015.

Fink, M. Time reversal of ultrasonic fields. I. Basic principles. *IEEE Transactions on Ultrasonics, Ferroelectrics and Frequency Control*, 39(5):555–566, 1992.

Fink, M., Montaldo, G., and Tanter, M. Time-reversal acoustics in biomedical engineering. *Annual Review of Biomedical Engineering*, 5:465–97, 2003.

Firouzi, K., Cox, B.T., Treeby, B.E., and Saffari, N. A first-order k -space model for elastic wave propagation in heterogeneous media. *The Journal of the Acoustical Society of America*, 132(3):1271–1283, 2012.

Fisher, J.A.N. and Gumenchuk, I. Low-intensity focused ultrasound alters the latency and spatial patterns of sensory-evoked cortical responses in vivo. *Journal of Neural Engineering*, 15(3):035004, 2018.

Flesher, S., Collinger, J., Foldes, S., Weiss, J., Downey, J., et al. Intracortical microstimulation of human somatosensory cortex. *Science Translational Medicine*, 8(361):1–11, 2016.

Foley, J.L., Little, J.W., and Vaezy, S. Effects of high-intensity focused ultrasound on nerve conduction. *Muscle and Nerve*, 37(2):241–250, 2008.

Folloni, D., Verhagen, L., Mars, R.B., Fouragnan, E., and Aubry, J.f. Manipulation of deep brain activity in primates using transcranial focused ultrasound stimulation. *bioRxiv*, 2018.

Fry, F., Ades, H., and Fry, W. Production of Reversible Changes in the Central Nervous System by Ultrasound. *Science*, 127(3289):83–84, 1958.

Fry, F.J. and Barger, J.E. Acoustical properties of the human skull. *The Journal of the Acoustical Society of America*, 63(5):1576–1590, 1978.

Fry, W., Barnard, J., Fry, F., Krumins, R., and Brennan, J. Ultrasonic Lesions in the Mammalian Central Nervous System. *Science*, 122(3168):517–518, 1955.

Fry, W.J., Fry, F.J., Meyers, R., and Eggleton, R.G. The Use of Ultrasound in Neurosugery. *Proceedings of the Third International Conference on Medical Electronics*, 453–458. 1960.

Fry, W.J., Wulff, V.J., Tucker, D., and Fry, F.J. Physical Factors Involved in Ultrasonically Induced Changes in Living Systems: I. Identification of Non-Temperature Effects. *The Journal of the Acoustical Society of America*, 22(6):867–876, 1950.

Gateau, J., Aubry, J.F., Chauvet, D., Boch, A.L., Fink, M., et al. In vivo bubble nucleation probability in sheep brain tissue. *Physics in Medicine and Biology*, 56(22):7001–7015, 2011.

Gâteau, J., Marsac, L., Pernot, M., Aubry, J.F., Tanter, M.e.l., et al. Transcranial ultrasonic therapy based on time reversal of acoustically innduced cavitation bubble signature. *IEEE Transactions on Biomedical Engineering*, 57(1):134–144, 2010.

Gavrilov, L.R. Use of Focused Ultrasound for Stimulation of Various Neural Structures. *Ultrasonics*, 22(3):132–138, 1984.

Gavrilov, L.R., Gersuni, G.V., Ilyinski, O.B., Tsirulnikov, E.M., and Shchekanov, E.E. A study of reception with the use of focused ultrasound. I. Effects on the skin and deep receptor structures in man. *Brain Research*, 135(2):265–277, 1977a.

Gavrilov, L.R., Gersuni, G.V., Ilyinsky, O.B., Tsirulnikov, E.M., and Shchekanov, E.E. A study of reception with the use of focused ultrasound. II. Effects on the animal receptor structures. *Brain Research*, 135(2):279–285, 1977b.

Gavrilov, L.R. and Tsirulnikov, E.M. Focused ultrasound as a tool to input sensory information to humans (Review). *Acoustical Physics*, 58(1):1–21, 2012.

Gellner, A.K., Reis, J., and Fritsch, B. Glia: A Neglected Player in Non-invasive Direct Current Brain Stimulation. *Frontiers in Cellular Neuroscience*, 10(August):1–8, 2016.

Giordano, J., Bikson, M., Kappenman, E.S., Clark, V.P., Coslett, H.B., et al. Mechanisms and effects of transcranial direct current stimulation. *Dose-Response*, 15(1):1–22, 2017.

Gordon, G.W., Berry, G., Liang, X.H., Levine, B., and Herman, B. Quantitative fluorescence resonance energy transfer measurements using fluorescence microscopy. *Biophysical Journal*, 74(5):2702–2713, 1998.

Grossman, N., Bono, D., Dedic, N., Kodandaramaiah, S.B., Rudenko, A., et al. Noninvasive Deep Brain Stimulation via Temporally Interfering Electric Fields. *Cell*, 169(6):1029–1041, 2017.

Gulick, D.W., Li, T., Kleim, J.A., and Towe, B.C. Comparison of Electrical and Ultrasound Neurostimulation in Rat Motor Cortex. *Ultrasound in Medicine and Biology*, 43(12):2824–2833, 2017.

Guo, H., Hamilton II, M., Offutt, S.J., Gloeckner, C.D., Li, T., et al. Ultrasound Produces Extensive Brain Activation via a Cochlear Pathway. *Neuron*, 98(5):1020–1030, 2018.

Haacke, E.M., Mittal, S., Wu, Z., Neelavalli, J., and Cheng, Y.C. Susceptibility-weighted imaging: Technical aspects and clinical applications, part 1. *American Journal of Neuroradiology*, 30(1):19–30, 2009.

Hajian, M., Gaspar, R., and Maev, R.G. Accurate 3-D Profile Extraction of Skull Bone Using an Ultrasound Matrix Array. *IEEE Transactions on Biomedical Engineering*, 64(12):2858–2871, 2017.

Hameroff, S., Trakas, M., Duffield, C., Annabi, E., Gerace, M.B., et al. Transcranial ultrasound (TUS) effects on mental states: A pilot study. *Brain Stimulation*, 6(3):409–415, 2013.

Hamilton, N.B. and Attwell, D. Do astrocytes really exocytose neurotransmitters? *Nature Reviews Neuroscience*, 11(4):227–238, 2010.

Han, S., Kim, M., Kim, H., Shin, H., and Youn, I. Ketamine Inhibits Ultrasound Stimulation-Induced Neuromodulation by Blocking Cortical Neuron Activity. *Ultrasound in Medicine and Biology*, 44:635–646, 201.

Harris, F.M., Best, K.B., and Bell, J.D. Use of laurdan fluorescence intensity and polarization to distinguish between changes in membrane fluidity and phospholipid order. *Biochimica et Biophysica Acta - Biomembranes*, 1565(1):123–128, 2002.

Hasgall, P.A., Di Gennaro, F., Baumgartner, C., Neufeld, E., Lloyd, B., et al. IT'IS Database for thermal and electromagnetic parameters of biological tissues Version 4.0. 2018.
URL http://itis.swiss/database

Hashimoto, T., Elder, C.M., Okun, M.S., Patrick, S.K., and Vitek, J.L. Stimulation of the subthalamic nucleus changes the firing pattern of pallidal neurons. *The Journal of Neuroscience*, 23(5):1916–1923, 2003.

Haslehurst, P., Yang, Z., Dholakia, K., and Emptage, N. Fast volume-scanning light sheet microscopy reveals transient neuronal events. *Biomedical Optics Express*, 9(5):2154, 2018.

Haworth, K.J., Fowlkes, J.B., Carson, P.L., and Kripfgans, O.D. Towards Aberration Correction of Transcranial Ultrasound Using Acoustic Droplet Vaporization. *Ultrasound in Medicine and Biology*, 34(3):435–445, 2008.

Heimburg, T. The capacitance and electromechanical coupling of lipid membranes close to transitions: The effect of electrostriction. *Biophysical Journal*, 103(5):918–929, 2012.

Heimburg, T. and Jackson, A.D. On soliton propagation in biomembranes and nerves. *Proceedings of the National Academy of Sciences*, 102(28):9790–9795, 2005.

Herbert, E., Pernot, M., Montaldo, G., Tanter, M., and Fink, M. Energy-based adaptive focusing of waves: Application to ultrasonic transcranial therapy. *IEEE Transactions on Ultrasonics, Ferroelectrics and Frequency Control*, 56(11):2388–2399, 2009.

Herrmann, C.S., Rach, S., Neuling, T., and Strüber, D. Transcranial alternating current stimulation: a review of the underlying mechanisms and modulation of cognitive processes. *Frontiers in Human Neuroscience*, 7(June):1–13, 2013.

Hersh, D.S., Anastasiadis, P., Mohammadabadi, A., Nguyen, B.A., Guo, S., et al. MR-guided transcranial focused ultrasound safely enhances interstitial dispersion of large polymeric nanoparticles in the living brain. *PLoS ONE*, 13(2):e0192240, 2018.

Hertzberg, Y., Volovick, A., Zur, Y., Medan, Y., Vitek, S., et al. Ultrasound focusing using magnetic resonance acoustic radiation force imaging: application to ultrasound transcranial therapy. *Medical Physics*, 37(6):2934–2942, 2010.

Histed, M.H., Bonin, V., and Reid, R.C. Direct Activation of Sparse, Distributed Populations of Cortical Neurons by Electrical Microstimulation. *Neuron*, 63(4):508–522, 2009.

Histed, M.H., Ni, A.M., and Maunsell, J.H.R. Insights into cortical mechanisms of behavior from microstimulation experiments. *Progress in Neurobiology*, 103:115–130, 2013.

Ho, D.X.K., Tan, Y.C., Tan, J., Too, H.P., and Ng, W.H. High-frequency stimulation of the globus pallidus interna nucleus modulates GFRα1 gene expression in the basal ganglia. *Journal of Clinical Neuroscience*, 21(4):657–660, 2014.

Hodgkin, A.L. and Huxley, A.F. A quantitative description of membrane current and its application to conduction and excitation in nerve. *The Journal of physiology*, 117(4):500–544, 1952.

Hodgkin, A.L., Huxley, A.F., and Katz, B. The effect of sodium ions on the electrical activity of the giant axon of the squid. *The Journal of Physiology*, 116:424–448, 1952.

Hoffman, J.J., Nelson, A.M., Holland, M.R., and Miller, J.G. Cancellous bone fast and slow waves obtained with Bayesian probability theory correlate with porosity from computed tomography. *The Journal of the Acoustical Society of America*, 132(3):1830–1837, 2012.

Hosokawa, A. and Otani, T. Acoustic anisotropy in bovine cancellous bone. *Journal of the Acoustical Society of America*, 103(5):2718–2722, 1998.

Huang, Y. and Parra, L.C. Fully automated whole-head segmentation with improved smoothness and continuity, with theory reviewed. *PLoS ONE*, 10(5):1–34, 2015.

Hutchins, D.A., Mair, H.D., Puhach, P.A., and Osei, A.J. Continuous-wave pressure fields of ultrasonic transducers. *The Journal of the Acoustical Society of America*, 80(1):1–12, 1986.

Hynynen, K., Clement, G.T., McDannold, N., Vykhodtseva, N., King, R., et al. 500-Element ultrasound phased array system for noninvasive focal surgery of the brain: A preliminary rabbit study with ex vivo human skulls. *Magnetic Resonance in Medicine*, 52(1):100–107, 2004.

Hynynen, K. and Jolesz, F.A. Demonstration of potential noninvasive ultrasound brain therapy through an intact skull. *Ultrasound in Medicine and Biology*, 24(2):275–283, 1998.

Hynynen, K., McDannold, N., Sheikov, N.A., Jolesz, F.A., and Vykhodtseva, N. Local and reversible blood-brain barrier disruption by noninvasive focused ultrasound at frequencies suitable for trans-skull sonications. *NeuroImage*, 24(1):12–20, 2005.

Hynynen, K. and Sun, J. Trans-skull Ultrasound Therapy: The Feasibility of Using Image-Derived Skull Thickness Information to Correct the Phase Distortion. *IEEE Transactions on Ultrasonics, Ferroelectrics and Frequency Control*, 46(3):752–755, 1999.

Ibsen, S., Tong, A., Schutt, C., Esener, S., and Chalasani, S.H. Sonogenetics is a non-invasive approach to activating neurons in Caenorhabditis elegans. *Nature Communications*, 6:1–12, 2015.

Jalali, R., Miall, R.C., and Galea, J.M. No consistent effect of cerebellar transcranial direct current stimulation on visuomotor adaptation. *Journal of Neurophysiology*, 118(2):655–665, 2017.

Jing, Y., Meral, F.C., and Clement, G.T. Time-reversal transcranial ultrasound beam focusing using a k-space method. *Physics in Medicine and Biology*, 57(4):901–917, 2012.

Juan, E.J., Gonzalez, R., Albors, G., Ward, M.P., and Irazoqui, P. Vagus Nerve Modulation Using Focused Pulsed Ultrasound: Potential Applications and Preliminary Observations in a Rat. *International Journal Imaging System Technology*, 24(1):67–71, 2014.

Kamimura, H., Wang, S., Chen, H., Wang, Q., Aurup, C., et al. Pupil dilation and

motor response elicitation by ultrasound neuromodulation. *IEEE International Ultrasonics Symposium*, 2015.

Kamimura, H.A.S., Wang, S., Chen, H., Wang, Q., Aurup, C., et al. Focused ultrasound neuromodulation of cortical and subcortical brain structures using 1.9 MHz. *Medical Physics*, 43(10):5730, 2016.

Kanwisher, N. and Yovel, G. The fusiform face area: a cortical region specialized for the perception of faces. *Philosophical transactions of the Royal Society of London B*, 361(1476):2109–2128, 2006.

Kaye, E.a., Hertzberg, Y., Marx, M., Werner, B., Navon, G., et al. Application of Zernike polynomials towards accelerated adaptive focusing of transcranial high intensity focused ultrasound. *Medical Physics*, 39(10):6254, 2012.

Kaye, E.A. and Pauly, K.B. Adapting MRI Acoustic Radiation Force Imaging For In Vivo Human Brain Focused Ultrasound Applications. *Magnetic Resonance in Medicine*, 69(3):724–733, 2014.

Khraiche, M.L., Phillips, W.B., Jackson, N., and Muthuswamy, J. Ultrasound induced increase in excitability of single neurons. *2008 30th Annual International Conference of the IEEE Engineering in Medicine and Biology Society*, 4246–4249. 2008.

Kim, C.K., Adhikari, A., and Deisseroth, K. Integration of optogenetics with complementary methodologies in systems neuroscience. *Nature Reviews Neuroscience*, 18(4):222–235, 2017a.

Kim, G.H., Kosterin, P., Obaid, A.L., and Salzberg, B.M. A mechanical spike accompanies the action potential in mammalian nerve terminals. *Biophysical Journal*, 92(9):3122–3129, 2007.

Kim, H., Chiu, A., Lee, S.D., Fischer, K., and Yoo, S.S. Focused ultrasound-mediated non-invasive brain stimulation: Examination of sonication parameters. *Brain Stimulation*, 7(5):748–756, 2014a.

Kim, H., Lee, S.D., Chiu, A., Yoo, S.S., and Park, S. Estimation of the spatial profile of neuromodulation and the temporal latency in motor responses induced by focused ultrasound brain stimulation. *Neuroreport*, 25(7):475–479, 2014b.

Kim, H., Park, M.Y., Lee, S.D., Lee, W., Chiu, A., et al. Suppression of EEG visual-evoked potentials in rats through neuromodulatory focused ultrasound. *NeuroReport*, 26(4):211–215, 2015.

Kim, H., Taghados, S.J., Fischer, K., Maeng, L.S., Park, S., et al. Noninvasive Transcranial Stimulation of Rat Abducens Nerve by Focused Ultrasound. *Ultrasound in Medicine and Biology*, 38(9):1568–1575, 2012.

Kim, H.B., Swanberg, K.M., Han, H.S., Kim, J.C., Kim, J.W., et al. Prolonged stimulation with low-intensity ultrasound induces delayed increases in spontaneous hippocampal culture spiking activity. *Journal of Neuroscience Research*, 95(3):885–896, 2017b.

King, R.L., Brown, J.R., Newsome, W.T., and Pauly, K.B. Effective parameters for ultrasound-induced in vivo neurostimulation. *Ultrasound in Medicine and Biology*, 39(2):312–331, 2013.

King, R.L., Brown, J.R., and Pauly, K.B. Localization of Ultrasound-Induced In Vivo Neurostimulation in the Mouse Model. *Ultrasound in Medicine and Biology*, 40(7):1512–1522, 2014.

Kleiner, M., Brainard, D.H., and Pelli, D.G. What's new in Psychtoolbox-3? *Perception 36 EVCP Abstract Supplement*. 2007.

Klomjai, W., Katz, R., and Lackmy-Vallée, A. Basic principles of transcranial magnetic stimulation (TMS) and repetitive TMS (rTMS). *Annals of Physical and Rehabilitation Medicine*, 58(4):208–213, 2015.

Kodandaramaiah, S.B., Franzesi, G.T., Chow, B.Y., Boyden, E.S., and Forest, C.R. Automated whole-cell patch-clamp electrophysiology of neurons in vivo. *Nature Methods*, 9(6):585–587, 2012.

Kolsky, H. *Stress Waves in Solids*. Courier Corporation, 1963.

Koroleva, V.I., Vykhodtseva, N.I., and Elagin, V.A. Cortical and subcortical spreading depression in rats produced by focused ultrasound. *Neurophysiology*, 18(1):43–48, 1986.

Kubanek, J., Brown, J., Ye, P.P., Butts Pauly, K., and Newsome III, W.T. Transcranial ultrasound impacts monkey choice behaviour. *Cell Symposia: Big Questions in Neuroscience*. 2017a.

Kubanek, J., Shi, J., Marsh, J., Chen, D., Deng, C., et al. Ultrasound modulates ion channel currents. *Scientific Reports*, 6:1–14, 2016.

Kubanek, J., Shukla, P., Das, A., Baccus, S., and Goodman, M.B.B. Ultrasound elicits behavioral responses through mechanical effects on neurons and ion channels in a simple nervous system. *bioRxiv*, 2017b.

Kubanek, J., Shukla, P., Das, A., Baccus, S.A., and Goodman, M.B. Ultrasound Elicits Behavioral Responses through Mechanical Effects on Neurons and Ion Channels in a Simple Nervous System. *The Journal of Neuroscience*, 38(12):3081–3091, 2018.

Kusch, J. and Zifarelli, G. Patch-clamp fluorometry: Electrophysiology meets fluorescence. *Biophysical Journal*, 106(6):1250–1257, 2014.

Kyriakou, A., Neufeld, E., Werner, B., Székely, G., and Kuster, N. Full-wave acoustic and thermal modeling of transcranial ultrasound propagation and investigation of skull-induced aberration correction techniques: a feasibility study. *Journal of Therapeutic Ultrasound*, 3(11):1–18, 2015.

Lampl, I., Reichova, I., and Ferster, D. Synchronous membrane potential fluctuations in neurons of the cat visual cortex. *Neuron*, 22(2):361–74, 1999.

Landau, L. and Lifshitz, E. *Fluid Mechanics. Course of Theoretical Physics.* Elsevier, 1987.

Larrat, B., Pernot, M., Montaldo, G., Fink, M., and Tanter, M. MR-guided adaptive focusing of ultrasound. *IEEE Transactions on Ultrasonics, Ferroelectrics, and Frequency Control*, 57(8):1734–1747, 2010.

Leduc, N., Okita, K., Sugiyama, K., Takagi, S., and Matsumoto, Y. Focus control in HIFU therapy assisted by time-reversal simulation with an iterative procedure for hot spot elimination. *Journal of Biomechanical Science and Engineering*, 7(1):43–56, 2012.

Lee, J.C.F., Callaway, J.C., and Foehring, R.C. Effects of Temperature on Calcium Transients and Ca 2+ -Dependent Afterhyperpolarizaions in Neocortical Pyramidal Neurons. *Journal of Neurophysiology*, 93:2012–2020, 2005.

Lee, J.H., Hong, H.K., Song, B.w., Jung, Y.J., Na, Y.C., et al. Preliminary study on Low Intensity Focused Ultrasound System For Neuromodulation. *Engineering in Medicine and Biology Society 39th Annual International Conference of the IEEE*, 4545–4548. 2017.

Lee, W., Chung, Y.A., Jung, Y., Song, I.U., and Yoo, S.S. Simultaneous acoustic stimulation of human primary and secondary somatosensory cortices using transcranial focused ultrasound. *BMC Neuroscience*, 17(1):1–11, 2016a.

Lee, W., Kim, H., Jung, Y., Song, I.U., Chung, Y.A., et al. Image-guided transcranial focused ultrasound stimulates human primary somatosensory cortex. *Scientific Reports*, 5:8743, 2015.

Lee, W., Kim, H., Lee, S., Yoo, S.S., and Chung, Y.A. Creation of various skin sensations using pulsed focused ultrasound: Evidence for functional neuromodulation. *International Journal of Imaging Systems and Technology*, 24(2):167–174, 2014.

Lee, W., Kim, H.C., Jung, Y., Chung, Y.A., Song, I.U., et al. Transcranial focused ultrasound stimulation of human primary visual cortex. *Scientific Reports*, 6(May):34026, 2016b.

Lee, W., Lee, S.D., Park, M.Y., Foley, L., Purcell-Estabrook, E., et al. Image-Guided

Focused Ultrasound-Mediated Regional Brain Stimulation in Sheep. *Ultrasound in Medicine and Biology*, 42(2):459–470, 2016c.

Legon, W., Ai, L., Bansal, P., and Mueller, J.K. Neuromodulation with single-element transcranial focused ultrasound in human thalamus. *Human Brain Mapping*, 39(5):1995–2006, 2018a.

Legon, W., Bansal, P., Tyshynsky, R., Ai, L., and Mueller, J.K. Transcranial focused ultrasound neuromodulation of the human primary motor cortex. *Scientific Reports*, 8(1):10007, 2018b.

Legon, W., Rowlands, A., Opitz, A., Sato, T.F., and Tyler, W.J. Pulsed Ultrasound Differentially Stimulates Somatosensory Circuits in Humans as Indicated by EEG and fMRI. *PLoS ONE*, 7(12):e51177, 2012.

Legon, W., Sato, T.F., Opitz, A., Mueller, J., Barbour, A., et al. Transcranial focused ultrasound modulates the activity of primary somatosensory cortex in humans. *Nature Neuroscience*, 17(2):322–329, 2014.

Lele, P. The effects of focused ultrasonic radiation on the peripheral nerves, with observations on local heating. *Ultrasonics*, 1(4):III, 1963.

Li, F., Yang, C., Yuan, F., Liao, D., Li, T., et al. Dynamics and mechanisms of intracellular calcium waves elicited by tandem bubble-induced jetting flow. *Proceedings of the National Academy of Sciences*, 115(3):E353–E362, 2018.

Li, G.F., Zhao, H.X., Zhou, H., Yan, F., Wang, J.Y., et al. Improved Anatomical Specificity of Non-invasive Neuro-stimulation by High Frequency (5 MHz) Ultrasound. *Scientific Reports*, 6:24738, 2016.

Lin, W.T., Chen, R.C., Lu, W.W., Liu, S.H., and Yang, F.Y. Protective effects of low-intensity pulsed ultrasound on aluminum-induced cerebral damage in Alzheimer's disease rat model. *Scientific Reports*, 5:9671, 2015.

Lipsman, N., Mainprize, T.G., Schwartz, M.L., Hynynen, K., and Lozano, A.M. Intracranial Applications of Magnetic Resonance-guided Focused Ultrasound. *Neurotherapeutics*, 11(3):593–605, 2014.

Lipsman, N., Meng, Y., Bethune, A.J., Huang, Y., Lam, B., et al. Blood–brain barrier opening in Alzheimer's disease using MR-guided focused ultrasound. *Nature Communications*, 9(1):1–8, 2018.

Little, S., Pogosyan, A., Neal, S., Zavala, B., Zrinzo, L., et al. Adaptive deep brain stimulation in advanced Parkinson disease. *Annals of Neurology*, 74(3):449–457, 2013.

Liu, S.H., Lai, Y.L., Chen, B.L., and Yang, F.Y. Ultrasound Enhances the Expression of Brain-Derived Neurotrophic Factor in Astrocyte Through Activation of

TrkB-Akt and Calcium-CaMK Signaling Pathways. *Cerebral Cortex*, 27(6):3152–3160, 2017.

Liu, Y., Fite, B.Z., Mahakian, L.M., Johnson, S.M., Larrat, B., et al. Concurrent Visualization of Acoustic Radiation Force Displacement and Shear Wave Propagation with 7T MRI. *PloS ONE*, 10(10):e0139667, 2015.

Lumen-Learning. Biological Foundations of Psychology. 2017. URL https://courses.lumenlearning.com/boundless-psychology/chapter/neurons/

Luzzati, V., Mateu, L., Marquez, G., and Borgo, M. Structural and electrophysiological effects of local anesthetics and of low temperature on myelinated nerves: Implication of the lipid chains in nerve excitability. *Journal of Molecular Biology*, 286(5):1389–1402, 1999.

Macé, E., Montaldo, G., Cohen, I., Baulac, M., Fink, M., et al. Functional ultrasound imaging of the brain. *Nature Methods*, 8(8):662–666, 2011.

Magara, A., Bühler, R., Moser, D., Kowalski, M., Pourtehrani, P., et al. First experience with MR-guided focused ultrasound in the treatment of Parkinson's disease. *Journal of Therapeutic Ultrasound*, 2(11), 2014.

Maimbourg, G., Houdouin, A., Deffieux, T., Tanter, M., and Aubry, J.F. 3D-printed adaptive acoustic lens as a disruptive technology for transcranial ultrasound therapy using single-element transducers. *Physics in Medicine and Biology*, 63:025026, 2018.

Marino, A., Arai, S., Hou, Y., Sinibaldi, E., Pellegrino, M., et al. Piezoelectric Nanoparticle-Assisted Wireless Neuronal Stimulation. *ACS Nano*, 9(7):7678–7689, 2015.

Marquet, F., Pernot, M., Aubry, J.F., Montaldo, G., Marsac, L., et al. Non-invasive transcranial ultrasound therapy based on a 3D CT scan: protocol validation and in vitro results. *Physics in Medicine and Biology*, 54(9):2597–613, 2009.

Marsac, L., Chauvet, D., Larrat, B., Pernot, M., Robert, B., et al. MR-guided adaptive focusing of therapeutic ultrasound beams in the human head. *Medical Physics*, 39(2):1141–9, 2012.

Martin, E., Werner, B., Bauer, R., Leyen, K.V., Coluccia, D., et al. Clinical neurological HIFU applications : the Zurich experience. *Translational Cancer Research*, 3(5):449–458, 2014.

McDannold, N., Arvanitis, C.D., Vykhodtseva, N., and Livingstone, M.S. Temporary disruption of the blood-brain barrier by use of ultrasound and microbubbles: Safety and efficacy evaluation in rhesus macaques. *Cancer Research*, 72(14):3652–3663, 2012.

McDannold, N., Vykhodtseva, N., and Hynynen, K. Effects of acoustic parameters and ultrasound contrast agent dose on focused-ultrasound induced blood-brain barrier disruption. *Ultrasound in Medicine and Biology*, 34(4):930–937, 2008.

Mehić, E., Xu, J.M., Caler, C.J., Coulson, N.K., Moritz, C.T., et al. Increased anatomical specificity of neuromodulation via modulated focused ultrasound. *PLoS ONE*, 9(2):e86939, 2014.

Mellow, T. On the sound field of a resilient disk in free space. *The Journal of the Acoustical Society of America*, 123(4):1880–1891, 2008.

Menz, M., Ye, P., Firouzi, K., Pauly, K.B., Khuri-Yakub, P., et al. Physical mechanisms of ultrasonic neurostimulation in the in vitro retina. *bioRxiv*, 2017.

Menz, M.D., Oralkan, O., Khuri-Yakub, P.T., and Baccus, S.A. Precise Neural Stimulation in the Retina Using Focused Ultrasound. *Journal of Neuroscience*, 33(10):4550–4560, 2013.

Mihran, R.T., Barnes, F.S., and Wachtel, H. Temporally-specific modification of myelinated axon excitability in vitro following a single ultrasound pulse. *Ultrasound in Medicine and Biology*, 16(3):297–309, 1990.

Min, B.K., Bystritsky, A., Jung, K.I., Fischer, K., Zhang, Y., et al. Focused ultrasound-mediated suppression of chemically-induced acute epileptic EEG activity. *BMC Neuroscience*, 12(23), 2011a.

Min, B.K., Yang, P.S., Bohlke, M., Park, S., Vago, D.R., et al. Focused Ultrasound Modulates the Level of Cortical Neurotransmitters: Potential as a New Functional Brain Mapping Technique. *International Journal of Imaging Systems and Technology*, 21(2):232–240, 2011b.

Min, R. and Nevian, T. Astrocyte signaling controls spike timing-dependent depression at neocortical synapses. *Nature Neuroscience*, 15(5):746–753, 2012.

Minarik, T., Berger, B., Althaus, L., Bader, V., Biebl, B., et al. The Importance of Sample Size for Reproducibility of tDCS Effects. *Frontiers in Human Neuroscience*, 10:453, 2016.

Monti, M.M., Schnakers, C., Korb, A.S., Bystritsky, A., and Vespa, P.M. Non-Invasive Ultrasonic Thalamic Stimulation in Disorders of Consciousness after Severe Brain Injury: a First-in-Man Report. *Brain Stimulation*, 9(6):940–941, 2016.

Moore, M.E., Loft, J.M., Clegern, W.C., and Wisor, J.P. Manipulating neuronal activity in the mouse brain with ultrasound: A comparison with optogenetic activation of the cerebral cortex. *Neuroscience Letters*, 604:183–187, 2015.

Morris, C.E. Why are so many ion channels mechanosensitive? *Cell Physiology Source Book*, 493–505, 2012.

Morse, P.M. and Ingard, K.U. *Theoretical Acoustics*, volume 38. Princeton University Press, 1968.

Mueller, J., Legon, W., Opitz, A., Sato, T.F., and Tyler, W.J. Transcranial focused ultrasound modulates intrinsic and evoked EEG dynamics. *Brain Stimulation*, 7(6):900–908, 2014.

Mueller, J.K., Ai, L., Bansal, P., and Legon, W. Numerical evaluation of the skull for human neuromodulation with transcranial focused ultrasound. *Journal of Neural Engineering*, 14(6):066012, 2017.

Mueller, J.K. and Tyler, W.J. A quantitative overview of biophysical forces impinging on neural function. *Physical Biology*, 11(5):051001, 2014.

Neher, E. and Sakmann, B. Single-channel currents recorded from membrane of denervated frog muscle fibres. *Nature*, 260(5554):799–802, 1976.

Newman, E.a. and Zahs, K.R. Modulation of neuronal activity by glial cells in the retina. *The Journal of Neuroscience*, 18(11):4022–4028, 1998.

Ni, X.J., Wang, X.D., Zhao, Y.H., Sun, H.L., Hu, Y.M., et al. The Effect of Low-Intensity Ultrasound on Brain-Derived Neurotropic Factor Expression in a Rat Sciatic Nerve Crushed Injury Model. *Ultrasound in Medicine and Biology*, 43(2):1–8, 2016.

Nitsche, M.A., Cohen, L.G., Wassermann, E.M., Priori, A., Lang, N., et al. Transcranial direct current stimulation: State of the art 2008. *Brain Stimulation*, 1(3):206–223, 2008.

Nyborg, W.L. *Acoustic streaming, Physical acoustics*. 1965.

Nyborg, W.L. Heat generation by ultrasound in a relaxing medium. *The Journal of the Acoustical Society of America*, 70(2):310–312, 1981.

Obien, M.E.J., Deligkaris, K., Bullmann, T., Bakkum, D.J., and Frey, U. Revealing neuronal function through microelectrode array recordings. *Frontiers in Neuroscience*, 9(JAN):423, 2015.

O'Neil, H. Theory of Focusing Radiators. *The Journal of the Acoustical Society of America*, 21(5):516–526, 1949.

Oostenveld, R., Fries, P., Maris, E., and Schoffelen, J.M. FieldTrip: Open source software for advanced analysis of MEG, EEG, and invasive electrophysiological data. *Computational Intelligence and Neuroscience*, 2011, 2011.

Padamsey, Z. and Emptage, N.J. Imaging synaptic plasticity. *Molecular Brain*, 4(1):1–10, 2011.

Palmeri, M.L. and Nightingale, K.R. Acoustic radiation force-based elasticity imaging methods. *Interface Focus*, 1(4):553–564, 2011.

Pan, Y., Yoon, S., Sun, J., Huang, Z., Lee, C., et al. Mechanogenetics for the remote and noninvasive control of cancer immunotherapy. *Proceedings of the National Academy of Sciences*, 115(16):992–997, 2018.

Paredes, R.M., Etzler, J.C., Watts, L.T., and Lechleiter, J.D. Chemical Calcium Indicators. *Methods*, 46(3):143–151, 2009.

Pennes, H.H. Analysis of Tissue and Arterial Blood Temperature in the Resting Human Forearm. *Journal of Applied Physiology*, 1(2):93–122, 1948.

Pérez Koldenkova, V. and Nagai, T. Genetically encoded Ca2+indicators: Properties and evaluation. *Biochimica et Biophysica Acta - Molecular Cell Research*, 1833(7):1787–1797, 2013.

Perlmutter, J.S. and Mink, J.W. Deep Brain Stimulation. *Annual Review of Neuroscience*, 29(1):229–257, 2006.

Pernot, M., Montaldo, G., Tanter, M., and Fink, M. "Ultrasonic stars" for time-reversal focusing using induced cavitation bubbles. *Applied Physics Letters*, 88(3):1–3, 2006.

Pierce, A. *Acoustics: An Introduction to Its Physical Principles and Applications*. Acoustical Society of America, 1990.

Pinton, G., Aubry, J.F., Bossy, E., Muller, M., Pernot, M., et al. Attenuation, scattering, and absorption of ultrasound in the skull bone. *Medical Physics*, 39(1):299, 2012a.

Pinton, G., Aubry, J.F., Fink, M., and Tanter, M. Effects of nonlinear ultrasound propagation on high intensity brain therapy. *Medical Physics*, 38(3):1207–1216, 2011.

Pinton, G.F., Aubry, J.F., Fink, M., and Tanter, M. Numerical prediction of frequency dependent 3D maps of mechanical index thresholds in ultrasonic brain therapy. *Proceedings - IEEE Ultrasonics Symposium*, 455(2012):2258–2261, 2010.

Pinton, G.F., Aubry, J.F., and Tanter, M. Direct phase projection and transcranial focusing of ultrasound for brain therapy. *IEEE Transactions on Ultrasonics, Ferroelectrics, and Frequency Control*, 59(6):1149–1159, 2012b.

Plaksin, M., Shoham, S., and Kimmel, E. Intramembrane cavitation as a predictive bio-piezoelectric mechanism for ultrasonic brain stimulation. *Physical Review X*, 4(1):1–10, 2014.

Plesset, M.S. and Prosperetti, A. Bubble Dynamics and Cavitation. *Annual Review of Fluid Mechanics*, 9(1):145–185, 1977.

Pogoda, K. and Janmey, P.A. Glial Tissue Mechanics and Mechanosensing by Glial Cells. *Frontiers in Cellular Neuroscience*, 12:25, 2018.

Polanía, R., Nitsche, M.A., and Ruff, C.C. Studying and modifying brain function with non-invasive brain stimulation. *Nature Neuroscience*, 21:174–187, 2018.

Prieto, M.L., Firouzi, K., Khuri-Yakub, B.T., and Maduke, M. Mechanical Activation Of Piezo1 But Not Nav1.2 Channels By Ultrasound. *Ultrasound in Medicine and Biology*, 44(6):1217–1232, 2018.

Pulkkinen, A., Huang, Y., Song, J., and Hynynen, K. Simulations and measurements of transcranial low-frequency ultrasound therapy: skull-base heating and effective area of treatment. *Physics in Medicine and Biology*, 56(15):4661–4683, 2011.

Rajasethupathy, P., Sankaran, S., Marshel, J.H., Kim, C.K., Ferenczi, E., et al. Projections from neocortex mediate top-down control of memory retrieval. *Nature*, 526(7575):653–659, 2015.

Ram, Z., Cohen, Z.R., Harnof, S., Tal, S., Faibel, M., et al. Magnetic resonance imaging-guided, high-intensity focused ultrasound for brain tumor therapy. *Neurosurgery*, 59(5):946–956, 2006.

Rho, J.Y., Hobatho, M.C., and Ashman, R.B. Relations of mechanical properties to density and CT numbers in human bone. *Medical Engineering and Physics*, 17(5):347–355, 1995.

Rieke, V. and Pauly, K.B. MR thermometry. *Journal of Magnetic Resonance Imaging*, 27(2):376–390, 2008.

Rinaldi, P.C., Jones, J.P., Reines, F., and Price, L.R. Modification by focused ultrasound pulses of electrically evoked responses from an in vitro hippocampal preparation. *Brain Research*, 558(1):36–42, 1991.

Robertson, J.L.B., Cox, B.T., Jaros, J., and Treeby, B.E. Simulation of transcranial ultrasound propagation for ultrasonic neuromodulation and stimulation. *The Journal of the Acoustical Society of America*, 141(3):1726–1738, 2017a.

Robertson, J.L.B., Martin, E., Cox, B.T., and Treeby, B.E. Sensitivity of simulated transcranial ultrasound fields to acoustic medium property maps. *Physics in Medicine and Biology*, 62(7):2559–2580, 2017b.

Rojas, C., Tedesco, M., Massobrio, P., and Marino, A. Acoustic stimulation can induce a selective neural network response mediated by piezoelectric nanoparticles. *Journal of Neural Engineering*, 15(3):036016, 2018.

Ross, W.N. and Manita, S. Understanding calcium waves and sparks in central neurons. *Nature Reviews Neuroscience*, 13(3):157–168, 2012.

Rossi, S., Hallett, M., Rossini, P.M., Pascual-Leone, A., Avanzini, G., et al. Safety, ethical considerations, and application guidelines for the use of transcranial magnetic stimulation in clinical practice and research. *Clinical Neurophysiology*, 120(12):2008–2039, 2009.

Rubin, J.E. and Terman, D. High frequency stimulation of the subthalamic nucleus eliminates pathological thalamic rhythmicity in a computational model. *Journal of Computational Neuroscience*, 16(3):211–235, 2004.

Sakmann, B. and Neher, E. Patch Clamp Techniques for Studying Ionic Channels in Excitable Membranes. *Annual Review of Physiology*, 46(1):455–472, 1984.

Sapozhnikov, O.A., Tsysar, S.A., Khokhlova, V.A., and Kreider, W. Acoustic holography as a metrological tool for characterizing medical ultrasound sources and fields. *The Journal of the Acoustical Society of America*, 138(3):1515–1532, 2015.

Sato, T., Shapiro, M.G., and Tsao, D.Y. Ultrasonic Neuromodulation Causes Widespread Cortical Activation via an Indirect Auditory Mechanism. *Neuron*, 98(5):1031–1041, 2018.

Saxe, R.R. The right temporo-parietal junction: a specific brain region for thinking about thoughts. *Handbook of Theory of Mind*, 1–35, 2010.

Schelling, G., Delius, M., Gschwender, M., Grafe, P., and Gambihler, S. Extracorporeal shock waves stimulate frog sciatic nerves indirectly via a cavitation-mediated mechanism. *Biophysical Journal*, 66(1):133–140, 1994.

Seip, R., VanBaren, P., and Ebbini, E.S. Dynamic focusing in ultrasound hyperthermia treatments using implantable hydrophone arrays. *IEEE Transactions on Ultrasonics, Ferroelectrics, and Frequency Control*, 41(5):706–713, 1994.

Shapiro, M.G., Homma, K., Villarreal, S., Richter, C.P., and Bezanilla, F. Infrared light excites cells by changing their electrical capacitance. *Nature Communications*, 3:310–376, 2012.

Sheikov, N., McDannold, N., Sharma, S., and Hynynen, K. Effect of Focused Ultrasound Applied With an Ultrasound Contrast Agent on the Tight Junctional Integrity of the Brain Microvascular Endothelium. *Ultrasound in Medicine and Biology*, 34(7):1093–1104, 2008.

Shrivastava, S. and Schneider, M.F. Evidence for two-dimensional solitary sound waves in a lipid controlled interface and its implications for biological signalling. *Journal of The Royal Society Interface*, 11(97):20140098, 2014.

Sineshchekov, O.A., Jung, K.H., and Spudich, J.L. Two rhodopsins mediate photo-

taxis to low- and high-intensity light in Chlamydomonas reinhardtii. *Proceedings of the National Academy of Sciences*, 99(13):8689–8694, 2002.

Song, J., Pulkkinen, A., Huang, Y., and Hynynen, K. Investigation of standing-wave formation in a human skull for a clinical prototype of a large-aperture, transcranial MR-guided focused ultrasound (MRgFUS) phased array: An experimental and simulation study. *IEEE Transactions on Biomedical Engineering*, 59(2):435–444, 2012.

Sun, J. and Hynynen, K. Focusing of therapeutic ultrasound through a human skull: A numerical study. *The Journal of the Acoustical Society of America*, 104(3):1705, 1998.

Tanter, M., Thomas, J.l., and Fink, M. Focusing and steering through absorbing and aberrating layers: Application to ultrasonic propagation through the skull. *The Journal of the Acoustical Society of America*, 103(5):2403–2410, 1998.

Tasaki, I. Mechanical and thermal changes in the Torpedo electric organ associated with its postsynaptic potentials. *Biochemical and Biophysical Research Communications*, 215(2):654–658, 1995.

Tasaki, I., Watanabe, A., and Takenaka, T. Resting and action potential of intracellularly perfused squid giant axon. *Proceedings of the National Academy of Sciences*, 48(7):1177–1184, 1962.

Tatat, D.B. and Dunn, F. Ultrasound and Model Membrane Systems: Analyses and Predictions. *The Journal of Physical Chemistry*, 3548–3555, 1992.

Tehovnik, E.J. Direct and Indirect Activation of Cortical Neurons by Electrical Microstimulation. *Journal of Neurophysiology*, 96(2):512–521, 2006.

ter Haar, G. Ultrasound bio-effects and safety considerations. *Proceedings of the Institution of Mechanical Engineers, Part H: Journal of Engineering in Medicine*, volume 224, 363–373. 2010.

Terney, D., Chaieb, L., Moliadze, V., Antal, A., and Paulus, W. Increasing Human Brain Excitability by Transcranial High-Frequency Random Noise Stimulation. *Journal of Neuroscience*, 28(52):14147–14155, 2008.

Thomas, J.L. and Fink, M.A. Ultrasonic beam focusing through tissue inhomogeneities with a time reversal mirror: application to transskull therapy. *IEEE Transactions on Ultrasonics, Ferroelectrics, and Frequency Control*, 43(6):1122–1129, 1996.

Thomas, J.L., Wu, F., and Fink, M. Time reversal focusing applied to lithotripsy. *Ultrasonic Imaging*, 18(2):106–21, 1996.

Thompson, S.M., Masukawa, L.M., and Prince, D.A. Temperature dependence

of intrinsic membrane properties and synaptic potentials in hippocampal CA1 neurons in vitro. *The Journal of Neuroscience*, 5(3):817–824, 1985.

Top, C.B., White, P.J., and McDannold, N.J. Nonthermal ablation of deep brain targets: A simulation study on a large animal model. *Medical Physics*, 43(2):870–882, 2016.

Treat, L.H., McDannold, N., Vykhodtseva, N., Zhang, Y., Tam, K., et al. Targeted delivery of doxorubicin to the rat brain at therapeutic levels using MRI-guided focused ultrasound. *International Journal of Cancer*, 121(4):901–907, 2007.

Treeby, B.E. and Cox, B.T. k-Wave: MATLAB toolbox for the simulation and reconstruction of photoacoustic wave fields. *Journal of Biomedical Optics*, 15(2), 2010a.

Treeby, B.E. and Cox, B.T. Modeling power law absorption and dispersion for acoustic propagation using the fractional Laplacian. *The Journal of the Acoustical Society of America*, 127(5):2741, 2010b.

Treeby, B.E. and Cox, B.T. Modeling power law absorption and dispersion in viscoelastic solids using a split-field and the fractional Laplacian. *The Journal of the Acoustical Society of America*, 136(4):1499–1510, 2014.

Treeby, B.E., Jaros, J., Rendell, A.P., and Cox, B.T. Modeling nonlinear ultrasound propagation in heterogeneous media with power law absorption using a k-space pseudospectral method. *The Journal of the Acoustical Society of America*, 131(6):4324–4336, 2012.

Treeby, B.E., Jaros, J., Rohrbach, D., and Cox, B.T. Modelling elastic wave propagation using the k-Wave MATLAB Toolbox. *IEEE International Ultrasonics Symposium*, 5, 146–149. 2014.

Trefethen, L. *Spectral methods in MATLAB*. Siam, 2000.

Tsairas, A. The Visual MD. 2014.
URL http://www.thevisualmd.com

Tsui, P.H., Wang, S.H., and Huang, C.C. In vitro effects of ultrasound with different energies on the conduction properties of neural tissue. *Ultrasonics*, 43(7):560–565, 2005.

Tufail, Y., Matyushov, A., Baldwin, N., Tauchmann, M.L., Georges, J., et al. Transcranial Pulsed Ultrasound Stimulates Intact Brain Circuits. *Neuron*, 66(5):681–694, 2010.

Tych, R.E., Gofeld, M., Jarvik, J.G., Kliot, M., Loeser, J.D., et al. Neuropathic tissue responds preferentially to stimulation by intense focused ultrasound. *Ultrasound in Medicine and Biology*, 39(1):111–116, 2013.

Tyler, W.J. The mechanobiology of brain function. *Nature Reviews Neuroscience*, 13(12):867–878, 2012.

Tyler, W.J., Tufail, Y., Finsterwald, M., Tauchmann, M.L., Olson, E.J., et al. Remote excitation of neuronal circuits using low-intensity, low-frequency ultrasound. *PLoS ONE*, 3(10), 2008.

Urban, M.W., Restrepo, M.B., and Greenleaf, J.F. Phase aberration correction using ultrasound radiation force and vibrometry optimization. *IEEE Transactions on Ultrasonics, Ferroelectrics and Frequency Control*, 54(6):132–135, 2007.

Van Essen, D.C., Ugurbil, K., Auerbach, E., Barch, D., Behrens, T.E., et al. The Human Connectome Project: A data acquisition perspective. *NeuroImage*, 62(4):2222–2231, 2012.

Verhagen, L., Gallea, C., Folloni, D., and Constans, C. Offline impact of transcranial focused ultrasound on cortical activation in primates. *bioRxiv*, 2018.

Wahab, R.A., Choi, M., Liu, Y., Krauthamer, V., Zderic, V., et al. Mechanical bioeffects of pulsed high intensity focused ultrasound on a simple neural model. *Medical Physics*, 39(7):4274–4283, 2012.

Walsh, V. and Cowey, A. Transcranial magnetic stimulation and cognitive neuroscience. *Nature Reviews Neuroscience*, 1(1):73–9, 2000.

Wang, J.H. and Thampatty, B.P. An introductory review of cell mechanobiology. *Biomechanics and Modeling in Mechanobiology*, 5(1):1–16, 2006.

Wang, T.R., Dallapiazza, R., and Elias, W.J. Neurological applications of transcranial high intensity focused ultrasound. *International Journal of Hyperthermia*, 31(3):285–291, 2015.

Wattiez, N., Constans, C., Deffieux, T., Daye, P.M., Tanter, M., et al. Transcranial ultrasonic stimulation modulates single-neuron discharge in macaques performing an antisaccade task. *Brain Stimulation*, 10(6):1024–1031, 2017.

White, D.N., Curry, G.R., and Stevenson, R.J. The acoustic characteristics of the skull. *Ultrasound in Medicine and Biology*, 4(3):225–252, 1978.

White, P.J., Hynynen, K., and Clement, G.T. Longitudinal and shear mode ultrasound propagation in human skull bone. *Ultrasound in Medicine and Biology*, 32(7):1085–1096, 2006.

Williams, J.L. Ultrasonic wave propagation in cancellous and cortical bone: Prediction of some experimental results by Biot's theory. *The Journal of the Acoustical Society of America*, 91(2):1106–1112, 1992.

Wilson, S., Lockwood, R., Thickbroom, G., and Mastaglia, F. The muscle silent

period following transcranial magnetic cortical stimulation. *Journal of the Neurological Sciences*, 114(2):216–222, 1993.

Wright, C.J., Haqshenas, S.R., Rothwell, J., and Saffari, N. Unmyelinated Peripheral Nerves Can Be Stimulated in Vitro Using Pulsed Ultrasound. *Ultrasound in Medicine and Biology*, 43(10):2269–2283, 2017.

Wright, C.J., Rothwell, J., and Saffari, N. Ultrasonic stimulation of peripheral nervous tissue: an investigation into mechanisms. *Journal of Physics: Conference Series*, volume 581, 012003. 2015.

Wunderlich, B., Leirer, C., Idzko, A.L., Keyser, U.F., Wixforth, A., et al. Phase-state dependent current fluctuations in pure lipid membranes. *Biophysical Journal*, 96(11):4592–4597, 2009.

Xu, Z., Carlson, C., Snell, J., Eames, M., Hananel, A., et al. Intracranial inertial cavitation threshold and thermal ablation lesion creation using MRI-guided 220-kHz focused ultrasound surgery: preclinical investigation. *Journal of Neurosurgery*, 122(1):152–161, 2015.

Yang, F.Y., Lu, W.W., Lin, W.T., Chang, C.W., and Huang, S.L. Enhancement of Neurotrophic Factors in Astrocyte for Neuroprotective Effects in Brain Disorders Using Low-intensity Pulsed Ultrasound Stimulation. *Brain stimulation*, 8(3):465–473, 2015.

Yang, P.S., Kim, H., Lee, W., Bohlke, M., Park, S., et al. Transcranial focused ultrasound to the thalamus is associated with reduced extracellular GABA levels in rats. *Neuropsychobiology*, 65(3):153–160, 2012.

Yang, T., Hakimian, S., and Schwartz, T.H. Intraoperative electroCorticoGraphy (ECog): Indications, techniques, and utility in epilepsy surgery. *Epileptic Disorders*, 16(3):271–279, 2014.

Yarkoni, T., Poldrack, R.A., Nichols, T.E., Van Essen, D.C., and Wager, T.D. Large-scale automated synthesis of human functional neuroimaging data. *Nature Methods*, 8(8):665–670, 2011.

Ye, P.P., Brown, J.R., and Pauly, K.B. Frequency Dependence of Ultrasound Neurostimulation in the Mouse Brain. *Ultrasound in Medicine and Biology*, 42(7):1512–1530, 2015.

Yin, X. and Hynynen, K. A numerical study of pulsed sonication for reducing thermal deposition in the skull during transcranial focused ultrasound surgery. *Proceedings - IEEE Ultrasonics Symposium*, volume 2, 1241–1244. 2005.

Yoo, S.S., Bystritsky, A., Lee, J.H., Zhang, Y., Fischer, K., et al. Focused ultrasound modulates region-specific brain activity. *NeuroImage*, 56(3):1267–1275, 2011a.

Yoo, S.S., Kim, H., Min, B.K., and Franck, S.P.E. Transcranial Focused Ultrasound to the Thalamus Alters Anesthesia Time in Rats. *Neuroreport*, 22(15):783–787, 2011b.

Younan, Y., Deffieux, T., Larrat, B., Fink, M., Tanter, M., et al. Influence of the pressure field distribution in transcranial ultrasonic neurostimulation. *Medical Physics*, 40(8):082902, 2013.

Young, R.R. and Henneman, E. Functional Effects of Focused Ultrasound on Mammalian Nerves. *Science*, 134(3489):1521–1522, 1961.

Yu, K., Sohrabpour, A., and He, B. Electrophysiological Source Imaging of Brain Networks Perturbed by Low-Intensity Transcranial Focused Ultrasound. *IEEE Transactions on Biomedical Engineering*, 63(9):1787–1794, 2016.

Zangen, A., Roth, Y., Voller, B., and Hallett, M. Transcranial magnetic stimulation of deep brain regions: Evidence for efficacy of the H-Coil. *Clinical Neurophysiology*, 116(4):775–779, 2005.

Zemelman, B.V., Lee, G.A., Ng, M., and Miesenböck, G. Selective photostimulation of genetically chARGed neurons. *Neuron*, 33(1):15–22, 2002.

Zhao, L., Feng, Y., Shi, A., Zhang, L., Guo, S., et al. Neuroprotective Effect of Low-Intensity Pulsed Ultrasound Against MPP+-Induced Neurotoxicity in PC12 Cells: Involvement of K2P Channels and Stretch-Activated Ion Channels. *Ultrasound in Medicine and Biology*, 43(9):1986–1999, 2017.

Ziemann, U., Rothwell, J.C., and Ridding, M.C. Interaction between intracortical inhibition and facilitation in human motor cortex. *Journal of Physiology*, 496(3):873–881, 1996.